# PALACKÝ UNIVERSITY OLOMOUC

## Faculty of Science

# Modeling of electronic and optical properties of two-dimensional materials

Habilitation thesis

František Karlický

Olomouc 2024

# UNIVERZITA PALACKÉHO V OLOMOUCI
## Přírodovědecká fakulta

# Modelování elektronických a optických vlastností dvojrozměrných materiálů

Habilitační práce

František Karlický

Olomouc 2024

The work was developed at the Department of Physics of the University of Ostrava in the period 2018 – 2024.

I declare that I carried out this habilitation thesis independently, and only with the cited sources, literature, and other professional sources.

In Olomouc 14. 11. 2024 . . . . . . . . . . . . . . .
F. Karlický

# Acknowledgement

# Contents

# List of publications enclosed to the thesis – Supplementary materials

(Ordered by the time of publication)

1. **Karlický F.**, Turoň J.: Fluorographane $C_2FH$: stable and wide band gap insulator with huge excitonic effect. *Carbon 135, 134-144*, **2018**, 10.1016/j.carbon.2018.04.006

2. Kolos M., **Karlický F.**: Accurate Many-Body Calculation of Electronic and Optical Band Gap of Bulk Hexagonal Boron Nitride. *Phys. Chem. Chem. Phys. 21, 3999-4005*, **2019**, 10.1039/C8CP07328G

3. Ketolainen T., Macháčová N., **Karlický F.**: Optical Gaps and Excitonic Properties of 2D Materials by Hybrid Time-Dependent Density Functional Theory: Evidences for Monolayers and Prospects for van der Waals Heterostructures. *J. Chem. Theory Comput. 16(9), 5876-5883*, **2020**, 10.1021/acs.jctc.0c00387

4. Dubecký M., **Karlický F.**, Minárik S., Mitas L.: Fundamental gap of fluorographene by many-body GW and fixed-node diffusion Monte Carlo methods. *J. Chem. Phys., 153(18), 184706*, **2020**, 10.1063/5.0030952

5. Ketolainen T., **Karlický F.**: Optical gaps and excitons in semiconducting transition metal carbides (MXenes). *J. Mater. Chem. C 10, 3312-3321*, **2022**, 10.1039/D2TC00246A

6. Sakhraoui T., **Karlický F.**: DFTB investigations of the electronic and magnetic properties of fluorographene with vacancies and with adsorbed chemical groups. *Phys. Chem. Chem. Phys. 24(3), 3312-3321*, **2022**, 10.1039/D1CP00995H

7. Kolos M., **Karlický F.**: The Electronic and Optical Properties of III-V Binary 2D Semiconductors: How to Achieve High Precision from Accurate Many-Body Methods. *Phys. Chem. Chem. Phys. 24, 27459-27466*, **2022**, 10.1039/D2CP04432C

8. Dubecký M., Minárik S., **Karlický F.**: Benchmarking fundamental gap of $Sc_2C(OH)_2$ MXene by many-body methods. *J. Chem. Phys., 158(5), 054703*, **2023**, 10.1063/5.0140315

9. Kumar N., **Karlický F.**: Oxygen-terminated $Ti_3C_2$ MXene as an excitonic insulator. *Appl. Phys. Lett. 122(18), 183102*, **2023**, 10.1063/5.0143313

10. Kumar N., Kolos M., Bhattacharya S., **Karlický F.**: Excitons, Optical Spectra, and Electronic Properties of Semiconducting Hf-based MXenes. *J. Chem. Phys. 160(12), 124707*, **2024**, 10.1063/5.0197238

11. Kalmár J., **Karlický F.**: Strain-induced changes of electronic and optical properties of Zr-based MXenes. *J. Appl. Phys. 135(24), 244302*, **2024**, 10.1063/5.0205991

12. Kalmár J., **Karlický F.**: $Mn_2C$ MXene Functionalized by Oxygen is a Semiconducting Antiferromagnet and Efficient Visible Light Absorber. *Phys. Chem. Chem. Phys. 26(29), 19733-19741*, **2024**, 10.1039/D4CP02264E

# 1   Foreword

Recent research led to the discovery of a new generation of atomically thin materials or quasi-two-dimensional (2D) materials, which we refer to as 2D materials. Started by the rise of graphene, a broad family of 2D materials with metallic, semiconducting, or insulating properties, have been fabricated in monolayer, bilayer, and few-layer forms. Our work is inspired by the current needs of applied research on two-dimensional (2D) materials for flexible and ultrathin functional devices.

Theoretical support of the materials design plays an important role in 2D materials research. Within the thesis, we are reporting computational predictions of the physical properties of 2D materials and their heterostructures like electronic and optical properties, including excitonic effects. For the presence of delicate interplay of multiple effects in 2D materials, accurate predictions of their properties require accurate and costly many-body methods instead of the usual density functional theory (DFT), which makes these computations demanding for single-layers and unfeasible for incommensurate van der Waals heterostructures. We will therefore devise and assess less demanding approximate methods that will be used as a tool for computer-aided design of new 2D materials with tailored properties for a new generation of solar cells and functional devices.

The author started his research in 2D materials in 2009 during his postdoc position at Palacký University in Olomouc, Czech Republic. He continued in modeling of structural, electronic, and optical properties of 2D materials as one of his topics also after moving to the University of Ostrava, Czech Republic. In this thesis, the author comments on selected 12 scientific publications published by him and co-workers from his Nanostructure Physics Group over last six years at the University of Ostrava [1, 2, 3, 4, 5, 6, 7, 8, 9, 10, 11, 12]. The selection from 60 authors' papers was done based on the topic and independent conceptualization in the group. Presented publications report on original research in the field of computational physics of nanostructures. In some cases, this research involves computational analyses of known or predicted structures, while in other cases tuning of suitable computational methods is included as well.

In this thesis, the author tried firstly to summarize the role of modeling in 2D material's prediction of electronic and optical properties. However, current challenges are listed and discussed too. Then, the results from reference calculations by many-body methods on several groups of 2D materials are very briefly commented: halogenated and hydrogenated graphenes (References [1, 4]), binary hexagonal materials (References [2, 7]), and transition metal carbides (MXenes, References [8, 9, 10, 11, 12]). Simultaneously, advanced material's properties are predicted and compared using DFT-based methods (References [3, 5]) or also using semiempirical methods (Reference [6]).

## 2 The Role of Modeling in Electronic and Optical Properties of Two-Dimensional Materials

### 2.1 Two-Dimensional (2D) Materials

Modern technologies such as electronics, communication, lighting, and solar energy have risen due to the revolution in modern semiconductor devices. Traditionally, silicon has been industrially used to fabricate electronic circuits, and materials like GaAs or GaN have been used in optoelectronics, typically in the form of thin films. Recent research led to the discovery of a new generation of atomically thin materials or quasi-two-dimensional (2D) materials, which we refer to as 2D materials. The first prepared 2D material was graphene [13], one-atom-thick honeycomb carbon, as shown in Figure 1a. This was a very important step in the world of physics because the stability of 2D layers was a long-standing problem: the Mermin–Wagner theorem predicted, simply said, that long-range fluctuations would destroy the long-range periodic structure of the 2D crystal. The thermodynamic stability of 2D crystals was explained by observation of its corrugation in the third dimension [14]. In addition, the finite size of 2D material flakes or the presence of defects leads to the stabilization of 2D materials too. Graphene is conducting material due to its $sp^2$ carbon atoms, namely, its band structure embodies linear dispersion of bands in the so-called Dirac point (K point of graphene Brillouin zone, marked by the red oval in Figure 1c) and it is labeled as zero band gap semiconductor (or semimetal).
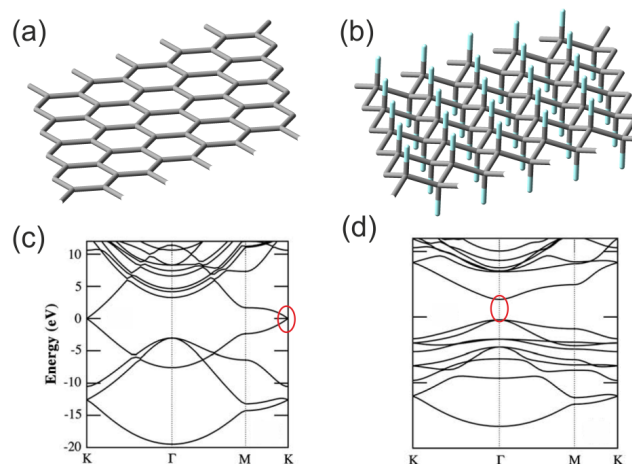


Figure 1: (a) Hexagonal structure of $sp^2$ carbons in graphene. (b) Transformation to $sp^3$ carbons by fluorination in the chair conformation of fluorographene. Electronic band structures of (c) graphene and (d) fluorographene. The original graphene zero band gap at the K point (Dirac point) is opened to a band gap with a minimal value of several eV at the $\Gamma$ point (red ovals). Taken from [15].

Started by the rise of graphene [16], a broad family of 2D materials with metallic, semiconducting, or insulating properties, have been fabricated in monolayer, bilayer, and few-layer form [17]. The important class of semiconducting or insulating 2D materials is graphene derivatives as halogenated (-F, -Cl, -Br),

hydrogenated (-H), or hydroxylated (-OH) graphenes [15]. Depending on surface coverage (i.e., number of $sp^3$ carbon atoms), the zero fundamental gap of graphene can be opened up to $\sim$7 eV in the fully fluorinated graphene, fluorographene ($C_1F_1$). Graphene, fluorographene, and their corresponding band structures are depicted in Figure 1. The most common 2D insulator is probably hexagonal boron nitride (hBN) with the fundamental gap of $\sim$6 eV. The analogical binary materials such as BP, BAs, AlN, etc., are also promising [7]. A typical 2D semiconductor is from the family of transition metal dichalcogenides (TMD) $MX_2$ (e.g., metal M = Mo, W, Ta, Nb, Ni, and X= S, Se, Te), on the other hand, many of TMDs are conducting. Another family of recent two-dimensional carbides, nitrides, and carbonitrides is called MXenes [18]. The typical composition of MXenes is $M_nX_{n-1}T_x$ with $2 \leq n \leq 5$ and $x \leq 2$, where M is metal (e.g., Ti, V, Sc, Cr, Zr, Nb, Mo, Hf), X is carbon or nitrogen, and T is the surface termination which includes groups 16 and 17 of the periodic table or hydroxyl and imido groups. This material's family is unusually broad concerning physical properties because of high sensitivity to composition, termination, or external conditions (pressure, support, solvent, etc.) and provides a rich set of its phases: metals, semiconductors, ferromagnets, antiferromagnets, topological insulators, or excitonic insulators.

Here monolayer refers to a material sheet consisting of fully saturated covalently bonded atoms in the periodic lattice, and, such layers, or single-layers, may be combined to form multilayer superstructures consisting of one or more individual 2D material types. If bonded by weak van der Waals (vdW) forces (Figure 2), the properties of participating materials do not change a lot, even in the presence of lattice mismatch, so their electronic properties remain essentially untouched. By combining the different properties of the building blocks (con-
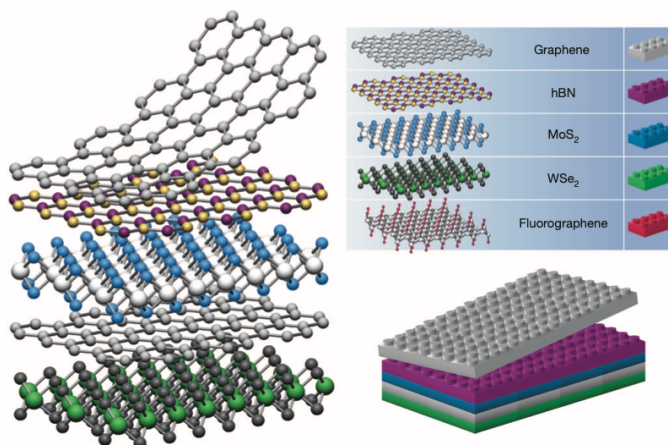


Figure 2: Building van der Waals heterostructures from 2D materials. The construction of a huge variety of layered structures becomes possible (2D crystals to be analogous to Lego blocks). Taken from [19].

ducting graphene, insulating hBN, etc., Figure 2), synthesized vdW structures may show additional integrated properties with respect to the segregated materials due to the interplay of possible additional effects (e.g., interlayer charge transfer). Due to the atomic thickness and exceptional physical properties,

vdW heterostructures can serve as a basis for flexible and ultrathin functional devices. It remains a challenge to design novel 2D materials and their combinations with specific properties, that are needed in fields like solar cell design or (opto)electronics. On the other hand, pioneering laboratory devices were prepared. One example can be 2D tunneling transisor consisting of a) relatively thick (20–30 nm) hBN crystals on top of oxidized (290 nm $SiO_x$) silicon wafer (back gate), b) first multilayer graphene (MGr), c) 3-layer hBN (tunnel barrier), and the second MGr (Figure 3). All three thin top layers were transferred using a dry transfer procedure.
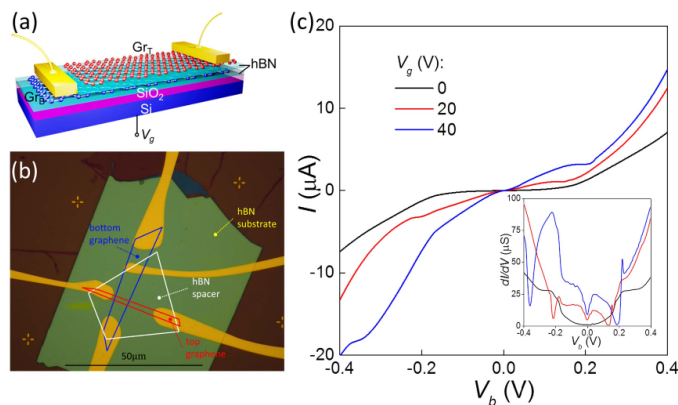


Figure 3: Tunnelling transistor from 2D materials: A 3-layer hBN tunnel barrier separates two MGr sheets: (a) Schematics and (b) optical micrograph, and (c) tunneling current $I$ as a function of $V_b$ at $T = 1.6$ K for different gate voltages. Taken from [20].

## 2.2 Modeling of Basic Materials Properties

Theoretical modeling of materials plays an important role in 2D materials research. In fact, several 2D materials (silicene, germanene, fully hydrogenated graphene, etc.) first came out of theoretical work before being successfully lab-prepared. In addition, the delicate interplay of multiple physical phenomena which theory points out may play a decisive role in these systems. In particular, it is known that collective excitations can be important in such systems so that independent electron models can provide poor spectra. The band gap is usually underestimated and bound exciton spectra are missing. Accurate predictions of 2D material's physical properties like the band gaps and optical spectra require, therefore, accurate many-body theories. On the other hand, the computational resource demands limit such predictions to small systems and the only way to overcome this problem is to use a mean-field method like the usual density functional theory (DFT) or semi-empirical tight-binding (TB) methods, first parameterized to reproduce many-body results on small systems/models. For incommensurate van der Waals heterostructures requiring large supercells, this problem is even more severe.

One of the most basic properties of a periodic material is its *fundamental energy gap*, which distinguishes insulators from metals and dominates many

properties. The gap $\Delta$ is defined as a difference of ground-state energies

$$\Delta = IE^{(N)} - EA^{(N)} = [E^{(N-1)} - E^{(N)}] - [E^{(N)} - E^{(N+1)}], \qquad (1)$$

the difference between the first ionization energy $IE^{(N)}$ and the first electron affinity $EA^{(N)}$ of the neutral material, where $E^{(N)}$ is the ground-state energy for material with a fixed number of nuclei and $N$ electrons obtained from electronic Schrödinger equation $\hat{H}|\Psi_{\mathbf{k}}\rangle = E|\Psi_{\mathbf{k}}\rangle$,[1] where $|\Psi_{\mathbf{k}}\rangle$ is $N$-electron periodic wavefunction.Whereas $\Delta$ can be measured for a macroscopic material (e.g., in photoemission experiments), it can also be computed from first principles, although for many-electron systems (of our interest) this is not a trivial task (see below). Therefore, the fundamental gap is often approximated by *electronic band gap* $\Delta_{\mathrm{el}}$ obtained from one-electron mean-field theories like DFT:

$$(\hat{T} + \hat{V}_{\mathrm{n-e}} + \hat{V}_{\mathrm{H}} + \hat{\nu}_{\mathrm{xc}})|\phi_{n\mathbf{k}}\rangle = \epsilon_{n\mathbf{k}}|\phi_{n\mathbf{k}}\rangle, \qquad (2)$$

where $\hat{T}$ is the kinetic energy operator for electron, $\hat{V}_{\mathrm{n-e}}$ the potential energy between electron and nuclei, $\hat{V}_{\mathrm{H}}$ the Hartree potential energy, $\hat{\nu}_{\mathrm{xc}}$ the exchange-correlation potential, and $|\phi_{n\mathbf{k}}\rangle$ one-electron wavefunction. One-electron theory produces a *band structure*, one-electron energies $\epsilon_{n\mathbf{k}}$ as functions of Bloch wavevector $\mathbf{k}$ and band index $n$, in which there can be a nonzero *electronic band gap*,

$$\Delta_{\mathrm{el}} = \epsilon_{\mathrm{CBM}} - \epsilon_{\mathrm{VBM}}, \qquad (3)$$

the difference between the *conduction* (lowest unoccupied) *band minimum* (CBM) and *valence* (highest occupied) *band maximum* (VBM). That is, DFT approximates $E^{(N\pm1)}$ from Equation 1 by solution for $E^{(N)}$ leading to guess $\Delta \approx \Delta_{\mathrm{el}}$. Finally, the difference between the lowest excitation energy and ground state energy of the material, $\Delta_{\mathrm{opt}} = E^{(N)*} - E^{(N)}$, is often called *optical gap* (* denotes the energy of excited state). The value also corresponds to the first optical transition in the measured optical absorption spectra. At the DFT level, the only approximation of the optical gap is again the electronic band gap, $\Delta_{\mathrm{opt}} \approx \Delta_{\mathrm{el}}$, i.e., the fundamental and optical gap cannot be distinguished at the DFT level and more advanced method should be used, if such differences are important (or projected in other quantities) in the material under study.

## 2.3 Challenges in Modeling of 2D Materials Properties

We would like to summarize here our interpretation of challenges related to the practical modeling of 2D materials using a typical best-tradeoff method in computational materials science – density functional theory (DFT). Limitations of standard DFT are emerging when applied to 2D materials because of at least:

(i) strong local interactions (intralayer covalent bonds) and weak non-local interactions (interlayer noncovalent interactions) are simultaneously present, and

(ii) strong exciton binding energies (typically one order of magnitude stronger than for the corresponding bulk) significantly bias optical absorptions based on DFT interband transition.

---

[1]We assume here, as usual, Born-Oppenheimer approximation, i. e., $\hat{H}$ is Hamiltonian for $N$-electrons interacting with corresponding fixed nuclei.

We note, that correct physics often requires the inclusion of relativistic effects and spin-orbit interactions (i.e., extended Hamiltonian of Equation 2 or some post-DFT corrections). Further, the description of the electronic and optical properties is principally limited as DFT is a one-particle ground state theory. This approach leads thus to inherent band gap problem [21], and subsequently

(iii) the band gap of semiconductors and insulators is underestimated by 30-50% in basic DFT.

We would like to stress some of the aforementioned problems via Figure 4, taken from [22]. Fundamental gaps $\Delta$ are typically larger in 2D materials than in the corresponding bulk and excitonic effects are stronger in 2D. Therefore, the binding energy of excitons, $E_{\mathrm{b}} = \Delta - \Delta_{\mathrm{opt}}$, is one or two orders larger in magnitude in monolayers than in the corresponding bulk analogs. For example, the binding energy of the first bright exciton in well-known bulk semiconductor GaAs is $E_b \approx 0.005$ eV, while in its 2D counterpart, $E_b \approx 0.7$ eV [7]. Or, bulk (layered) $WS_2$ provides $E_b \approx 0.05$ eV, while monolayer $E_b \approx 0.32$ eV [22]. This is because some many-body effects, as properties of excitons (i.e., electron and hole pairs interacting by Coulomb force) are significantly amplified in 2D materials due to reduced dielectric screening (as illustrated in Figure 4). In addition, DFT band gap underestimation is also larger in the 2D case.
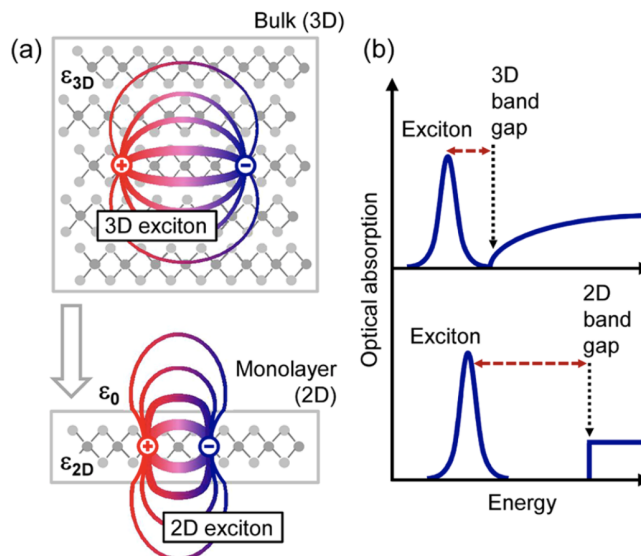


Figure 4: (a) Illustration of electrons and holes bound into excitons for the three-dimensional bulk and a quasi-two-dimensional monolayer. The changes in the dielectric environment are indicated schematically by different dielectric constants $\epsilon_{3D}$ and $\epsilon_{2D}$ and by the vacuum permittivity $\epsilon_0$. (b) Impact of the dimensionality on the electronic and excitonic properties, schematically represented by optical absorption. The transition from 3D to 2D is expected to lead to an increase in both the band gap and the exciton binding energy (indicated by the dashed red line). Taken from [22].

In addition, modeling of 2D crystals itself typically

(iv) assumes perfectly flat planes without ripples, deformations, or defects,

(v) neglects thermal effects,

(vi) neglect 2D layer-substrate interaction or solvent/environment,

(vii) requires large supercells for modeling of vdW heterostructures, because of lattice mismatch (Moiré pattern), and

(viii) requires slab approach (by inserting vacuum layer) in the 3D computational codes in order to avoid spurious interactions between 2D slabs in the 3rd dimension.

Removing/solution of such aforementioned problems/challenges was our work for several years, using both many-body methods (targeting on its precision) and approximative methods tuned on benchmark results (targeting on its efficiency).

## 2.4 Possible Solutions for Modeling of 2D Materials Electronic and Optical Properties

While aforementioned problems (iv)-(vii) are subjects of a physical model of 2D material and (viii) represents rather a numerical approach to 2D material, DFT problems (i)-(iii) are solvable by "better" method beyond standard DFT. The right electron-electron interaction is possible to include by the solution of Hedin equations, which is also approximated by perturbative quasiparticle GW correction of DFT. In molecular systems, post-Hartree-Fock (HF) methods from quantum chemistry are available (like coupled clusters theory), which are, however, not yet spread in periodic calculations because of their extremely computationally demanding implementation. A very different set of many-body methods are stochastic quantum Monte Carlo methods. We also should not omit tricky DFT corrections as hybrid density functionals, which use certain cancellation effects of standard DFT gap underestimation and HF gap overestimation. Concerning proper electron-hole interaction inclusion, the Bethe-Salpeter equation is nowadays a state-of-the-art method. Below, we would like to briefly introduce such methods, which we used in our work as successful solutions for the 2D materials we studied.

### 2.4.1 Hybrid Density Functionals

One of the possible approaches to overcome band gap underestimation in standard DFT is the use of exchange-correlation functionals based on the admixture of generalized gradient approximation (GGA) and exact non-local Hartree-Fock (HF) exchange (EXX). Since the band gaps in the HF method are systematically overestimated, such hybrid functionals often offer more accurate predictions. Global hybrid (H) density functionals replace fraction $\alpha$ of GGA exchange by EXX, as in hybrid PBE0 density functional [23, 24],

$$E_{\text{xc}}^{\text{H}} = \alpha E_{\text{x}}^{\text{HF}} + (1 - \alpha) E_{\text{x}}^{\text{PBE}} + E_{\text{c}}^{\text{PBE}}, \qquad (4)$$

where $\alpha = 0.25$. Screened hybrid (SH) functionals additionally screen the interelectronic Coulomb potential in the exchange term (via another variable,

screening $\omega$, switching short-range (SR) and long-range (LR) parts) as in HSE06 density functional [25],

$$E_{\text{xc}}^{\text{SH}} = \alpha E_{\text{x}}^{\text{HF,SR}}(\omega) + (1 - \alpha)E_{\text{x}}^{\text{PBE,SR}}(\omega) + E_{\text{x}}^{\text{PBE,LR}}(\omega) + E_{\text{c}}^{\text{PBE}}, \quad (5)$$

where $\alpha = 0.25$ and $\omega = 0.2$ Å$^{-1}$. Such range-separated hybrid density functionals are more suitable for periodic systems (as long-range Coulomb tails are restricted) and typically improve results for semiconducting crystals, however, admixing HF-based part is not good in the cases, where the multireference character of the material's electronic structure is indicated.

### 2.4.2 Many-Body GW Approximation

Due to big progress of highly powerful computers, accurate many-body perturbation theories beyond DFT became accessible and enable accurate descriptions of electronic and optical properties of materials in recent decades. The quasiparticle (QP) energies $E_{n\mathbf{k}}^{\text{QP}}$ can be calculated by solving eigenvalue equation

$$[\hat{T} + \hat{V}_{\text{n}-\text{e}} + \hat{V}_{\text{H}} + \hat{\Sigma}]|\phi_{n\mathbf{k}}^{\text{QP}}\rangle = \epsilon_{n\mathbf{k}}^{\text{QP}}|\phi_{n\mathbf{k}}^{\text{QP}}\rangle, \quad (6)$$

where the exchange-correlation potential $\hat{\nu_{\text{xc}}}$ in DFT equations 2 is replaced by many-body self-energy operator $\hat{\Sigma}$, which is obtained together with the Green's function $G$, the screened Coulomb potential $W$, polarizability $\chi$, and vertex function $\Gamma$ in self-consistent procedure [26]. In the so-called GW approximation, the whole setup is significantly simplified. Instead of a self-consistent cycle, a series of subsequent calculations are done starting from 1) non-interacting Green's function $G$ from one-electron orbitals and energies followed by 2) calculation of polarizability $\chi$ from $G$, 3) screened Coulomb potential $W$, and finally 4) self-energy $\Sigma$ using $G$ and $W$. In practical calculations, input orbitals $|\phi_{n\mathbf{k}}\rangle$ are used from DFT and self energy $\Sigma$ is linearized enabling iterative formulation

$$\epsilon_{n\boldsymbol{k}}^{\text{QP},0} = \epsilon_{n\boldsymbol{k}} + Z_{n\boldsymbol{k}}\text{Re}[\langle\phi_{n\boldsymbol{k}}|\hat{T} + \hat{V}_{\text{n}-\text{e}} + \hat{V}_{\text{H}} + \hat{\Sigma}(G, W; \epsilon_{n\boldsymbol{k}})|\phi_{n\boldsymbol{k}}\rangle - \epsilon_{n\boldsymbol{k}}], \quad (7)$$

where the quasiparticle energies $\epsilon_{n\boldsymbol{k}}^{\text{GW}}$ are calculated as first-order corrections to the DFT single-particle energies $\epsilon_{n\boldsymbol{k}}$, $n$ is the band index, $\mathbf{k}$ is the Bloch vector, and $Z$ is the normalization factor [27]. Original DFT orbitals remain unchanged and the corresponding single-shot energies are henceforth referred to as $G_0W_0$. The quasiparticle gap is computed similarly to Equation 3 for DFT electronic gap as $\Delta^{\text{QP}} = \epsilon_{\text{CBM}}^{\text{QP}} - \epsilon_{\text{VBM}}^{\text{QP}}$. Next iterations of quasiparticle energies of Equation 7 are possible through better guess of self energy $\Sigma$ (using updated $G$ or both $G$ and $W$)

$$\epsilon_{n\boldsymbol{k}}^{\text{QP},\text{i}+1} = \epsilon_{n\boldsymbol{k}}^{\text{QP},\text{i}} + Z_{n\boldsymbol{k}}\text{Re}[\langle\phi_{n\boldsymbol{k}}|\hat{T} + \hat{V}_{\text{n}-\text{e}} + \hat{V}_{\text{H}} + \hat{\Sigma}(G, W; \epsilon_{n\boldsymbol{k}}^{\text{QP},\text{i}})|\phi_{n\boldsymbol{k}}\rangle - \epsilon_{n\boldsymbol{k}}^{\text{QP},\text{i}}], \quad (8)$$

until self-consistency is achieved if $i$ is enough large to converge eigenvalues. If the input DFT orbitals remain and only eigenvalues are changed, the method is labeled evGW$_0$ or evGW depending on updated quantities ($G$ or both $G$ and $W$, respectively).

### 2.4.3 Bethe-Salpeter Equation

Excitonic effects are accounted for by the Bethe-Salpeter equation[28] which corresponds to the excitonic equation (eigenvalue problem)[29, 30, 31]

$$(\epsilon_{ck}^{\mathrm{QP}} - \epsilon_{vk}^{\mathrm{QP}})A_{cvk}^{\lambda} + \sum_{c'v'\boldsymbol{k'}} [2\langle \phi_{ck}\phi_{vk}|\nu|\phi_{c'\boldsymbol{k'}}\phi_{v'\boldsymbol{k'}}\rangle$$
$$-\langle \phi_{ck}\phi_{c'\boldsymbol{k'}}|W|\phi_{vk}\phi_{v'\boldsymbol{k'}}\rangle]A_{c'v'\boldsymbol{k'}}^{\lambda} = E_{\mathrm{exc}}^{\lambda}A_{cvk}^{\lambda} \qquad (9)$$

where $c$ and $v$ represent the band indexes of the conduction and valence bands, respectively. The $A_{vck}^{\lambda}$ values are obtained by diagonalization of Eq. (9) and correspond to the amplitudes of a free electron-hole pair configuration composed of the electron states $|\phi_{ck}\rangle$ and hole states $|\phi_{vk}\rangle$, the $E_{\mathrm{exc}}^{\lambda}$ values are eigenenergies corresponding to exciton excitation energies (with optical gap $\Delta_{\mathrm{opt}} \equiv E_{\mathrm{exc}}^{\lambda}$ with $\lambda$ from first nonzero transition, i.e., first bright exciton), and $\nu$ is the Coulomb kernel, $1/|\boldsymbol{r} - \boldsymbol{r'}|$. After computing the energy-dependent dielectric function $\epsilon(E) = \epsilon_1(E) + i\epsilon_2(E)$, where $\epsilon_1(E)$ and $\epsilon_2(E)$ are the real and imaginary part of the dielectric function, properties as energy-dependent refraction index, extinction coefficient, absorption coefficient, and others can be derived. The optical absorptance in 2D materials can be approximated in the limit of atomic-thick material as [3] $A(E) = 1 - \exp(-\epsilon_2(E)EL_z/\hbar c)$, where $E$ is the energy of incoming photon, $L_z$ is the height of the computational unit cell, $\hbar$ is reduced Planck's constant, and $c$ is speed of light. The character of each particular exciton is possible to examine using the $A_{cvk}^{\lambda}$ coefficients from Equation 9, because the excitonic wave function is expressed in an electron-hole product basis as $\sum_{cvk} A_{cvk}^{\lambda}\phi_{ck}\phi_{vk}$.

To summarize the many-body perturbational calculations, we present typical practical steps for DFT-GW-BSE calculation in the scheme of Figure 5. The first step is DFT calculation (Equation 2) providing the band structure (eigen energies as functions of k-space coordinates) of the material and electronic band gap $\Delta_{\mathrm{el}}$ from its valence and conduction bands. Such one-particle energies and orbitals are inputs for the second step, GW calculations (Equation 7) providing quasiparticle corrections, providing an approximation of fundamental gap $\Delta_{\mathrm{QP}} \approx \Delta$. This is the realization of a much better description of electron-electron interaction. The third step, using quasiparticle energies, orbitals (either from DFT or from GW), and screened Coulomb potential $W$, is the Bethe-Salpeter equation (Equation 9), i.e., the inclusion of electron-hole interaction. The exciton binding energy is finally estimated as $E_{\mathrm{b}} = \Delta_{\mathrm{QP}} - \Delta_{\mathrm{opt}}$.

### 2.4.4 Fixed-Node Diffusion Monte Carlo

For completeness, we further mention a very different many-body approach, from which good fundamental gaps can be obtained, quantum Monte Carlo (QMC). QMC is a real-space stochastic projector many-body electronic structure total energy method [32], promising for its accuracy, massive parallelism, low-order CPU cost scaling, and direct treatment of extended models. Here we will mention a fixed-node diffusion Monte Carlo (FNDMC) variant of QMC. For a given electronic Hamiltonian $\hat{H}$ mentioned in Section 2.2, FNDMC imaginary time projection extracts the exact ground-state that has non-zero overlap
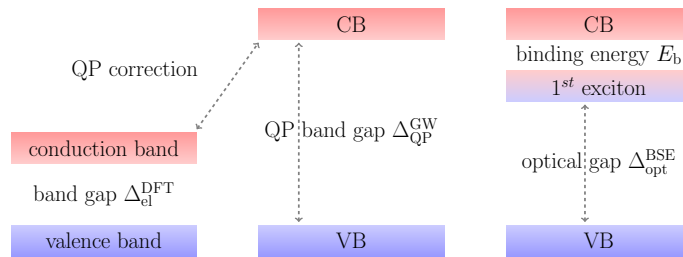
Figure 5: Typical calculation of fundamental and optical gaps is done in three principal steps: DFT calculations (Equation 2), GW quasiparticle (QP) corrections (Equation 7), and solution of Bethe-Salpeter equation (Equation 9).

with the supplied approximate antisymmetric trial state $\Psi_T$ that affects final FNDMC accuracy, i.e.,

$$\Psi^{FN} = \lim_{\tau \to \infty} \exp[-\tau(\hat{H} - E_T)]\Psi_T, \qquad (10)$$

where $E_T$ is a total energy offset that keeps norm of $\Psi^{FN}$ asymptotically constant. The superscript FN indicates that $\Psi^{FN}$ and $\Psi_T$ share the same fixed node $\gamma = \{\mathbf{R}; \Psi_T(\mathbf{R}) = 0\}$, where $\mathbf{R}$ is a $3N$ dimensional position vector of $N$ simulated electrons. In our comparative works [4, 8], $\Psi_T = \Psi_S J$, where $\Psi_S$ is a single Slater determinant and $J$ is a parametric explicitly correlated positive-definite Jastrow term. $\Psi_T$ is variationally improved within variation Monte Carlo (VMC) and then it serves as an input to FNDMC calculation. The $\Psi_T$s for low energy excitations are simply constructed using *promotion approach* [4, 8] by the population of the appropriate one-electron states (e.g., electron sitting at VB is promoted to CB orbital, i.e., occupancies [. . . ,2,2,0,0,. . . ] and [. . . ,2,1,1,0,. . . ] are used, respectively).

### 2.4.5 Precision of Many-Body Methods

Concerning to achieved precision of many-body GW calculations, it is possible to do a direct comparison with experimental values of fundamental gaps. In the typical bulk semiconductors or insulators, GW approximation in its basic single-shot variant using GGA DFT input orbitals, $G_0W_0$@PBE, predicts well experiment (see Figure 6, [27]), although iterations in $G$ can slightly help. $G_0W_0$@PBE generally gives good agreement with experiments for extended, moderately correlated materials because of a cancellation of errors originating from the lack of self-consistency and the absence of vertex corrections $\Gamma$. In any case, the perfect convergence of technical parameters (k-point grid, basis set, number of bands) is essential. The disadvantage is, on the other hand, the results (due to their perturbative nature) depend on the starting one-electron energies and orbitals, which are usually obtained from the solution of the Kohn-Sham (KS) equations (our preferred variant is $G_0W_0$@PBE when possible). This problem can be overcome by performing the calculations self-consistently. Eigenvalue self-consistent GW (Equation 8), which updates the eigenvalues either only in the Green's functions $G$ (ev$GW_0$), or both in $G$ and the screened interactions $W$ (ev$GW$), while the orbitals remain fixed, generally improves the description of band gaps
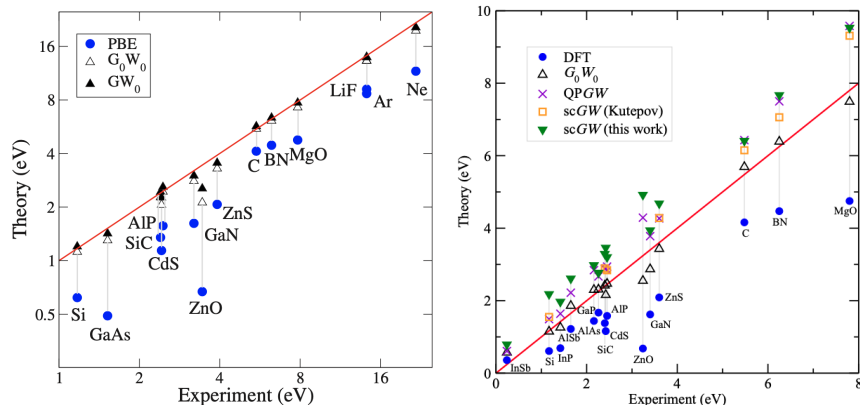
Figure 6: Comparison of band gaps obtained from different theoretical methods and experiments (including single-shot $G_0W_0$@PBE variant). (left) Set of typical semiconductors (Si, SiC, GaAs, GaN, ZnO, ZnS, CdS, and AlP), small gap semiconductors (PbS, PbSe, and PbTe), insulators (C, BN, MgO, and LiF), and noble gas solids (Ar and Ne). A logarithmic scale is used for both axes. Taken from [27]. (right) Different sets of semiconductors and insulators. Taken from [33].

towards the experimental values as compared to $G_0W_0$. Quasiparticle self-consistent GW (QPGW) removes the starting-point dependence entirely by determining an optimum effective non-local static exchange-correlation potential. However, it overestimates band gaps in solids due to the underestimation of the dielectric screening in the random phase approximation (RPA). Self-consistent GW (scGW) avoids the quasiparticle approximation, and the Dyson equation for the Green's function and W are solved fully self-consistently. Nevertheless, without vertex corrections, scGW shows a significant overestimation of the bandwidth for metals and band gaps for gapped systems (see Figure 6b, [33]). Unfortunately, experimental fundamental gaps for pure (clean) 2D materials are typically not available, because of a large number of defects, vacations, dopants, adsorbates, etc. appear during preparation. The comparison study on 2D materials analogic to the 3D study (Figure 6) therefore doesn't exist yet. We just tried to compare four 2D materials in Reference [5]. We note, that the Vienna *ab initio* simulation package (VASP) [34] implementing projector augmented-wave (PAW) method [35, 34] was used in the majority of GW, BSE, and underlying DFT calculations. Since these calculations serve here as a cross-validating reference, it is worth noting that VASP plane-wave calculations based on PAWs can be considered as highly accurate as shown in Ref. [36] using all-electron full-potential linearized-augmented plane waves (FLAPW) method, which is regarded as an established reference method in condensed matter physics. The precision achieved by the convergence of technical parameters in 2D materials is typically $\pm 0.1$ eV [8].

Concerning precision of predicted optical absorption spectra, at least the 2D $MoS_2$ case shows, that $G_0W_0$@PBE can be a good candidate for subsequent BSE calculations. The study of reference [37], which includes spin-orbit interaction correction, shows that agreement with experimental optical absorp-

tion spectra can be achieved (Figure 7) if an *ab initio* broadening based on the electron-phonon interactions is used and technical convergence is saturated. An extremely slow convergence was observed for the number of included bands
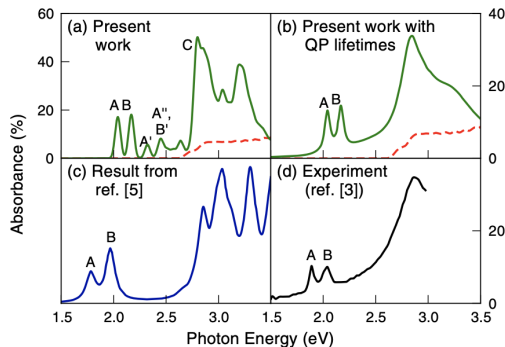


Figure 7: Precision of optical absorption spectra prediction in 2D material from BSE on top of $G_0W_0$@PBE. The $MoS_2$ spectrum without (dashed red curve) and with (solid green curve) electron-hole interactions using (a) a constant broadening of 25 meV and (b) an *ab initio* broadening based on the electron-phonon interactions. (c) Previous BSE calculation (in arbitrary units) and (d) experimental absorbance. Taken from [37].

(6000 bands) and the density of the k-point grid ($300 \times 300$ k-points). The final optical transitions were obtained around $\pm 0.1$ eV of experimental value (2.04 eV and 2.17 eV for A and B peaks from BSE@$G_0W_0$@PBE vs. 1.93 eV and 2.08 eV from experiment, respectively).

Concerning FNDMC, $E^{FN}$ is an upper bound to the exact total energy of a ground state of $\hat{H}$ having the same symmetry as $\Psi_T$. The total energy bias depends quadratically on the inaccuracy of fixed node $\gamma$. Although $\Psi_T$s can be systematically improved, this is not practical for large systems (of our interest here), and compact yet effective Slater-Jastrow type is used, where the Slater determinant is filled with orbitals from DFT. For transitions in crystals, such an approach most often leads to predictive accuracy ($\pm 0.1$ eV) [4, 8].

### 2.4.6 Time-Dependent Density Functional Theory (TD-DFT)

Finally, we would like to briefly introduce more approximative methods often fitted on reference ones. Broadly used DFT in its time-dependent (TD) formulation is principally capable of providing absorption spectra too. However, usually, local and semilocal TD-DFT approximations underestimate band gaps and do not introduce excitonic effects in solids. On the other hand, it has been found that the inclusion of a fraction of nonlocal exact exchange (EXX) gives rise to excitonic effects and considerably improves the optical absorption spectra of solids compared to the adiabatic local-density approximation. The linear-response TD-DFT formulated as a generalized eigenvalue equation is called the Casida equation. A commonly used approximation neglecting the non-resonant component (corresponding to deexcitation from unoccupied to occupied bands), known as the Tamm-Dancoff approximation, leaves only the resonant (occupied

$\rightarrow$ unoccupied) component

$$(E_{c\boldsymbol{k}} - E_{v\boldsymbol{k}})A^\lambda_{cv\boldsymbol{k}} + \sum_{c'v'\boldsymbol{k}'} [2\langle \phi_{c\boldsymbol{k}}\phi_{v\boldsymbol{k}}|\nu|\phi_{c'\boldsymbol{k}'}\phi_{v'\boldsymbol{k}'}\rangle$$

$$+ 2\langle \phi_{c\boldsymbol{k}}\phi_{v\boldsymbol{k}}|f_{\mathrm{XC}}|\phi_{c'\boldsymbol{k}'}\phi_{v'\boldsymbol{k}'}\rangle]A^\lambda_{c'v'\boldsymbol{k}'} = E^\lambda_{\mathrm{exc}}A^\lambda_{cv\boldsymbol{k}}, \qquad (11)$$

(see Reference [3] for derivation of this form), where $f_{\mathrm{XC}}$ is a static exchange-correlation kernel and the other symbols are the same as in BSE (Equation 9).

### 2.4.7 Density Functional Tight Binding

The tight-binding (TB) semiempirical method is an approximate approach to the calculation of the electronic structure of periodic materials. The wave function is constructed as a superposition of wave functions for isolated atoms located at individual atomic sites in TB. TB approximation was generalized to density functional-based tight binding (DFTB). The DFTB method was further improved by a self-consistent redistribution of Mulliken charges (SCC-DFTB) including a Coulomb interaction between charge fluctuations and by empirical dispersion correction (SCC-DFTB-D). SCC-DFTB accounts for long-range electrostatic forces and self-interaction contributions. The accuracy of the DFTB method is always crucially depending on parametrization, i.e., quality of Slater-Coster files (precomputed integral tables).

# 3  Results and Discussion on Particular 2D Materials

In this thesis, we would like to introduce our own results achieved during the last six years in the field of electronic and optical properties of 2D materials. We were focused (in parallel) in two main directions: 1) accurate methods for reference electronic structure and optical spectra, and 2) approximate methods useful for predictions in larger systems. The first line of calculations was precision-based and we were forced to explore all important physical contributions and technical parameters of calculations using many-body methods with respect to desired properties, however, we were limited by computational resources. The second line was not so technically complicated, however, calculations had to be regularly checked for various materials families with respect to the reference calculations (or available experiments, if any). Almost all our systems (with exceptions such as phosphorene) were of hexagonal symmetry with simple unit cells containing several atoms only as documented by examples in Figure 8: fluorographene in
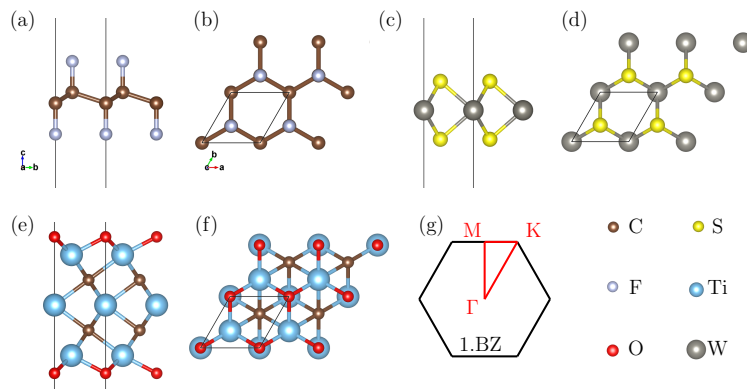


Figure 8: Typical 2D materials and their geometries (side and top view): (a), (b) fluorographene CF, (c), (d) tungsten disulfide $WS_2$, and (e), (f) oxygen-terminated titanium carbide $Ti_3C_2O_2$ (MXene). The thin black lines indicate the unit cell. Sketch of the first Brillouin zone (1. BZ) and high-symmetry points $\Gamma$, M, and K in reciprocal space are added in panel (g).

its chair conformation has four atoms in the unit cell ($C_2F_2$), tungsten disulfide three atoms ($WS_2$), while oxygen-terminated titanium carbide has seven atoms ($Ti_3C_2O_2$).

## 3.1  Accurate Calculations on Electronic, Optical, and Excitonic Properties of 2D Materials

While current DFT implementation is "user-friendly", namely very robust and insensitive to setup (but inaccurate sometimes), the many-body methods are currently not suitable for a "black box" user approach. A disadvantage of many-body methods is the necessity of careful technical convergence (of more parameters) with respect to required quantities. In 2D materials and for excited states these are namely: number of included unoccupied states, number of used

k-points (density of reciprocal space grid), vacuum space, basis set size, etc. Also "physics" can be different in various materials (e.g., the radius of excitons, the shape of important orbitals) with impact on necessary setup. In addition, the usage of many-body methods is often limited to several atoms in the computational cell. In contrast to many-body methods, the DTF is generally accepted, validated, and tested across various implementations and software, resulting in few meV differences between codes [38] (despite such an results can be inaccurate with respect to experiment). The whole statuses of traditional GGA DFTs and many-body methods are schematically depicted in Figure 9.
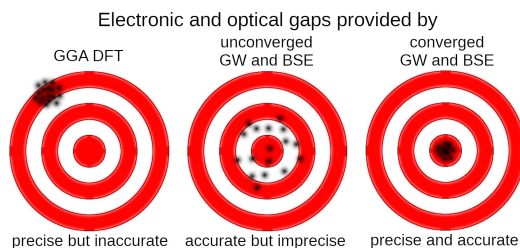


Figure 9: Precision vs. accuracy in DFT and many-body methods. Taken from Supplementary Material [7].

Here, we are therefore targeting precision in reference/benchmark calculations of electronic and optical properties of selected 2D materials. Our GW+BSE calculations would be ideally compared to experiment or independent many-body QMC results. Firstly, we focused on $s$ and $p$ elements containing compounds in Sections 3.1.1 and 3.1.2, and then we tried to achieve some results also on $d$ elements-containing systems in Section 3.1.3.

### 3.1.1 Halogenated and Hydrogenated Graphenes

Halogenated and hydrogenated graphenes attracted our attention far earlier, from times of 2D materials discovery. Therefore, we would like to mention also previous achievements. During the postdoc stay, the author had an opportunity to be a member of the team participating in fluorographene CF discovery [39], when he contributed by pioneering CH, CF, CCl, and CBr band structures. The fluorographene preparation by chemical exfoliation [39] was done simultaneously using mechanical exfoliation and fluorination by Nobel price winners Novoselov, Geim et al. [40].[2]

Inspired by halogenated graphenes preparation, the author prepared methodology for band gap calculations using localized orbitals and hybrid density functionals applied on full halogenation of graphene with mixed group [41]. Combinations of -H, -F, -Cl, Br, and -I atoms chemically functionalized graphene were considered and continuous changes in gaps by surface stoichiometry ratios were achieved. Calculations on periodic materials using localized orbitals are not very common, long tails of diffuse basis functions are problematic. However, with certain cutoffs, the approach is very efficient, especially for short-range hybrid density functionals and 2D periodic code (i.e., without the use of vacuum space

---

[2]Interestingly, published in one issue of Wiley's Small journal as subsequent articles.

in the third dimension). Other periodic calculations were done using standard plane-wave basis sets.

The main achievement was the subsequent many-body solution to the fluorographene gap problem. While experiments predicted a few eV gaps, many-body GW calculations provided a fundamental gap of 7-8 eV. This inconsistency was mainly explained by the large excitonic effect in fluorographene ($\approx$ 2 eV) [42], which forced the community to carefully distinguish between its optical and fundamental gap. In fact, the available experiments were dominantly from optical measurements. In addition, other factors such as impurities, defects, partial fluorination, etc. are responsible for minor disagreements between calculated gaps on ideal fluorographene and real experiments [43, 44, 45]. Later, we compared excitonic effects and band gaps in monolayer, double-layer, and bulk of CF (fluorographite) [46] and showed that the position of the first absorption peak in optical absorption spectra is almost the same for all cases.

Inspired by experimental preparation of mixed hydrogenated/halogenated graphenes, we recently decided to continue on our older work [41] and examine specific stoichiometry of $C_2FH$ [1], called fluorographane (this is the content of the Supplementary Material [1]). We generated several possible geometric configurations of $C_2FH$ monolayer and evaluated the stability and energetics of such structural conformers. Subsequently, for the most probable chair conformer, we performed accurate GW and BSE calculations [1]. The most stable conformer was the chair conformer alternating F up and H down (with respect to the graphene layer) in the zigzag direction of a rectangular unit cell (Figure 10). The electronic and optical calculations with the inclusion of quasiparti-
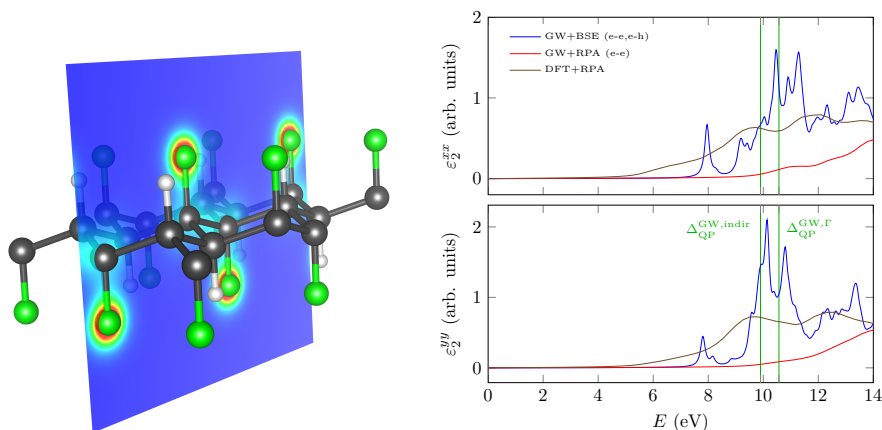


Figure 10: (left) Optimized structure of the most stable conformer of fluorographane $C_2FH$ and corresponding cut through the electron density in (010) plane. (right) Components of the imaginary part of the dielectric function of $C_2FH$ calculated by (i) DFT+RPA, (ii) GW+RPA including electron-electron (e-e) interaction, and (iii) GW+BSE including both e-e and e-h (electron-hole) correlations. Taken from Supplementary Material [1].

cle and excitonic effects performed by many-body methods (GW, BSE) were found to be overly sensitive to the computational setup (number of conduction bands, vacuum thickness, k-point sampling, etc.) and careful convergence and

extrapolations were needed to achieve the desired accuracy. One can easily obtain significantly biased gaps for $C_2FH$ ($\sim$0.7 eV) if one uses the GW or BSE method as a black box without a careful convergence study. Although one would expect the band gap of the studied $C_2FH$ to lie somewhere between the band gap of graphane ($C_2H_2$, $\sim$5 – 6 eV) and fluorographene ($C_2F_2$, $\sim$7 – 8 eV; both CH and CF can be considered as "mother materials" with respect to $C_2FH$), or close to one of them, this is not the case. Unexpectedly, we find that fluorographane $C_2FH$ embodies an extremely wide indirect band gap of $\sim$10 eV (Figure 10). We attributed this quite surprising fact to local environment effects, i.e., specific combinations of -F and -H adsorbates on the graphene surface. These effects were also responsible for the significant difference in electronic and optical properties of the two considered subsets of fluorographane $C_2FH$ conformers: while the Janus structures (i.e., fluorine atoms covering one side and hydrogen atoms another side) have smaller direct band gaps ($\sim$6 eV) and excitonic effects ($\sim$1.9 eV), similar to CH and CF, respectively; the highly stable homogeneous $C_2FH$ conformers embody extremely wide indirect band gaps (8.7 – 10 eV; direct gaps 9.3 – 10.7 eV) and huge binding energies of exciton ($\sim$3 eV, Figure 10). Homogeneous fluorographane has therefore the largest known excitonic effect and the largest known band gap value in the field of currently known 2D materials.

Finally, our newest contribution in the field of reference calculations of halogenated graphenes was reinvestigation of the first material - fluorographene CF [4], which is Supplementary Material 4 of the thesis. The experiments on fluorographene did not a big progress from its discovery in 2010. Simultaneously, stochastic quantum Monte Carlo methods were developed enough to use growing available computational resources. We therefore decided to examine the performance and predictability of both independent many-body methods (GW vs. QMC) by obtaining CF fundamental gaps (Figure 11). The results were
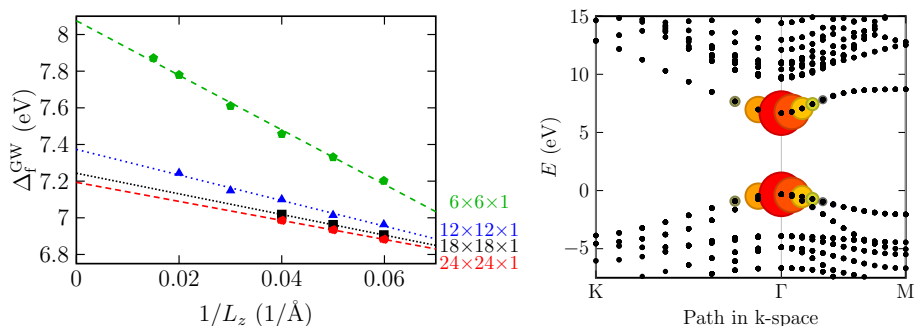


Figure 11: (left) Quasiparticle band gaps of a single-layer of fluorographene CF depending on inter-sheet distance $L_z$ for various k-point grids. Linear extrapolations for $1/L_z \to 0$ are included as lines. (right) Electronic band structure of F from GW calculation (black dots) and all $|A_{cv\mathbf{k}}^\lambda|$ coefficients from BSE (represented by the radius of colored circles) visually show which electron-hole pairs contribute to the first excitonic peak, i.e., to a particular BSE eigenstate $\lambda = 1$. The Fermi energy is set to zero. Taken from Supplementary Material [4].

published at the time of the 10th anniversary of fluorographene, in 2020. GW methods converged quite reasonably with a number of k-points and a number of

unoccupied bands. But slowly with vacuum thickness $L_z$ (Figure 11) and therefore we used linear extrapolation in $1/L_z$ in form $\Delta^{\mathrm{GW}}(\frac{1}{L_z}) = C\frac{1}{L_z} + \Delta^{\mathrm{GW}}(0)$ where $C$ and $\Delta^{\mathrm{GW}}(0)$ are fitting parameters, significantly differs for various k-point grids (Fig. 11). This procedures results in $\Delta^{\mathrm{GW}} = 7.14 \pm 0.05$ eV. QMC gap, in its fixed-node diffusion Monte Carlo variant (FNDMC), was constructed using linear extrapolations for supercell sizes ranging from $2 \times 2$ to $5 \times 5$ leading to $\Delta^{\mathrm{FN}} = 7.1 \pm 0.1$ eV. In addition, we pointed out a possibility to extract approximations to $\Delta$ from neutral single-reference Bloch-orbital FNDMC computations of promotion gaps in finite small-to-medium supercell sizes (vs the actual exciton size) extrapolated to the thermodynamic limit. Such an approach is appreciable since only two total energy FNDMC computations of neutral systems are required to obtain reasonable estimates of the fundamental gap. The alternative involves the usual three total energies (Equation 1) that involve charged states and that can typically exhibit further complications such as more profound finite-size effects. Both approaches have been pushed to their limits independently and have arrived at the benchmark value of $\Delta^{\mathrm{theor}} \approx 7.1 \pm 0.1$ eV for a freestanding CF material sheet free of defects at zero temperature, making little room for further corrections at the 0.1 eV accuracy level. Bethe-Salpeter equation determined the first exciton stabilization of $E_{\mathrm{b}}^{\mathrm{BSE}} = 1.92$ eV, so that our best optical gap estimate amounts to $\Delta_{\mathrm{opt}}^{\mathrm{theor}} \approx 5.2 \pm 0.1$ eV.

The character of the first bright exciton in terms of exciton wave function (expressed in an electron-hole product basis $\sum_{cv\boldsymbol{k}} A_{cv\boldsymbol{k}}^{\lambda} \phi_{c\boldsymbol{k}} \phi_{v\boldsymbol{k}}$) says here using the $A_{cv\boldsymbol{k}}^{\lambda}$ coefficients from Equation 9, that only the highest occupied band and the lowest unoccupied band in the k-space region very close to the $\Gamma$ point contribute to the first excitonic state ($\lambda = 1$, Figure 11). Other regions of the Brillouin zone and other bands provide only negligible contributions to the first excitonic state because circles in Figure 11, with a size proportional to $|A_{cv\boldsymbol{k}}^{\lambda}|$, are smaller than points expressing quasiparticle band structure.

### 3.1.2 Binary Hexagonal 2D Semiconductors

Discoveries of new 2D materials renewed interest in well-known layered bulk materials. One of the most important layered materials is bulk hexagonal boron nitride (hBN), which is the bulk variant of 2D hexagonal boron nitride. There was a long-lasting discussion on the value and the nature of the hBN gap (indirect vs. direct material). New experimental studies [47, 48] (2016) brought a turning point, hence showed the nature of the band gap as indirect and reported a very accurate value of (indirect) fundamental gap of 6.08 eV [47], optical gap of 5.69 eV [48], and minimal direct band gap of 6.42 eV [48]. We decided to reconcile its electronic and optical gaps as these values could be directly compared to theoretical predictions. Our benchmark calculations of before-mentioned energy gaps and optical properties of the most stable conformers of h-BN [2] are enclosed as Supplementary Material 2 to the thesis. We investigated the most probable stacking conformations AA' and AB using GW and BSE. Resulting fundamental gaps $\Delta$, optical gap $\Delta_{\mathrm{opt}}$, and exciton binding $E_{\mathrm{b}}$ energy are directly compared to experiments in Table 1; the guess of precision was of $\pm 0.1$ eV. The carefully converged results revealed h-BN as an indirect material (indirect gap $\approx 6.1$ eV) with a huge excitonic effect ($\approx 0.8$ eV, also visible in absorption spectra of Figure 12) in perfect agreement with recent experiments [47, 48]. The K-H region of the first Brillouin zone has been shown as the most important for

Table 1: Comparison of calculated bulk hBN gap values [2] in two most important stacking configurations, AA′ and AB, with experimental values.

|  | $\Delta^{\mathrm{indir}}$ | $\Delta^{\mathrm{dir}}$ | $\Delta_{\mathrm{opt}}$ | $E_{\mathrm{b}}$ |
|---|---|---|---|---|
| calc. AA′ | 6.08 | 6.53 | 5.71 | 0.82 |
| calc. AB | 6.17 | 6.39 | 5.61 | 0.78 |
| exp.[47, 48] | 6.08 | 6.42 | 5.69 | 0.73 |

lowest optical excitations in h-BN (circles in Figure 12) due to flat bands there. Surprisingly, simple scissor-corrected DFT (PBE+$\Delta_{\mathrm{sc}}$, where $\Delta_{\mathrm{sc}}$ is rigid energy level correction obtained from the difference of quasiparticle and electronic gaps) has described h-BN band structure at GW level (this will be discussed in Section 3.2.)
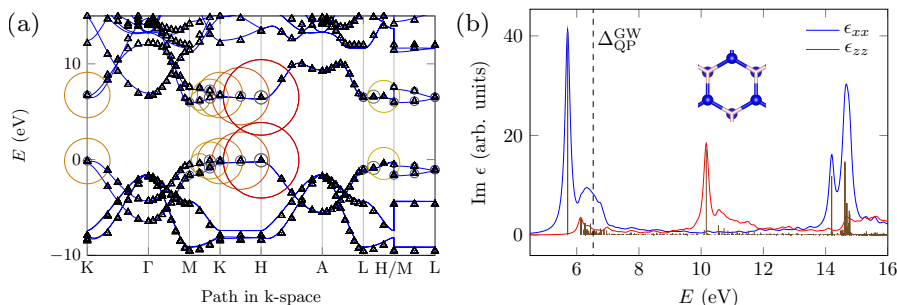


Figure 12: (a) Electronic band structure and (b) optical absorption spectra of h-BN in AA′ structure (corresponding geometry is depicted in the subplot, B – pink, N – blue). $G_0W_0$ band structure (black triangles) includes all $|A_{vc\boldsymbol{k}}^S|$ coefficients from Eq. 9 (represented by the radius of colored circles), which visually inspect which electron-hole pairs contribute to a first excitonic peak. Scissor corrected DFT (PBE) band structure, DFT+$\Delta$ (blue lines) is added, and Fermi energy is set as zero. Several bound excitonic states (vertical brown lines) are below the direct band gap (dashed black line). Our choice of the coordinate system (xy plane is equivalent to BN plane) implies zero off-diagonal and nonzero diagonal elements $\epsilon_{xx} = \epsilon_{yy}$ and $\epsilon_{zz}$ of the frequency-dependent dielectric matrix $\epsilon$. Taken from Supplementary Material [2].

Later, we continued to other properties of hBN and expanded the problem of the BN stacking to infrared (vibrational) spectroscopy [49]. We also investigated interlayer binding energies in BN conformers and compared various DFT approaches to the quantum Monte Carlo [50]. However, both papers are beyond the thesis topic (on electronic and optical properties), therefore we are not commenting on these results more.

Our recent contribution in the field is the precise calculations for semiconducting 2D binary materials from III-V group elements [7], enclosed as Supplementary Material [7]. The set of materials includes 2D hexagonal BN, BP, BAs, AlN, GaN, GaP, and GaAs. Simultaneous convergence in all principal parameters of the accurate many-body perturbational GW approach and the subsequent Bethe–Salpeter equation (BSE) was necessary to achieve precise fundamental and optical gaps, exciton binding energies, and absorbance spec-

tra. We visualized and explained various convergence rates of studied properties in the case of different materials, as shown in Figure 13. We can deduce from
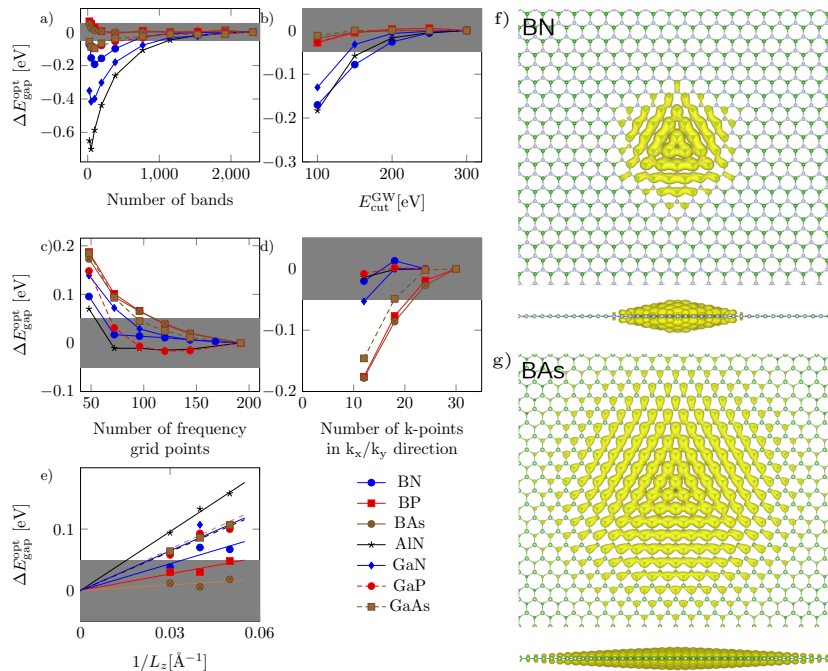


Figure 13: Representative differences of optical band-gaps from BSE calculations $\Delta E_{\text{gap}}^{\text{opt}}$ from converged values of seven 2D materials with respect to a) the number of bands, b) GW energy cut-off $E_{\text{cut}}^{\text{GW}}$, c) a number of frequency grid points for GW calculation, and d) number of k-points in x and y direction; e) extrapolation of $\Delta E_{\text{gap}}^{\text{indir}}$ to infinite height of computational cell ($L_z \to \infty$). Grey bars show regions within a target $\pm 0.05$ eV threshold. Top and side views of the isosurface of the first bound exciton with a fixed hole for BN (f) and BAs (g) plotted with the same level of isosurface. Taken from Supplementary Material [7].

Figures 13a-13e that one can easily obtain biased values of electronic and optical properties up to several tenths of eV despite using state-of-the-art GW/BSE methods. Relative errors of the optical gaps can therefore be up to 30% from a single parameter (BAs k-point case) and the target precision in many-body calculations can be challenging. We observed some general trends concerning parameter convergence and optical properties in this set of materials. For the two direct materials, BP and BAs, in contrast to other indirect materials, we observed a much stronger sensitivity to k-point sampling and a lower sensitivity to the number of virtual bands included in the calculation and energy cut-off in the GW calculations. These direct materials show much lower absorbance than all indirect materials. The reason for the slow convergence of optical gaps with respect to the k-point sampling of these two materials can be explained by the localization of the first bound exciton. In Figures 13f and 13g we plotted the excitonic probability density by fixing the hole position of the first excitons for

BN and BAs, as contrast materials concerning the k-point sampling needed in optical gaps. We used k-point grids of 18×18×1 and 30×30×1 points for BN and BAs, respectively. The first BN exciton is much more localized with an exciton size of ca. 10 real unit cells. On the other hand, the first BAs exciton is very delocalized, and one needs a supercell size larger than 20 real unit cells to ensure wave function fade-out on the border of the supercell (Figure 13g). We remind here, that the delocalization (radius) of the exciton in real space is indicated by the k-point density necessary for reliable calculation of optical gap value (Figure 13d). An exciton wave function covering a $n \times n$ real-space supercell can be reasonably mapped at least by $n \times n$ grid in reciprocal space. Therefore, artificial confinement of the exciton by a too-coarse grid will lead to a biased optical gap (and will untruly increase the predicted binding energy of the exciton). The exciton wave function analysis similar to Figure 11 for fluorographene ($|A_{cvk}^{\lambda}|$ coefficients from BSE – Equation 9) indicates that the locations of electron-hole pair contributions differ in investigated materials. In AlN, GaN, and GaAs, it is located at the $\Gamma$ point of the Brillouin zone, and in all other materials it is located in the vicinity of the K point. The main contribution, therefore, grows dominantly from the location of the minimal direct quasiparticle band gap of all materials. Benchmark calculations show several 2D materials from this set that strongly absorb the visible and ultraviolet parts of the spectra, and therefore can be promising materials for (opto)electronic applications.

For completeness, we would like to mention the research on other hexagonal 2D semiconductors led by our foreign colleagues with our participation. Hypothetical binary materials from the V-V group of elements were studied including temperature effects [51, 52]. We demonstrated exceptionally large exciton-driven responses such as the fundamental exciton binding energy (2 eV), zero-point band-gap renormalization (200 meV), and nonlinear second and third harmonic coefficients (800 pm/V and $1.4\times10^{-18}$ m$^2$/V$^2$ respectively) from an atomically thin binary group-V NP semiconductor [51]. NAs and NSb hexagonal monolayers [52] embody less strongly bound exciton (1.62 and 1.30 eV, respectively) and weaker zero-point band-gap renormalization (105 and 80 meV).

### 3.1.3 Monolayer Transition Metal Carbides (MXenes)

The last family of materials we were interested in detail most recently are MXenes introduced in Section 2.1. From a computational point of view, $d$ elements could bring new problems. Some of the investigated materials are indirect, complicated by magnetism (spin-polarized calculations are necessary), and are of possible multi-reference character. E.g., our analysis of some excitons (e.g., in Cr-based MXenes) showed broad contributions of electron-hole pairs from k-space and bands. After such an introductory search of semiconducting $3d$ transition metal carbides presented in Supplementary Material [5] (by approximative methods, more commented in Section 3.2.1), we started a particular investigation of interesting MXenes by precise many-body methods.

To check the predictivity and precision of many-body methods (GW vs. QMC) in the case of metal carbides, we bring a comparative study on simple nonmagnetic direct $\Gamma$ semiconductor $Sc_2C(OH)_2$ [8], which is the content of the Supplementary Material 8. However, such MXene was finally rather difficult for reliable many-body prediction. Figure 14a shows the deformation of the

lowest unoccupied orbital in $\Gamma$ point when vacuum space thickness $L_z$ in the third direction is too small. Dependence on $L_z$ occurs principally in all 2D
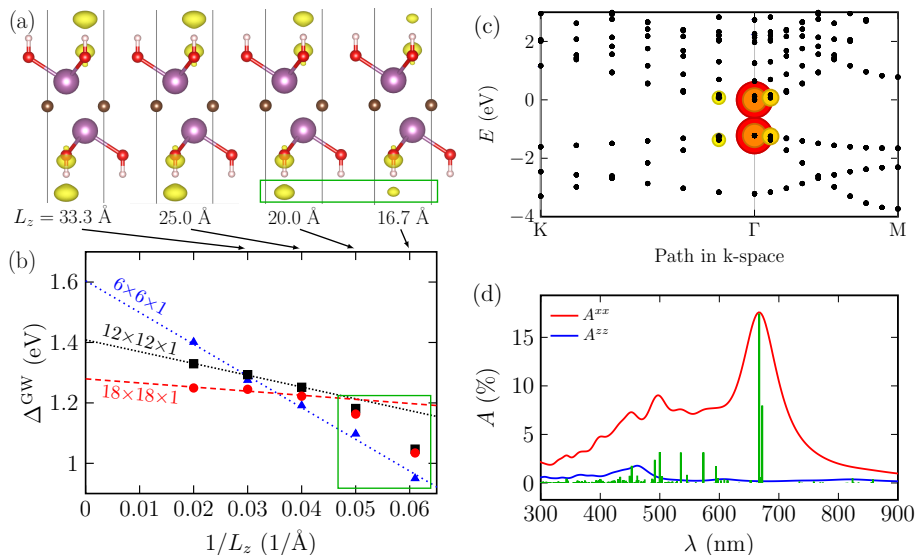


Figure 14: (a) Lowest unoccupied orbitals in $\Gamma$ and (b) quasiparticle band gaps of a single-layer of $Sc_2C(OH)_2$ depending on inter-sheet distance $L_z$ for (a) $12\times12\times1$ k-point grid and (b) various k-point grids. Linear extrapolations for $1/L_z \to 0$ are included as lines. The points in the green box (b) correspond to the deformed orbitals in the green box (a) and were excluded from the fitting procedure. (c) Quasiparticle (GW) band structure of $Sc_2C(OH)_2$ (black dots) and all $|A_{cv\boldsymbol{k}}^{\lambda}|$ coefficients from BSE (represented by radius of the colored circles) visually show which electron-hole pairs contribute to the first excitonic peak, i.e., to a particular BSE eigenstate $\lambda = 1$. The Fermi energy is set to zero. (d) The absorptance $A^{\alpha\beta}$ of $Sc_2C(OH)_2$ calculated by GW+BSE in the near ultraviolet and visible regions as a function of wavelength. Taken from Supplementary Material [8].

materials (later expanded by the work of Fanta and Dubecký [53]), but this case represents bias from expected linearity (Figure 14b) and extremely bad convergence not only within vacuum thickness, but also in number of k-points, number of empty states, etc. All parameters were finally extrapolated and possible errors were evaluated. Final fundamental gap was $\Delta^{\mathrm{GW}} = 1.28 \pm 0.10$ eV. Similarly to fluorographene, the first bright exciton was strongly k-space-localized in the center $\Gamma$ of the Brillouin zone. The corresponding FNDMC gap from the promotion approach was $\Delta^{\mathrm{FN}} = 1.3 \pm 0.2$ eV. Both approaches independently arrive at a similar value of $\Delta \sim 1.3$ eV, suggesting the validity of both methods. Finally, the absorptance $A$, within the photovoltaics-relevant photon energy window [54] $(1.5 - 3$ eV, 400-800 nm), amounts to $A \approx 5 - 15\%$.

Further, we would like to present the calculations on the system, where the precision was of extreme importance for physics itself. The investigated material $Ti_3C_2O_2$ (one of firstly discovered MXenes, the geometrical structure shown in Figure 8) is indirect material with almost zero fundamental gap as shown in

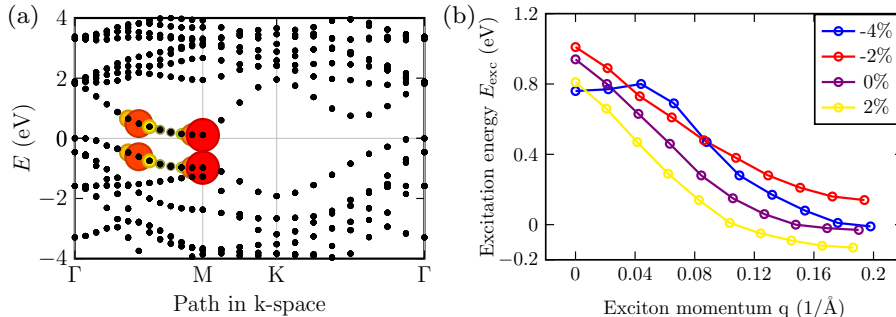Figure 15 (our work [9] is included in the Supplementary Material 9). We, there-



Figure 15: (a) Quasiparticle (GW) band structure of $Ti_3C_2O_2$ (black dots) and all $|A^\lambda_{cv\boldsymbol{k}}|$ coefficients from BSE (represented by the radius of the colored circles) visually show which electron-hole pairs contribute to the first excitonic peak. (b) Excitation energy of the MXene $Ti_3C_2O_2$ monolayer with exciton momentum $\boldsymbol{q}$ along $\Gamma$ to M path. BSE data (circles) are calculated for several strains (legend), and solid lines are guides to the eye. The M point position in units of $\text{Å}^{-1}$ shifts with the strain. Taken from Supplementary Material [9].

fore, remind the case, where the quasiparticle gap is smaller than the binding energy of the first bright exciton. Such a phenomenon is called the excitonic insulator (EI). But, the band structure shows that the $Ti_3C_2O_2$ monolayer has a small indirect band gap (Fig. 15a). Then, the criterion for an EI should be that the binding energy of the corresponding momentum-indirect exciton overcomes the indirect band gap. We, therefore, also performed calculations of excitons in $Ti_3C_2O_2$ with the inclusion of exciton momentum $\boldsymbol{q}$ along the $\Gamma M$ direction. The whole situation is documented in Figure 15b (purple curve). The calculations clearly show that the excitation energies are rapidly decreasing going to slightly negative values, with a minimal value for $\boldsymbol{q} = \Gamma M$, and are therefore relevant for the ground state of the system. The condition of the exciton insulator is fulfilled for $Ti_3C_2O_2$: $E_b^{\text{ind}} = 0.12\text{-}(\text{-}0.03) = 0.15$ eV $> \Delta^{\text{ind}} = 0.12$ eV, where "ind" index denotes "indirect" word. In addition, the excitonic insulator is stable over the $\pm 4\%$ range of compressive and tensile biaxial strain.

Other MXenes, containing heavy elements, are recently prepared hafnium-based MXenes. We studied two candidates on semiconducting behavior, $Hf_3C_2O_2$, and $Hf_2CO_2$ [10] (the Supplementary Material 10 of the thesis). Both $Hf_3C_2O_2$ and $Hf_2CO_2$ MXenes have an indirect quasiparticle gap of 1.08 eV and 2.18 eV, respectively. Both $Hf_3C_2O_2$ and $Hf_2CO_2$ MXenes showed strong first exciton binding energies of 0.51 eV and 0.76 eV, respectively. The first bright excitons are quite delocalized in real space, as visible in Figure 16. The excitation energies of direct excitons can be significantly decreased by considering indirect excitons with exciton momentum $\boldsymbol{q} = \Gamma M$. The observed 4% and 13% absorptance in the infrared region and the remarkable 17% peak at 4.8 eV in the near UV region highlight the rich excitonic landscape of MXene $Hf_3C_2O_2$. Additionally, MXene $Hf_2CO_2$ exhibited a significant 28% absorptance peak in the visible spectra. The emission properties of the Hf-based MXenes are illustrated by the radiative lifetimes of the lowest-energy excitons. We observed almost three or-

ders' lifetime difference between three-Hf-layered and two-Hf-layered materials at room temperature: very long-lived ($\sim$ ten nanoseconds) excitons in $Hf_3C_2O_2$ (longer than in transition metal dichalcogenides) vs. short living ($\sim$ tens of picoseconds) in $Hf_2CO_2$.
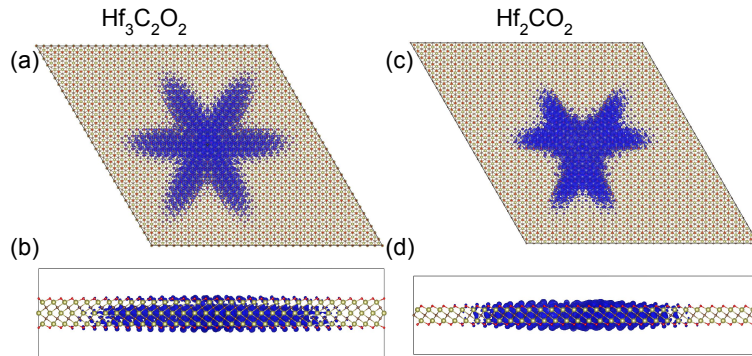


Figure 16: Isosurface for the real space electron probability density of the first bright exciton in (a,b) $Hf_3C_2O_2$ and (c,d) $Hf_2CO_2$. The hole is located above a carbon atom, 1 Å away in the z-direction in both materials. Taken from Supplementary Material [10].

We also did calculations on Zr-based MXenes [11] (which is Supplementary Material 11 of the thesis). Zr-based MXenes recently attracted attention because of their experimental preparation showing temperature stability, mechanical strength, and promising energy, sensors, and electrochemistry applications. However, necessary theoretical predictions at a precise/predictive level are complicated due to essential excitonic features and strong electron correlation (i.e., a necessity to go beyond standard density functional theory, DFT). Contrary to the prevailing focus on oxygen-terminated MXenes and standard predictions of other Zr-based MXenes as conductors, based on the hybrid DFT and GW many-body perturbational theory, we were able to find seven different semiconductors (five of them for their equilibrium geometry and two others under slight tensile biaxial strain) in the case of two- and three-layered $Zr_2CT_2$ and $Zr_3C_2T_2$ configurations with various terminations (T = O, F, S, Cl). We observed semiconductor-to-conductor transition induced by strain in the majority of such Zr-based MXenes at experimentally achievable strain range. Furthermore, using the Bethe-Salpeter equation (BSE), we demonstrated that selected semiconducting Zr-based MXenes possess high optical absorption efficiency (20-30%) in the visible light range, underscoring their potential in photonic applications. The high sensitivity of Zr-based MXenes to external conditions and functionalization combined with the thermal stability make the materials promising for applications at operational temperatures in electronic and optical technologies.

Finally, we would like to mention Mn-based MXenes [12], which are one of the possible magnetic MXenes. Manganese-based MXenes are promising two-dimensional materials due to the broad palette of their magnetic phases and the possibility of experimental preparation because the corresponding MAX phase was already prepared. Here, we systematically investigated geometrical conformers and spin solutions of oxygen-terminated $Mn_2C$ MXene and per-

formed subsequent many-body calculations to obtain reliable electronic and optical properties. Allowing energy-lowering using the correct spin ordering via supercell magnetic motifs is essential for the $Mn_2CO_2$ system. The stable ground-state $Mn_2CO_2$ conformation is an antiferromagnetic (AFM) one with zigzag lines of up and down spins on Mn atoms. The AFM nature is consistent with the parent MAX phase and even the clean depleted $Mn_2C$ sheet. Other magnetic states and geometrical conformations are energetically very close, providing state-switching possibilities in the material. Subsequent many-body GW and Bethe-Salpeter equation (BSE) calculations provide indirect semiconductor characteristics of AFM $Mn_2CO_2$ with a fundamental gap of 2.1 eV (and a direct gap of 2.4 eV), the first bright optical transition at 1.3 eV and extremely strongly bounded (1.1 eV) first bright exciton. $Mn_2CO_2$ absorbs efficiently the whole visible light range and near ultraviolet range (between 10 - 20%).

## 3.2 Approximative Calculations Applicable on Larger 2D Computational Supercells

As we mentioned in the introduction to Section 3.1, accurate many-body calculations are quite demanding concerning computer resources. Before-mentioned precise GW and BSE calculations on particular materials in subsections 3.1.1-3.1.3 are performed for unit cells with up to 20 atoms. In addition, the precision of such calculations is strongly influenced by the slow convergence of many technical parameters. For more realistic conditions and materials, one can ask for less demanding scalable approaches in order to study larger computational supercells (with a huge number of explicitly treated electrons). One urgently needs larger supercells in the case of 2D materials with defects, with complicated magnetism (e.g., antiferromagnetic cells are often larger than unit cells), with more complicated functionalization (e.g., mixed surface functionalization in MXenes), or one needs to correctly describe vdW heterostructures (incommensurate cells of building 2D materials necessary because of different in-plane lattice constants of particular 2D materials). Here we tried to find computationally "cheaper" solutions, namely methods in the direction of 1) time-dependent density functional theory (TD-DFT), and 2) semiempirical Hamiltonians as in density functional tight-binding (DFTB). Of course, machine-learning potentials and properties can also be a suitable solution for the future in this direction.

### 3.2.1 Effective Optical Spectra for 2D Materials and Incommensurate vdW Heterostructures from TD-DFT

Our first attempt to check the possibilities of computationally "less-expensive" methods for reasonable electronic and optical properties was on before mentioned hexagonal BN material (Section 3.1.2 and the Supplementary Material [2]). We observed that the simple scissor-corrected PBE+$\Delta$ band structure[3] is a good approximation of $G_0W_0$ band structure (Figure 12 in Section 3.1.2). One could therefore ask, if is there any extension to include computationally "cheap" excitonic effects and obtain reliable approximate optical absorption spectra. We tried TD-DFT based on PBE+$\Delta$ band structure, just a portion of exact-exchange (EXX) in TD kernel was necessary to add. The evolution of

---

[3]So called "scissor correction" is simple rigid shift of unoccupied bands by difference of quasiparticle and electronic band gap, $\delta = \Delta_{QP}^{GW} - \Delta_{el}^{DFT}$.

such resulting imaginary dielectric function is depicted in Figure 17: blue BSE curve is most similar to TD-PBE$+\Delta$ curve with EXX/GGA ratio of 0.3/0.7. Thus, the whole situation on various approximations can be summarized in
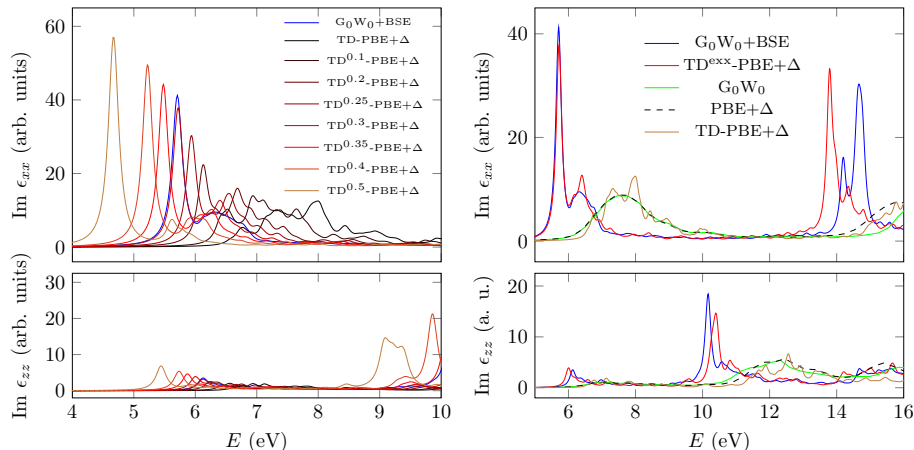


Figure 17: Optical absorption spectra (imaginary part of dielectric function $\epsilon$) of h-BN (AA$'$) using TD-DFT and the reference $G_0W_0$+BSE (blue line): (left) The electron-hole ladder diagrams in present TD-DFT calculations are approximated by the exact exchange (EEX) and different EXX/GGA ratio is evaluated (and labeled by the EXX part as TD$^{\text{exx}}$-PBE$+\Delta$). (right) General comparison of various approaches (with and without electron-hole interaction). The exact exchange kernel with EXX/GGA ratio of 0.3/0.7 in TD-DFT (red TD$^{\text{eex}}$-PBE$+\Delta$ curve) is a promising computationally cheap approximation correctly fitting excitonic effects in h-BN. Taken from Supplementary Material [2].

the right panel of Figure 17: Approximate inclusion of better electron-electron interaction by rigid shift of unoccupied band is responsible to dielectric function from PBE$+\Delta$ (red dashed line) similar to $G_0W_0$ spectra (green line). The approximative addition of electron-hole interaction by admixture of EXX into the subsequent Casida equation kernel (red TD$^{\text{eex}}$-PBE$+\Delta$ line) is approaching BSE curve (blue line), while without EXX, excitonic effects are not achieved (brown TD-PBE$+\Delta$ line).

We therefore systematically tested a set of 2D materials in Reference [3], which is included as Supplementary Material no. [3] of the thesis. We derived formal similarity of the Bethe-Salpeter equation (Equation 9) and the Casida equation (Equation 11) and therefore differences between BSE and TD-DFT become easily comparable. Changes of $E_{n\mathbf{k}}^{\text{QP}}$ and $W(\boldsymbol{q}, \boldsymbol{G}, \boldsymbol{G}')$ with $\boldsymbol{q} = \boldsymbol{k} - \boldsymbol{k}' + \boldsymbol{G_0}$ to $E_{n\mathbf{k}}$ and $f_{\text{XC}}(q \to 0, \boldsymbol{G}, \boldsymbol{G}')$ indicate that it is impossible to exactly reproduce BSE. However, one can reproduce a portion of the BSE coupling matrix with adiabatic TD-DFT. Without exact exchange (EXX), excitonic effects are not present in TD-DFT calculations and a reasonable part of EXX must be included in order to mimic exact Coulomb exchange $W$ (*cf.* term $-W$ *vs.* $2f_{\text{XC}}$ in Eqs. (9) and (11), respectively). We, therefore, decided to find the fraction $\alpha$ of EXX by using the formula for screened hybrid functionals (Equation 5), also containing another variable, screening $\omega$. We selected a broad gap range of $1 - 6$ eV of important semiconducting and insulating 2D materials, for which GW+BSE
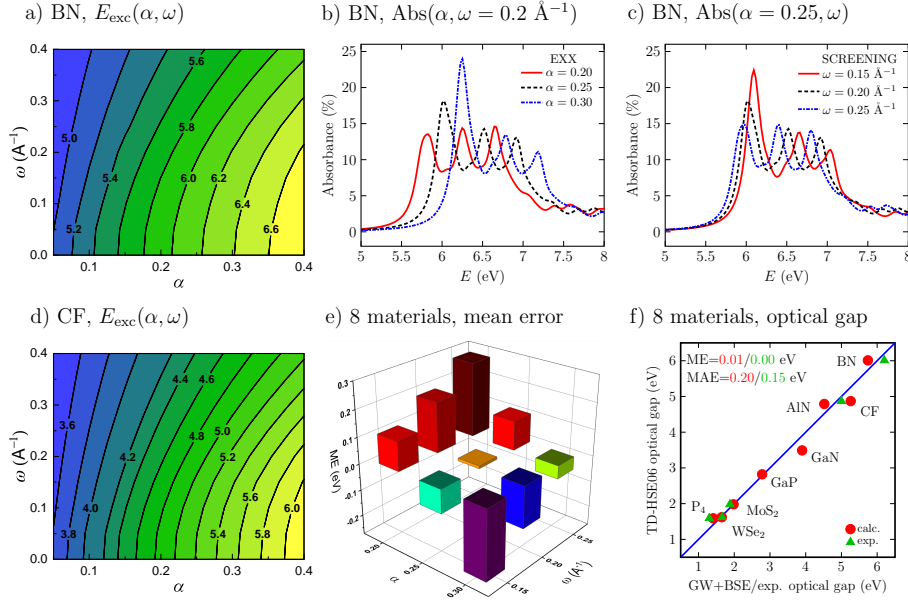
Figure 18: Search for the optimal fraction $\alpha$ of EXX and screening parameter $\omega$ in TD-DFT based on the SH functional of Eq. (5): a) optical gap of BN as a function of $\alpha$ and $\omega$, b) optical absorbance of BN depending on $\alpha$ and c) on $\omega$, d) optical gap of CF as a function of $\alpha$ and $\omega$, e) mean error for TD-SH with respect to GW+BSE optical gaps as a function of $\alpha$ and $\omega$, f) TD-HSE06 optical gaps in relation to GW+BSE and experimental optical gaps; the blue solid line is an ideal case. Taken from Supplementary Material [3].

optical gaps were available: phosphorene ($P_4$), two transition metal dichalcogenides (tungsten diselenide $WSe_2$ and molybdenum disulfide $MoS_2$), several hexagonal III-V group semiconductors (gallium phosphide GaP, gallium nitride GaN, aluminum nitride AlN, and boron nitride BN) and fluorographene (CF). We started with wide-gap semiconductors/insulators BN and CF, as computing the optical spectrum for them is more difficult. The dependence of optical gap $\Delta_{\mathrm{opt}}$ of BN on $\alpha$ and $\omega$ is shown in Figure 18a; the same for CF is presented in Figure 18d. Based on this systematic search (BN and CF), only a subset of previous $\alpha$ and $\omega$ values were used for all eight 2D materials leading to the evaluation of the TD-DFT with respect to the BSE optical gap in terms of mean errors. The minimal errors were found for the values of $\alpha = 0.25$ and $\omega = 0.30$ (Figure 18e). These values are surprisingly corresponding to the definition of hybrid density functional HSE06 [25]. We therefore labeled this variant of TD-DFT as TD-HSE06. The resulting errors of TD-HSE06 were very small: Mean error (ME) = 0.01 eV, mean absolute error (MAE) = 0.2 eV and mean absolute percent error = 5.6% (Figure 18f).

Later, we applied the derived TD-HSE06 approach on MXenes, namely in the Supplementary Material [5]. We first show the performance of the TD-HSE06 approach on the simplest material, $Sc_2CF_2$ MXene, which is a nonmagnetic direct material, by comparison to BSE@GW (Figure 19). There was a 0.17 eV difference in the optical gap and also the shape of the spectra was similar.
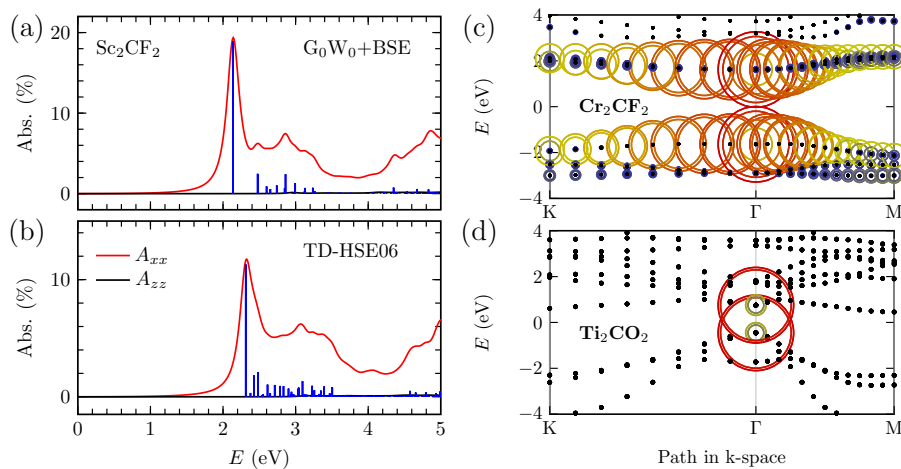
Figure 19: Direct comparison of optical absorbance $A$ ($A_{xx} = A_{yy}$ and $A_{zz}$ components) for $Sc_2CF_2$ computed with (a) $G_0W_0$+BSE and (b) TD-HSE06 methods. Particular excitonic states are shown using vertical blue lines. Electronic band structures from HSE06 calculations (black dots) and all $|A_{vck}^S|$ coefficients from Equation 11 (represented by the radii of colored circles) for the first bright exciton in (c) $Cr_2CF_2$ and (d) $Ti_2CO_2$. Taken from Supplementary Material [5].

Other investigated materials (Cr-, Mn-, Sc-, and Ti-based semiconducting MXenes) are indirect and complicated by magnetism (spin-polarized calculations) and are of possible multi-reference character: our analysis of excitons (e.g., in Cr-based MXenes) showed broad contributions of electron-hole pairs from k-space and bands (Figure 19, note the possibility to do such analysis as in BSE case). The considered MXene materials are ideal absorbers: the absorptance is about 10–20% in the 1-3 eV energy range only with 2.2-4.4 Å monolayer thickness, which is significantly better performance than 5–10% in the $MoS_2$ case with a thickness of 3.1 Å (one of the most used semiconducting materials). Finally, we also showed unintuitive behavior of optical gaps with the biaxial strain of the materials: While tension leads to an increase in the optical gap of Sc-based MXenes, the optical gap of Ti- and Mn-based MXenes decreases. Such combinations of optical, magnetic, and mechanical properties indicate the potential applications of MXenes in photovoltaics, sensors, or electronics.

Finally, we would like to present applications of TD-HSE06 on larger supercells. For the first time, *ab initio* optical spectra of van der Waals heterostructures containing incommensurate cells of different monolayers (containing tens of atoms in computational supercell) were calculated. We focused on prototypical hetero-bilayer interfaces boron nitride/tungsten diselenide and molybdenum disulfide/tungsten diselenide. We generated large sets of possible incommensurate supercells of bilayers by rotating them mutually and attaching them to achieve minimal strain and a reasonable number of atoms. Finally, $BN/WSe_2$ results in 26 atoms and 15° rotation and $MoS_2/WSe_2$ had 75 atoms and 15° rotation, as shown in Figure 20. Concerning optical spectra (absorptance), new exciton features in the TD-HSE06 curves (with respect to PBE and HSE06
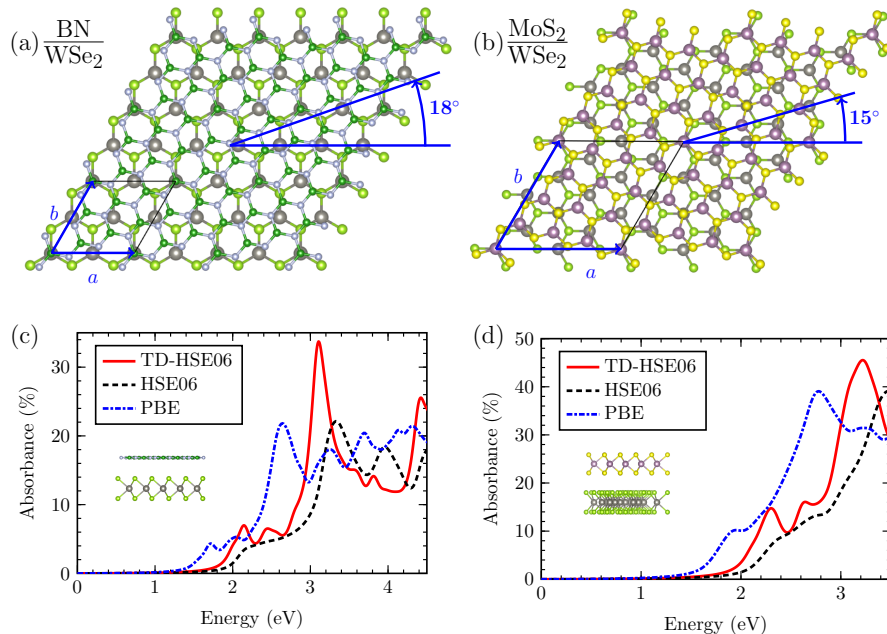
Figure 20: Schematic of (a) the BN/WSe$_2$ and (b) MoS$_2$/WSe$_2$ vdW heterostructures presenting the hexagonal calculation cells with a $a = b = 6.6$ Å (26 atoms, 18° rotation between both lattices) and 11.4 Å (75 atoms, 15° rotation). (c-d) In-plane optical absorbance is computed with the TD-HSE06 method, the HSE06 functional, and the PBE functional. Taken from Supplementary Material [3].

spectra) are clearly visible (Figure 20). BN/WSe$_2$ is an example of type-I band alignment [55] at hetero-bilayer interfaces and the lowest excitations are given by the valence band maximum and conduction band minimum of WSe$_2$. I.e., intra-layer exciton is responsible for the first excitonic peak in BN/WSe$_2$. On the other hand, MoS$_2$/WSe$_2$ is a typical example of type-II (staggered) alignment [55] at the interface. The first bright exciton in MoS$_2$/WSe$_2$ is therefore interlayer. Such an approach is therefore approximately accounting for many-body effects, provides necessary analyses, and is of intermediate computational expenses.

### 3.2.2 Semiempirical Electronic Structure of 2D Materials

Concerning semiempirical calculations, we were inspired by tight-binding (TB) calculations on electronic and optical properties of partially and fully fluorinated graphene [56], which were performed with rectangular supercells consisting of $2400 \times 2400$ carbon atoms. This seemed a model of quite realistic samples on the scale of micrometers, where predictivity was ensured by fitting TB parameters on GW band structure. We were also inspired by our previous study on hydroxofluorographene [57], where certain magnetic motifs were important (and larger supercells were needed). As the tight-binding method also exists in variant with DFT-derived parameters, DFTB (Section 3.2.2), we started to

test such semiempirical Hamiltonians on well-explored fluorographene material [6] – this is enclosed as the Supplementary Material no. [6] to the thesis. After some testing, we realized, that the present semiempirical DFTB simulations in combination with pbc-0-3 set of the Slater–Koster parameters provide a realistic description of the electronic band gap of fluorographene of $\Delta_{\mathrm{el}}^{\mathrm{DFTB}} = 7.12$ eV, which is in excellent agreement with our previous benchmark calculation of the fundamental band gap of (Section 3.1.1, $\Delta^{\mathrm{theor}} \approx 7.1 \pm 0.1$ eV from GW and QMC). Then, to study the effect of F-vacancy and the substitution of F atom by a chemical group we used a 9×9 CF supercell ($C_{162}F_{162}$). We show that the F-vacancy and/or chemical groups influence the magnetic structure, which depends on the number of defects and their distribution between the two sides of the graphene plane. Interestingly, we pointed out a possibility of imprinting local magnetism not only by F-vacancy and -OH combinations but also using F-vacancy and -CN or $-NH_2$ groups. In such structures, the magnetic ordering and the total magnetic moments depend on their adsorption sites and their presence on the same or opposite sides. Moreover, we show that the zigzag-like direction is most preferred for defluorination, and NM, FM, AFM, and ferrimagnetic (FiM) are present depending on the number of F-vacancies and their distribution around the fluorographene cell. Ferrimagnetic zigzag chains are a basic stable magnetic motif in perturbed fluorographene and can be driven by F-atom desorption/adsorption. In follow-up works, we also tested the DFTB method on $Ti_2CO_2$ MXene [58] and later for mixed termination of $Ti_2C$ [59]. We note, that often limitation of DFTB method is unavailable parametrization for particular system. Therefore, new GFN1-xTB Hamiltonian appeared recently [60], which is more general and provides parameters for elements up to $Z \leq 86$, and it was recently supported by the DFTB+ code.

# 4  Conclusions and Outlooks

In this thesis, we briefly inspected the behavior of 2D materials in two directions: 1) using accurate methods for electronic structure and optical spectra, focused on the precision of our results (target predictivity comparable to experiment) 2) using more approximate methods useful for larger systems. We are not developers and we "only" applied methods to materials descriptions and obtained reliable material properties. However, we prefer to develop a methodology, tune methods, and validate setups so that our work can also be used by the community as useful protocols for future research. We also summarized actual challenges in 2D materials modeling in this thesis (namely electronic and optical properties) and offered some systematic solutions focused on precision in the case of small periodic computational supercells of materials and the effectiveness of larger supercell descriptions.

The research on 2D materials is perspective *per se*. Currently, new 2D materials are still being discovered (e.g., in the MXenes, MBenes, and perovskites families), and new phases of 2D materials are being prepared (metals, semiconductors, ferromagnets, antiferromagnets, topological insulators, or excitonic insulators). The broad palette of physical properties of 2D materials is interesting, e.g., high optical absorption efficiency, as we discussed above. Different combinations of these materials in layers then create the so-called van der Waals heterostructures (Figure 2), the resulting properties of which are highly variable and depend on the properties of the individual components. This area of research is highly innovative and is likely to be one of the main research topics in solid-state physics and materials science in the future. Let us add that in a relatively short time since the discovery of graphene in 2004, the Nobel Prize for research into two-dimensional materials was already awarded in 2010 (Novoselov and Geim) [61]. The importance of this area of research was also evaluated and manifested by the European Commission, which in 2013 approved the Graphene Flagship (so far the largest European research initiative aimed at the great scientific and technological challenges of the present time through multidisciplinary research) [62]. Currently, the first implementations of ultrathin devices based on graphene and 2D materials are appearing, e.g. transistors implemented as van der Waals heterostructures (Figure 3), ultrathin memories, solar cells, supercapacitors, sensors, and other flexible devices [63]. Researchers are therefore often returning to a careful examination of the properties of basic 2D materials and their layered bulk counterparts that have been known for a long time. Fundamental knowledge and basic science are required in line with technological progress.

# References

[1] František Karlický and Josef Turoň. Fluorographane c2fh: Stable and wide band gap insulator with huge excitonic effect. *Carbon*, 135:134 – 144, 2018.

[2] Miroslav Kolos and František Karlický. Accurate many-body calculation of electronic and optical band gap of bulk hexagonal boron nitride. *Phys. Chem. Chem. Phys.*, 21(7):3999–4005, 2019.

[3] Tomi Ketolainen, Nikola Macháčová, and František Karlický. Optical gaps and excitonic properties of 2d materials by hybrid time-dependent density functional theory: Evidences for monolayers and prospects for van der waals heterostructures. *J. Chem. Theory Comput.*, 16(9):5876–5883, 2020.

[4] Matúš Dubecký, František Karlický, Stanislav Minárik, and Lubos Mitas. Fundamental gap of fluorographene by many-body gw and fixed-node diffusion monte carlo methods. *J. Chem. Phys.*, 153(18):184706, 2020.

[5] Tomi Ketolainen and Frantisek Karlický. Optical gaps and excitons in semiconducting transition metal carbides (mxenes). *J. Mater. Chem. C*, 10:3919–3928, 2022.

[6] Taoufik Sakhraoui and Frantisek Karlický. Dftb investigations of the electronic and magnetic properties of fluorographene with vacancies and with adsorbed chemical groups. *Phys. Chem. Chem. Phys.*, 24:3312–3321, 2022.

[7] Miroslav Kolos and František Karlický. The electronic and optical properties of III–v binary 2d semiconductors: how to achieve high precision from accurate many-body methods. *Phys. Chem. Chem. Phys.*, 24(44):27459–27466, 2022.

[8] Matúš Dubecký, Stanislav Minárik, and František Karlický. Benchmarking fundamental gap of $sc_2c(oh)_2$ MXene by many-body methods. *J. Chem. Phys.*, 158(5):054703, 2023.

[9] Nilesh Kumar and František Karlický. Oxygen-terminated $Ti_3C_2$ MXene as an excitonic insulator. *Appl. Phys. Lett.*, 122(18):183102, 2023.

[10] Nilesh Kumar, Miroslav Kolos, Sitangshu Bhattacharya, and František Karlický. Excitons, optical spectra, and electronic properties of semiconducting hf-based mxenes. *J. Chem. Phys.*, 160(12):124707, 2024.

[11] Jiří Kalmár and František Karlický. Strain-induced changes of electronic and optical properties of Zr-based MXenes. *J. Appl. Phys.*, 135(24):244302, 2024.

[12] Jiří Kalmár and František Karlický. Mn2c mxene functionalized by oxygen is a semiconducting antiferromagnet and an efficient visible light absorber. *Phys. Chem. Chem. Phys.*, 26:19733–19741, 2024.

[13] K. S. Novoselov, A. K. Geim, S. V. Morozov, D. Jiang, Y. Zhang, S. V. Dubonos, I. V. Grigorieva, and A. A. Firsov. Electric field effect in atomically thin carbon films. *Science*, 306(5696):666–669, 2004.

[14] Jannik C. Meyer, A. K. Geim, M. I. Katsnelson, K. S. Novoselov, T. J. Booth, and S. Roth. The structure of suspended graphene sheets. *Nature*, 446(7131):60–63, 2007.

[15] F. Karlický, K. K. R. Datta, M. Otyepka, and R. Zbořil. Halogenated graphenes: Rapidly growing family of graphene derivatives. *ACS Nano*, 7(8):6434–6464, 2013.

[16] Mikhail I. Katsnelson. *Graphene: Carbon in Two Dimensions*. Cambridge University Press, 2012.

[17] K. S. Novoselov, D. Jiang, F. Schedin, T. J. Booth, V. V. Khotkevich, S. V. Morozov, and A. K. Geim. Two-dimensional atomic crystals. *Proc. Natl. Acad. Sci.*, 102(30):10451–10453, 2005.

[18] Babak Anasori and Yury Gogotsi, editors. *2D Metal Carbides and Nitrides (MXenes)*. Springer, Switzerland, 2020.

[19] A. K. Geim and I. V. Grigorieva. Van der waals heterostructures. *Nature*, 499(7459):419–425, 2013.

[20] Mengjian Zhu, Davit Ghazaryan, Seok-Kyun Son, Colin R Woods, Abhishek Misra, Lin He, Takashi Taniguchi, Kenji Watanabe, Kostya S Novoselov, Yang Cao, and Artem Mishchenko. Stacking transition in bilayer graphene caused by thermally activated rotation. *2D Materials*, 4(1):011013, 2016.

[21] John P. Perdew, Weitao Yang, Kieron Burke, Zenghui Yang, Eberhard K. U. Gross, Matthias Scheffler, Gustavo E. Scuseria, Thomas M. Henderson, Igor Ying Zhang, Adrienn Ruzsinszky, Haowei Peng, Jianwei Sun, Egor Trushin, and Andreas Görling. Understanding band gaps of solids in generalized kohn–sham theory. *PNAS*, 114(11):2801–2806, 2017.

[22] Alexey Chernikov, Timothy C. Berkelbach, Heather M. Hill, Albert Rigosi, Yilei Li, Burak Aslan, David R. Reichman, Mark S. Hybertsen, and Tony F. Heinz. Exciton binding energy and nonhydrogenic rydberg series in monolayer $ws_2$. *Phys. Rev. Lett.*, 113:076802, 2014.

[23] Carlo Adamo and Vincenzo Barone. Toward reliable density functional methods without adjustable parameters: The PBE0 model. *J. Chem. Phys.*, 110(13):6158–6170, 1999.

[24] Matthias Ernzerhof and Gustavo E. Scuseria. Assessment of the Perdew–Burke–Ernzerhof exchange-correlation functional. *J. Chem. Phys.*, 110(11):5029–5036, 1999.

[25] Aliaksandr V. Krukau, Oleg A. Vydrov, Artur F. Izmaylov, and Gustavo E. Scuseria. Influence of the exchange screening parameter on the performance of screened hybrid functionals. *J. Chem. Phys.*, 125(22):224106, 2006.

[26] Lars Hedin. New method for calculating the one-particle green's function with application to the electron-gas problem. *Phys. Rev.*, 139:A796–A823, 1965.

[27] M. Shishkin and G. Kresse. Implementation and performance of the frequency-dependent gw method within the paw framework. *Phys. Rev. B*, 74(3):035101, 2006.

[28] H.A. Bethe and E.E. Salpeter. A relativistic equation for bound state problems. *Phys. Rev.*, 82(2):309–310, 1951.

[29] G. Strinati. Effects of dynamical screening on resonances at inner-shell thresholds in semiconductors. *Phys. Rev. B*, 29(10):5718–5726, May 1984.

[30] Michael Rohlfing and Steven G. Louie. Electron-hole excitations and optical spectra from first principles. *Phys. Rev. B*, 62(8):4927–4944, 2000.

[31] F. Fuchs, C. Rödl, A. Schleife, and F. Bechstedt. Efficient $\mathcal{O}(N^2)$ approach to solve the bethe-salpeter equation for excitonic bound states. *Phys. Rev. B*, 78(8):085103, 2008.

[32] W. M. C. Foulkes, L. Mitas, R. J. Needs, and G. Rajagopal. Quantum monte carlo simulations of solids. *Rev. Mod. Phys.*, 73:33–83, 2001.

[33] Manuel Grumet, Peitao Liu, Merzuk Kaltak, Ji ří Klimeš, and Georg Kresse. Beyond the quasiparticle approximation: Fully self-consistent *gw* calculations. *Phys. Rev. B*, 98:155143, 2018.

[34] G. Kresse and D. Joubert. From ultrasoft pseudopotentials to the projector augmented-wave method. *Phys. Rev. B*, 59:1758–1775, 1999.

[35] P. E. Blöchl. Projector augmented-wave method. *Phys. Rev. B*, 50:17953–17979, 1994.

[36] Dmitrii Nabok, Andris Gulans, and Claudia Draxl. Accurate all-electron $G_0W_0$ quasiparticle energies employing the full-potential augmented plane-wave method. *Phys. Rev. B*, 94:035118, 2016.

[37] Diana Y. Qiu, Felipe H. da Jornada, and Steven G. Louie. Erratum: Optical spectrum of mos$_2$: Many-body effects and diversity of exciton states [phys. rev. lett. 111, 216805 (2013)]. *Phys. Rev. Lett.*, 115:119901, 2015.

[38] Kurt Lejaeghere, Gustav Bihlmayer, Torbjörn Björkman, Peter Blaha, Stefan Blügel, and et al. Reproducibility in density functional theory calculations of solids. *Science*, 351(6280):aad3000, 2016.

[39] R. Zbořil, F. Karlický, A. B. Bourlinos, T. A. Steriotis, A. K. Stubos, and V. Georgakilas et al. Graphene fluoride: A stable stoichiometric graphene derivative and its chemical conversion to graphene. *Small*, 6(24):2885–2891, 2010.

[40] R. R. Nair, W. Ren, R. Jalil, I. Riaz, V. G. Kravets, and L. Britnell et al. Fluorographene: A two-dimensional counterpart of teflon. *Small*, 6(24):2877–2884, 2010.

[41] F. Karlický, R. Zbořil, and M. Otyepka. Band gaps and structural properties of graphene halides and their derivates: A hybrid functional study with localized orbital basis sets. *J. Chem. Phys.*, 137(3):034709, 2012.

[42] F. Karlický and M. Otyepka. Band gaps and optical spectra of chlorographene, fluorographene and graphane from $G_0W_0$, $GW_0$ and GW calculations on top of PBE and HSE06 orbitals. *J. Chem. Theory Comput.*, 9(9):4155–4164, 2013.

[43] Ki-Joon Jeon, Zonghoon Lee, Elad Pollak, Luca Moreschini, Aaron Bostwick, Cheol-Min Park, Rueben Mendelsberg, Velimir Radmilovic, Robert Kostecki, Thomas J. Richardson, and Eli Rotenberg. Fluorographene: A wide bandgap semiconductor with ultraviolet luminescence. *ACS Nano*, 5(2):1042–1046, 2011.

[44] Bei Wang, Justin R. Sparks, Humberto R. Gutierrez, Fujio Okino, Qingzhen Hao, Youjian Tang, Vincent H. Crespi, Jorge O. Sofo, and Jun Zhu. Photoluminescence from nanocrystalline graphite monofluoride. *Appl. Phys. Lett.*, 97(14):141915, 2010.

[45] Vlastimil Mazánek, Ondrej Jankovský, Jan Luxa, David Sedmidubský, Zbynek Janoušek, Filip Šembera, Martin Mikulics, and Zdenek Sofer. Tuning of fluorine content in graphene: towards large-scale production of stoichiometric fluorographene. *Nanoscale*, 7(32):13646–13655, 2015.

[46] F. Karlický and M. Otyepka. Band gaps and optical spectra from single- and double-layer fluorographene to graphite fluoride: many-body effects and excitonic states. *Ann. Phys.*, 526(9-10):408–414, 2014.

[47] G. Cassabois, P. Valvin, and B. Gil. Hexagonal boron nitride is an indirect bandgap semiconductor. *Nat. Photonics*, 10(4):262–266, 2016.

[48] T. C. Doan, J. Li, J. Y. Lin, and H. X. Jiang. Bandgap and exciton binding energies of hexagonal boron nitride probed by photocurrent excitation spectroscopy. *Appl. Phys. Lett.*, 109(12):122101, 2016.

[49] Luigi Cigarini, Michal Novotný, and František Karlický. Lattice dynamics in the conformational environment of multilayered hexagonal boron nitride (h-bn) results in peculiar infrared optical responses. *Phys. Chem. Chem. Phys.*, 23:7247–7260, 2021.

[50] Michal Novotný, Matúš Dubecký, and František Karlický. Toward accurate modeling of structure and energetics of bulk hexagonal boron nitride. *J. Comput. Chem.*, 45(2):115–121, 2024.

[51] Miroslav Kolos, Luigi Cigarini, Rekha Verma, František Karlický, and Sitangshu Bhattacharya. Giant linear and nonlinear excitonic responses in an atomically thin indirect semiconductor nitrogen phosphide. *J. Phys. Chem. C*, 125(23):12738–12757, 2021.

[52] Miroslav Kolos, Rekha Verma, František Karlický, and Sitangshu Bhattacharya. Large exciton-driven linear and nonlinear optical processes in monolayers of nitrogen arsenide and nitrogen antimonide. *J. Phys. Chem. C*, 126(35):14931–14959, 2022.

[53] Roman Fanta and Matúš Dubecký. Toward automated screening of band gap sensitivity in 2d materials. *J. Phys.: Mater.*, 6(4):045004, 2023.

[54] Marco Bernardi, Maurizia Palummo, and Jeffrey C. Grossman. Extraordinary sunlight absorption and one nanometer thick photovoltaics using two-dimensional monolayer materials. *Nano Lett.*, 13(8):3664–3670, 2013.

[55] Marco Bernardi, Can Ataca, Maurizia Palummo, and Jeffrey C. Grossman. Optical and electronic properties of two-dimensional layered materials. *Nanophotonics*, 6(2):479–493, 2017.

[56] Shengjun Yuan, Malte Rösner, Alexander Schulz, Tim O. Wehling, and Mikhail I. Katsnelson. Electronic structures and optical properties of partially and fully fluorinated graphene. *Phys. Rev. Lett.*, 114:047403, 2015.

[57] Jiří Tuček, Kateřina Holá, Athanasios B. Bourlinos, Piotr Błoński, Aristides Bakandritsos, Juri Ugolotti, Matúš Dubecký, František Karlický, Václav Ranc, Klára Čépe, Michal Otyepka, and Radek Zbořil. Room temperature organic magnets derived from sp3 functionalized graphene. *Nature Commun.*, 8:14525, 2017.

[58] Taoufik Sakhraoui and Frantisek Karlický. Electronic nature transition and magnetism creation in vacancy-defected ti2co2 mxene under biaxial strain: A dftb + u study. *ACS Omega*, 7(46):42221–42232, 2022.

[59] Taoufik Sakhraoui and František Karlický. Prediction of induced magnetism in 2d ti2c based mxenes by manipulating the mixed surface functionalization and metal substitution computed by xtb model hamiltonian of the dftb method. *Phys. Chem. Chem. Phys.*, 26:12862–12868, 2024.

[60] Christoph Bannwarth, Eike Caldeweyher, Sebastian Ehlert, Andreas Hansen, Philipp Pracht, Jakob Seibert, Sebastian Spicher, and Stefan Grimme. Extended tight-binding quantum chemistry methods. *WIREs Comput. Mol. Sci.*, 11:e1493, 2021.

[61] Nobel Prize organisation. The nobel prize in physics 2010. `https://www.nobelprize.org/prizes/physics/2010/summary/`, 2010. Accessed: 2024-11-11.

[62] European Commission. Graphene flagship. `https://graphene-flagship.eu`, 2013. Accessed: 2024-11-11.

[63] Ajit Kumar Katiyar, Anh Tuan Hoang, Duo Xu, Juyeong Hong, Beom Jin Kim, Seunghyeon Ji, and Jong-Hyun Ahn. 2d materials in flexible electronics: Recent advances and future prospectives. *Chemical Reviews*, 124(2):318–419, 2024.
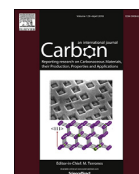
# Supplementary Materials

# Supplementary Material 1

# Fluorographane C$_2$FH: Stable and wide band gap insulator with huge excitonic effect

František Karlický[*], Josef Turoň

*Department of Physics, Faculty of Science, University of Ostrava, 30. dubna 22, 701 03 Ostrava, Czech Republic*

## ARTICLE INFO

## ABSTRACT

We present structural, vibrational, electronic and optical properties of recently prepared fully fluorinated and hydrogenated graphene, called fluorographane. We consider 1:1 ratio of F and H adatoms and we carefully investigate possible structural conformers in C$_2$FH stoichiometric material. The reported results show that all conformers are dynamically stable and homogeneous structures with F and H atoms on both sides of carbon honeycomb structure are more stable than the Janus structures with F atoms on one side and all H atoms on the other. While the main structural and vibrational features are roughly similar for various conformers, electronic and optical properties are very sensitive to local structure (namely specific combinations of F and H adatoms on the graphene surface) and differ significantly. Our highly accurate results based on many-body methods (GW and BSE) indicate that homogeneous fluorographane has unusually wide indirect electronic band gap of ~10 eV (larger than both pure graphane CH and pure fluorographene CF) and embodies a huge excitonic effect (~3 eV). Fluorographane C$_2$FH is therefore a material with the widest electronic gap and a largest binding energy of exciton in the class of currently known 2D materials.

© 2018 Elsevier Ltd. All rights reserved.

## 1. Introduction

Simultaneously hydrogenated and fluorinated graphene, called fluorographane, is the new member of graphene-based 2D material family. It was theoretically predicted as a thermodynamically stable compound with a large band gap [1], however, dynamical instability was confirmed for all possible structural conformers of C$_2$FH stoichiometry with exception of the so called Janus chair conformer [2]. On the other hand, despite of theoretical predictions, the first experimental report on the synthesis of fluorographane has been published recently by Šofer et al. [3]. Fluorographanes with varied ratios of H and F atoms, C$_1$H$_x$F$_{1-x-\delta}$, were obtained from graphene by hydrogenation via Birch reaction with consequent fluorination of the resulting graphane. Fluorographanes had high hydrophobic properties and showed fast heterogeneous electron transfer properties. Disagreement of experiment [3] and calculations [2] concerning the stability of fluorographanes led us to careful investigation of its vibrational properties in this work. It is worth to note, that fluorographane monolayer with H atoms on one side and

F on the opposite side of the C layer (predicted as the only dynamically stable C$_2$FH conformer in Ref. [2]), i.e. the mentioned Janus material, was shown to embody piezoelectric properties [4,5] and is also promising as a suitable substrate for MoS$_2$ [6]. Contacting MoS$_2$ to the hydrogen (fluorine) terminated side of fluorographane results in a strong n- (p-) type doping of MoS$_2$ of technological interest. Hydrofluorinated Janus graphene can also self-assembly into Janus nanoscroll at room temperature [7].

Density functional theory (DFT) is a powerful tool for modeling graphene and its halogenated derivatives [8,9]. However, description of the electronic and optical properties is principally limited by the one-particle ground state essence of DFT. Difference between the highest occupied and lowest unoccupied eigenenergies of the corresponding Kohn-Sham orbitals are used as the band gap guess but this approach leads to an inherent band gap problem [10]. Traditional generalized gradient approximation (GGA) DFT functionals therefore highly underestimate the band gaps of insulating or semiconducting graphene derivatives (often by several eV) [1,11]. One of the possible approaches to overcome this limitation is use of exchange-correlation functionals based on admixture of GGA and exact non-local Hartree-Fock (HF) exchange. Since the band gaps in HF method are systematically overestimated [12], such hybrid functionals often offer their more accurate predictions. Due to big

---

* Corresponding author.
*E-mail address:* frantisek.karlicky@osu.cz (F. Karlický).

progress of highly powerful computers, accurate many-body perturbation theories beyond DFT became accessible and enable accurate description of electronic and optical properties of materials in recent decades. Nowadays, the GW approximation [13] is considered as state-of-the-art method for reliable prediction of band gaps. The electronic band gaps predicted for fluorographene [14,15] ($C_1F_1$) and graphane [16,17] ($C_1H_1$) using the GW approximation were 7—8 eV [11,18—23] and 5—6 eV [11,18,19,24], respectively. The experimentally determined optical gap of fluorographene was, however, significantly lower (>3 eV [14], >3.8 eV [25], or >3.5—3.9 eV [26]), because these values were derived from optical absorption or photoluminescence spectra and electron transitions observed in optical spectra involve formation of an exciton. The optical gap can be estimated using the Bethe-Salpeter equation (BSE) [27], which includes excitonic effects. Fluorographene has a high exciton binding energy (~2 eV) [11,22,23], which may partially explain discrepancy between the experimental data and the GW prediction of a fundamental gap. The effect of point defects in real fluorographene was predicted to be synergistic to exciton binding energy (lowering gap) but rather small [11,28] and therefore the problem of optical gap discrepancy between GW + BSE calculations and experiments remains open. There exists just one similar measurement on graphane. Recently, Yang et al. [29] used UV—vis spectroscopy to predict the optical gap of 4.3 eV for nearly perfect pure graphane $C_{1.04}H$. Experimental guess of the optical band gap is in line with the earlier accurate GW + BSE optical gap predictions of 4.1—4.8 eV [11] or 3.8 eV [24].

The aim of this work is to provide structural motifs of fluorographane $C_2FH$ and to accurately predict its vibrational, electronic and optical properties. First, we predict relative and dynamical stability, thermodynamics and electronic properties of $C_2FH$ conformers at the DFT level (Section 3.1). Careful convergence tests for GW electronic gaps (electron-electron interaction included) and BSE optical gaps (electron-hole interaction included) are shown as the essential part of the calculations (Section 3.2). Finally (Section 3.3), we report on the accurate electronic and optical properties of $C_2FH$ with inclusion of quasiparticle and excitonic effects.

## 2. Methods

The unit cell of fluorographene CF (graphane CH) in its most stable chair conformation contains 4 atoms: 2 carbon atoms and 2 fluorine (hydrogen) atoms. If one considers fluorographane and expects H atom on one side and F atom on the opposite side of the carbon layer, the primitive cell of the Janus chair conformer contains still 4 atoms: $C_2F_1H_1$. On the other hand, when H and F atoms on both sides of C layer appear, the smallest computational cell contains 8 atoms: $C_4F_2H_2$. Following the experimental fluorographane composition (see XPS on sample [24 + 24 h:5 + 12 bar] of Ref. [3] and the structure suggested in Scheme S1 therein) we will consider the same number of fluorine and hydrogen atoms in this work, i.e., the unit cell containing $C_4F_2H_2$ as a model of periodic $C_2FH$ fluorographanes. Subsequently, the chair conformer can exist in three forms (FhHf, FfHh, and FhFh; see Fig. 1); boat conformer (FhfH, FfhH, FhhF) and zigzag conformer (FHfh, FHhf, FFhh) too, i.e., we consider nine different $C_4F_2H_2$ unit cells. Adsorbates oriented up (down) with respect to carbon plane will be labeled by capital (small) letters in the following text and in Fig. 1.

The projector augmented wave (PAW) method [30] and DFT as implemented in the Vienna ab initio simulation package (VASP) [31] was used to perform the total energy, phonon, quasiparticle and absorption spectra calculations on the structures generated by geometry optimization using the Perdew-Burke-Ernzerhof (PBE) GGA functional [32]. We used two-dimensional $C_4F_2H_2$ rectangular

unit cell in xy plane (Fig. 1) and we used distance $L_z = 20$ Å in perpendicular (z) direction to avoid spurious interaction between layers (this distance has been further studied for suitability in estimation of quasiparticle electronic and optical properties, see Section 3.2). We used $E_{cut} = 500$ eV and $9 \times 15 \times 1$ Γ-centered k-point grid. Atomic positions and unit cells were relaxed until the forces on each atom were smaller than $5 \times 10^{-4}$ eV/Å (electronic steps were converged to $1 \times 10^{-7}$ eV). Phonon spectra were calculated using Phonopy [33] and finite displacement (0.015 Å, central difference) method in VASP. Subsequently, we improved our total energies by harmonic zero-point vibrational energies, *ZPE* (obtained by summing the frequencies over phonon branches and averaging over the Brillouin zone), and corrections to free-energy, entropy and constant volume specific heat [33].

The imaginary part $\varepsilon_2(\omega)$ of the frequency-dependent dielectric function, $\varepsilon(\omega) = \varepsilon_1(\omega) + i\varepsilon_2(\omega)$, was calculated [34] using the cell-periodic parts $u_{nk}$ of DFT orbitals $\phi_{nk}$ and its eigenenergies $E_{nk}$

$$\varepsilon_2^{\alpha\beta}(\omega) = \frac{4\pi^2 e^2}{\Omega} \lim_{q \to 0} \frac{1}{q^2} \sum_{c,v,\mathbf{k}} 2w_{\mathbf{k}}\delta(E_{c\mathbf{k}} - E_{v\mathbf{k}} - \omega)$$
$$\times \left\langle u_{c\mathbf{k}+\mathbf{e}_\alpha q} | u_{v\mathbf{k}} \right\rangle \left\langle u_{c\mathbf{k}+\mathbf{e}_\beta q} | u_{v\mathbf{k}} \right\rangle^*, \tag{1}$$

where $\alpha, \beta \in \{x, y, z\}$ denote matrix element indices, the vectors $\mathbf{e}_\alpha$ are unit vectors for three Cartesian directions, $\Omega$ the volume of the primitive cell, indices $n = c, v$ are band indices restricted to the conduction and the valence band states, respectively, $\mathbf{k}$ is a k-point index, and $w_{\mathbf{k}}$ is a weight of the corresponding k-point. Local field effects, that is, changes in the cell periodic part of the potential, were included within the random phase approximation (RPA). The real part $\varepsilon_1(\omega)$ was obtained using Kramers-Kronig relations. A Gaussian broadening of 50 meV and 512 sampling points were used for the dielectric function.

The quasi-particle (QP) energies $E_{nk}^{QP}$ can be calculated by solving quasiparticle equations as introduced by Hedin [13].

$$\left(T + V_{n-e} + V_H - E_{nk}^{QP}\right)\phi_{nk}(\mathbf{r}) + \int \sum \left(\mathbf{r}, \mathbf{r}'; E_{nk}^{QP}\right)\phi_{nk}(\mathbf{r}')\mathrm{d}^3\mathbf{r}'$$
$$= 0, \tag{2}$$

where $T$ is the kinetic energy operator, $V_{n-e}$ is the operator that accounts for the nuclear-electron interactions, $V_H$ is the Hartree potential, and, $n$ is the band index. The self energy operator Σ has the form [35].

$$\sum \left(\mathbf{r}, \mathbf{r}'; E_{nk}^{QP}\right) = \frac{i}{2\pi} \int_{-\infty}^{\infty} e^{iE\delta} G\left(\mathbf{r}, \mathbf{r}'; E_{nk}^{QP} + E\right) W(\mathbf{r}, \mathbf{r}'; E)\mathrm{d}E \tag{3}$$

in the GW approximation, where $G$ is the Green's function, $W$ is the screened Coulomb interaction, and $\delta$ is a positive infinitesimal number. Firstly, $G$ and $W$ were calculated using DFT eigenvalues and eigenfunctions, and, eigenstates $E_{nk}^{QP}$ of quasiparticle equation (2) were approximated by DFT single-particle energies $E_{nk}$ as well (non-self-consistent GW approximation denoted $G_0W_0$, i.e. the first-order correction to the DFT). That is, QP energies were calculated as

$$E_{nk}^{QP,0} = E_{nk} + Z_{nk}\mathrm{Re}[\langle\phi_{nk}|T + V_{n-e} + V_H + \Sigma(G, W; E_{nk})|\phi_{nk}\rangle$$
$$- E_{nk}], \tag{4}$$

where $Z$ is the normalization factor [36]. The updated quasiparticle
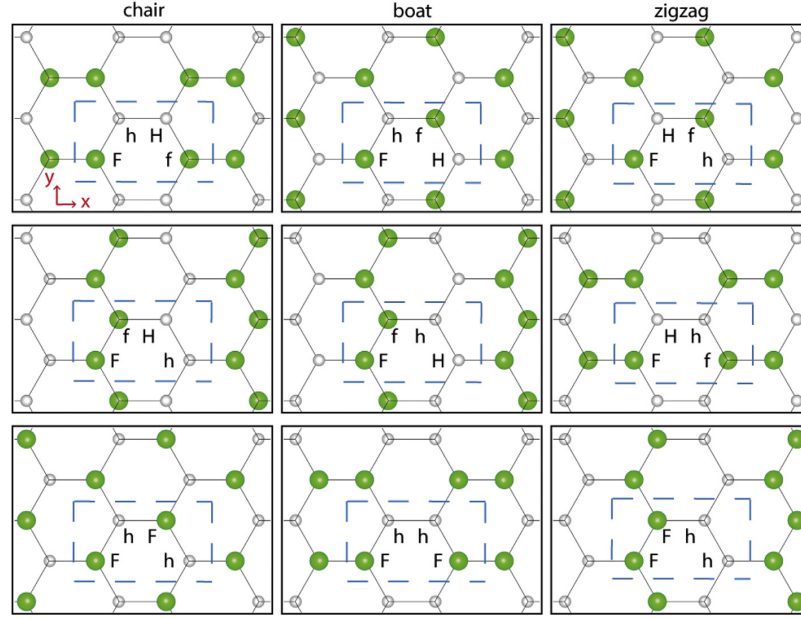
**Fig. 1.** Conformers of fluorographane $C_2FH$: schematic structures of all combinations of two fluorines and two hydrogens in rectangular unit cell containing 8 atoms ($C_4F_2H_2$). Empty/crossed balls denote adsorbates oriented up/down with respect to carbon plane and assigned by capital/small letters. The unit cells are highlighted by dashed line, green balls correspond to fluorine atoms, white balls to hydrogen atoms. The bottom structures are of Janus type. (A colour version of this figure can be viewed online.)

energy $E_{n\boldsymbol{k}}^{QP,i+1}$ was obtained from the previous $E_{n\boldsymbol{k}}^{QP,i}$ as

$$E_{n\boldsymbol{k}}^{QP,i+1} = E_{n\boldsymbol{k}}^{QP,i} + Z_{n\boldsymbol{k}} \mathrm{Re}\left[\left\langle \phi_{n\boldsymbol{k}} \left| T + V_{n-e} + V_H + \Sigma\left(G, W; E_{n\boldsymbol{k}}^{QP,i}\right) \right. \right.\right.$$
$$\left.\left.\left. \times \left| \phi_{n\boldsymbol{k}} \right\rangle - E_{n\boldsymbol{k}}^{QP,i}\right],\right. \tag{5}$$

that is, the eigenvalues were iteratively updated in the calculations of $G$ (denoted as $G_iW_0$) or also $W$ ($G_iW_i$). The corresponding $\varepsilon_2(\omega)$ was calculated using quasiparticle energies $E_{n\boldsymbol{k}}^{QP}$ in Eq. (1) with the inclusion of local field effects at RPA level (GW + RPA).

Excitonic effects were accounted for by the Bethe-Salpeter equation [27], which corresponds to the excitonic equation (eigenvalue problem) [37–39]:

$$\left(E_{c\boldsymbol{k}}^{QP} - E_{v\boldsymbol{k}}^{QP}\right)A_{vc\boldsymbol{k}}^S + \sum_{v'c'\boldsymbol{k}'}\langle vc\boldsymbol{k}|K_{e-h}|v'c'\boldsymbol{k}'\rangle = \Omega^S A_{vc\boldsymbol{k}}^S. \tag{6}$$

The $A_{vc\boldsymbol{k}}^S$ values were obtained by diagonalization of Eq. (6) and correspond to the amplitudes of a free electron-hole pair configuration composed of electron state $|c\boldsymbol{k}\rangle$ and hole state $|v\boldsymbol{k}\rangle$, the $\Omega^S$ values are eigenenergies (corresponding to the exciton excitation energies), and $K_{e-h}$ is the electron-hole interaction kernel. After solving Eq. (6), the dielectric function was calculated in analogy to Eq. (1) using $A_{vc\boldsymbol{k}}^S$ and $E_{n\boldsymbol{k}}^{QP}$ (GW + BSE).

Given the complex dielectric function $\varepsilon(\omega)$, various linear optical properties such as the refractive index (index of refraction) $n(\omega) =$
$$\sqrt{\frac{1}{2}\left(\sqrt{\varepsilon_1^2(\omega) + \varepsilon_2^2(\omega)} + \varepsilon_1(\omega)\right)},$$ the extinction coefficient $k(\omega) =$
$$\sqrt{\frac{1}{2}\left(\sqrt{\varepsilon_1^2(\omega) + \varepsilon_2^2(\omega)} - \varepsilon_1(\omega)\right)},$$ the absorption coefficient (absorption spectrum) $\alpha(\omega) = \frac{2\omega k(\omega)}{c}$ the reflectivity $R(\omega) = \frac{(n(\omega)-1)^2+k^2(\omega)}{(n(\omega)+1)^2+k^2(\omega)}$, or energy loss spectrum $L(\omega) = \frac{\varepsilon_2(\omega)}{\varepsilon_1^2(\omega)+\varepsilon_2^2(\omega)}$ can be

calculated.

## 3. Results and discussion

### 3.1. Structural, vibrational and electronic properties from DFT calculations

#### 3.1.1. Structural properties and cohesive energy

We optimized all nine conformations of fluorographane $C_2FH$ depicted in Fig. 1. The obtained optimal lattice parameters and bond lengths are reported in Table 1. The conformers are ordered according to cohesive energy given by the formula

$$E_{coh} = \frac{E - N_C \cdot E_C - N_F \cdot E_F - N_H \cdot E_H}{N_C + N_F + N_H} \tag{7}$$

where $E$, $E_C$, $E_F$, and $E_H$ correspond to the total energy of a unit cell, carbon atom, fluorine atom, and hydrogen atom, respectively ($N_X$ denotes the number of atoms of type X in the supercell). Lower cohesive energy corresponds to a more stable conformer. Our earlier work [1] indicates that hydrogenated graphene fluorides, $C_1H_xF_{1-x}(x<1)$, are generally more stable than graphane CH and its stability is approaching stability of fluorographene CF with increasing fluorine content. We therefore focus here on relative stability of $C_2FH$ conformers. We show in Table 1 the chair FhHf conformer as the most stable system followed by chair FfHh and zigzag FHfh (for structures, see Fig. 1). In general, conformers with F and H atoms mixed on both sides of carbon plane are more stable than those with F atoms on one side and only H atoms on the opposite (Janus type structures). See the most stable optimized structures from both types of conformers and the corresponding electronic density maps in Fig. 2. For both such subsets of conformers the order is the same: the preferred chair conformers are followed by zigzag conformers and boat conformers are the last.

**Table 1**
Structural properties and energetics of fluorographane. Lattice constants $a$, $b$, bond lengths C-F, C-H and C-C (all in Å), cohesive energies $E_{coh}$, zero-point energies $ZPE$, ZPE corrected cohesive energies $E_{coh}^{ZPE}$ (all in eV/atom), differences of cohesive energies with respect to the most stable conformer ($\Delta E_{coh}$ and $\Delta E_{coh}^{ZPE}$ in meV/atom), and differences of total energies per cell with respect to the most stable conformer ($\Delta E$ and $\Delta E^{ZPE}$ in eV/cell). The last three lines correspond to structures of the Janus type.

| conformation | | $a$ | $b$ | $d$(C-F) | $d$(C-H) | $d$(C-C) | $E_{coh}$ | $ZPE$ | $E_{coh}^{ZPE}$ | $\Delta E_{coh}$ | $\Delta E_{coh}^{ZPE}$ | $\Delta E$ | $\Delta E^{ZPE}$ |
|---|---|---|---|---|---|---|---|---|---|---|---|---|---|
| chair | FhHf | 4.38 | 2.55 | 1.42 | 1.10 | 1.53—1.54 | −5.324 | 0.183 | −5.141 | 0 | 0 | 0.000 | 0.000 |
| chair | FfHh | 4.36 | 2.56 | 1.42 | 1.10 | 1.52—1.55 | −5.313 | 0.183 | −5.130 | 11 | 11 | 0.089 | 0.091 |
| zigzag | FHfh | 3.97 | 2.58 | 1.43 | 1.10 | 1.54—1.56 | −5.307 | 0.181 | −5.126 | 17 | 15 | 0.135 | 0.120 |
| zigzag | FHhf | 4.01 | 2.58 | 1.43 | 1.10 | 1.55—1.56 | −5.294 | 0.181 | −5.113 | 30 | 28 | 0.244 | 0.230 |
| boat | FhfH | 4.32 | 2.55 | 1.43 | 1.10 | 1.54—1.56 | −5.288 | 0.182 | −5.106 | 36 | 35 | 0.294 | 0.285 |
| boat | FhhH | 4.34 | 2.55 | 1.42 | 1.10 | 1.54—1.56 | −5.262 | 0.183 | −5.079 | 62 | 62 | 0.502 | 0.500 |
| chair | FhFh | 4.43 | 2.56 | 1.39 | 1.11 | 1.55 | −5.243 | 0.181 | −5.062 | 81 | 79 | 0.654 | 0.640 |
| zigzag | FFhh | 4.10 | 2.61 | 1.38 | 1.11 | 1.56—1.59 | −5.197 | 0.179 | −5.018 | 127 | 124 | 1.020 | 0.992 |
| boat | FhhF | 4.46 | 2.54 | 1.38 | 1.10 | 1.55—1.62 | −5.172 | 0.181 | −4.991 | 152 | 150 | 1.221 | 1.206 |
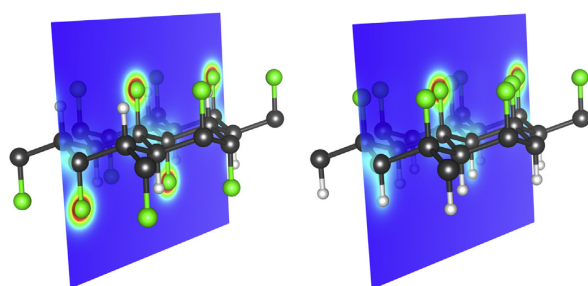


**Fig. 2.** Optimized structures ($2 \times 2$ supercell) of the most stable conformers of fluorographane $C_2FH$ with F and H atoms on both sides of C layer (the chair FhHf; left panel) and of Janus type (FhFh; right panel). Cuts through the electron density in (010) plane (i.e. xz plane - Fig. 1) with the scale from 0.0 a.u. (dark blue) to 1.04 a.u. (red) are added. (A colour version of this figure can be viewed online.)



**Fig. 3.** Phonon dispersion curves and partial phonon density of states (PDOS) of fluorographane $C_2FH$ in the chair FhHf conformation. Tetrahedron method was used for PDOS. (A colour version of this figure can be viewed online.)

The lower stability of Janus structures is attributed to the planarity restrictions enforced by periodic boundary conditions: as F-F interactions differ from H-H ones, the structures naturally tend to self-assemble into Janus nanoscrolls at room temperature [7].

The main structural features are similar for various conformers, $d$(C-F) = 1.42—1.43 Å, $d$(C-H) = 1.10 Å, and $d$(C-C) = 1.52—1.56 Å with exception of longer C-C bonds and shorter C-F bonds appearance in less stable Janus structures, $d$(C-C) = 1.59—1.62 Å, $d$(C-F) = 1.38—1.39 Å. We note that the values for chair Janus $C_2FH$ structure, $d$(C-F) = 1.387 Å, $d$(C-H) = 1.106 Å, are the same as the corresponding bond distances in chair fluorographene and graphane [11].

### 3.1.2. Vibrational properties

In order to check if the optimized structures are dynamically stable, we calculated phonon dispersion relations for all conformers. Our phonon calculations used large ($6 \times 6$) supercell of fluorographane ($C_{144}F_{72}H_{72}$) and $\Gamma$ point calculation, and, we also enabled additional support grid for the evaluation of the augmentation charges to attain high accuracy. Fig. 3 shows the calculated phonon dispersion relations and partial phonon density of states (PDOS) for the chair FhHf conformation of fluorographane, selected as the energetically most favorable crystal configuration (see cohesive energies, Table 1). The absence of any imaginary frequency indicates that the chair FhHf conformation is dynamically stable. The same is also valid for other eight conformations (see phonon dispersions in Supplementary Data, Figs. S1, S2, and S3). This is in line with similar finding in graphane CH where all of its conformers were found to be stable [40] and in contrast to fluorographene CF or chlorographene CCl where some of the studied conformers are dynamically unstable [41,42]. Interestingly, earlier study [2] predicted instability of all possible $C_2FH$
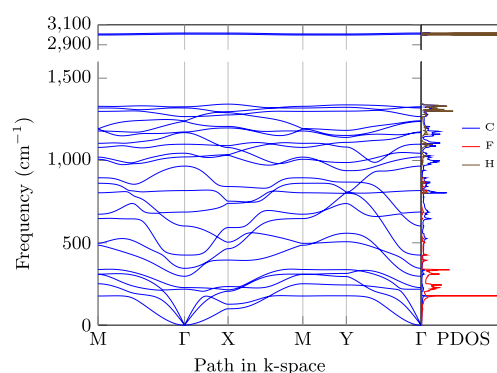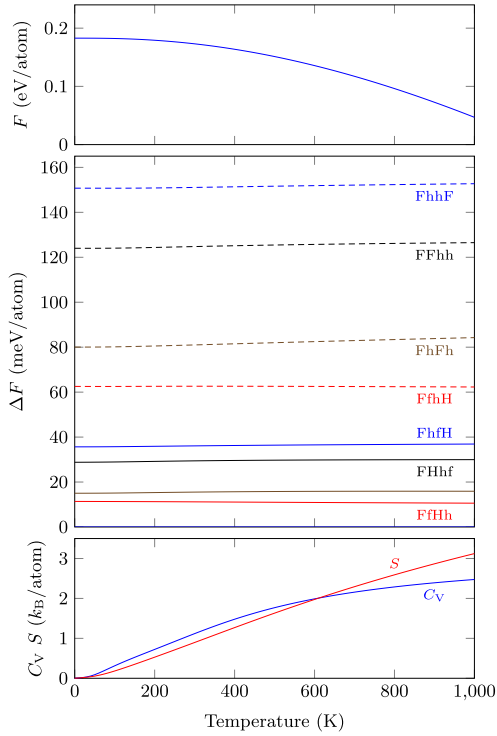
conformations except one − Janus chair conformation (FhFh). Moreover, the stability of FhfH structure was restored only in the presence of a compressive 3% strain along the zigzag direction (~800 cm$^{-1}$ for imaginary frequency without applied stress). Although the relative order of conformers in our work and Ref. [2] is similar, differences in vibrational properties may stem from the different setup (pseudopotential, plane-wave code, and other technical details) in both calculations because vibrational properties are very sensitive to such settings. In any case, fluorographane with F and H atoms on both sides of carbon layer was successfully synthesized [3], that confirms its stability.

It is apparent from phonon dispersion curves and PDOS in Fig. 3 that the phonons of fluorographane can be divided into high-frequency and low-/intermediate-frequency groups of phonons. One can immediately identify the high-frequency modes ($\approx$ 3000 cm$^{-1}$) as dominantly H modes, as can be expected from the C-H stretching modes (see brown color in PDOS of Fig. 3 for hydrogen character). Our theoretical value is consistent with infrared active mode found experimentally in Ref. [3] at 2950 cm$^{-1}$. The low-frequency phonons appear due to the presence of F modes (red color in PDOS of Fig. 3, up to $\approx$ 500 cm$^{-1}$). There are two linear and one quadratic acoustic phonon branch arising from F and C modes around $\Gamma$ point. Finally, intermediate frequency phonons correspond mainly to C modes (500—1000 cm$^{-1}$) changed to C and H modes (1000—1300 cm$^{-1}$).

We note, that the stability of 2D materials was a long standing puzzle because infinite perfect 2D structures are destroyed by long-wavelength fluctuations [43]. Specifically, this is related to the quadratic dispersion of the lowest phonon band near $\Gamma$ point (instead of linear dispersion as expected for acoustic modes) [44] as

appears on Fig. 3. However, these fluctuations are suppressed by anharmonic coupling between bending and stretching long-wavelength modes, i.e., the thermodynamic stability of 2D crystals is explained by observed microscopic corrugations (moreover, a limited size of 2D flakes or presence of crystal defects lead to
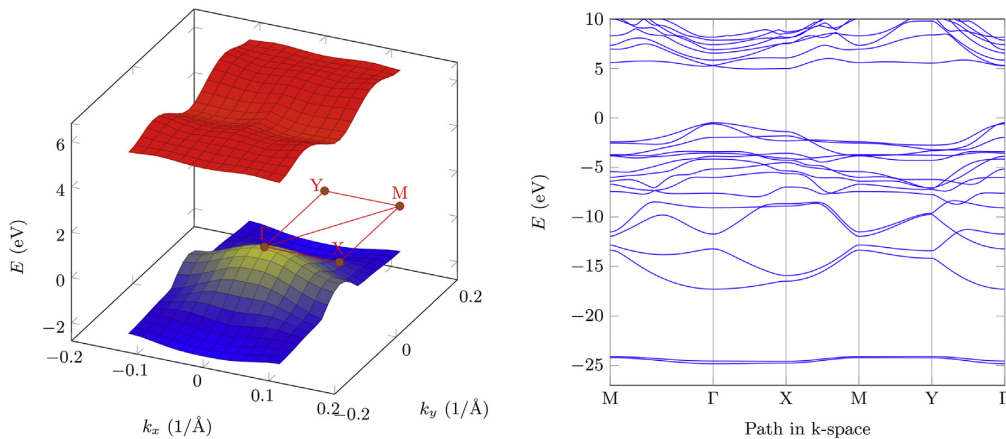
stability too). For instance, the ripples in graphene spontaneously appear owing to thermal fluctuations with a lateral size of 50–100 Å [43].

We found that the harmonic zero-point vibrational energy (ZPE) contributions are almost identical for all nine fluorographane conformers ($\approx 0.18$ eV/atom, see Table 1) and do not change relative order of conformers. Finally, we calculated free energy $F$, vibrational entropy $S$ and specific heat $C_V$, see Fig. 4. All the quantities are very similar for all fluorographane conformers despite their different structures. We therefore report on properties of the most stable FhHf conformer only, and, in order to illustrate how the relative stability behaves with the increasing temperature, we report on the free energy of other conformers vs. the most stable one (FhHf; see Fig. 4 middle panel). Note that the relative order of conformers does not depend on temperature within the considered window.

### 3.1.3. Electronic properties

We present here the electronic band structure of the most stable chair FhHf conformation of fluorographane, $C_2FH$. As seen in Fig. 5 (left panel) with the PBE highest valence band and lowest conduction band, the valence band maximum is located at $\Gamma$ point, conduction band minimum is located near the X point of the Brillouin zone. The band gap is therefore indirect. GGA PBE band structure through the high symmetry points in Brillouin zone is included in Fig. 5 (right panel); band structures for all other conformers are plotted in Supplementary Data (Figs. S4, S5, and S6). As GGA PBE band gaps are highly underestimated (Section I), we used hybrid functional for subsequent band gap calculations. We selected short-range hybrid HSE06 functional [45], because range-separated hybrid functionals are computationally tractable for periodic materials [46] and HSE06 gives quantitative right order of band gaps for various graphene halides [1,11]. For instance, HSE06 predicts the same trend of band gaps as GW: $E_{gap}^{HSE06}(CF) = 4.93$ eV $> E_{gap}^{HSE06}(CH) = 4.38$ eV; however, for PBE the opposite order was observed, $E_{gap}^{PBE}(CF) = 3.09$ eV $< E_{gap}^{PBE}(CH) = 3.53$ eV [1,11]. Band gaps for all conformers (both indirect and direct at $\Gamma$ and $M$ points) are collected in Table 2. The trend of PBE and HSE06 band gaps is similar for $C_2FH$ (see also its difference, last column of Table 2). The gaps obtained for Janus structures (last three rows of Table 2) are systematically smaller and direct in $\Gamma$ point.



**Fig. 4.** Top: Harmonic free energy $F$ for chair FhHf conformation of fluorographane $C_2FH$ as a function of temperature. Middle: Relative harmonic free energies $\Delta F$ of the nine phases of fluorographane $C_2FH$ studied in this work. The free energy of the chair FhHf conformation at each temperature (top panel) is chosen as the reference. Bottom: Constant volume specific heat $C_V$ and vibrational entropy $S$ for the chair FhHf conformation. (A colour version of this figure can be viewed online.)



**Fig. 5.** Electronic band structure of fluorographane $C_2FH$ in the most stable chair FhHf conformation. Left panel: highest valence band and lowest conduction band in the first Brillouin zone. Right panel: band structure along the k-path depicted in left panel. The Fermi level was set as zero. The band gap is indirect, because valence band maximum is located at $\Gamma$ point and conduction band minimum near the X point. (A colour version of this figure can be viewed online.)

**Table 2**

Electronic properties of fluorographanes: electronic band gaps $E_{gap}$ (indirect, $\Gamma$, M) in eV calculated by the PBE and HSE06 density functional.

| conformer | | PBE | | | HSE06 | | | diff | |
|---|---|---|---|---|---|---|---|---|---|
| | | $E_{gap}^{ind}$ | $E_{gap}^{\Gamma}$ | $E_{gap}^{M}$ | $E_{gap}^{ind}$ | $E_{gap}^{\Gamma}$ | $E_{gap}^{M}$ | $\Delta^{ind}$ | $\Delta^{\Gamma}$ |
| chair | FhHf | 5.44 | 5.76 | 8.00 | 7.03 | 7.18 | 10.17 | 1.59 | 1.42 |
| chair | FfHh | 4.52 | 4.57 | 9.04 | 6.19 | 6.28 | 11.19 | 1.67 | 1.71 |
| zigzag | FHfh | 5.61 | 5.77 | 9.89 | 7.25 | 7.25 | 12.38 | 1.65 | 1.49 |
| zigzag | FHhf | 5.11 | 5.27 | 8.38 | 6.76 | 6.95 | 10.72 | 1.65 | 1.68 |
| boat | FhfH | 5.52 | 5.71 | 8.63 | 7.14 | 7.28 | 10.89 | 1.62 | 1.57 |
| boat | FfhH | 3.89 | 4.34 | 9.91 | 5.55 | 6.03 | 12.36 | 1.65 | 1.69 |
| chair | FhFh | 2.95 | 2.95 | 7.77 | 4.20 | 4.20 | 9.90 | 1.25 | 1.25 |
| zigzag | FFhh | 2.91 | 2.91 | 9.25 | 4.13 | 4.13 | 11.29 | 1.22 | 1.22 |
| boat | FhhF | 2.98 | 2.98 | 7.97 | 4.26 | 4.26 | 9.86 | 1.28 | 1.28 |

Band gaps presented in Table 2 are in rough agreement with the values from literature: The only available theoretical direct band gap for both-side-occupied C$_2$FH with FhHf unit cell is $E_{gap}^{HSE06,\Gamma} \approx 7.5$ eV [1] calculated using localized Gaussian orbitals, that is slightly larger than the present value, $E_{gap}^{HSE06,\Gamma} = 7.18$ eV, based on plane-wave basis set (Table 2). For the Janus structures there are more available literature data: $E_{gap}^{PBE}$ for the chair FhFh was reported as 2.57 eV [5], 2.6 eV [6], 2.61 eV [4], 2.82 eV [47], 2.97 eV [48] (most similar to ours 2.95 eV, see Table 2), 3.11 eV [18], and 3.34 eV [2]. Such a wide range of the gaps for such a simple material with a four-atom unit cell F-C-C-H is surprising and the reason probably lies in different setup in particular calculations because the geometrical parameters are similar. For example, the lattice constants used are 2.575 Å [5], 2.57 Å [6], 2.55 Å [47], 2.54 Å [48], 2.57 Å [18], and 2.57 Å [2], respectively. It is known, that electronic properties are more sensitive on computational setup (basis set size, k-point sampling or pseudopotential/PAW construction) than geometrical structures (most of currently used DFT codes predict almost identical lattice constants, bond lengths or bulk modulus) [1,46,49]. The overall trend in band gaps with respect to pristine graphane and fluorographene is $E_{gap}^{HSE06}$(C$_2$FH, F and H on both sides) = 5.55–7.25 eV > $E_{gap}^{HSE06}$(CF) = 4.93 eV > $E_{gap}^{HSE06}$(CH) = 4.38 eV > $E_{gap}^{HSE06}$(Janus C$_2$FH, i.e. F and H on opposite sides) = 4.13–4.26 eV.

## 3.2. Convergence of many-body methods

Experience shows that it is essential to perform a convergence study covering several technical parameters for quasiparticle and excitonic calculations (because these can significantly affect the results): number of conduction bands included in the calculation, energy cut-off, vacuum layer thickness, or k-point sampling. We have performed a careful convergence study for the most stable configuration FhHf and we suppose that trends will be similar for other conformers. In any case, the most stable configuration will be dominant in statistically averaged properties.

### 3.2.1. Number of bands and energy cut-off in GW

At first, we studied a dielectric matrix energy cutoff $E_{cut}^{GW}$ and number of bands $N_B$ included in many-body calculations to achieve convergence of the electronic band gap $E_{gap}$ and excitation energy $E_{exc}$ (optical gap) values, see Fig. 6. Our target accuracy for the prediction of band gaps was chosen to attain $\approx 0.05$ eV. To ensure accuracy of difference between the highest occupied valence band and the lowest unoccupied conduction band, we report indirect band gap $E_{gap}^{indir}$, direct gap in $\Gamma$ point $E_{gap}^{\Gamma}$ and direct gap in M point $E_{gap}^{M}$ (see the Brillouin zone, Fig. 5). We updated $N_B^{GW} = 32$ band energies in GW calculations (16 occupied and 16 virtual levels). We ultimately selected $E_{cut} = 500$ eV, $N_B = 1024$ and $E_{cut}^{GW} = 200$ eV.
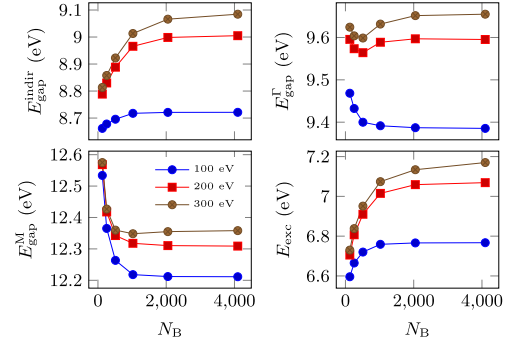


**Fig. 6.** Convergence of C$_2$FH(FhHf) band gaps $E_{gap}$ (indirect, $\Gamma$, M) and excitation energy $E_{exc}$ with respect to the number of bands $N_B$ and energy cut-off $E_{cut}^{GW}$ for G$_0$W$_0$. (A colour version of this figure can be viewed online.)

Fig. 6 also clearly shows that attempts to converge $N_b$ with an unconverged $E_{cut}^{GW}$ value may lead to false convergence behavior. Such behavior was found in studies on single-layered MoS$_2$ [50], CF [11], and bulk ZnO [51]. The band gap error due to the use of an unconverged $E_{cut}^{GW}$ value was 0.2–0.4 eV ($E_{cut}^{GW} = 300$ eV, $N_B = 2048 \rightarrow 100$ eV, 512 bands; Fig. 6). Similar behavior was observed for BSE excitation energy, $E_{exc}$, however, the convergence was slower and possible error due to the bad convergence was larger (~0.5 eV, Fig. 6).

### 3.2.2. Vacuum layer thickness

Other computational problems can arise from the fact that 2D materials are typically treated in 3D plane-wave codes in a slab approach (using vacuum layer in direction perpendicular to the 2D material); i.e., quasi-2D problem related to the Ewald summation technique may occur [52,53]. The choice of a reasonable interlayer distance $L_z$ (typically > 10 Å) ensures reliable band gap in the DFT calculation. On the other hand, a curious behavior of the quasiparticle band gaps with increasing interlayer distance was observed for some 2D materials (BN [54] and MoS$_2$ [55]) where they never reach a constant value. Instead, due to the nonlocal nature of the GW approximation, the gaps keep on increasing as $1/L_z$. We therefore calculated G$_0$W$_0$ bands gaps and the corresponding BSE excitation energies for $L_z = 16.5$, 20, 25, 30, 40 and 50 Å with coarser $6 \times 10 \times 1$ k-grid and we concluded (see Fig. 7), that the band gap of C$_2$FH also increases with $1/L_z$ and an extrapolation to $1/L_z \rightarrow 0$ ($L_z \rightarrow \infty$) is necessary. The slope of the corresponding linear fit slightly differs for various computational setups (see Fig. 7). We verified that the set of $L_z = 16.5$, 20 and 25 Å is large enough for a reliable extrapolation to infinite $L_z$. Finally, the band gap error due to the use of $L_z = 20$ Å was 0.2–0.5 eV depending on the band gap type and technical setup.

### 3.2.3. K-point sampling

Excitation energies and linear optical properties obtained from BSE solution are sensitive to k-point density in the Brillouin zone [51]. For the solution of the BSE we used the same set of 32 band energies as in GW calculations (16 occupied and 16 virtual levels), which provide spectra reliable up to $\approx 14$ eV (see Fig. S7, Supplementary Data, for tests of number of included levels). The evolution of the imaginary part of the dielectric function with the incoming photon energy is reported in Fig. 8. Our choice of the coordinate system (see Section II and Fig. 1) implies zero off-diagonal and nonzero diagonal elements $\varepsilon^{xx}$, $\varepsilon^{yy}$ and $\varepsilon^{zz}$ of the frequency dependent dielectric matrix. The absorption spectra curve obtained
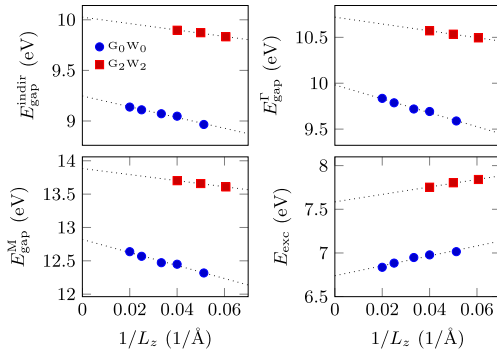
**Fig. 7.** Convergence of $C_2$FH(FhHf) band gaps $E_{gap}$ (indirect, $\Gamma$, M) and excitation energy $E_{exc}$ in eV with respect to interlayer distance $L_z$ for $G_0W_0$ and $G_2W_2$ calculations with $6 \times 10 \times 1$ and $9 \times 15 \times 1$ k-grid, respectively. Dashed lines represent the corresponding extrapolations. (A colour version of this figure can be viewed online.)
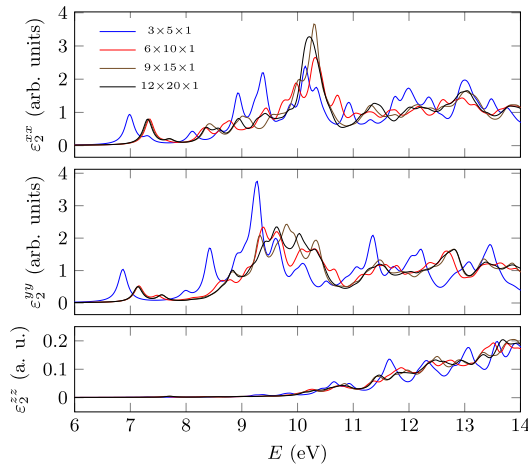


**Fig. 8.** Convergence of $C_2$FH(FhHf) imaginary dielectric function $\varepsilon_2$ with respect to k-point sampling. Note different scale for $\varepsilon_2^{xx}$ and $\varepsilon_2^{yy}$ vs. $\varepsilon_2^{zz}$. (A colour version of this figure can be viewed online.)

with $9 \times 15 \times 1$ k-grid is almost identical to $12 \times 20 \times 1$ curve up to 8.5 eV and overall shape of the spectra is same for these two curves. We therefore considered the $9 \times 15 \times 1$ k-grid as a reasonable choice with an error $< 0.05$ eV for the position of the first excitonic peak. $C_2$FH is highly anisotropic: the $\varepsilon^{zz}$ element of dielectric matrix (corresponding to absorption spectra of $C_2$FH for light polarization perpendicular to the surface plane) is zero up to 10 eV and very small for higher photon energies (about one magnitude smaller than in case of $\varepsilon^{xx}$ and $\varepsilon^{yy}$; cf. Fig. 8). Therefore, we will not consider $\varepsilon^{zz}$ element in the following. We note that GW band gaps are less sensitive to the k-point sampling density than the BSE transition energies.

### 3.2.4. Level of GW

In our previous work on fluorographene, the band gap values from various levels of GW method were found to differ significantly (from 6.9 to 8.3 eV) [11]. We therefore calculated eigenvalues iterated with $G$ or both $G$ and $W$ (Eq. (5)) for $C_2$FH(FhHf) and plotted indirect and direct band gaps in $\Gamma$ and M and the corresponding excitation energy from BSE (Fig. 9). We considered
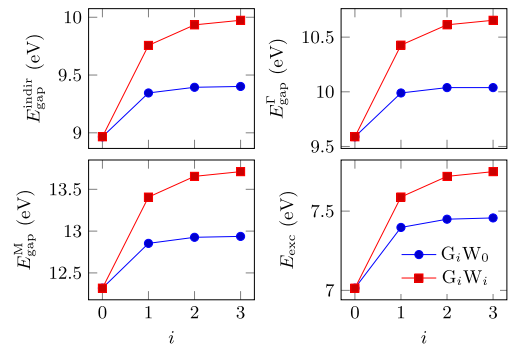


**Fig. 9.** Convergence of $C_2$FH(FhHf) band gaps $E_{gap}$ (indirect, $\Gamma$, M) and excitation energy $E_{exc}$ in eV with respect to the number of iteration $i$ in $G_iW_0$ and $G_iW_i$ calculations following Eq. (5). (A colour version of this figure can be viewed online.)

$G_2W_2$ level as converged with errors smaller than 0.05 eV.

In summary, our production run settings with target accuracy of 0.05 eV consist of $G_2W_2$ level of theory, $9 \times 15 \times 1$ k-grid, $N_B = 1024$ bands and $E_{cut} = 500$ eV ($E_{cut}^{GW} = 200$ eV) energy cut-off. We showed that it is easy to obtain significantly underestimated ($\sim 0.7$ eV) quasiparticle gaps and excitation energies for $C_2$FH when the technical setup of many-body methods is not considered carefully. The use of higher levels of GW method leads to substantially larger ($> 1$ eV) band gaps than the single-shot $G_0W_0$ method.

### 3.3. Electronic and optical properties: quasiparticle and excitonic effects

We have performed production $G_2W_2$ and BSE computations for all nine $C_2$FH conformers with the technical setup presented in the previous part (Section 3.2). The final band gaps (both indirect and direct in $\Gamma$ and M) and excitation energies for all conformers are collected in Table 3.

GW band gap trends are in line with HSE06 gaps of Table 2 with exception of zigzag FHfh conformer which became direct material in GW. I.e., chair FhHf, chair FfHh, zigzag FHhf, boat FhfH, and boat FfhH conformers are indirect materials, while zigzag FHfh, Janus chair FhFh, Janus zigzag FFhh, and Janus boat FhhF conformers are direct materials. The $G_2W_2$ band gap values are roughly 150% of HSE06 band gap values (cf. Tables 2 and 3).

The general trend in comparison with the known materials is $E_{gap}^{GW}(C_2FH,$ F and H on both sides$) = 8.74-10.03$ eV $> E_{gap}^{GW}(CF) = 8.12$ eV $> E_{gap}^{GW}(CH) = 6.28$ eV $> E_{gap}^{GW}(Janus\ C_2FH) = 5.97-6.12$ eV. It is quite surprising, that the band gap value for $C_2$FH is not between values for CF and CH or, at least, similar to CH or CF values. In addition, there is a large difference (3—4 eV) between the band gaps corresponding to homogeneous conformers and Janus conformers of $C_2$FH. We attribute such band gap trends to the local geometrical structure. Related local environment effects have been detected in fluorinated graphenes and emerge in various properties including C and F core-level energy shifts, ionicity of the C—F bond, the formation energy, the C—F bond dissociation energy, etc. [56,57]. In fact, there are some differences in both subgroups of conformers considered here: C-F bonds in Janus structures are shorter ($d$(C-F) = 1.38—1.39 Å) than in the homogeneous conformers ($d$(C-F) = 1.42—1.43 Å). For $d$(C-C) the opposite trend occurs (see Table 1). The Bader analysis indicates a charge transfer of 0.60—0.63 $e$ from carbon honeycomb lattice to fluorine atoms and transfer of 0.08—0.16 $e$ from hydrogen atoms to carbon lattice in homogeneous

**Table 3**

Electronic and optical properties of fluorographanes obtained from GW and BSE calculations: electronic band gaps $E_{gap}^{GW}$ (indirect, Γ, M), the excitation energy $E_{exc}^{BSE}$ and the exciton binding energy $E_b = E_{gap}^{GW,\Gamma} - E_{exc}^{BSE}$ in eV. The reported values are for converged parameters of Section B and for extrapolated $1/L_z \rightarrow 0$ limit.

| conformation | | $E_{gap}^{GW,indir}$ | $E_{gap}^{GW,\Gamma}$ | $E_{gap}^{GW,M}$ | $E_{exc}^{BSE}$ | $E_b$ |
|---|---|---|---|---|---|---|
| chair | FhHf | 10.03 | 10.72 | 13.88 | 7.58 | 3.14 |
| chair | FfHh | 9.41 | 9.54 | 14.64 | 6.76 | 2.78 |
| zigzag | FHfh | 10.01 | 10.01 | 15.85 | 7.64 | 2.37 |
| zigzag | FHhf | 9.87 | 10.04 | 14.52 | 7.50 | 2.54 |
| boat | FhfH | 10.01 | 10.47 | 17.06 | 7.60 | 2.87 |
| boat | FfhH | 8.74 | 9.28 | 16.10 | 6.40 | 2.88 |
| chair | FhFh | 6.09 | 6.09 | 13.12 | 4.13 | 1.96 |
| zigzag | FFhh | 5.97 | 5.97 | 12.93 | 4.14 | 1.83 |
| boat | FhhF | 6.12 | 6.12 | 11.90 | 4.19 | 1.93 |

conformers. In Janus conformers, charge transfer of 0.57–0.61 $e$ to F is observed and no charge transfer for H (see Table 4 for Bader analysis). In addition, charge on C atoms is distributed in slightly different manner in both subgroups of conformers. The homogeneous $C_2FH$ structures are therefore more ionic, charge transfer is more pronounced and hence the gap opens more [11].

We note, that band gap value of ~10 eV for five most stable $C_2FH$ conformers posts fluorographane as 2D material with the widest band gap which is known at present (CF, hBN, 1T-HfO$_2$ and 1T-ZrO$_2$ are typically considered as 2D materials with largest band gap value of 7–8 eV [58–60]). The only literature $C_2FH$ GW data are available for Janus FhFh conformer: $E_{gap}^{G_0W_0}$ of 6.38 eV [18], 6.0 eV [5], and 5.96 eV [48] were reported, all in acceptable agreement with our value of 6.12 eV (see Table 3).

Electron-hole excitations (not included in GW approximation itself) were responsible for the optical absorption at energies lower than GW band gap. In order to uncover the physical origin of different features in optical spectra we plotted imaginary dielectric function in Fig. 10 at several levels of theory: DFT + RPA which neglects both the inter-electron and the electron-hole interaction, (ii) GW + RPA which includes the electron-electron interaction, and (iii) full solution of Bethe-Salpeter equation on top of the GW band structure (GW + BSE) which accounts the excitonic effects. Inclusion of electron-electron interaction (DFT + RPA → GW + RPA in Fig. 10) led to large blue shift in absorption due to quasiparticle correction, however, with similar shape of the spectra. On the other hand, inclusion of electron-hole interaction effects led to significant red shift in absorption spectra (GW + RPA → GW + BSE in Fig. 10) and dominant absorption region comes partially back to the original DFT + RPA position (10–13 eV). However, BSE yielded significantly redistributed oscillator strengths (bottom panel of Fig. 10) leading to a large number of bound excitonic states below GW gap. For the most stable FhHf conformer, there was lowest energy transition of $E_{exc,L_z \rightarrow \infty}^{BSE} = 7.52$ eV (Table 3; however, value 7.75 eV is visible in spectra of Fig. 10 for $L_z = 25$ Å).
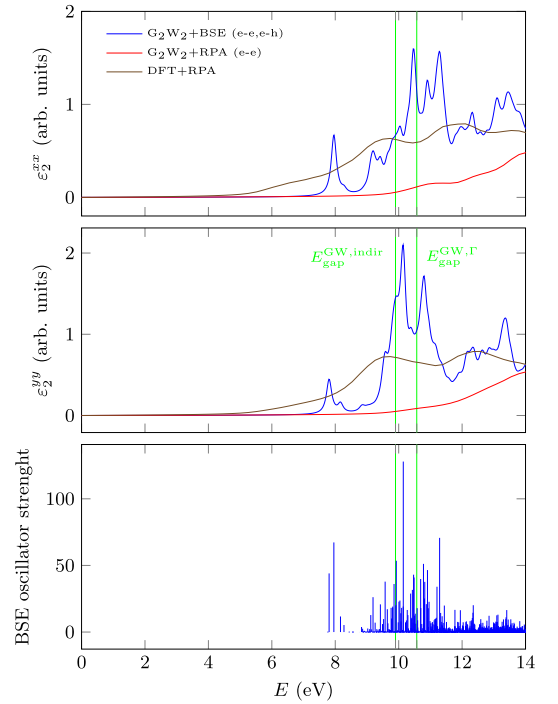


**Fig. 10.** Top and middle panels: components of imaginary part of dielectric function of $C_2FH$(FhHf) calculated by (i) DFT + RPA, (ii) GW + RPA including electron-electron (e–e) interaction, and (iii) GW + BSE including both e-e and e-h (electron-hole) correlations. Bottom panel: Large number of bound excitonic states with energies below band gap (green vertical lines) as computed by BSE. $L_z = 25$ Å was used. (A colour version of this figure can be viewed online.)

**Table 4**

Differences of charges (in $e$) obtained from Bader analysis of $C_2FH$ unit cell and atomic charges of separated atoms (4 $e$, 7 $e$, and 1 $e$ for C, F and H atom, respectively). The following atoms are bonded: 1C-5F, 2C-6F, 3C-7H, 4C-8H, i.e., Bader analysis indicates a charge transfer of 0.63 $e$ to F and 0.09 $e$ from H in chair FhHf structure etc. The last three columns correspond to structures of the Janus type.

| atom | element | chair | chair | zigzag | zigzag | boat | boat | chair | zigzag | boat |
|---|---|---|---|---|---|---|---|---|---|---|
| | | FhHf | FfHh | FHfh | FHhf | FhfH | FfhH | FhFh | FFhh | FhhF |
| 1 | C | 0.52 | 0.55 | 0.50 | 0.51 | 0.46 | 0.51 | 0.59 | 0.57 | 0.49 |
| 2 | C | 0.49 | 0.51 | 0.51 | 0.48 | 0.46 | 0.46 | 0.59 | 0.55 | 0.63 |
| 3 | C | 0.05 | 0.00 | −0.06 | −0.04 | 0.03 | −0.03 | 0.02 | −0.02 | 0.06 |
| 4 | C | 0.02 | 0.04 | −0.03 | −0.01 | 0.03 | 0.03 | 0.02 | 0.03 | −0.06 |
| 5 | F | −0.63 | −0.63 | −0.60 | −0.60 | −0.61 | −0.60 | −0.61 | −0.57 | −0.59 |
| 6 | F | −0.63 | −0.63 | −0.61 | −0.60 | −0.61 | −0.60 | −0.61 | −0.57 | −0.57 |
| 7 | H | 0.09 | 0.08 | 0.16 | 0.14 | 0.12 | 0.11 | −0.01 | 0.00 | 0.02 |
| 8 | H | 0.09 | 0.08 | 0.12 | 0.14 | 0.12 | 0.11 | −0.01 | 0.01 | 0.02 |

The vertical $\Gamma - \Gamma$ transition was found to be responsible for the first excitation peak in the spectrum FhHf conformer of fluorographane. The binding energy of the first exciton was therefore $E_b = E_{gap}^{GW,\Gamma} - E_{exc}^{BSE} = 10.72 - 7.59 = 3.14$ eV. Lowest energy absorption peaks (6.4—7.6 eV, Table 3) for other $C_2FH$ conformers with F and C atoms on both sides are also significantly lower than corresponding GW band gaps (8.7—10 eV) and therefore with large exciton binding energies in range 2.5—2.9 eV. On the other hand, Janus conformers with $E_b = 1.8$—2.0 eV are more similar to fluorographene with $E_b = 1.9$ eV [11,23]. Imaginary part of BSE dielectric function and corresponding oscillator strengths for all conformers are collected in Supplementary Data (Figs. S8 and S9). Large binding energy of the exciton ($E_b \approx 3.1$ eV) in $C_2FH$ is significantly larger than prediction ($E_b^{pred} = 2.65$ eV) from a scaling law $E_b = \alpha E_{gap}^{GW} + \beta$ ($\alpha = 0.21$, $\beta = 0.40$) from Ref. [58]. Currently, CF or hexagonal BN are typically considered as 2D materials with largest $E_b \approx 2$ eV [58—60]. Exciton binding energy value of 3.1 eV for FhHf conformer (and also 2.5—2.9 eV for other conformers) posts therefore fluorographane as 2D material with the largest excitonic effect which is known at present. It is worth to mention that excitonic effects are typically several orders of magnitude smaller in a bulk semiconductors and insulating materials with high dielectric constant: $E_b = 27$ meV for CdS, 15 meV for CdSe, 5.1 meV for InP and 4.9 meV for GaAs [61]. By contrast, bulk ionic crystals have much larger binding energies of exciton: 1.5 eV for LiF, 0.5 eV for LiCl [38]. For completeness, we note that the bulk rare gases stable at very low temperatures are also reported as bulk materials with pronounced excitonic binding energies: $E_b \approx 2.1$ eV for argon (melting point 84 K) and 4.2 eV for neon (25 K) [62].

We note that the only $C_2FH$ BSE excitation energy available in the literature is 4.26 eV for Janus chair conformer $C_2FH$ (FhFh) with the corresponding excitonic binding energy of $E_b = 1.7$ eV [48]. These values are in agreement with our calculations (see Table 3). The exciton is delocalized over several units cells, with exciton radius of about 7.5 Å [48] which approximately corresponds to our $4 \times 6$ supercell. This is also confirmed by our k-point sampling study in Section 3.2.3: at least $6 \times 10 \times 1$ k-points was necessary to reach a good convergence of the first excitonic peak, while the spectra for smaller grids like $3 \times 5 \times 1$ were significantly biased. In general, $n \times n \times 1$ k-sampling in the reciprocal space allows spread the exciton wave function in the $n \times n \times 1$ real space supercell. I.e., inadequately sparse grid leads to unwanted confinement of the exciton into inadequately small supercell causing bias in the position of the first excitonic peak (with artificially overestimated binding energy of the exciton).

All the linear optical properties (refractive index, extinction coefficient, absorption coefficient, reflectivity and energy loss spectrum; see Section 2 for definitions) obtained at the production GW + BSE level are displayed in ultraviolet and visible regions (Fig. 11) and serve for comparison with future experimental measurements not yet available. In the visible region, all the mentioned properties are almost constant (e.g. refractive index $n_{\lambda \to \infty} = 1.17$).

## 4. Conclusions

We reported on structural, vibrational, electronic and optical properties of the recently prepared carbon-based 2D material known as fluorographane. Following the experimental stoichiometry [3], we considered fully functionalized graphene with 1:1 ratio of F and H atoms (denoted as $C_2FH$ fluorographane). Prior to this work, the ongoing debate in the literature suggested that hydrofluorinated graphene is dynamically unstable and should not exist (except for one particular Janus conformer). Using highly-accurate phonon calculations, we were able to prove that all nine possible
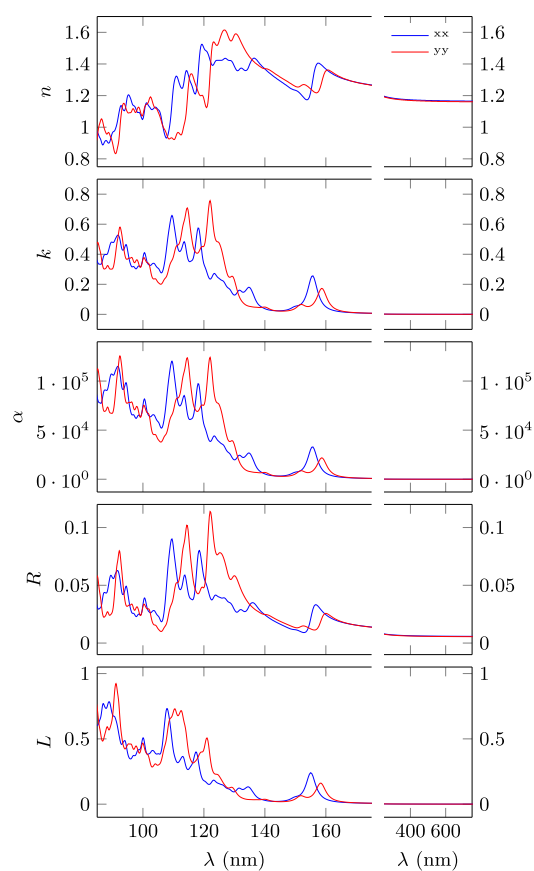


**Fig. 11.** Optical properties of $C_2FH$(FhHf) calculated by GW + BSE in ultraviolet and visible regions: the refractive index $n$, the extinction coefficient $k$, the absorption coefficient $\alpha$, the reflectivity $R$, and energy loss spectrum $L$ as a function of wavelength. (A colour version of this figure can be viewed online.)

structural $C_2FH$ conformers are stable, in line with the recent experiment. Moreover, all homogeneous structures, with both F and H atoms on both sides of honeycomb carbon lattice, were more stable than the Janus structures with only F atoms on one side and only H atoms on the opposite one. The most stable conformer was the chair conformer alternating F up and H down (with respect to graphene layer) in zigzag direction of a rectangular unit cell.

The electronic and optical calculations with inclusion of quasiparticle and excitonic effects performed by many-body methods (GW, BSE) were found to be overly sensitive to the computational setup (number of conduction bands, vacuum thickness, k-point sampling etc.) and careful convergence and extrapolations were needed to achieve the desired accuracy. One can easily obtain significantly biased results for $C_2FH$ (~0.7 eV) if one uses GW or BSE method as a black box without a careful convergence study.

Although one would expect the band gap of the studied $C_2FH$ to lie somewhere between the band gap of $C_1H_1$ (~5—6 eV) and $C_1F_1$ (~7—8 eV; both CH and CF can be considered as "mother materials" with respect to $C_2FH$), or close to one of them, this is not the case. Unexpectedly, we find that fluorographane $C_2FH$ embodies extremely wide indirect band gap of ~10 eV. We attributed this quite surprising fact to local environment effects, i.e., specific combinations of -F and -H adsorbates on the graphene surface.

These effects were also responsible for the significant difference in electronic and optical properties of the two considered subsets of fluorographane $C_2FH$ conformers: while the Janus structures have smaller direct band gaps ($\sim$6 eV) and excitonic effects ($\sim$1.9 eV), similar to CH and CF, respectively; the highly stable homogeneous $C_2FH$ conformers embody extremely wide indirect band gaps (8.7—10 eV; direct gaps 9.3—10.7 eV) and huge binding energies of exciton ($\sim$3 eV). Homogeneous fluorographane has therefore the largest known excitonic effect and the largest known band gap value in the field of currently known 2D materials.

## Note added in proof

During work on our paper, preparation of fluorographane with lower contents of F a H atoms and enhanced nonlinear optical properties was reported [63].

## Acknowledgments

## Appendix A. Supplementary data

Supplementary data related to this article can be found at https://doi.org/10.1016/j.carbon.2018.04.006.

## References

[1] F. Karlický, R. Zbořil, M. Otyepka, Band gaps and structural properties of graphene halides and their derivates: a hybrid functional study with localized orbital basis sets, J. Chem. Phys. 137 (2012) 034709.

[2] R. Singh, G. Bester, Hydrofluorinated graphene: two-dimensional analog of polyvinylidene fluoride, Phys. Rev. B 84 (2011) 155427.

[3] Z. Šofer, P. Šimek, V. Mazánek, F. Šembera, Z. Janoušek, M. Pumera, Fluorographane $(C_1H_xF_{1-x-\delta})_n$: synthesis and properties, Chem. Commun. 51 (2015) 5633—5636.

[4] M.T. Ong, K.-A.N. Duerloo, E.J. Reed, The effect of hydrogen and fluorine coadsorption on the piezoelectric properties of graphene, J. Phys. Chem. C 117 (2013) 3615—3620.

[5] H.J. Kim, M. Noor-A-Alam, J.Y. Son, Y.-H. Shin, Origin of piezoelectricity in monolayer halogenated graphane piezoelectrics, Chem. Phys. Lett. 603 (2014) 62—66.

[6] D. Cakir, F.M. Peeters, Fluorographane: a promising material for bipolar doping of MoS2, Phys. Chem. Chem. Phys. 17 (2015) 27636—27641.

[7] Y. Jin, Q. Xue, L. Zhu, X. Li, X. Pan, J. Zhang, et al., Self-assembly of hydrofluorinated janus graphene monolayer: a versatile route for designing novel janus nanoscrolls, Sci. Rep. 6 (2016) 26914.

[8] M. Pykal, P. Jurečka, F. Karlický, M. Otyepka, Modelling of graphene functionalization, Phys. Chem. Chem. Phys. 18 (2016) 6351—6372.

[9] F. Karlický, K.K.R. Datta, M. Otyepka, R. Zbořil, Halogenated graphenes: rapidly growing family of graphene derivatives, ACS Nano 7 (2013) 6434—6464.

[10] J.P. Perdew, W. Yang, K. Burke, Z. Yang, E.K.U. Gross, M. Scheffler, et al., Understanding band gaps of solids in generalized kohnsham theory, Proc. Natl. Acad. Sci. U. S. A 114 (2017) 2801—2806.

[11] F. Karlický, M. Otyepka, Band gaps and optical spectra of chlorographene, fluorographene and graphane from $G_0W_0$, $GW_0$ and $GW$ calculations on top of PBE and HSE06 orbitals, J. Chem. Theor. Comput. 9 (2013) 4155—4164.

[12] S. Kümmel, L. Kronik, Orbital-dependent density functionals: theory and applications, Rev. Mod. Phys. 80 (2008) 3—60.

[13] L. Hedin, New method for calculating the one-particle Greens function with application to the electron-gas problem, Phys. Rev. 139 (1965) A796—A823.

[14] R.R. Nair, W. Ren, R. Jalil, I. Riaz, V.G. Kravets, L. Britnell, et al., Fluorographene: a two-dimensional counterpart of teflon, Small 6 (2010) 2877—2884.

[15] R. Zbořil, F. Karlický, A.B. Bourlinos, T.A. Steriotis, A.K. Stubos, V. Georgakilas, et al., Graphene fluoride: a stable stoichiometric graphene derivative and its chemical conversion to graphene, Small 6 (2010) 2885—2891.

[16] M.H.F. Sluiter, Y. Kawazoe, Cluster expansion method for adsorption:

[17] application to hydrogen chemisorption on graphene, Phys. Rev. B 68 (2003) 085410.

[18] J.O. Sofo, A.S. Chaudhari, G.D. Barber, Graphane: a two-dimensional hydrocarbon, Phys. Rev. B 75 (2007) 153401.

[19] M. Klintenberg, S. Lebègue, M.I. Katsnelson, O. Eriksson, Theoretical analysis of the chemical bonding and electronic structure of graphene interacting with group IA and group VIIA elements, Phys. Rev. B 81 (085433) (2010).

[20] O. Leenaerts, H. Peelaers, A.D. Hernández-Nieves, B. Partoens, F.M. Peeters, First-principles investigation of graphene fluoride and graphane, Phys. Rev. B 82 (2010) 195436.

[21] D.K. Samarakoon, Z.F. Chen, C. Nicolas, X.Q. Wang, Structural and electronic properties of fluorographene, Small 7 (2011) 965—969.

[22] Y. Liang, L. Yang, Electronic structure and optical absorption of fluorographene, MRS Proc. 1370 (2011) 137.

[23] W. Wei, T. Jacob, Electronic and optical properties of fluorinated graphene: a many-body perturbation theory study, Phys. Rev. B 87 (2013) 115431.

[24] F. Karlický, M. Otyepka, Band gaps and optical spectra from single- and double-layer fluorographene to graphite fluoride: many-body effects and excitonic states, Ann. Phys. 526 (2014) 408—414.

[25] P. Cudazzo, C. Attaccalite, I.V. Tokatly, A. Rubio, Strong charge-transfer excitonic effects and the bose-einstein exciton condensate in graphane, Phys. Rev. Lett. 104 (2010) 226804.

[26] K.-J. Jeon, Z. Lee, E. Pollak, L. Moreschini, A. Bostwick, C.M. Park, et al., Fluorographene: a wide bandgap semiconductor with ultraviolet luminescence, ACS Nano 5 (2011) 1042—1046.

[27] V. Mazánek, O. Jankovský, J. Luxa, D. Sedmidubský, Z. Janoušek, F. Šembera, et al., Tuning of fluorine content in graphene: towards large-scale production of stoichiometric fluorographene, Nanoscale 7 (2015) 13646—13655.

[28] H.A. Bethe, E.E. Salpeter, A relativistic equation for bound state problems, Phys. Rev. 82 (1951) 309—310.

[29] S. Yuan, M. Rösner, A. Schulz, T.O. Wehling, M.I. Katsnelson, Electronic structures and optical properties of partially and fully fluorinated graphene, Phys. Rev. Lett. 114 (2015) 047403.

[30] Y. Yang, Y. Li, Z. Huang, X. Huang, $(C_{1.04}H)_n$: a nearly perfect pure graphane, Carbon 107 (2016) 154—161.

[31] P.E. Blöchl, Projector augmented-wave method, Phys. Rev. B 50 (1994) 17953—17979.

[32] G. Kresse, D. Joubert, From ultrasoft pseudopotentials to the projector augmented-wave method, Phys. Rev. B 59 (1999) 1758—1775.

[33] J.P. Perdew, K. Burke, M. Ernzerhof, Generalized gradient approximation made simple, Phys. Rev. Lett. 77 (1996) 3865—3868.

[34] A. Togo, I. Tanaka, First principles phonon calculations in materials science, Scripta Mater. 108 (2015) 1—5.

[35] M. Gajdoš, K. Hummer, G. Kresse, J. Furthmüller, F. Bechstedt, Linear optical properties in the projector-augmented wave methodology, Phys. Rev. B 73 (2006) 045112.

[36] G. Strinati, H.J. Mattausch, W. Hanke, Dynamical aspects of correlation corrections in a covalent crystal, Phys. Rev. B 25 (1982) 2867—2888.

[37] M. Shishkin, G. Kresse, Implementation and performance of the frequency-dependent $gw$ method within the paw framework, Phys. Rev. B 74 (2006) 035101.

[38] G. Strinati, Effects of dynamical screening on resonances at inner-shell thresholds in semiconductors, Phys. Rev. B 29 (1984) 5718—5726.

[39] M. Rohlfing, S.G. Louie, Electron-hole excitations and optical spectra from first principles, Phys. Rev. B 62 (2000) 4927—4944.

[40] F. Fuchs, C. Roedl, A. Schleife, F. Bechstedt, Efficient $O(n^2)$ approach to solve the bethe-salpeter equation for excitonic bound states, Phys. Rev. B 78 (2008) 085103.

[41] E. Cadelano, P.L. Palla, S. Giordano, L. Colombo, Elastic properties of hydrogenated graphene, Phys. Rev. B 82 (2010) 235414.

[42] H. Şahin, M. Topsakal, S. Ciraci, Structures of fluorinated graphene and their signatures, Phys. Rev. B 83 (2011) 115432.

[43] H. Şahin, S. Ciraci, Chlorine adsorption on graphene: Chlorographene, J. Phys. Chem. C 116 (2012) 24075—24083.

[44] J.C. Meyer, A.K. Geim, M.I. Katsnelson, K.S. Novoselov, T.J. Booth, S. Roth, The structure of suspended graphene sheets, Nature 446 (2007) 60.

[45] B. Lepetit, B. Jackson, Sticking of hydrogen on supported and suspended graphene at low temperature, Phys. Rev. Lett. 107 (2011) 236102.

[46] A.V. Krukau, O.A. Vydrov, A.F. Izmaylov, G.E. Scuseria, Influence of the exchange screening parameter on the performance of screened hybrid functionals, J. Chem. Phys. 125 (2006) 224106.

[47] J. Paier, M. Marsman, K. Hummer, G. Kresse, I.C. Gerber, J.G. Ángyán, Screened hybrid density functionals applied to solids, J. Chem. Phys. 124 (2006) 154709.

[48] F. Li, Y. Li, Band gap modulation of janus graphene nanosheets by interlayer hydrogen bonding and the external electric field: a computational study, J. Mater. Chem. C 3 (2015) 3416—3421.

[49] W. Aggoune, K. Rezouali, M.A. Belkhir, Strong excitonic effects in hydrogen graphene—fluorine janus graphene, Phys. Status Solidi B 253 (2016) 712—717.

[50] K. Lejaeghere, G. Bihlmayer, T. Björkman, P. Blaha, S. Blügel, et al., Reproducibility in density functional theory calculations of solids, Science 351 (2016) 6280.

[51] D.Y. Qiu, F.H. da Jornada, S.G. Louie, Optical spectrum of MoS2: many-body effects and diversity of exciton states, Phys. Rev. Lett. 111 (2013) 216805.

[52] B.-C. Shih, Y. Xue, P. Zhang, M.L. Cohen, S.G. Louie, Quasiparticle band gap of ZnO: high accuracy from the conventional $G_0W_0$ approach, Phys. Rev. Lett.

105 (2010) 146401.

[52] M. Mazars, Long ranged interactions in computer simulations and for quasi-2d systems, Phys. Rep. 500 (2011) 43–116.

[53] I.-C. Yeh, M.L. Berkowitz, Ewald summation for systems with slab geometry, J. Chem. Phys. 111 (1999) 3155–3162.

[54] L. Wirtz, A. Marini, A. Rubio, Excitons in boron nitride nanotubes: dimensionality effects, Phys. Rev. Lett. 96 (2006) 126104.

[55] H.-P. Komsa, A.V. Krasheninnikov, Effects of confinement and environment on the electronic structure and exciton binding energy of $MoS_2$ from first principles, Phys. Rev. B 86 (2012) 241201.

[56] S. Zhou, S.D. Sherpa, D.W. Hess, A. Bongiorno, Chemical bonding of partially fluorinated graphene, J. Phys. Chem. C 118 (2014) 26402–26408.

[57] M. Dubecký, E. Otyepková, P. Lazar, F. Karlický, M. Petr, K. Čépe, P. Banáš, R. Zbořil, M. Otyepka, Reactivity of fluorographene: a facile way toward graphene derivatives, J. Phys. Chem. Lett. 6 (2015) 1430–1434.

[58] J.-H. Choi, P. Cui, H. Lan, Z. Zhang, Linear scaling of the exciton binding energy versus the band gap of two-dimensional materials, Phys. Rev. Lett. 115 (2015) 066403.

[59] F.A. Rasmussen, K.S. Thygesen, Computational 2D materials database: electronic structure of transition-metal dichalcogenides and oxides, J. Phys. Chem. C 119 (2015) 13169–13183.

[60] K.S. Thygesen, Calculating excitons, plasmons, and quasiparticles in 2D materials and van der waals heterostructures, 2D Mater. 4 (2017) 022004.

[61] G.D. Scholes, G. Rumbles, Excitons in nanoscale systems, Nat. Mater. 5 (2006) 683–696.

[62] S. Galamić-Mulaomerović, C.H. Patterson, Ab initio many-body calculation of excitons in solid Ne and Ar, Phys. Rev. B 72 (2005) 035127.

[63] I. Papadakis, Z. Bouza, S. Couris, A.B. Bourlinos, V. Mouselimis, A. Kouloumpis, et al., Hydrogenated fluorographene: a 2D counterpart of graphane with enhanced nonlinear optical properties, J. Phys. Chem. C 121 (2017) 22567–22575.

# Supplementary Material 2

## PAPER

# Accurate many-body calculation of electronic and optical band gap of bulk hexagonal boron nitride†

Miroslav Kolos 🅾 and František Karlický 🅾 *

Many-body perturbational GW approximation in conjunction with the Bethe–Salpeter equation (BSE) has been employed to calculate accurate electronic and optical band gaps of bulk hexagonal boron nitride (h-BN) in the two most important stacking configurations, AA′ and AB. The carefully converged results revealed h-BN as an indirect material (indirect gap $\approx$ 6.1 eV) with a huge excitonic effect ($\approx 0.8$ eV) in perfect agreement with recent experiments [*Nat. Photonics*, 2016, **10**, 262; *Appl. Phys. Lett.*, 2016, **109**, 122101]. The $K$–$H$ region of the first Brillouin zone has been shown as the most important for lowest optical excitations in h-BN. Surprisingly, simple scissor corrected DFT has described h-BN band structure at the GW level and subsequent time-dependent DFT with a suitable exchange correlation kernel has provided absorption spectra similar to the full GW+BSE spectra.

## 1 Introduction

Recent interest in two-dimensional (2D) materials has re-initiated intensive discussion on the electronic and optical properties of bulk layered materials. The debate concerning the band gap of bulk hexagonal boron nitride (h-BN), its nature and excitonic properties was re-opened by recent experiments[1–4] and theoretical studies.[5–7] While graphite (and its 2D analogue called graphene) is a zero band gap semi-metal, h-BN is a wide gap semiconductor with very high thermal and chemical stability suitable in devices operating under extreme conditions and showing a luminescence peak around 215 nm (5.77 eV).[8–10] Experimental estimation of the bulk h-BN band gap has been a long-debated issue and results from different experiments have varied.[11–15] The nature of the band gap was controversial too, however, Watanabe *et al.*[14] (2004) established bulk h-BN as a direct band gap semiconductor with a 5.97 eV band gap for several years. Recent experimental studies[1,2] (2016) brought a turning point in this consensus, and showed the nature of the band gap as indirect and reported very accurate values of the electronic band gap of 6.08 eV,[1] optical gap of 5.69 eV,[2] and direct band gap of 6.42 eV.[2] These values can be directly compared to theoretical predictions. We therefore performed benchmark calculations of the before-mentioned energy gaps for the most stable conformers of h-BN.

Density functional theory (DFT) is a powerful tool for modeling materials, however, its one-particle ground state essence is the principal limit in predicting a fundamental energy gap, the difference between the first ionization energy and the first electron affinity of the neutral material. One-electron DFT energies $E_{n\boldsymbol{k}}$ (functions of Bloch wavevector $\boldsymbol{k}$ and band index $n$) approximate the fundamental gap by the electronic band gap, $E_{\text{gap}} = E_{\text{CBM}} - E_{\text{VBM}}$, the difference between a conduction band minimum $E_{\text{CBM}} = \min\{E_{v\boldsymbol{k}}\}$ and a valence band maximum $E_{\text{VBM}} = \max\{E_{c\boldsymbol{k}}\}$, $c, v \in \{n\}$. Therefore, the electronic gap from traditional generalized gradient approximation (GGA) DFT typically underestimates experimental gap values of bulk semiconducting and insulating materials by about 30–50%.[16] A typical approach to overcome this limitation of GGA density functionals is use of exchange–correlation functionals based on admixture of GGA and exact non-local Hartree–Fock (HF) exchange. Such hybrid functionals provide quite good band gaps using cancellation of errors, because the HF method systematically overestimates band gaps. In any case, accurate band structures are provided by the many-body perturbational GW method (where $G$ is the Green's function, and $W$ the screened Coulomb potential).[17] The band gap computed with GW is called a quasiparticle gap, $E_{\text{gap}}^{\text{QP}}$, and as such agrees closely with the electronic gap measured in scanning tunneling spectroscopy and photoemission experiments. The gap measured in optical absorption experiments (the lowest excitation energy, optical gap) can be modeled by taking into account electron–hole interactions *via* the Bethe–Salpeter equation (BSE).[18] In opposition to DFT, many-body GW and BSE methods are still computationally challenging mainly due to problematic issues such as the slow convergence of the QP energies with respect to basis-set size[19,20] or the requirement of fine $\boldsymbol{k}$-space sampling for accurate description of excitonic states.[21] Remarkably, even after several decades of research, publications with technically converged QP energies are rare and often resolve inconsistencies between previous GW+BSE calculations.[19–22]

*Department of Physics, Faculty of Science, University of Ostrava, 30. dubna 22, 701 03 Ostrava, Czech Republic. E-mail: frantisek.karlicky@osu.cz; Tel: +420 553 46 2155*

This journal is © the Owner Societies 2019

*Phys. Chem. Chem. Phys.*, 2019, **21**, 3999–4005 | 3999

A pioneering computational study based on the GW+BSE method (2006)[23] described bulk h-BN as an indirect band gap material with a gap of 5.95 eV, direct gap of 6.47 eV and a huge excitonic effect of 0.72 eV incoming from direct $\pi \to \pi^*$ transitions. Other studies reported indirect QP gap values of 5.4 eV,[24] 6.07 eV[25] or 6.25 eV.[19] Such variability of the band gap value from various independent calculations indicates questionable numerical reliability of particular calculations. In this paper we use many-body methods (GW, BSE) with the accent on accuracy, we evaluate the most stable h-BN stacking conformers and we provide benchmark values of quasiparticle (indirect and direct) and optical gaps which are in perfect agreement with recent experiments.[1,2]

## 2 Methods

We use recent h-BN experimental lattice constants of $a$ = 2.502 Å and $c$ = 6.617 Å[1] in all our calculations. The Vienna ab initio simulation package (VASP)[26] implementing projector augmented-wave (PAW) method,[26,27] GW set of PAWs,[28] and cut-off energy $E_{cut}$ = 500 eV are used in all calculations (2s1p electrons are explicitly treated).[29] We use GW approximation with input orbitals $|n\mathbf{k}\rangle$ from DFT and Perdew, Burke and Ernzerhof (PBE) functional[30] for electronic structure calculations (see Table S1, ESI†). That is, the quasi-particle energies $E_{n\mathbf{k}}^{QP}$ are calculated as first-order corrections to the DFT single-particle energies $E_{n\mathbf{k}}$

$$E_{n\mathbf{k}}^{QP,0} = E_{n\mathbf{k}} + Z_{n\mathbf{k}}\text{Re}[\langle n\mathbf{k}|T + V_{n-e} + V_H + \Sigma(G,W;E_{n\mathbf{k}})|n\mathbf{k}\rangle - E_{n\mathbf{k}}],$$
(1)

where $Z$ is the normalization factor,[31] $T$ is the kinetic energy operator, $V_{n-e}$ the potential of the nuclei, and $V_H$ the Hartree potential. The corresponding single-shot total energies are henceforth referred to as $G_0W_0$. The break condition for the electronic step is an energy difference of $1 \times 10^{-6}$ eV. Excitonic effects are accounted for by the Bethe–Salpeter equation,[18] which corresponds to the excitonic equation (eigenvalue problem):[32–34]

$$\left(E_{c\mathbf{k}}^{QP} - E_{v\mathbf{k}}^{QP}\right)A_{vc\mathbf{k}}^S + \sum_{v'c'\mathbf{k}'}\langle vc\mathbf{k}|K_{e-h}|v'c'\mathbf{k}'\rangle = E_{exc}^S A_{vc\mathbf{k}}^S.$$
(2)

The $A_{vc\mathbf{k}}^S$ values are obtained by diagonalization of eqn (2) and correspond to the amplitudes of a free electron–hole pair configuration composed of electron state $|c\mathbf{k}\rangle$ and hole state $|v\mathbf{k}\rangle$, the $E_{exc}^S$ values are eigenenergies (corresponding to the exciton excitation energies), and $K_{e-h}$ is the electron–hole interaction kernel. A broadening of 50 meV and 128 sampling points are used for the final dielectric function (77 grid points regularly in the range 0–25 eV; 51 points for the coarser grid up to 500 eV).

## 3 Results and discussion

### 3.1 Stacking configurations

Several stacking configurations are considered for the bulk h-BN structure,[35–37] see Fig. 1. These are similar in total energy, see Table 1 for their energy differences obtained by various DFT functionals. However, some stackings are reported as
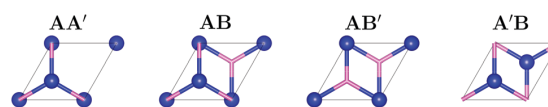


**Fig. 1** Various stacking configurations of h-BN (B – pink, N – blue) together with the unit cell (gray lines).

dynamically unstable.[35] We therefore consider both stable h-BN stackings, labeled as AA′ (space group $P6_3/mmc$ (194), $D_{6h}^4$ in Schoenflies notation) and AB ($P3m1$ (156), $C_{3v}^1$), which are also lowest in energy (Table 1).

### 3.2 Accuracy of many-body methods

In our calculations, we start with a careful convergence study of the electronic and optical gaps of AA′ h-BN with respect to the cut-off energy for the plane wave basis set $E_{cut}$, number of bands $N_B$, response (GW) cut-off energy $E_{cut}^{GW}$, number of $k$-points, and GW level, because slow convergence of quasiparticle energies, band gaps, or excitonic binding energies is proved for many-body methods and unconverged parameters can cause significant bias in predicted properties.[19–22] For instance, to obtain a band gap for $MoS_2$ with an accuracy better than 0.1 eV, it is necessary to employ a significantly higher $E_{cut}^{GW}$ value of 476 eV than has been reported for previous calculations and also to include a greater number of bands (more than an order of magnitude more ($N_b$ = 6000) than any previous calculation).[21] Bulk ZnO embodies extremely difficult convergence ($E_{cut}^{GW}$ = 1100 eV and $N_b$ = 3000 do not seem to be high enough for accurate band gaps[22]) and older calculations were underestimated up to $\sim 1$ eV. Finally, we have shown in our previous works on bulk and single-layered fluorinated/hydrogenated graphenes that one can easily obtain significantly biased results ($\approx 0.7$ eV) if one uses GW or BSE method as a black box without a careful convergence study.[40,41]

We set the cut-off energy $E_{cut}$ to 500 eV, hence $E_{cut}$ = 600 eV induced only 0.002 eV difference in GW gaps. Direct, indirect and optical band gaps are then satisfactorily converged for $N_B$ = 768 bands and $E_{cut}^{GW}$ = 400 eV, see Fig. 2. We can also see that a bad choice of the before-mentioned two parameters can lead to band gap errors up to 0.3 eV (Fig. 2) and attempts to converge $N_B$ with an unconverged $E_{cut}^{GW}$ value may lead to false convergence behavior (similarly to the behavior of the before-mentioned materials[21,22,40,41]). We note, that Gulans[19] recommended to extrapolate band gaps, because of not converging $E_{cut}^{GW}$ in his h-BN calculations.

Further, the $k$-point grid is very important for unbiased optical properties.[22,40] It seems that the $12 \times 12 \times 4$ $\Gamma$-centered grid is an adequate choice for h-BN. A difference lower than 0.005 eV in all types of gaps is obtained for the denser $18 \times 18 \times 6$ grid. We note that the number of $k$-points in the $k_x$ and $k_y$ directions must be divisible by 6 if one would like to include the $K$ point of the Brillouin zone which is important for transitions in h-BN, see below.

Finally, different levels of the GW method predict various band gap widths for bulk semiconductors and insulators.[16]

**4000** | *Phys. Chem. Chem. Phys.*, 2019, **21**, 3999–4005

This journal is © the Owner Societies 2019

**Table 1** Energy (meV per atom) of bulk h-BN in different stacking configurations with respect to the lowest energy stacking configuration. DFT methods implemented in VASP package are used. Namely, the empirically corrected[38] PBE[30] density functional, as well as nonlocal correlation functionals vdW-DF, vdW-DF2, and optB86b-vdW.[39] Note that experimental lattice constants[1] were used in all calculations
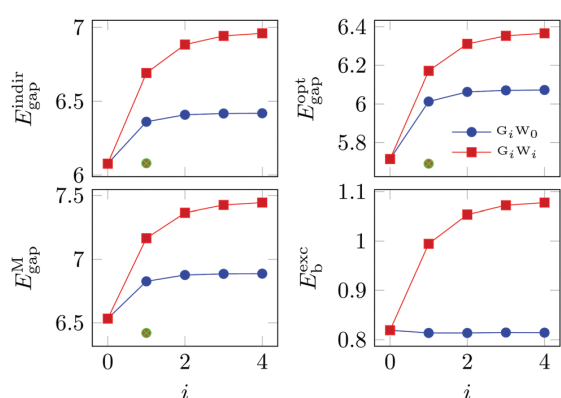
| Conf. | PBE-D2 | PBE-D3 | PBE-D3[a] | PBE-TS | PBE-TS[b] | PBE-TS+SCS | PBE-MBD@rsSCS | PBE-dDsC | vdW-DF | vdW-DF2 | optB86b-vdW |
|---|---|---|---|---|---|---|---|---|---|---|---|
| AA′ | 0.28 | 0.02 | 0.37 | 2.88 | 1.54 | 2.57 | 0.92 | 0.40 | 0.00 | 0.00 | 0.37 |
| AB | 0.00 | 0.00 | 0.00 | 0.83 | 0.00 | 1.34 | 0.00 | 0.00 | 0.06 | 0.46 | 0.00 |
| A′B | 2.27 | 2.79 | 1.97 | 0.00 | 0.74 | 0.00 | 1.42 | 11.92 | 2.52 | 3.25 | 2.07 |
| AB′ | 15.52 | 15.81 | 15.57 | 15.96 | 15.65 | 16.44 | 15.55 | 7.34 | 15.98 | 16.51 | 16.22 |

[a] D3 method with Becke–Johnson damping. [b] Tkatchenko–Scheffler method with iterative Hirshfeld partitioning.
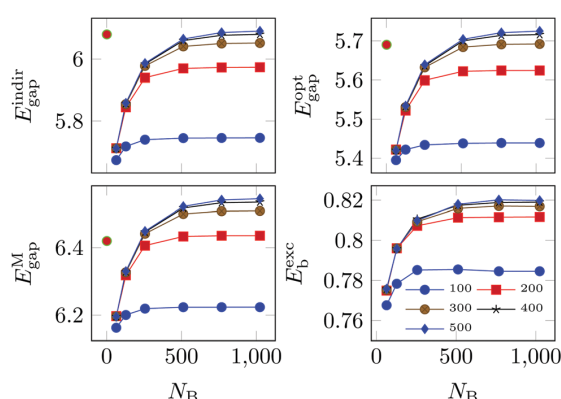


**Fig. 2** Convergence of h-BN (AA′) band gaps $E_{gap}$ (indirect, direct in M, optical) and exciton binding energy $E_b^{exc} = E_{gap}^M - E_{gap}^{opt}$ in eV with respect to number of bands $N_B$ and energy cut-off $E_{cut}^{GW}$ (indicated in the legend, in eV) for $G_0W_0$. $12 \times 12 \times 4$ $k$-grid was used. Green points are experimental values.[1,2]

In the h-BN case, a basic single-shot $G_0W_0$ version of GW provides gaps very close to experiment (if converged carefully), while higher levels of theory ($GW_0$ and GW) broadly overestimate the gap, see Fig. 3 for plot of gaps as function of theory level. For bulk materials, there is consensus that GW approximation approaches the experimental band gap of semiconductors and
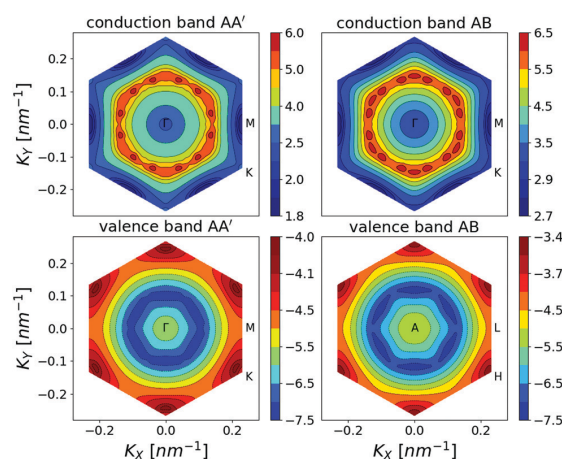
insulators. Specifically, calculated single shot $G_0W_0$ band gaps are often within 10% of experimental values (typically underestimated) and the best agreement with experiment is achieved by iterating G (labeled as $GW_0$) because GW band gaps are sometimes slightly overestimated.[16] It is evident that the basic single-shot $G_0W_0$ version of GW provides gaps of h-BN close to experiment, while $GW_0$ overestimates the gap by about 0.25 eV and GW overestimates it even more, by about 0.9 eV.
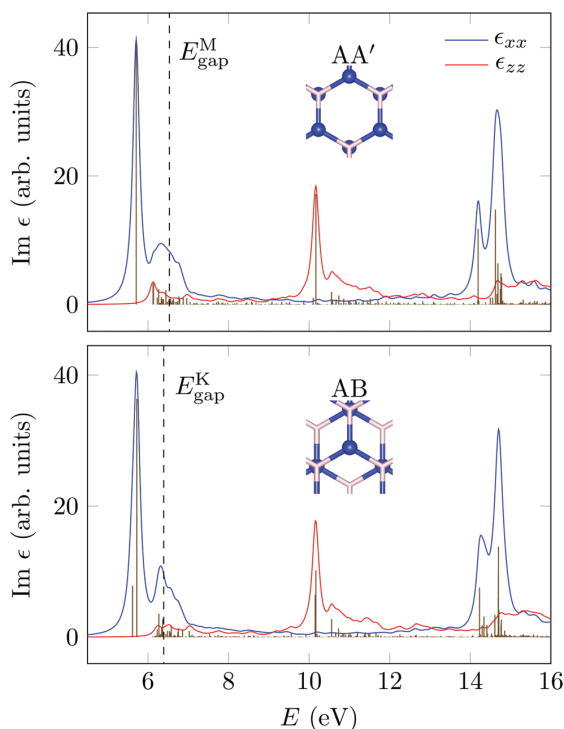
### 3.3 Electronic and optical properties of h-BN

The nature of the band gap in h-BN was controversial for a long time. We therefore calculated and plotted (Fig. 4) accurate quasiparticle conduction and valence bands. The conduction band minimum is located in the M point for both AA′ and AB stackings. The valence band maximum for AA′ h-BN is located close to the K point in the $\Gamma$ direction (closest $k$-point in our resolution), while in the AB case, the H point is the maximum (see Fig. 4). The direct band gap (the closest vertical distance between the valence and conduction bands) is located in the M point for AA′ stacking and in the K point for AB stacking. We note that previous work[23] reported a direct gap in the H point.

The optical absorption spectra from $G_0W_0$+BSE represented by imaginary dielectric function $\varepsilon$ is depicted in Fig. 5 for both



**Fig. 3** Convergence of h-BN (AA′) band gaps $E_{gap}$ (indirect, direct in M, optical) and exciton binding energy $E_b^{exc} = E_{gap}^M - E_{gap}^{opt}$ in eV with respect to number of iteration $i$ in $G_iW_0$ and $G_iW_i$ calculations. Green points are experimental values.[1,2]
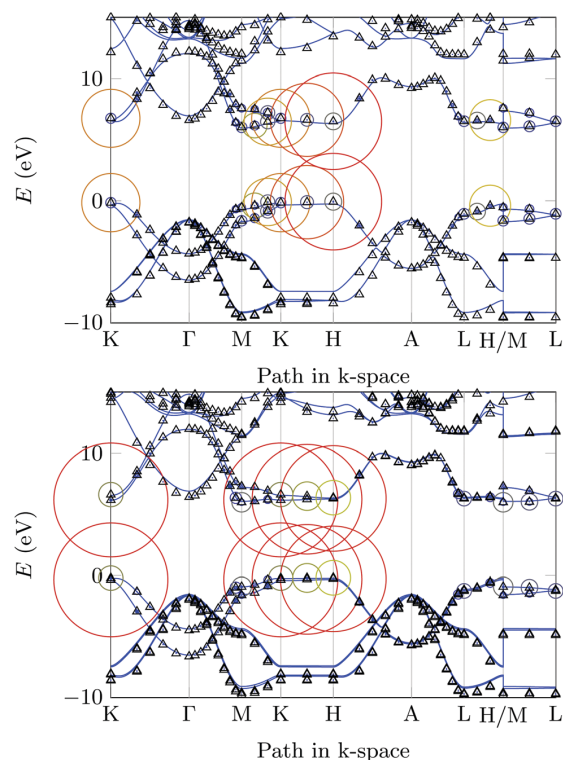


**Fig. 4** Conduction (top) and valence (bottom) bands of h-BN obtained from $G_0W_0$ calculation as cuts through the plane $\Gamma - M - K$ or $A - L - H$ in the corresponding first Brillouin zone ($24 \times 24 \times 2$ $k$-point grid is used for visualization purposes). Both h-BN stacking configurations, AA′ (left) and AB (right), are considered.

This journal is © the Owner Societies 2019

*Phys. Chem. Chem. Phys.*, 2019, **21**, 3999–4005 | **4001**

**Fig. 5** Optical absorption spectra of h-BN from $G_0W_0$+BSE calculation with 6 valence bands and 8 conduction bands included. Both h-BN stackings, AA′ (top) and AB (bottom), are considered and corresponding structures are depicted in subplots (B – pink, N – blue). Several bound excitonic states (vertical brown lines) are below the direct electronic band gap (dashed black line). Our choice of the coordinate system ($xy$ plane is equivalent to BN plane) implies zero off-diagonal and nonzero diagonal elements $\varepsilon_{xx} = \varepsilon_{yy}$ and $\varepsilon_{zz}$ of the frequency dependent dielectric matrix $\varepsilon$.



**Fig. 6** Electronic band structure of h-BN from $G_0W_0$ calculation (black triangles) and all $|A^S_{vck}|$ coefficients from eqn (2) (represented by radius of coloured circles; red = maximum, yellow = middle, grey = minimum) visually inspect which electron–hole pairs contribute to a first excitonic peak, *i.e.*, to a particular BSE eigenstate $S = 3$ for the AA′ structure (top) and eigenstate $S = 1$ for the AB structure (bottom). Scissor corrected DFT (PBE) band structure, DFT+$\Delta$ (blue lines), seems a very good approximation to the $G_0W_0$ band structure. Fermi energy is set as zero.

AA′ and AB stacking configurations of h-BN. General features of both spectra are almost same and it is therefore difficult to distinguish between stacking configurations of h-BN from optical absorption experiments. However, in the AA′ structure, double degenerated dark excitons (*i.e.* with energies $E^1_{\text{exc}} = E^2_{\text{exc}}$; *cf.* eqn (2)) are followed by double degenerated bright excitons (68 meV above dark exciton), whose energy is equal to the optical band gap, $E^3_{\text{exc}} = E^4_{\text{exc}} = E^{\text{opt}}_{\text{gap}}$. On the other hand, the optical band gap for the AB structure is equal to the energy of the lowest double degenerated BSE eigenstate $E^1_{\text{exc}} = E^2_{\text{exc}}$ (bright excitons). Other double degenerated bright excitons are 110 meV above the first pair.

The exciton wave function of the $S$-th exciton is expressed in an electron–hole product basis as $\sum_{vck} A^S_{vck}|ck\rangle|vk\rangle$. In order to decipher which region of the Brillouin zone is important for the optical gap (and corresponding exciton wave function), the eigenstate corresponding to the first bright exciton from the generalized BSE eigenvalue problem of eqn (2) is visualized in Fig. 6 by plotting circles with $|A^S_{vck}|$ radius into the band structure.[42] Pairs of large circles visible in Fig. 6 represent electron–hole pairs, which contribute the most to the first

excitonic peak. Only two highest occupied bands ($v = 7, 8$) and two lowest unoccupied bands ($c = 9, 10$) are of essential importance. The most important part of the Brillouin zone responsible for the first excitonic peak in the absorption spectra of both configurations (arising from the first bright exciton, *i.e.*, $S = 3, 4$ for AA′, $S = 1, 2$ for AB) is the region close to the $K$–$H$ line, while $M$–$K$ and $M$–$L$ lines contribute only weakly. On the other hand, regions in the vicinity of the $\Gamma$ and $A$ points of the Brillouin zone provide zero contribution to the first excitonic peak (Fig. 6; circles are less than the triangle symbols corresponding to the $G_0W_0$ band structure). Full inspection of the first four excitonic transitions is provided in Fig. S1 (ESI†); the $K$–$H$ region of the Brillouin zone is always important.

We stress that the $G_0W_0$+BSE approach is very demanding concerning computational time and memory used and its usage for a larger supercell is almost unfeasible. We therefore also show in Fig. 6 that computationally cheap approximation such as rigid scissor correction is very accurate for the h-BN particular case. We chose the scissor correction $\Delta = 1.91$ eV (as the difference between DFT (PBE) and $G_0W_0$ direct band gaps) which resulted

**4002** | *Phys. Chem. Chem. Phys.,* 2019, **21**, 3999–4005

This journal is © the Owner Societies 2019

in a simple DFT+$\Delta$ band structure very close to the accurate $G_0W_0$ band structure; *i.e.*, direct and indirect gaps are of the same nature and width (same location of CBM and VBM in the Brillouin zone). Subsequent optical spectra from DFT+$\Delta$ should be similar to $G_0W_0$ spectra because one-particle energies $E_{n\mathbf{k}}^{\text{DFT}+\Delta}$ are similar to $E_{n\mathbf{k}}^{\text{QP}}$ and identical one-particle wavefunctions $|n\mathbf{k}\rangle$ are used in both methods. This hypothesis is numerically confirmed by our calculations, both spectra are almost identical up to $\sim$10 eV in Fig. 7 (for detailed comparison see Fig. S2, ESI†). A computationally cheaper approximative method describing excitonic effects in conjunction with DFT+$\Delta$ should therefore provide absorption spectra and optical gap similar to full $G_0W_0$+BSE spectra with negligible computational cost. Such a simple approach is promising for the right physical description of absorption spectra of defected h-BN, h-BN surfaces *etc.* and should be tested. We consider time-dependent (TD) DFT as an effective method, which partially includes many-body effects.[43] In VASP, by solving the Casida equation within Tamm–Dancoff approximation, we obtain a TD-PBE+$\Delta$ curve, which is, however, far from the reference $G_0W_0$+BSE (absorption onset is shifted $\sim$1 eV to higher energies) and rather similar to the PBE+$\Delta$ curve (Fig. 7 and Fig. S3, ESI†). That is, despite the input one-particle energies $E_{n\mathbf{k}}^{\text{DFT}+\Delta}$ being similar to quasiparticle energies $E_{n\mathbf{k}}^{\text{QP}}$, the electron–hole ladder diagrams approximated by the exchange correlation kernel probably describe excitonic effects poorly. On the other hand, inclusion of the electron–hole attraction leads to a redshift in the bulk absorption spectrum[43,44] and we are therefore able to obtain more reasonable absorption curves if we use a better electron–hole description, *i.e.*, the electron–hole

ladder diagrams approximated by the exact exchange (EXX). This is still not so accurate as the screened exchange Coulomb potential $W$ in BSE, but the main features of the BSE curve are present. We show that it is possible to tune the EXX/GGA ratio in order to shift the main absorption peak to the reference $G_0W_0$+BSE value (Fig. S3, ESI†). We achieve the best agreement with EXX/GGA ratio of 0.3/0.7 and input PBE+$\Delta$ orbitals; such particular TD$^{\text{exx}}$-PBE+$\Delta$ curve is depicted in Fig. 7. We would like to stress that the computation time used for TD$^{\text{exx}}$-PBE+$\Delta$ is negligible with respect to the demanding full $G_0W_0$+BSE calculation. Further testing of various approximative methods is needed.

We also compare our results with recent experiments (Table 2): our indirect band gap widths of 6.077 eV and 6.175 eV for AA′ stacking and AB stacking, respectively, are in perfect agreement with the experimental indirect gap 6.08 eV.[1] Similarly, direct band gaps of 6.53 eV and 6.39 eV for AA′ stacking and AB stacking, respectively, are also nearly the same as the experimental one of 6.42 eV.[2] The same agreement is observed in the case of the calculated optical gap (5.71 eV with AA′ stacking and 5.61 eV with AB stacking with respect to the experimental value 5.69 eV[2]). As the last property suitable for comparison, we present the binding energy of the exciton from the before-mentioned gaps as the difference $E_{\text{b}}^{\text{exc}} = E_{\text{gap}}^{M[K]} - E_{\text{gap}}^{\text{opt}}$ for the AA′ [AB] stacking configuration. Our $E_{\text{b}}^{\text{exc}} = 0.82$ eV and $E_{\text{b}}^{\text{exc}} = 0.78$ eV for AA′ and AB h-BN, respectively, is also very close to the experimental value of 0.73 eV.[2]

Finally, we compare our results with previous theoretical predictions. As our indirect band gap widths of 6.077 eV and 6.175 eV for AA′ stacking and AB stacking of h-BN, respectively, differ from previous calculations (indirect band gap of 5.4 eV,[24] 5.95 eV,[23] 6.07 eV,[25] or 6.25 eV[19]) one can speculate on the reason for the differences ($\sim$0.7 eV distribution of predicted GW band gaps). We proved in Section 3.2 that nonconverged calculations can bias the band gap up to $\sim$0.3 eV. We also observed that the difference growing from different PAWs is 0.1 eV in VASP[28] (can be larger for pseudopotentials (PPs) used in different software) and $\sim$0.1 eV is the difference caused by the use of different stacking geometries (Table 2). Lastly, geometrical structures used in various calculations are slightly different. The $a$ lattice constant is typically the same as the experimental one and therefore often not reported in previous studies (as no variability is there for covalent bonds in the BN plane: $a = 2.502$ Å,[1] 2.503 Å,[23] or 2.504 Å[45]). On the other hand, the $c$ lattice constant can be a source of uncertainties. We found slightly different $c$ parameters used in previous calculations (6.658 Å,[23] 6.68 Å,[24] or 6.7 Å[19]) and experiments (6.66 Å,[14] 6.66 Å,[4] and 6.617 Å[1]). We therefore calculated electronic and optical band gaps from many-body methods for h-BN with $c$ in
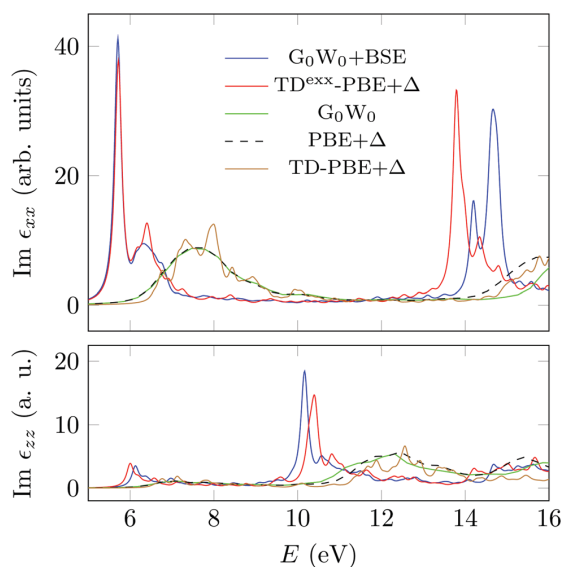


**Fig. 7** Optical absorption spectra (imaginary part of dielectric function $\varepsilon$) of h-BN (AA′) using various approximative methods and the reference $G_0W_0$+BSE curve. The exact exchange kernel with EXX/GGA ratio of 0.3/0.7 in TD-DFT (red TD$^{\text{exx}}$-PBE+$\Delta$ curve) is a promising computationally cheap approximation correctly fitting excitonic effects in h-BN.

**Table 2** Comparison of calculated gap values with experimental values

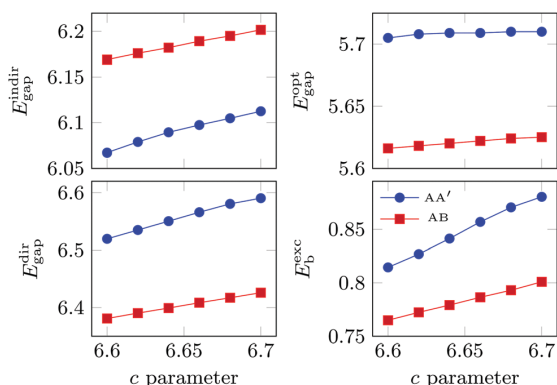|            | $E_{\text{gap}}^{\text{indir}}$ | $E_{\text{gap}}^{M/K}$ | $E_{\text{gap}}^{\text{opt}}$ | $E_{\text{b}}^{\text{exc}}$ |
|------------|------|------|------|------|
| Calc. AA′  | 6.08 | 6.53 | 5.71 | 0.82 |
| Calc. AB   | 6.17 | 6.39 | 5.61 | 0.78 |
| Exp.[1,2]  | 6.08 | 6.42 | 5.69 | 0.73 |

**Fig. 8** Change in h-BN band gaps $E_{gap}$ (indirect, direct in $M/K$, optical) from $G_0W_0$+BSE and exciton binding energy $E_b^{exc} = E_{gap}^{dir} - E_{gap}^{opt}$ in eV with respect to $c$ lattice parameter. Both h-BN stacking configurations, AA' and AB, are considered.

the range from 6.60 Å to 6.70 Å. It can be seen from Fig. 8 that a $G_0W_0$ electronic band gap variance of 0.1 eV appears for the $c$ lattice parameter in the chosen interval and the band gap linearly increases with increasing $c$ (we note that for single layer h-BN, *i.e.* $c \to \infty$, we have direct gap $\sim 7.7$ eV). On the other hand, the optical gap remains almost constant and the nature of the band gap is the same. We can therefore conclude that all discrepancies in the literature and present calculations of the h-BN band gap can be accounted for by different technical setups (convergence of technical parameters, PAWs/PPs) and different geometries (lattice $c$ parameter, stacking). As we used recent experimental geometries and we did a careful convergence study of all important input parameters of the calculations, we believe that our gaps are currently of the best accuracy.

## 4 Conclusions

In summary, the nature of exciton transitions in h-BN is investigated by a many-body pertubational $G_0W_0$+BSE approach. Our carefully converged results on the two most important h-BN stacking configurations, AA' and AB, reveal h-BN as an indirect material (indirect gap $\approx 6.1$ eV) with a huge excitonic effect ($\approx 0.8$ eV) in agreement with recent revolutionary experiments.[1,2] Because of very similar band structure and spectra, it is difficult to distinguish between AA' and AB stacking configurations of h-BN from optical and electronic properties. The total energy difference of both structures is very small too. We show that the $K$–$H$ region of the first Brillouin zone is mainly responsible for the lowest optical excitations in h-BN. We further consider factors leading to discrepancies in literature $G_0W_0$+BSE data. Variability of previous theoretical predictions and our convergence tests indicate that many-body methods should be used carefully and numerical convergence should be always performed. On the other hand, based on benchmark $G_0W_0$ results we suggest a computationally cheap scissor corrected DFT approach providing band structure comparable with the $G_0W_0$

band structure. Time-dependent DFT with a suitable exchange correlation kernel can provide absorption spectra that mimic the full $G_0W_0$+BSE spectra.

## Note added in proof

During work on our paper, another study on stacking configurations and optical excitations in h-BN was published.[46] Our findings are in good agreement with recent calculations, namely, the nature of the lowest-energy excitons and the shape of the optical absorption spectra.

## Conflicts of interest

There are no conflicts to declare.

## Acknowledgements

## References

1 G. Cassabois, P. Valvin and B. Gil, *Nat. Photonics*, 2016, **10**, 262–266.
2 T. C. Doan, J. Li, J. Y. Lin and H. X. Jiang, *Appl. Phys. Lett.*, 2016, **109**, 122101.
3 J. Li, X. K. Cao, T. B. Hoffman, J. H. Edgar, J. Y. Lin and H. X. Jiang, *Appl. Phys. Lett.*, 2016, **108**, 122101.
4 X. Z. Du, M. R. Uddin, J. Li, J. Y. Lin and H. X. Jiang, *Appl. Phys. Lett.*, 2017, **110**, 092102.
5 G. Fugallo, M. Aramini, J. Koskelo, K. Watanabe, T. Taniguchi, M. Hakala, S. Huotari, M. Gatti and F. Sottile, *Phys. Rev. B: Condens. Matter Mater. Phys.*, 2015, **92**, 165122.
6 J. Koskelo, G. Fugallo, M. Hakala, M. Gatti, F. Sottile and P. Cudazzo, *Phys. Rev. B*, 2017, **95**, 035125.
7 L. Sponza, H. Amara, F. Ducastelle, A. Loiseau and C. Attaccalite, *Phys. Rev. B*, 2018, **97**, 075121.
8 K. Watanabe, T. Taniguchi and H. Kanda, *Phys. Status Solidi A*, 2004, **201**, 2561–2565.
9 Y. Kubota, K. Watanabe, O. Tsuda and T. Taniguchi, *Science*, 2007, **317**, 932–934.
10 T. Taniguchi and K. Watanabe, *J. Cryst. Growth*, 2007, **303**, 525–529.
11 R. Mamy, J. Thomas, G. Jezequel and J. Lemonnier, *J. Phys., Lett.*, 1981, **42**, 473–475.

**4004** | *Phys. Chem. Chem. Phys.*, 2019, **21**, 3999–4005

This journal is © the Owner Societies 2019

12 C. Tarrio and S. E. Schnatterly, *Phys. Rev. B: Condens. Matter Mater. Phys.*, 1989, **40**, 7852–7859.

13 V. Solozhenko, A. Lazarenko, J.-P. Petitet and A. Kanaev, *J. Phys. Chem. Solids*, 2001, **62**, 1331–1334.

14 K. Watanabe, T. Taniguchi and H. Kanda, *Nat. Mater.*, 2004, **3**, 404–409.

15 D. A. Evans, A. G. McGlynn, B. M. Towlson, M. Gunn, D. Jones, T. E. Jenkins, R. Winter and N. R. J. Poolton, *J. Phys.: Condens. Matter*, 2008, **20**, 075233.

16 M. Shishkin and G. Kresse, *Phys. Rev. B: Condens. Matter Mater. Phys.*, 2007, **75**, 235102.

17 L. Hedin, *Phys. Rev.*, 1965, **139**, A796–A823.

18 H. Bethe and E. Salpeter, *Phys. Rev.*, 1951, **82**, 309–310.

19 A. Gulans, *J. Chem. Phys.*, 2014, **141**, 164127.

20 J. Klimeš, M. Kaltak and G. Kresse, *Phys. Rev. B: Condens. Matter Mater. Phys.*, 2014, **90**, 075125.

21 D. Y. Qiu, F. H. da Jornada and S. G. Louie, *Phys. Rev. Lett.*, 2013, **111**, 216805.

22 B.-C. Shih, Y. Xue, P. Zhang, M. L. Cohen and S. G. Louie, *Phys. Rev. Lett.*, 2010, **105**, 146401.

23 B. Arnaud, S. Lebègue, P. Rabiller and M. Alouani, *Phys. Rev. Lett.*, 2006, **96**, 026402.

24 X. Blase, A. Rubio, S. G. Louie and M. L. Cohen, *Phys. Rev. B: Condens. Matter Mater. Phys.*, 1995, **51**, 6868–6875.

25 N. Berseneva, A. Gulans, A. V. Krasheninnikov and R. M. Nieminen, *Phys. Rev. B: Condens. Matter Mater. Phys.*, 2013, **87**, 035404.

26 G. Kresse and D. Joubert, *Phys. Rev. B: Condens. Matter Mater. Phys.*, 1999, **59**, 1758–1775.

27 P. E. Blöchl, *Phys. Rev. B: Condens. Matter Mater. Phys.*, 1994, **50**, 17953–17979.

28 We have done the calculation with a standard PBE PAW set as well, however, all gaps were about 0.1 eV underestimated. See the VASP manual at http://www.vasp.at for definitions and versions of PAWs in VASP.

29 For the unit cell with four atoms, $B_2N_2$, 16 valence electrons $(2 \times 2s^2 1p^1, 2 \times 2s^2 1p^3)$ are in 8 occupied bands $\nu = 1, 2, \ldots, 8$, $c = 9, 10, \ldots$.

30 J. P. Perdew, K. Burke and M. Ernzerhof, *Phys. Rev. Lett.*, 1996, **77**, 3865–3868.

31 M. Shishkin and G. Kresse, *Phys. Rev. B: Condens. Matter Mater. Phys.*, 2006, **74**, 035101.

32 G. Strinati, *Phys. Rev. B: Condens. Matter Mater. Phys.*, 1984, **29**, 5718–5726.

33 M. Rohlfing and S. Louie, *Phys. Rev. B: Condens. Matter Mater. Phys.*, 2000, **62**, 4927–4944.

34 F. Fuchs, C. Roedl, A. Schleife and F. Bechstedt, *Phys. Rev. B: Condens. Matter Mater. Phys.*, 2008, **78**, 085103.

35 L. Liu, Y. Feng and Z. Shen, *Phys. Rev. B: Condens. Matter Mater. Phys.*, 2003, **68**, 104102.

36 N. Marom, J. Bernstein, J. Garel, A. Tkatchenko, E. Joselevich, L. Kronik and O. Hod, *Phys. Rev. Lett.*, 2010, **105**, 046801.

37 G. Constantinescu, A. Kuc and T. Heine, *Phys. Rev. Lett.*, 2013, **111**, 036104.

38 See the VASP manual at http://www.vasp.at for definitions of empirical corrections and references. Advanced semi-empirical schemes have been implemented in VASP by T. Bučko, *et al.*, *Phys. Rev. B: Condens. Matter Mater. Phys.*, 2011, **87**, 064110; *J. Phys.: Condens. Matter*, 2016, **28**, 045201.

39 See the VASP manual at http://www.vasp.at for definitions of vdW functionals and references. This feature has been implemented in VASP by J. Klimeš, *et al.*, *Phys. Rev. B: Condens. Matter Mater. Phys.*, 2011, **83**, 195131.

40 F. Karlický and M. Otyepka, *Ann. Phys.*, 2014, **526**, 408–414.

41 F. Karlický and J. Turoň, *Carbon*, 2018, **135**, 134–144.

42 M. Bokdam, T. Sander, A. Stroppa, S. Picozzi, D. D. Sarma, C. Franchini and G. Kresse, *Sci. Rep.*, 2016, **6**, 28618.

43 L. E. Ramos, J. Paier, G. Kresse and F. Bechstedt, *Phys. Rev. B: Condens. Matter Mater. Phys.*, 2008, **78**, 195423.

44 F. Karlický and M. Otyepka, *J. Chem. Theory Comput.*, 2013, **9**, 4155–4164.

45 R. Wyckoff, *Crystal Structures – Volume 1*, Interscience Publishers, 1963.

46 W. Aggoune, C. Cocchi, D. Nabok, K. Rezouali, M. A. Belkhir and C. Draxl, *Phys. Rev. B: Condens. Matter Mater. Phys.*, 2018, **97**, 241114.

This journal is © the Owner Societies 2019

*Phys. Chem. Chem. Phys.*, 2019, **21**, 3999–4005 | **4005**

# Supplementary Material 3

Article

# Optical Gaps and Excitonic Properties of 2D Materials by Hybrid Time-Dependent Density Functional Theory: Evidences for Monolayers and Prospects for van der Waals Heterostructures

Tomi Ketolainen, Nikola Macháčová, and František Karlický*

Cite This: *J. Chem. Theory Comput.* 2020, 16, 5876−5883

Read Online

ACCESS | Metrics & More | Article Recommendations | Supporting Information

**ABSTRACT:** The optical properties of two-dimensional (2D) materials are accurately described by many-body methods including specifically pronounced electron−electron and electron−hole effects. Such methods are, however, computationally demanding and applicable on small computational cells only. We provide approximate optical gaps for 2D materials from time-dependent (TD) density functional theory based on a set of specific screened hybrid functionals and show that this approach effectively accounts for all important physical effects including excitons. Optical gap values obtained from the TD-HSE06 approach for a broad gap range 1−6 eV of eight 2D materials are in agreement with both experimental optical gaps and accurate GW+BSE calculations. Further, we show that such an approach is eligible and practicable for van der Waals heterostructures containing incommensurate cells of different monolayers and enables detailed analysis of intra- and interlayer excitonic wave functions. TD-HSE06 is therefore a suitable method for a reliable description of the optical properties of extended periodic 2D systems.
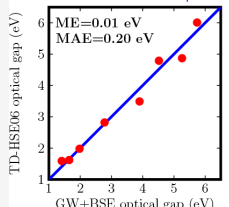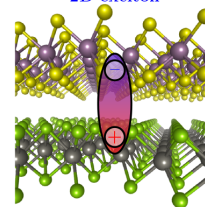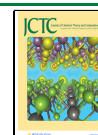
## 1. INTRODUCTION

Current needs of applied research on two-dimensional (2D) materials for flexible and ultrathin functional devices require reliable computational predictions and computer-aided design.[1,2] Specifically, van der Waals (vdW) heterostructures, in which different 2D materials are superimposed in a stacked configuration, represent a versatile experimental and theoretical platform for studying the fundamental properties for materials science and device physics.[3,4] Atomically thin novel devices based on these heterolayers have been demonstrated, such as p−n junctions, tunneling and light-emitting diodes, transistors, and photovoltaic devices.[5−8] Reliable predictions of the electronic and optical properties of 2D materials and their heterostructures are therefore of essential importance. Excitonic effects are, however, extremely pronounced in 2D materials (binding energies of excitons typically in the hundreds of meV range, up to 3 eV)[9] compared to bulk materials (typically in meV), and electron correlations and dielectric screening must be therefore described very carefully.[10] For the presence of delicate interplay of such multiple effects in 2D materials, correct predictions of their properties require accurate and costly many-body methods instead of usual density functional theory (DFT) making these computations demanding for single layers and almost unfeasible for large incommensurate vdW heterostructures. Intermediately demanding approximate methods will be therefore devised and assessed as a tool for reliable computer-aided design of new 2D materials with tailored

properties for a new generation of solar cells and functional devices.

The many-body perturbational GW approximation for the electron self-energy[11] followed by a subsequent solution of the Bethe-Salpeter equation (BSE)[12] describes the optical properties of materials accurately. Such methods are currently rather routine,[13] however, computationally demanding and applicable on small unit cells only. Broadly used DFT in its time-dependent (TD) formulation is principally capable of providing absorption spectra too. However, regular local and semilocal TD-DFT approximations underestimate band gaps and do not introduce excitonic effects in solids.[14,15] On the other hand, it has been found that the inclusion of a fraction of nonlocal exact exchange (EXX) gives rise to excitonic effects and considerably improves the optical absorption spectra of solids compared to the adiabatic local-density approximation.[16,17] We have also shown recently that TD-DFT with a suitable exchange correlation kernel provides absorption spectra similar to the full GW+BSE spectra in the case of layered bulk materials.[18] Finally, this way seems to be promis-

ing due to a possibility to show similarity of BSE and TD-DFT formalisms.

In this work, we provide approximate optical gaps for a set of 2D materials from TD-DFT based on screened hybrid functionals and show that such an approach with the specific HSE06 functional[19] effectively accounts for electron−electron and electron−hole effects through a good agreement with both experimental and GW+BSE optical gaps. We chose for this purpose eight important semiconducting and insulating 2D materials with optical gaps ranging from 1 to 6 eV: phosphorene ($P_4$), two transition metal dichalcogenides (tungsten diselenide $WSe_2$ and molybdenum disulfide $MoS_2$), several hexagonal III−V group semiconductors (gallium phosphide GaP, gallium nitride GaN, aluminum nitride AlN, and boron nitride BN), and fluorographene (CF). Further, we showed on selected vdW heterostructures ($BN/WSe_2$ and $MoS_2/WSe_2$) that the hybrid TD-DFT approach is practicable on such systems with tens of atoms, and therefore our approach is a good method for a reliable description of the optical properties of extended 2D systems.

## 2. RESULTS AND DISCUSSION

We showed in our previous study on bulk hexagonal BN[18] that tuning of the EXX fraction is responsible for significant shifts in TD-DFT optical absorption spectra and, in addition, it is possible to systematically tune spectra to achieve shape/peak positions of accurate GW+BSE spectra. However, our approach was not very practical as we used scissor-corrected DFT for single-particle energies, and thus we needed a GW calculation as the first step for the scissor correction. Subsequently, the ratio of EXX was tuned only in the exchange-correlation kernel of the second step of the TD-DFT calculation. This approach is therefore dependent on materials and not so useful for broader applications. However, the method may be useful for studies of defected materials etc. Here, we use a slightly different approach to avoid the necessity of any information from the demanding many-body method (GW), and we focus on the similarity of equation for TD-DFT and the BSE. With restriction to materials with completely unoccupied conduction bands and occupied valence bands ($c$ and $v$ indices, respectively) as in semiconductors and insulators, the BSE can be rewritten as the eigenvalue problem

$$(E_{ck}^{QP} - E_{vk}^{QP})A_{cvk}^S + \sum_{c'v'k'} [2\langle ckvk|\nu|c'k'v'k'\rangle - \langle ckc'k'|W|vkv'k'\rangle]A_{c'v'k'}^S = E_{exc}^S A_{cvk}^S \tag{1}$$

(see the Supporting Information for derivation of this form), where the eigenvectors $A_{cvk}^S$ correspond to the amplitudes of free electron−hole pair configurations composed of electron states $|ck\rangle$ and hole states $|vk\rangle$ and the eigenenergies $E_{exc}^S$ correspond to the excitation energies. $W$ is screened Coulomb potential, $\nu$ is the Coulomb kernel $1/|r − r'|$, and the quasi-particle energies $E_{nk}^{QP}$ are calculated as the first-order corrections to the DFT single-particle energies $E_{nk}$. We further use linear-response TD-DFT formulated as a generalized eigenvalue equation called the Casida equation.[20] A commonly used approximation neglecting the nonresonant component (deexcitation: unoccupied → occupied), known as the Tamm-Dancoff approximation, leaves only the resonant (occup. → unoccup.) component:

$$(E_{ck} - E_{vk})A_{cvk}^S + \sum_{c'v'k'} [2\langle ckvk|\nu|c'k'v'k'\rangle + 2\langle ckvk|f_{XC}|c'k'v'k'\rangle]A_{c'v'k'}^S = E_{exc}^S A_{cvk}^S \tag{2}$$

(see Supporting Information for derivation of this form), where $f_{XC}$ is the static exchange-correlation kernel. Due to the same form of eqs 1 and 2, differences between the BSE and TD-DFT become easily comparable. Changes of $E_{nk}^{QP}$ and $W(q, G, G')$ with $q = k − k' + G_0$ to $E_{nk}$ and $f_{XC}(q \to 0, G, G')$ indicate that it is impossible to exactly reproduce the BSE.[21] However, one can reproduce a fraction of the BSE coupling matrix with adiabatic TD-DFT.[22]

Without exact exchange (EXX), excitonic effects are not present in the TD-DFT calculations. A reasonable part of EXX must be included in order to mimic exact Coulomb exchange $W$ (cf. term $−W$ vs $2f_{XC}$ in eqs 1 and 2, respectively). Therefore, the general problem in our study is to find a reasonable fraction of EXX. Typically, values around 25% are reasonable (as derived using perturbation theory).[23] In addition, the macroscopic dielectric constant $\epsilon$ of a 3D material determines it because $W \propto \epsilon^{-1}\nu$.[17,24] However, this is problematic for 2D materials, because the macroscopic dielectric constant of the unit cell approaches one when the size of the vacuum in the computational unit cell becomes infinite,[25] see also Figure S1 for $\epsilon$ of CF. We therefore decided to find the fraction $\alpha$ of EXX by using the formula for screened hybrid (SH) functionals (containing another variable, screening $\omega$)[19]

$$E_{xc}^{SH} = \alpha E_x^{HF,SR}(\omega) + (1 - \alpha)E_x^{PBE,SR}(\omega) + E_x^{PBE,LR}(\omega) + E_c^{PBE} \tag{3}$$

containing short-range (SR) and long-range (LR) contributions of PBE[26] exchange and correlation and Hartree−Fock (HF) exchange (only in SR part). We decided to tune both parameters with respect to the optical gaps from GW+BSE (we used $G_0W_0$+BSE from the C2DB database[13] as reference, and we also collected experimental data). We started with wide-gap semiconductors/insulators BN and CF, as computing the optical spectrum for them is more difficult.[27] The dependence of the optical gap $E_{exc}^1$ of BN on $\alpha$ and $\omega$ is shown in Figure 1a; the same for CF is presented in Figure 1d. We also show the dependence of the optical absorbance on EXX fraction $\alpha$ (Figure 1b) and screening $\omega$ (Figure 1c). These materials were evidently described well with an EXX fraction around $\alpha = 0.25$ and $\omega = 0.2$ Å$^{-1}$. We subsequently performed a limited search around these values for the rest of the materials too. After performing statistics on all eight materials, we obtained parameters $\alpha = 0.25$ and $\omega = 0.2$ Å$^{-1}$ as the best compromise and also taking into account that this choice of parameters in eq 3 corresponds just to the hybrid density functional called HSE06.[19] Mean error (with respect to GW+BSE) for several $(\alpha, \omega)$ is depicted in Figure 1e. Other statistics as mean absolute error and root-mean-square deviation are reported in Table S2. The final optical gaps are presented in Table 1 in comparison to the GW+BSE data of the C2DB database[13] and experiments (full data including the band gaps are collected in Table S1). Usage of the described method (we label it as TD-HSE06) leads to a nice correlation of the optical gaps from TD-HSE06 and GW+BSE (and experiment) as shown in Figure 1f for photon energies between 1 and 6 eV.

Computing reliable optical spectra on some reasonable energy interval is a more difficult task. As we have shown in

Table 1. First Excitation Energies (Optical Gaps; In Units of eV) for Two-Dimensional Materials

| material | $E_{exc}^{TD\text{-}HSE06}$ | $E_{exc,C2DB}^{BSE,[13]}$ | $E_{exc}^{exp}$ |
|---|---|---|---|
| $P_4$ | 1.59 | 1.41 | 1.30 (ref 28) |
| $WSe_2$ | 1.62 | 1.65 | 1.66 (ref 29) |
| $MoS_2$ | 1.98 | 1.98 | 1.88 (ref 29) |
| GaP | 2.82 | 2.78 | |
| GaN | 3.49 | 3.90 | |
| AlN | 4.79 | 4.52 | |
| CF | 4.87 | 5.26 | 5.00 (ref 30) |
| BN | 6.01 | 5.74 | 6.20 (ref 31) |

our previous study,[9] a careful convergence study is necessary for the GW+BSE method and the same is valid for TD-HSE06, because excitonic effects are effectively accounted for. Therefore, especially the k-point grid must be tested, to avoid artificial confinement of excitons.[9,32] Achieving the converged spectra for BN and CF with increasing density of the k-point grid was quite difficult. At least a 24 × 24 × 1 k-point grid was necessary to recover main spectrum features between 0 and 7 eV (see Figures S2 and S3). The convergence of the spectra of other materials was slightly easier and we therefore used 18 × 18 × 1 k-points with the only exception of $P_4$ (Figure S4). We present TD-HSE06 absorbance spectra (Figure 2) in comparison with traditional PBE and HSE06 spectra obtained from interband transitions.[33] We added also experimental data for five 2D materials (three curves and two values). Obtained spectra seem to be reasonable compared to experiments both in amplitudes (absorbance values) and peak

positions. Further, we directly compared TD-HSE06 absorbance spectra with our reference GW+BSE spectra in Figure 3. The overall agreement for $P_4$ is good, but not perfect, because the value $\alpha = 0.25$ is the result of certain compromise for the whole set of considered materials (Figure 1e) and slightly smaller $\alpha$ would be better for particular $P_4$ material. This overall agreement is in contrast to absorbance values from C2DB GW+BSE, which are probably overestimated, cf. Figure 3 and S6 and experimental curves in Figure 2.

We note that the method presented here, TD-HSE06, is a full ab initio approach, is of moderate computational cost, and effectively accounts for excitons (as shown in Figures 1−3). On the other hand, TD-HSE06 features of the absorbance are not consistently well described. This is partially solved by other empirical attempts at generating a simplified dielectric function, e.g., "bootstrap kernel".[34] Further, some semi-empirical schemes which are computationally cheaper were developed recently. In particular, ones that explicitly include the 2D character of the screening are very promising.[35] Optical gap values ($E_{exc}$) for $MoS_2$ (1.98 eV) and BN (6.10 eV) produced by this model[35] are very close to our values (Table 1). However, only exciton binding energies ($E_b$) were calculated within a model and fundamental gaps ($E_{gap}$; $E_{exc} = E_{gap} - E_b$) were modeled by the tight-binding method with parameters ensuring agreement between experimental and theoretical exciton features, i.e., some information about the described system is needed. In contrast, presently TD-HSE06 does not require any preceding information about materials from experiments or higher theories.
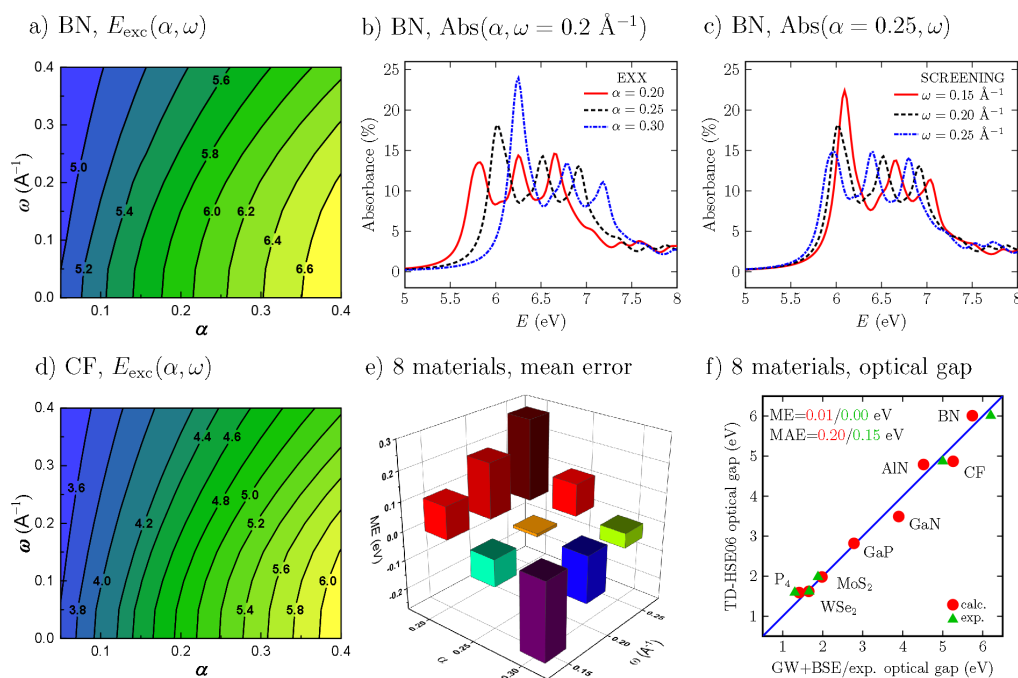


Figure 1. Search for the optimal fraction $\alpha$ of EXX and screening parameter $\omega$ in TD-DFT based on the SH functional of eq 3: (a) optical gap of BN as a function of $\alpha$ and $\omega$, (b) optical absorbance of BN depending on $\alpha$ and (c) on $\omega$, (d) optical gap of CF as a function of $\alpha$ and $\omega$, (e) mean error for TD-HSE06 with respect to GW+BSE optical gaps as a function of $\alpha$ and $\omega$, (f) TD-HSE06 optical gaps in relation to GW+BSE and experimental optical gaps; the blue solid line is an ideal case.
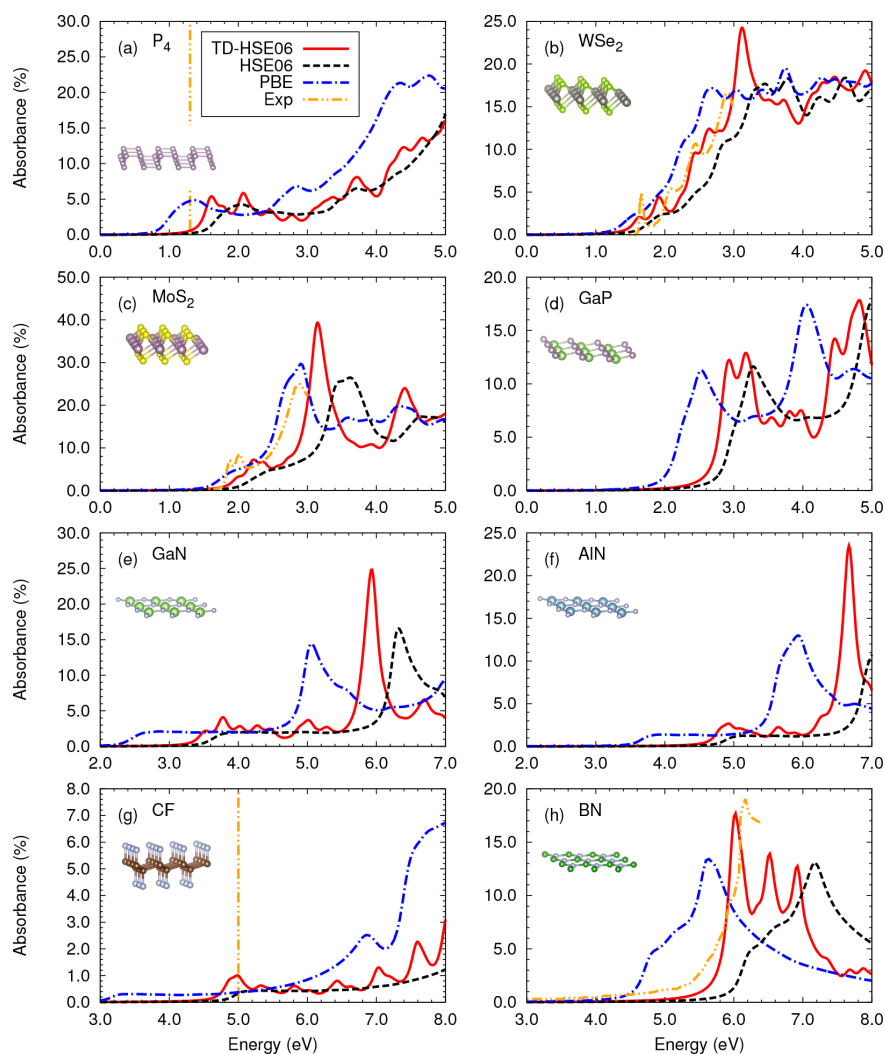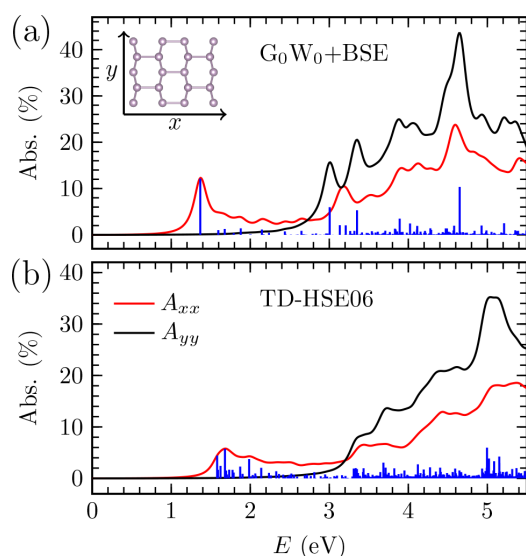
**Figure 2.** In-plane optical absorbance computed with the TD-HSE06 method, HSE06 functional, and PBE functional for two-dimensional (a) $P_4$ (absorbance in armchair direction), (b) $WSe_2$, (c) $MoS_2$, (d) GaP, (e) GaN, (f) AlN, (g) CF, and (h) BN. In addition, the experimental curves of the optical absorbance are shown for $WSe_2$ (ref 29), $MoS_2$ (ref 29), and BN (ref 31). The orange vertical lines represent the positions of the first excitation peaks in the experiments where the curves are not available. The insets in the panels show the atomic structures of the 2D materials.

Because the TD-HSE06 approach was quite successful on our set of eight materials, we decided to apply it also to larger supercells, namely, vdW heterostructures. Larger supercells (useful also for a description of defects, support-material interfaces, etc.) are computationally challenging because these systems contain a large number of atoms/electrons and thus the GW+BSE method is almost intractable. Therefore, optical absorption curves without excitonic effects are standardly reported in the literature or the optical spectrum is determined in a semiempirical way.[36] We chose two examples of vdW heterostructures including three different materials from our set of eight materials, namely, $BN/WSe_2$ and $MoS_2/WSe_2$. We generated large sets of possible incommensurate supercells of different monolayers by rotating them and attaching them to achieve minimal strain and a reasonable number of atoms.[37]

After establishing suitable supercells with 26 and 75 atoms, respectively, we obtained numerically correct results: we appreciated that the optical absorbance spectra converged quickly with respect to the k-point grid for considered heterostructures (Figures S7 and S8), as the TD-HSE06 calculations were very demanding (mainly HSE06 part) for such systems. Resulting converged absorbances together with computational cells are presented in Figure 4. New exciton features in the TD-HSE06 curves (with respect to PBE and HSE06 absorbances) are clearly visible. The optical gaps obtained for the $BN/WSe_2$ and $MoS_2/WSe_2$ heterostructures were 2.01 eV (the most dominant peak at 3.10 eV) and 1.78 eV (the most dominant peak at 3.22 eV), respectively.

Finally, we performed another analysis provided by the TD-HSE06 method, namely, exciton wave function analysis. The

**Figure 3.** Direct comparison of optical absorbance $A$ ($A_{xx}$ and $A_{yy}$ components) for phosphorene ($P_4$) computed with (a) $G_0W_0$+BSE and (b) TD-HSE06 methods. Particular excitonic states are shown using vertical blue lines. See Figures S4 and S5 for the technical setup and the convergence properties of the spectra from both methods.

wave function of the $S$-th exciton is expressed in an electron–hole product basis as $\sum_{cvk} A_{cvk}^{S}|c k\rangle|v k\rangle$. The eigenstate corresponding to the first bright exciton in phosphorene from the generalized BSE and the Casida eigenvalue problem of eqs 1 and 2, respectively, is visualized in Figure 5 by plotting arrows with $|A_{cvk}^{1}|$ thickness into the band structures.[38] Red arrows connecting some of the bands depicted in Figure 5 represent electron–hole pairs, which contribute the most to the first excitonic peak $E_{exc}^{I}$ (and to the corresponding exciton wave function). Only the region close to the $\Gamma$ point (for the highest occupied band and lowest unoccupied band) is of essential importance. Other regions of the Brillouin zone provide almost zero contribution to the first excitonic peak because of corresponding negligible $|A_{cvk}^{1}|$ coefficients (and we therefore omitted the rest of arrows with almost zero thickness). Figure 5 and S9 (for the first 10 excitations in phosphorene) show good correspondence of $A_{cvk}^{S}$ coefficients distribution in the k-space from the TD-HSE06 method with respect to the reference BSE+GW distribution. We just observed that this k-space distribution is slightly more localized in the TD-HSE06 case (visually expressed by a smaller number of red arrows in Figure 5). We did similar exciton analyses for vdW heterostructures too. BN/WSe$_2$ is an example of type-I band alignment[10] at heterobilayer interfaces, and the lowest excitations are therefore given by the valence band maximum and conduction band minimum of WSe$_2$ (Figure 6a; red dotted lines are helpful to identify the WSe$_2$ bands in the band structure of the BN/WSe$_2$ heterostructure), i.e., an intralayer exciton is responsible for the first excitonic peak in BN/WSe$_2$. On the other hand, MoS$_2$/WSe$_2$ is a typical example of type-II
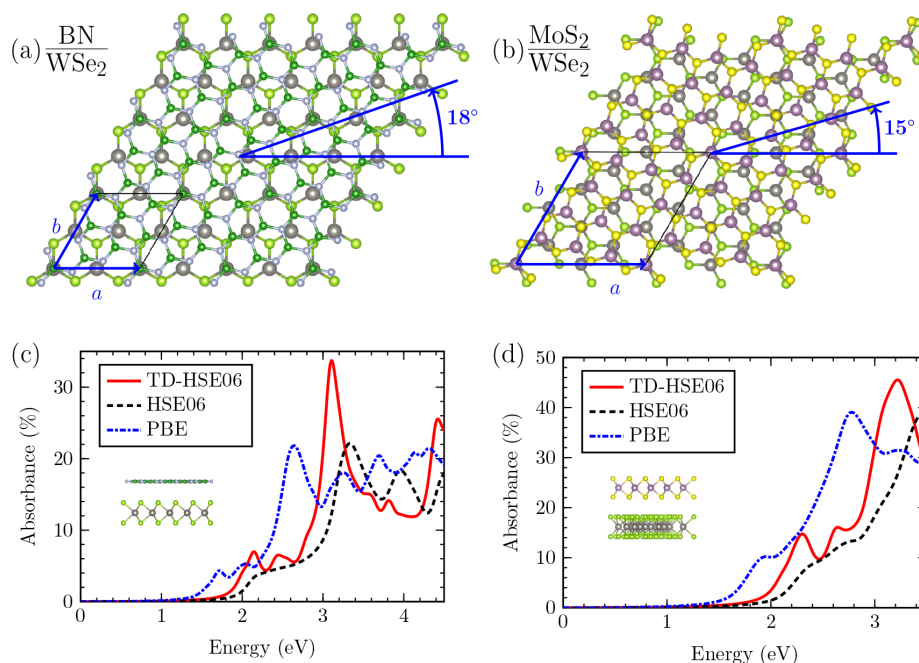


**Figure 4.** Schematic of (a) the BN/WSe$_2$ and (b) MoS$_2$/WSe$_2$ vdW heterostructures presenting the hexagonal calculation cells with lattice parameters $a = b = 6.6$ Å (26 atoms, 18° rotation between both lattices) and 11.4 Å (75 atoms, 15° rotation). Corresponding absorbances (c,d) are reported in the same way as in Figure 2. W and Se atoms are in gray and light green, respectively, while B and N are in light blue and green, Mo and S are in purple and yellow.
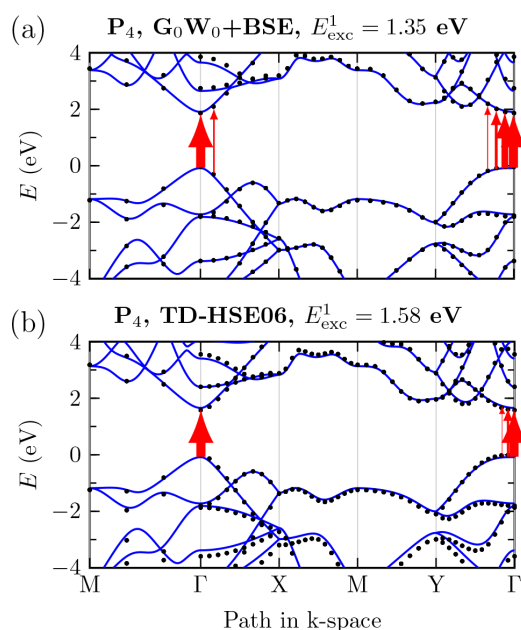
**Figure 5.** Electronic band structure of phosphorene from (a) a $G_0W_0$ calculation (black dots) and significant $|A^S_{cvk}|$ coefficients from eq 1 (represented by the thickness of the red arrows) visually show which electron−hole pairs contribute to the first excitonic peak, i.e., to a particular BSE eigenstate $S = 1$. Similarly, (b) the TD-HSE06 calculation is analyzed (eq 2, eigenstate $S = 1$). A scissor-corrected DFT (PBE) band structure, DFT+$\Delta$ (blue lines), serves as an eye-guide and seems to be a very good approximation to accurate band structures. The Fermi energy is set to zero.
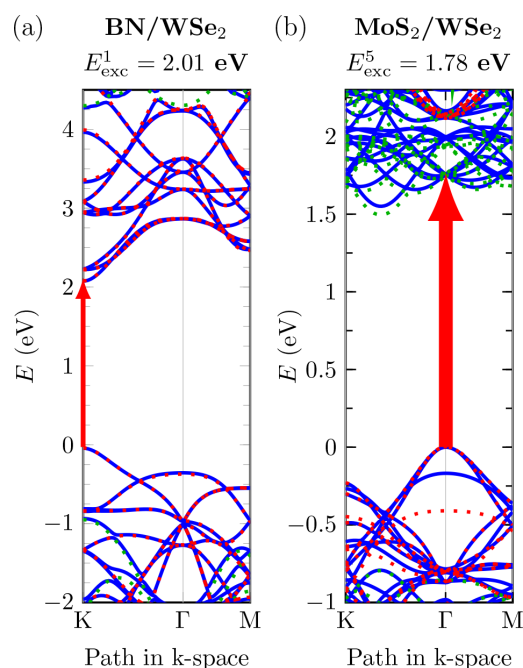


**Figure 6.** TD-HSE06 analysis of the first bright exciton (red arrows; see Figure 5 for details) on the electronic band structure (blue solid lines) for vdW heterostructure supercells of Figure 4. The PBE+$\Delta$ $b$ and structure is also added for each separated monolayer (dotted lines: red for WSe$_2$, green for (a) BN and (b) MoS$_2$). The Fermi energy is set to zero.

(staggered) alignment[10] at the interface. Figure 6b shows a distribution of the $A^S_{cvk}$ coefficients in k-space for the first bright exciton with energy $E^S_{exc}$: the only important part of the k-space is the valence band maximum region of the WSe$_2$ monolayer (labeled as $\Gamma$ in the Brillouin zone of the heterostructure). The corresponding region of the conduction band belongs to the MoS$_2$ monolayer as clearly labeled in Figure 6b using a red arrow representing the important electron−hole pair. The first bright exciton in MoS$_2$/WSe$_2$ is therefore the interlayer. The valence band is doubly degenerated at the $\Gamma$ point of Figure 6b, and the conduction band is sixtuply degenerated there, i.e., 12 important electron−hole pairs ($A^S_{cvk}$ coefficients) are represented by the large red arrow in Figure 6b.

## 3. CONCLUSIONS

We proved that the TD-HSE06 approach is capable of effectively predicting excitonic effects in the optical absorbance spectra, it is of good accuracy concerning optical gaps, and it is practicable also for vdW heterostructures containing various 2D materials. This approach does not require any preceding information about materials from experiments or higher theories, is of moderate computational cost, and can be therefore considered as a candidate for the high-throughput screening of optical properties of 2D materials. The TD-HSE06 method approximately includes all important physical effects needed for a detailed description and analysis of

excitonic wave functions, including distinction of intra- and interlayer excitons in vdW heterostructures.

## 4. COMPUTATIONAL DETAILS

All calculations were carried out using the Vienna ab initio simulation package (VASP)[39,40] based on plane waves and the projector augmented-wave technique.[41] The optimized geometries of the 2D systems originated from the C2DB database,[13] i.e., we used the height of the computational unit cell at least $\Delta z = 15$ Å (in perpendicular direction to 2D layers) to avoid spurious interaction between the layers. A larger height $\Delta z$ did not change the final TD-DFT spectra. The cutoff energy for the plane waves was set to 500 eV. The spin−orbit coupling was applied on the systems WSe$_2$, MoS$_2$, GaP, GaN, and AlN containing heavier elements. After computing the energy-dependent dielectric function,[33] we determined the actual optical absorbance[42] $A(E) = 1 - \exp(-\epsilon_2(E)E\Delta z/\hbar c)$, where $E$ is the energy of the photon, $\epsilon_2$ is the imaginary part of the dielectric function, $\hbar$ is the reduced Planck's constant, and $c$ is the speed of light. We used 8 occupied (o) and 16 unoccupied (u) states in TD-HSE06 calculations on the III−V group semiconductors (4o only in BN), 12o and 16u states for dichalcogenides, 8o and 10u states for CF, and 10o and 16u states for P$_4$. The polarization of the light was always parallel to the surfaces of the 2D systems. The computational setup and convergence parameters of our additional $G_0W_0$+BSE calculations are discussed in the Supporting Information (Figure S5). Heterostructures were generated using CellMatch software[37] from particular 2D materials. Subsequent optimiza-

tion was done using the PBE-D3 functional.[43] We used (26o,26u) states in combination with $12 \times 12 \times 1$ k-points and (63o,63u) states plus $6 \times 6 \times 1$ k-points in the final TD-HSE06 calculations on $BN/WSe_2$ and $MoS_2/WSe_2$, respectively.

## ■ ASSOCIATED CONTENT

### ⓈⒾ Supporting Information

The Supporting Information is available free of charge at https://pubs.acs.org/doi/10.1021/acs.jctc.0c00387.

Derivations of eqs 1 and 2, electronic band gaps, statistics on TD-HSE06 and GW+BSE optical gaps, convergence of absorbance spectra with respect to the number of k-points, and exciton analysis (PDF)

Data from a database corresponding to ref 13 of the main text (PDF)

## ■ AUTHOR INFORMATION

### Corresponding Author

František Karlický − *Department of Physics, Faculty of Science, University of Ostrava, 701 03 Ostrava, Czech Republic;* ⓞ orcid.org/0000-0002-2623-3991; Phone: +420 553 46 2155; Email: frantisek.karlicky@osu.cz

### Authors

Tomi Ketolainen − *Department of Physics, Faculty of Science, University of Ostrava, 701 03 Ostrava, Czech Republic*

Nikola Macháčová − *Department of Physics, Faculty of Science, University of Ostrava, 701 03 Ostrava, Czech Republic; Grammar School Matiční, 728 04 Ostrava, Czech Republic*

Complete contact information is available at:
https://pubs.acs.org/10.1021/acs.jctc.0c00387

### Notes

The authors declare no competing financial interest.

## ■ ACKNOWLEDGMENTS

## ■ REFERENCES

(1) Akinwande, D.; Petrone, N.; Hone, J. Two-dimensional flexible nanoelectronics. *Nat. Commun.* 2014, 5, 5678.

(2) Yu, K. J.; Yan, Z.; Han, M.; Rogers, J. A. Inorganic semiconducting materials for flexible and stretchable electronics. *npj Flexible Electron.* 2017, 1, 4.

(3) Geim, A. K.; Grigorieva, I. V. Van der Waals heterostructures. *Nature* 2013, 499, 419−425.

(4) Novoselov, K. S.; Mishchenko, A.; Carvalho, A.; Castro Neto, A. H. 2D materials and van der Waals heterostructures. *Science* 2016, 353, aac9439.

(5) Lee, C.-H.; Lee, G.-H.; van der Zande, A. M.; Chen, W.; Li, Y.; Han, M.; Cui, X.; Arefe, G.; Nuckolls, C.; Heinz, T. F.; Guo, J.; Hone, J.; Kim, P. Atomically thin p−n junctions with van der Waals heterointerfaces. *Nat. Nanotechnol.* 2014, 9, 676−681.

(6) Withers, F.; Del Pozo-Zamudio, O.; Mishchenko, A.; Rooney, A. P.; Gholinia, A.; Watanabe, K.; Taniguchi, T.; Haigh, S. J.; Geim, A. K.; Tartakovskii, A. I.; Novoselov, K. S. Light-emitting diodes by band-structure engineering in van der Waals heterostructures. *Nat. Mater.* 2015, 14, 301−306.

(7) Xia, W.; Dai, L.; Yu, P.; Tong, X.; Song, W.; Zhang, G.; Wang, Z. Recent progress in van der Waals heterojunctions. *Nanoscale* 2017, 9, 4324−4365.

(8) Cheng, R.; Wang, F.; Yin, L.; Wang, Z.; Wen, Y.; Shifa, T. A.; He, J. High-performance, multifunctional devices based on asymmetric van der Waals heterostructures. *Nat. Electron.* 2018, 1, 356−361.

(9) Karlický, F.; Turoň, J. Fluorographane $C_2FH$: Stable and wide band gap insulator with huge excitonic effect. *Carbon* 2018, 135, 134−144.

(10) Bernardi, M.; Ataca, C.; Palummo, M.; Grossman, J. C. Optical and Electronic Properties of Two-Dimensional Layered Materials. *Nanophotonics* 2017, 6, 479−493.

(11) Hedin, L. New Method for Calculating the One-Particle Green's Function with Application to the Electron-Gas Problem. *Phys. Rev.* 1965, 139, A796−A823.

(12) Salpeter, E. E.; Bethe, H. A. A Relativistic Equation for Bound-State Problems. *Phys. Rev.* 1951, 84, 1232.

(13) Haastrup, S.; Strange, M.; Pandey, M.; Deilmann, T.; Schmidt, P. S.; Hinsche, N. F.; Gjerding, M. N; Torelli, D.; Larsen, P. M; Riis-Jensen, A. C; Gath, J.; Jacobsen, K. W; Mortensen, J. J.; Olsen, T.; Thygesen, K. S The Computational 2D Materials Database: high-throughput modeling and discovery of atomically thin crystals. *2D Mater.* 2018, 5, 042002.

(14) Hirata, S.; Head-Gordon, M.; Bartlett, R. J. Configuration interaction singles, time-dependent Hartree-Fock, and time-dependent density functional theory for the electronic excited states of extended systems. *J. Chem. Phys.* 1999, 111, 10774−10786.

(15) Onida, G.; Reining, L.; Rubio, A. Electronic excitations: density-functional versus many-body Green's-function approaches. *Rev. Mod. Phys.* 2002, 74, 601−659.

(16) Izmaylov, A. F.; Scuseria, G. E. Why are time-dependent density functional theory excitations in solids equal to band structure energy gaps for semilocal functionals, and how does nonlocal Hartree-Fock-type exchange introduce excitonic effects? *J. Chem. Phys.* 2008, 129, 034101.

(17) Paier, J.; Marsman, M.; Kresse, G. Dielectric properties and excitons for extended systems from hybrid functionals. *Phys. Rev. B: Condens. Matter Mater. Phys.* 2008, 78, 121201R.

(18) Kolos, M.; Karlický, F. Accurate many-body calculation of electronic and optical band gap of bulk hexagonal boron nitride. *Phys. Chem. Chem. Phys.* 2019, 21, 3999−4005.

(19) Krukau, A. V.; Vydrov, O. A.; Izmaylov, A. F.; Scuseria, G. E. Influence of the exchange screening parameter on the performance of screened hybrid functionals. *J. Chem. Phys.* 2006, 125, 224106.

(20) Jamorski, C.; Casida, M. E.; Salahub, D. R. Dynamic polarizabilities and excitation spectra from a molecular implementation of time-dependent density-functional response theory: N2 as a case study. *J. Chem. Phys.* 1996, 104, 5134−5147.

(21) Yang, Z.-h.; Li, Y.; Ullrich, C. A. A minimal model for excitons within time-dependent density-functional theory. *J. Chem. Phys.* 2012, 137, 014513.

(22) Reining, L.; Olevano, V.; Rubio, A.; Onida, G. Excitonic Effects in Solids Described by Time-Dependent Density-Functional Theory. *Phys. Rev. Lett.* 2002, 88, 066404.

(23) Perdew, J. P.; Ernzerhof, M.; Burke, K. Rationale for mixing exact exchange with density functional approximations. *J. Chem. Phys.* 1996, 105, 9982−9985.

(24) Skone, J. H.; Govoni, M.; Galli, G. Self-consistent hybrid functional for condensed systems. *Phys. Rev. B: Condens. Matter Mater. Phys.* 2014, 89, 195112.

(25) Hüser, F.; Olsen, T.; Thygesen, K. S. How dielectric screening in two-dimensional crystals affects the convergence of excited-state calculations: Monolayer $MoS_2$. *Phys. Rev. B: Condens. Matter Mater. Phys.* 2013, 88, 245309.

(26) Perdew, J. P.; Burke, K.; Ernzerhof, M. Generalized Gradient Approximation Made Simple. *Phys. Rev. Lett.* 1996, 77, 3865−3868.

(27) Ramasubramaniam, A.; Wing, D.; Kronik, L. Transferable screened range-separated hybrids for layered materials: The cases of MoS$_2$ and h-BN. *Phys. Rev. Materials* **2019**, *3*, 084007.

(28) Wang, X.; Jones, A. M.; Seyler, K. L.; Tran, V.; Jia, Y.; Zhao, H.; Wang, H.; Yang, L.; Xu, X.; Xia, F. Highly anisotropic and robust excitons in monolayer black phosphorus. *Nat. Nanotechnol.* **2015**, *10*, 517−521.

(29) Li, Y.; Chernikov, A.; Zhang, X.; Rigosi, A.; Hill, H. M.; van der Zande, A. M.; Chenet, D. A.; Shih, E.-M.; Hone, J.; Heinz, T. F. Measurement of the optical dielectric function of monolayer transition-metal dichalcogenides: MoS$_2$, MoSe$_2$, WS$_2$, and WSe$_2$. *Phys. Rev. B: Condens. Matter Mater. Phys.* **2014**, *90*, 205422.

(30) Wang, B.; Sparks, J. R.; Gutierrez, H. R.; Okino, F.; Hao, Q.; Tang, Y.; Crespi, V. H.; Sofo, J. O.; Zhu, J. Photoluminescence from nanocrystalline graphite monofluoride. *Appl. Phys. Lett.* **2010**, *97*, 141915.

(31) Ba, K.; Jiang, W.; Cheng, J.; Bao, J.; Xuan, N.; Sun, Y.; Liu, B.; Xie, A.; Wu, S.; Sun, Z. Chemical and Bandgap Engineering in Monolayer Hexagonal Boron Nitride. *Sci. Rep.* **2017**, *7*, 45584.

(32) Karlický, F.; Otyepka, M. Band gaps and optical spectra from single- and double-layer fluorographene to graphite fluoride: many-body effects and excitonic states. *Ann. Phys. (Berlin, Ger.)* **2014**, *526*, 408−414.

(33) Gajdoš, M.; Hummer, K.; Kresse, G.; Furthmüller, J.; Bechstedt, F. Linear optical properties in the projector-augmented wave methodology. *Phys. Rev. B: Condens. Matter Mater. Phys.* **2006**, *73*, 045112.

(34) Sharma, S.; Dewhurst, J. K.; Sanna, A.; Gross, E. K. U. Bootstrap Approximation for the Exchange-Correlation Kernel of Time-Dependent Density-Functional Theory. *Phys. Rev. Lett.* **2011**, *107*, 186401.

(35) Trolle, M. L.; Pedersen, T. G.; Véniard, V. Model dielectric function for 2D semiconductors including substrate screening. *Sci. Rep.* **2017**, *7*, 39844.

(36) Thygesen, K. S. Calculating excitons, plasmons, and quasiparticles in 2D materials and van der Waals heterostructures. *2D Mater.* **2017**, *4*, 022004.

(37) Lazic, P. CellMatch: Combining two unit cells into a common supercell with minimal strain. *Comput. Phys. Commun.* **2015**, *197*, 324.

(38) Bokdam, M.; Sander, T.; Stroppa, A.; Picozzi, S.; Sarma, D. D.; Franchini, C.; Kresse, G. Role of Polar Phonons in the Photo Excited State of Metal Halide Perovskites. *Sci. Rep.* **2016**, *6*, 28618.

(39) Kresse, G.; Furthmüller, J. Efficiency of ab-initio total energy calculations for metals and semiconductors using a plane-wave basis set. *Comput. Mater. Sci.* **1996**, *6*, 15−50.

(40) Kresse, G.; Furthmüller, J. Efficient iterative schemes for ab initio total-energy calculations using a plane-wave basis set. *Phys. Rev. B: Condens. Matter Mater. Phys.* **1996**, *54*, 11169−11186.

(41) Blöchl, P. E. Projector augmented-wave method. *Phys. Rev. B: Condens. Matter Mater. Phys.* **1994**, *50*, 17953−17979.

(42) Bernardi, M.; Palummo, M.; Grossman, J. C. Extraordinary Sunlight Absorption and One Nanometer Thick Photovoltaics Using Two-Dimensional Monolayer Materials. *Nano Lett.* **2013**, *13*, 3664−3670.

(43) Grimme, S.; Antony, J.; Ehrlich, S.; Krieg, H. A consistent and accurate ab initio parametrization of density functional dispersion correction (DFT-D) for the 94 elements H-Pu. *J. Chem. Phys.* **2010**, *132*, 154104.

# Supplementary Material 4

# Fundamental gap of fluorographene by many-body GW and fixed-node diffusion Monte Carlo methods

Matúš Dubecký,[1,2,a)] František Karlický,[1,b)] Stanislav Minárik,[2] and Lubos Mitas[3]

### AFFILIATIONS

[1] Department of Physics, Faculty of Science, University of Ostrava, 30. dubna 22, 701 03 Ostrava, Czech Republic
[2] ATRI, Faculty of Materials Science and Technology in Trnava, Slovak University of Technology in Bratislava, J. Bottu 25, 917 24 Trnava, Slovakia
[3] Department of Physics and CHiPS, North Carolina State University, Raleigh, North Carolina 27695, USA

Note: This paper is part of the JCP Special Topic on Frontiers of Stochastic Electronic Structure Calculations.
a) Author to whom correspondence should be addressed: matus.dubecky@osu.cz
b) frantisek.karlicky@osu.cz

### ABSTRACT

Fluorographene (FG) is a promising graphene-derived material with a large bandgap. Currently existing predictions of its fundamental gap ($\Delta_f$) and optical gap ($\Delta_{opt}$) significantly vary when compared with experiment. We provide here an ultimate benchmark of $\Delta_f$ for FG by many-body GW and fixed-node diffusion Monte Carlo (FNDMC) methods. Both approaches independently arrive at $\Delta_f \approx 7.1 \pm 0.1$ eV. In addition, the Bethe–Salpeter equation enabled us to determine the first exciton binding energy, $E_b = 1.92$ eV. We also point to the possible misinterpretation problem of the results obtained for gaps of solids by FNDMC with single-reference trial wave functions of Bloch orbitals. We argue why instead of $\Delta_{opt}$, in the thermodynamic limit, such an approach results in energy differences that rather correspond to $\Delta_f$, and we also outline conditions when this case actually applies.

Published under license by AIP Publishing. https://doi.org/10.1063/5.0030952

## I. INTRODUCTION

Fluorographene[1,2] (FG) is a two-dimensional (2D) stoichiometric graphene derivative ($C_1F_1$) material exhibiting a large direct bandgap. This 2D material has attracted a significant amount of research activity over the past years due its promising physical and chemical properties.[3,4] Some of the key properties of interest include its large bandgap, dielectric characteristics, and potential surface physics and chemistry applications. Despite this attention, several crucial quantities that determine the electronic properties of FG has not been fully and unequivocally established. In the first place, this involves the fundamental and optical bandgaps as well as related derived properties.

Motivated by the existing discrepancies between theory and experiment[5–7] described below, we focus on fundamental electronic and optical FG properties. Among our key interests is the fundamental (energy) gap,

$$\Delta_f = I - A = E_{N-1} + E_{N+1} - 2E_N, \quad (1)$$

also interpreted as a quasiparticle gap (an energy to create a non-interacting electron–hole pair), where $I$ is a first ionization potential and $A$ is an electron affinity of a studied periodic solid, while $E_{N(\pm 1)}$ are total energies of $N(\pm 1)$-electron ground states. Another quantity that is important in practical applications is an optical gap,

$$\Delta_{opt} = E_N^* - E_N, \quad (2)$$

where $E_N^*$ is total energy of the first optically active excited state. The optically accessible $\Delta_{opt}$ state is, by definition, lower in energy than $\Delta_f$ that corresponds to the continuum limit of the exciton series, and the difference between the two is referred to as the exciton binding energy,

$$E_b = \Delta_f - \Delta_{opt}, \quad (3)$$

which may range from a few meV in bulk solid-state semiconductors such as Si to a few eV in materials exhibiting strong excitonic effects, such as gapped 2D nanomaterials.[8,9]

At present, the onset of the FG optical absorption spectrum, $\Delta_{opt}$, has been estimated by experiments to lie between 3 eV and 5 eV.[1,10–12] This range is simply too large to provide a reliable information for applications as well as for cross-validating existing theoretical estimations. On the theoretical side, $\Delta_f$ of FG predicted by the many-body perturbational GW approximation for the electron self-energy[13] points to the interval of 7 eV–8 eV,[5,7,14] which indicates the presence of strong excitonic effects. Indeed, the Bethe–Salpeter equation (BSE) building upon the GW level of theory for the quasiparticle spectrum confirmed that $E_b$ of FG is quite generally close to 2 eV,[5,7,14] irrespective of input sets of orbitals and technical parameters. However, the best available theoretical estimates of $\Delta_{opt}$ for FG [Eq. (3)] lead to a range ~5 eV to 6 eV, i.e., they still embody a significant uncertainty that complicates a reliable cross-check with respect to the available experiments.[5,6]

The main goal of the present study is to establish a reference quality estimation of $\Delta_f$ for a freestanding FG free of defects at a desired benchmark accuracy level of ~0.1 eV. We employ two independent state-of-the-art and complementary many-body approaches,[15] namely, GW perturbation theory pushed to its limits and real-space continuum fixed-node diffusion Monte Carlo (FNDMC) method that gained momentum in (correlated) materials research in past years.[16–21] In order to settle the exciton binding energy $E_b$ as well, we build upon our high accuracy GW inputs and we solve the Bethe–Salpeter equation (BSE) so as to settle the value of $\Delta_{opt}$ at the mentioned accuracy level.

An important methodological part of this study is a discussion of an option to extract $\Delta_f$ estimates in solids (or periodic systems in general) from energy differences of neutral state total energies. The total energies are provided by FNDMC using single-reference/single-determinant trial wave functions, $\Psi^T$, with the symmetry of the periodic (super)cells Bloch orbitals. We present arguments that using periodic Bloch orbitals with built-in symmetries of ideal crystal structure under consideration very significantly restrict the possibilities for the occurrence of significant, localized excitonic effects. The basic argument is straightforward. The wave function built from Bloch orbitals is translation invariant. It is well-known that the corresponding nodal surface share the same property.[22,23] However, the localized exciton with significant binding would nominally break this translation symmetry. The nodal surface is simply too restrictive[24] for a significant charge restructuring that would enable appreciable electron–hole interactions, i.e., $E_b = 0$ in the thermodynamic limit. In such a situation, the energy difference of Eq. (2) that is formally equivalent to $\Delta_{opt}^{FN}$ nominally corresponds to $\Delta_f^{FN}$ [by Eq. (3)]. That is, in the thermodynamic limit, we arrive at an expression

$$\Delta_f^{FN} = \Delta_{opt}^{FN} \tag{4}$$

that can be realized in calculations by constructing proper symmetry $\Psi^T$ (see Sec. II C for details). Note that this is, in particular, pertinent to materials with large values of dielectric constants that also naturally suppress the formation of excitons. Here, we show that a similar

conclusion can be reached also in the system where significant excitonic effects are present. Note that we emphasize the fact that the system is neutral. This simplifies the treatment of the finite size effects as well as the influence of charges that could decrease symmetries of the considered state and further complicate reliable estimations of the total energies that are consistent in the thermodynamical limit.[25] We also specify the limits when the equality above can become problematic, and we offer some insight into how this can be potentially treated. Experience[26–30] and rigorous arguments[31] suggest that the FNDMC method provides unique information about bandgaps of periodic systems in a fully many-body framework, which is typically out of range of other correlated wave function methods. In most cases, the results are of benchmark quality so that we can write

$$\Delta_f^{FN} \approx \Delta_f, \tag{5}$$

and existing imperfections in this regard can be ascribed to current technical limitations, for example, sizes of supercells that truly reach the scaling regime with respect to the thermodynamic limit. The key FNDMC ingredients seem to be its following of proper constraints on $E_N$ as a continuous function of $N$ expected for an exact electronic structure theory,[32–34] linearity of $E_N$, and discontinuity of $\frac{\partial E_N}{\partial N}$ at integer $N$ values.[31]

Equation (4) resembles a similar (but not quite the same) result derived for Kohn–Sham (KS) density functional theory (DFT) of solids,[35]

$$\Delta_f^{DFT} = g^{DFT}, \tag{6}$$

where $g^{DFT}$ is a one-electron KS valence band maximum (VBM)—conduction band minimum (CBM) gap. This equation holds for generic exchange-correlation (xc) functionals missing $E_N$ derivative discontinuity when continuously crossing integer $N$.[35] The physics and accuracy of these two approximations to $\Delta_f$ [Eq. (4) vs Eq. (6)], however, fundamentally differ [see Sec. II C for a rigorous derivation of Eq. (4) valid for FNDMC; see Refs. 35 and 36 for a discussion of KS gaps in solids].

This paper is organized as follows: Sec. II introduces details on the used FG structure model (Sec. II A), GW and BSE setup (Sec. II B), FNDMC and promotion approach (Sec. II C), and quantum Monte Carlo (QMC) simulation setup used in production calculations (Sec. II D). The individual results for GW/BSE and FNDMC are presented in Secs. III and IV, respectively. Discussion of the agreement of methods vs each other in the context of experiment (Sec. IV) is followed by conclusions (Sec. V).

## II. METHODS

### A. Fluorographene model

The unit cell of FG containing four atoms, $C_2F_2$, was assumed to adopt a chair-like conformation shown to be the most stable FG structure.[3] Input geometrical parameters of FG were obtained by Perdew, Burke, and Ernzerhof (PBE) optimization from our previous studies[5,14] and were as follows: a lattice constant of $a$ = 2.6074 Å, a C–C bond length of 1.5825 Å, a C–F bond length of 1.3833 Å, and a C–C–C bond angle of 110.9°. Reported DFT gaps have been only marginally dependent on minor FG structure variations[37] (as seen in structures optimized with various DFT functionals).[5,14] FG is a direct material with the electronic

bandgap at the $\Gamma$ point (for more details on the band structure, see Sec. III).

### B. GW and BSE settings

The Vienna *ab initio* simulation package (VASP)[38] implementing the projector augmented-wave (PAW) method[38,39] was used in all GW, BSE, and underlying DFT calculations. Since these calculations serve here as the cross-validating reference, it is worth noting that the VASP plane wave calculations based on PAWs can be considered as highly accurate, as shown in Ref. 40 using the all-electron full-potential linearized–augmented plane waves (FLAPW) method, which is regarded as an established reference method in condensed matter physics.

We have used the GW approximation (where $G$ is the Green's function and $W$ is the screened Coulomb potential) for the electron self-energy $\Sigma$ with input orbitals $\phi_{nk}(\mathbf{r})$ from DFT and Perdew, Burke, and Ernzerhof (PBE) xc functional[41] electronic structure calculations. Therefore, the quasi-particle energies $\epsilon_{nk}^{\mathrm{GW}}$ are calculated as first-order corrections to the DFT single-particle energies $\epsilon_{nk}$,

$$\epsilon_{nk}^{\mathrm{GW}} = \epsilon_{nk} + Z_{nk}\mathrm{Re}\big[\langle\phi_{nk}|T + V_{\mathrm{n-e}} + V_{\mathrm{H}} + \Sigma(G, W; \epsilon_{nk})|\phi_{nk}\rangle - \epsilon_{nk}\big], \tag{7}$$

and the quasiparticle gap as $\Delta_{\mathrm{f}}^{\mathrm{GW}} = \epsilon_{\mathrm{CBM}}^{\mathrm{GW}} - \epsilon_{\mathrm{VBM}}^{\mathrm{GW}}$ [analogous to Eq. (6)], where $Z$ is the normalization factor,[42] $T$ is the kinetic energy operator, $V_{\mathrm{n-e}}$ is the potential of the nuclei, and $V_{\mathrm{H}}$ is the Hartree potential. Recently, it was shown on layered BN,[43] monolayer $MoS_2$,[44] and bulk ZnO[45] that well converged GW with starting orbitals from PBE agrees very well with experiment and that there is no necessity to use higher level of GW theory by iterating $G$ or $W$. In order to reach the desired accuracy of our calculations, we used GW set of PAWs, cut-off energy $E_{\mathrm{cut}} = 600$ eV, and strict electronic step convergence criterion ($1 \times 10^{-7}$ eV). Convergence of the critical parameters (plane wave cutoff, number of bands considered in GW, size of the vacuum region in the simulation cell, and k-point grid) is elaborated in more detail in Sec. III.

For insulating FG, the materials with completely unoccupied conduction bands and occupied valence bands ($c$ and $v$ indices, respectively), the Bethe–Salpeter equation can be rewritten as the eigenvalue problem[46–48]

$$(\epsilon_{ck}^{\mathrm{GW}} - \epsilon_{vk}^{\mathrm{GW}})A_{cvk}^{\lambda} + \sum_{c'v'k'}\big[2\langle\phi_{ck}\phi_{vk}|v|\phi_{c'k'}\phi_{v'k'}\rangle$$
$$- \langle\phi_{ck}\phi_{c'k'}|W|\phi_{vk}\phi_{v'k'}\rangle\big]A_{c'v'k'}^{\lambda} = E_{\mathrm{exc}}^{\lambda}A_{cvk}^{\lambda},$$

where $v$ is the Coulomb kernel $1/|\mathbf{r} - \mathbf{r}'|$, the eigenvectors $A_{cvk}^{\lambda}$ correspond to the amplitudes of free electron–hole pair configurations composed of electron states $|\phi_{ck}\rangle$ and hole states $|\phi_{vk}\rangle$, and the eigenenergies $E_{\mathrm{exc}}^{\lambda}$ correspond to the excitation energies (with $\Delta_{\mathrm{opt}}^{\mathrm{BSE}} \equiv E_{\mathrm{exc}}^{\lambda=1}$).

### C. FNDMC and promotion approach

FNDMC is a stochastic many-body real-space projector *ab initio* method[49–52] that can be effectively applied to systems with tens to hundreds of valence electrons. Therefore, it has been gaining traction in electronic structure calculations of real solids due to its accuracy, scalability, and versatility.[26,27,29,53–58] For a Hamiltonian $\hat{H}$, it projects out the most optimal ground state within the fixed-node

constraint, which has non-zero overlap with the antisymmetric trial state $\Psi^{\mathrm{T}}$. Using imaginary time $\tau$, we can write

$$\Psi^{\mathrm{FN}} = \lim_{\tau\to\infty}\exp\big[-\tau(\hat{H} - E_T)\big]\Psi^{\mathrm{T}}, \tag{8}$$

where $E_T$ is an offset energy that keeps the norm of $\Psi^{\mathrm{FN}}$ asymptotically constant. The superscript FN indicates that $\Psi^{\mathrm{FN}}$ and $\Psi^{\mathrm{T}}$ share the same fixed node $F = \{\mathbf{R}; \Psi(\mathbf{R}) = 0\}$, where $\mathbf{R}$ is an electron position vector. FNDMC simulation provides a stochastic estimation of the total energy expectation value, $E^{\mathrm{FN}} \pm \frac{\sigma}{\sqrt{K}}$, where $\sigma$ is a local energy $[E_{\mathrm{L}}(\mathbf{R}) = \frac{\hat{H}\Psi^{\mathrm{T}}(\mathbf{R})}{\Psi^{\mathrm{T}}(\mathbf{R})}]$ dispersion and $K$ is the number of independent samples. $E^{\mathrm{FN}}$ is an upper bound to the exact ground state[59] energy of $\hat{H}$ within the same symmetry class as $\Psi^{\mathrm{T}}$, thus enabling the study of excited states by picking $\Psi^{\mathrm{T}}$ orthogonal to the lower states.[60–63] The related FN bias grows quadratically with the increasing inaccuracy of $F$.[52] Viable sophistication in constructions of trial states is used to marginalize the FN bias as much as possible.[64,65] Practical FNDMC computations that are feasible for large systems nevertheless require computationally efficient *Ansätze*, such as the widely used Slater–Jastrow trial wave functions,[66] $\Psi^{\mathrm{T}} = \Psi^{\mathrm{S}}J$. Here, $\Psi_{\mathrm{S}}$ is a single-reference Slater determinant part and $J$ is an explicitly correlated Jastrow term[67] that is appropriately parametrized. The trial wave function is variationally refined, and then, it serves as a starting point for the FNDMC calculation.

In periodic systems, it is a usual practice to pick $\Psi^{\mathrm{S}}$ of Bloch orbitals[20,25,26,68] for a ground state and then use the same orbital set for a construction of an electron-promoted state,

$$\Psi_N^{\mathrm{S}*} = a_{\mathrm{CBM}}^{\dagger}a_{\mathrm{VBM}}\Psi_N^{\mathrm{S}}, \tag{9}$$

and charged states,

$$\Psi_{N+1}^{\mathrm{S}} = a_{\mathrm{CBM}}^{\dagger}\Psi_N^{\mathrm{S}}, \tag{10}$$

$$\Psi_{N-1}^{\mathrm{S}} = a_{\mathrm{VBM}}\Psi_N^{\mathrm{S}}, \tag{11}$$

where $a$ and $a^{\dagger}$ are usual creation and annihilation operators in second quantization of electrons in VBM and CBM, respectively. Note that in the thermodynamic limit, orbital relaxation is irrelevant.[69] Clearly, a one-electron perturbation (electron addition or removal) of an infinite crystal is negligible so that the $i$th orbital in $N$ and $N \pm 1$-electron system is indistinguishable, $\phi_i(N \pm 1) \approx \phi_i(N)$. We continue with a textbook-level derivation of symbolic expressions leading to $\Delta_{\mathrm{f}}$ and $\Delta_{\mathrm{opt}}$ so that the explicit difference is apparent [Eq. (3)] in order to stress that in special cases, theoretical estimates of these quantities may be nominally equivalent.

Consider a system of $N$ electrons where two electrons in two unrelaxed orbitals, $\phi_1(\mathbf{r})$ and $\phi_2(\mathbf{r})$ (single doubly occupied and single unoccupied orbital, e.g., VBM and CBM), will be considered explicitly. The remaining unspecified part (other $N - 2$ electrons, external potentials, etc.) is denoted as "rest" ($R$). The total ground state energy of a neutral state in one-determinant approximation with two electrons in $\phi_1$ amounts to[70]

$$\tilde{E}_N = 2\epsilon_1 + J_{11} + 2J_{1R} - 2K_{1R} + E_R, \tag{12}$$

where $\epsilon_i$ is an energy of an electron in orbital $i$, $E_R$ is a total energy of a subsystem $R$, and $J_{ij}$ ($K_{ij}$) is a Coulomb (exchange) interaction of electrons in orbitals $\phi_i(\mathbf{r})$ and $\phi_j(\mathbf{r})$, respectively, or an interaction of

an electron in orbital $\phi_i(\mathbf{r})$ with $R$ (tilde indicates an approximation). The total energy of a system where one of the electrons has been "promoted" from $\phi_1$ to $\phi_2$ amounts to

$$\tilde{E}_N^* = \epsilon_1 + \epsilon_2 + J_{12} + J_{1R} + J_{2R} - K_{1R} - K_{2R} + E_R. \qquad (13)$$

An optical gap approximation follows immediately [Eq. (2)]

$$\tilde{\Delta}_{\text{opt}} = \epsilon_2 - \epsilon_1 + J_{12} - J_{11} + J_{2R} - J_{1R} + K_{1R} - K_{2R}. \qquad (14)$$

The total energy of an anion state with $N + 1$ electrons (one electron added to $\phi_2$) may be expressed as

$$\tilde{E}_{N+1} = 2\epsilon_1 + \epsilon_2 + J_{11} + 2J_{12} - K_{12} + 2J_{1R} + J_{2R} - 2K_{1R} - K_{2R} + E_R, \quad (15)$$

whereas the total energy of a cation state with $N - 1$ electrons (single electron removed from $\phi_1$) amounts to

$$\tilde{E}_{N-1} = \epsilon_1 + J_{1R} - K_{1R} + E_R. \qquad (16)$$

The corresponding ionization potential and electron affinity $\tilde{I}$ and $\tilde{A}$ read

$$\begin{aligned} \tilde{I} &= \tilde{E}_{N-1} - \tilde{E}_N \\ &= -(\epsilon_1 + J_{11} + J_{1R} - K_{1R}), \end{aligned} \qquad (17)$$

$$\begin{aligned} \tilde{A} &= \tilde{E}_N - \tilde{E}_{N+1} \\ &= -(\epsilon_2 + 2J_{12} - K_{12} + J_{2R} - K_{2R}), \end{aligned} \qquad (18)$$

respectively, enabling us to express

$$\begin{aligned} \tilde{\Delta}_f &= \tilde{I} - \tilde{A} \\ &= \epsilon_2 - \epsilon_1 + 2J_{12} - J_{11} - K_{12} + J_{2R} - J_{1R} + K_{1R} - K_{2R}. \end{aligned} \qquad (19)$$

Finally, we arrive at the desired explicit approximation to the exciton binding energy [using Eqs. (3), (14), and (19)],

$$\tilde{E}_b = J_{12} - K_{12}, \qquad (20)$$

that is independent of $R$. It depends on the initially selected orbitals occupied by the explicitly considered electrons. $J_{12}$ is a Coulomb repulsion of the electrons in orbitals $\phi_1$ and $\phi_2$, respectively. Since $\phi_1$ is also a hole orbital left behind by the promoted electron, energy $-J_{12}$ can be interpreted as an electron–hole attraction (in electron–hole picture, $\tilde{E}_b = K_{12} - J_{12}$). $K_{12}$ is an exchange energy that can be alternatively computed from the total energy difference involving triplet (spin–flip) promotion

$$\tilde{E}_N^{\text{T}} = \epsilon_1 + \epsilon_2 + J_{12} - K_{12} + J_{1R} + J_{2R} - K_{1R} - K_{2R} + E_R, \qquad (21)$$

leading to

$$K_{12} = \tilde{E}_N^* - \tilde{E}_N^{\text{T}}. \qquad (22)$$

Note that the expression of Eq. (20) is valid in a system of arbitrary size, including the thermodynamic limit since in a unit cell containing $N$ electrons, $N - 2$ of them are swept into $R$. In the same way, for supercells containing $\kappa$ unit cells (used to approach the thermodynamic limit by taking $\kappa \to \infty$), $R$ contains $\kappa N - 2$ electrons.

In addition, Eq. (20), based on one-determinant total energies, is a very accurate approximation of the exact $E_b$ in systems with a large number of electrons $N$ approaching the size-extensive limit, if the corresponding exact wave functions are all dominated by the

one-determinant and the selected orbitals are eigenstates of the one-particle reduced density matrix of the exact solution. In such a case, one can observe that analogous derivation using

$$\begin{aligned} E_N &= \tilde{E}_N + C_N, \\ E_N^* &= \tilde{E}_N^* + C_N^*, \\ E_{N+1} &= \tilde{E}_{N+1} + C_{N+1}, \\ E_{N-1} &= \tilde{E}_{N-1} + C_{N-1}, \end{aligned} \qquad (23)$$

where $C_N$, etc., denote the correlation energies missing at the corresponding mean-field level, will result in

$$E_b = J_{12} - K_{12} + C, \qquad (24)$$

where $C = C_{N-1} + C_{N+1} - C_N - C_N^*$. In the size-extensive limit, it follows that

$$\frac{C_N}{N} = \frac{C_{N\pm 1}}{N \pm 1} \equiv c, \qquad (25)$$

and, together with an assumption $C_N \approx C_N^*$ that is reasonable for large $N$, that implies

$$C = (N - 1)c + (N + 1)c - 2Nc = 0. \qquad (26)$$

Therefore, the correlation energy contributions largely cancel out. We can therefore state that to a very good approximation in systems with a large $N$,

$$\tilde{E}_b \approx E_b. \qquad (27)$$

Equation (20) is therefore very relevant for a vast class of orbital-based methods, including many-body approaches such as FNDMC. This result reaches beyond just formal importance. One can check that the FNDMC correlation energy converges rapidly with respect to the supercell size, reaching a constant already for sizes of practical relevance such as 2D ~4 × 4, as has been observed in phosphorene.[20]

Before focusing on FNDMC, we are interested in general $\tilde{E}_b$ of an extended system. Let us identify three possible scenarios with respect to the nature of the chosen orbitals $\phi_1$ and $\phi_2$:

(i)   Both orbitals are of Bloch type (e.g., VBM and CBM).
(ii)  One of the orbitals is of Bloch type, whereas the other one is localized (translation symmetry is broken).
(iii) Both orbitals are localized.

For the scenarios (i) and (ii), it is possible to demonstrate that

$$\lim_{\kappa \to \infty} J_{12}(\kappa) = 0 \qquad (28)$$

and

$$\lim_{\kappa \to \infty} K_{12}(\kappa) = 0 \qquad (29)$$

so that $\tilde{E}_b = 0$, whereas for the scenario (iii), one gets finite non-zero results in the $\kappa \to \infty$ limit, allowing also nonzero $\tilde{E}_b$. An important and perhaps obvious conclusion is that the result is orbital dependent. If any of the orbitals is a Bloch state obeying the crystal translation symmetry, in the thermodynamic limit, an electron and hole effectively do not interact, $\tilde{E}_b = 0$, and $\tilde{\Delta}_f = \tilde{\Delta}_{\text{opt}}$.

As an example, let us sketch the critical steps of the proof for Eq. (28) in 2D and scenario (i). Let $\phi_i(\tilde{r}_1)$ and $\phi_j(\tilde{r}_2)$ be one-particle Bloch orbitals, expanded in a plane wave basis set,

$$\phi_i(\vec{r}_1) = \frac{1}{\kappa L} \sum_{\vec{k}=1}^{\infty} \{ a_{\vec{k}} e^{i\vec{k}\cdot\vec{r}_1} + a_{\vec{k}}^* e^{-i\vec{k}\cdot\vec{r}_1} \}, \tag{30}$$

$$\phi_j(\vec{r}_2) = \frac{1}{\kappa L} \sum_{\vec{w}=1}^{\infty} \{ a_{\vec{w}} e^{i\vec{w}\cdot\vec{r}_2} + a_{\vec{w}}^* e^{-i\vec{w}\cdot\vec{r}_2} \}, \tag{31}$$

normalized on region $\Sigma = (\kappa L) \times (\kappa L)$, where $\kappa$ is an integer, $\vec{k} = \frac{\pi}{\kappa L}[n_1, n_2]$, and $\vec{w} = \frac{\pi}{\kappa L}[m_1, m_2]$, where $n_1$, $n_2$, $m_1$, and $m_2$ are integers, respectively, and $L$ is a constant unit cell size. The Coulomb integral of our interest may be expressed as

$$J_{ij}(\kappa) = \int_{\Sigma} \int_{\Sigma} d\vec{r}_1 d\vec{r}_2 \frac{|\phi_i(\vec{r}_1)|^2 |\phi_j(\vec{r}_2)|^2}{|\vec{r}_1 - \vec{r}_2|}. \tag{32}$$

Substituting Eqs. (30) and (31) into (32) leads to an expression that contains the integrals of type

$$\int_{\Sigma} \int_{\Sigma} d\vec{r}_1 d\vec{r}_2 \frac{e^{i\vec{\lambda}\cdot\vec{r}_1} e^{i\vec{\mu}\cdot\vec{r}_2}}{|\vec{r}_1 - \vec{r}_2|} \approx (\kappa L)^3 \left( \sum_{m,l} W_{ml}^{\vec{\lambda}\vec{\mu}} + \ln|\kappa L| \sum_{m,l} F_{ml}^{\vec{\lambda}\vec{\mu}} \right) \equiv Q_{\vec{\lambda}\vec{\mu}}, \tag{33}$$

where $\vec{\lambda} = \vec{k} + \vec{w}$, $\vec{\mu} = \vec{k}' + \vec{w}'$ and $W_{ml}^{\vec{\lambda}\vec{\mu}}$ and $F_{ml}^{\vec{\lambda}\vec{\mu}}$ are expansion coefficients. The solution leads to

$$J_{12}(\kappa) \approx \frac{1}{(\kappa L)^4} \sum_{\vec{k}\vec{k}'\vec{w}\vec{w}'} A_{\vec{k}\vec{k}'\vec{w}\vec{w}'} Q_{\vec{k}\vec{k}'\vec{w}\vec{w}'}, \tag{34}$$

where $A_{\vec{k}\vec{k}'\vec{w}\vec{w}'}$ is an expansion coefficient independent of $\kappa$ (see the supplementary material for more details). The limit of our interest [Eq. (28)] clearly vanishes, since the logarithmic singularity from the Coulomb interaction operator in $Q$ is suppressed by the normalization factor. Similar conclusions hold for the case of $K_{12}$ [Eq. (29)]. In addition, both conclusions were also verified analytically for 1D and scenario (i) (see the supplementary material for details) and numerically (using dense real-space grids) for scenarios (i) and (ii) with a few specific cases of sine orbitals in 1D and 2D.

We can finally discuss consequences of the presented conclusions for FNDMC simulations using the $\Psi^T$ determinant constructed of Bloch one-particle orbitals in combination with Eq. (2). What do we obtain from a single-electron promotion approach within the commonly used single-reference (single-determinant) FNDMC?

As mentioned above, FNDMC projects out an exact ground state consistent with the nodal boundary condition fixed by $F(\Psi^T)$, which enforces antisymmetry and periodicity of the simulated state $\Psi^{FN}$ [Eq. (8)]. In this way, $F$ imposes a hard bound for the lowering of FNDMC energy in such calculation. The orbital promotion leads to another $F$ with a different shape if the state is of different symmetry, but still translation invariant, and therefore, it locks in corresponding bound for the excitation. In case the excited state symmetry is the same as that of the ground state and there is no degeneracy, the same holds to a significant degree since any overlap is usually negligible, and the systematic errors are dominated by the fixed-node bias. It is also known that if there is a degeneracy in excited orbitals, this might not hold, but this is a different issue, which has little to do with excitonic effects considered here. Clearly, in a system where an exact exciton many-body state $\Psi_N^{exciton}$ is an eigenstate of $\hat{H}$, for $F(\Psi_N^{T*})$ based on Eq. (9) where VBM and CBM are Bloch states obeying the lattice translation symmetry, we have

$\langle \Psi_N^{T*} | \Psi_N^{exciton} \rangle \approx 0$. Therefore, FNDMC projects out the total energy solution that corresponds to the promotion in the considered band structure. Of course, this would change if the promotion would be built from orbitals that would enable translation symmetry breaking so as to approximate the electron–hole pair (for a broken-symmetry state, $\langle \Psi_N^{T*,bs} | \Psi_N^{exciton} \rangle \neq 0$). There is an additional issue of finite sizes that forces the electron and the hole to be "closer" than in the true thermodynamic limit. However, this does not change the above argument based on the fixed boundary stemming from the nodal surface. It would affect only the Mott–Wannier limit where the exciton is so delocalized that within the given supercell, it appears as translation invariant; however, the corresponding effects are tiny and usually fall below the error bars.[71]

Let us partially summarize possible outcomes of the single-reference single-electron promotion FNDMC calculations. For molecules, energy differences based on the described promotion approach are expected to approximate optical transition energies since all involved orbitals are localized in space and the translation symmetry is absent.[15] Any inaccuracies originate from mundane issues such as virtual orbital imperfections, energetic ordering, and amount of multi-reference mixing. At least partial charge restructuring is common since the system has no boundary, and the charge can shift from inside to outside and vice versa as the energetics dictates, to the extent that the nodal surface allows it.[72] This is straightforward to check in anions[73] where it is common that the tails of the trial wave functions might not be correct but can be repaired by the FNDMC solution. As we argued already before, in the low density limit, the fixed-node errors become less significant and provide exceedingly accurate energy differences.[57]

In solids, nodal surfaces of trial wave functions with Bloch orbitals impose new restriction[24] so that the promotion into another Bloch orbital will nominally result in $\Delta_f^{FN}$. At the same time, we have to clearly state that this is not universal. Let us consider cases where at least part of the orbitals (occupied and virtuals) remain localized on constituents even in the thermodynamic limit (molecular crystal) or where periodicity is broken to a significant extent (defects, impurities, etc.). In such systems, the promotion FNDMC method result will be somewhere between the corresponding optical and fundamental gaps. For example, in van der Waals molecular crystals, the periodicity affects the ground states only marginally, and even the lowest excitations might not be changed too significantly. Therefore, this would apply provided that (i) there is "enough space" for local charge restructuring similar to an isolated molecule, and (ii) that there are low-lying excited orbitals that mimic the isolated molecular states very closely even within the Bloch periodicity. In such cases, one can expect that the resulting energy difference would be a better approximation to the optical transition(s), i.e., $\Delta_{opt}^{FN}$ will result. It is therefore important to probe for the character of corresponding states in order to find out the relevant limit.

In the case of "in between" situations, one has to work on the trial wave function to build better approximation to one or both limits, and the interpretation of the results has to be verified accordingly. Note that one can obtain some indications, although for the time being a bit crude, when the band limit applies. For example, in another project (to be published elsewhere), the band energies/gaps do not change regardless of how the promotion is built in the spin

symmetry channels. In particular, in the Si solid, one can check that the promotion energies remain essentially constant for the following three types of trial wave functions:[74]

(i) promotion of an electron in a given spin channel (i.e., really a mix of true singlet and triplet states),

(ii) promotion of an electron with simultaneous spin flip (true triplet state), and

(iii) two-determinant single-electron excitation in the proper singlet state (i.e., open-shell singlet).

Some of such tests have been carried out also in the present calculations, as explained in Sec. IV. These results indicate that the exchange and correlation effects are indeed delocalized, and the Bloch periodicity provides essentially a full lock on the corresponding energy difference. Note that the electron correlation still matters since the obtained bandgap differs from the mean-field. Although this is most probably far from being universal and it requires further study on more systems, it provides an illustration that the presented analysis above is essentially correct. It is also intuitively clear that in a contrasting case of an isolated molecule, reasonably localized singlet and triplet excitations would differ rather significantly.

It is highly desirable to reach beyond the current status and to build accurate trial wave functions for both limits. At present, however, we still encounter significant difficulties in achieving such a goal. The complications are mostly on the technical side due to restricted availability of efficient tools for multi-reference trial functions in periodic setting. This can change in the near future so that this is clearly a promising subject for further research.

### D. QMC simulation setup

The QMC total energy computations consisted of the commonly used stages:[20,75]

(i) DFT one-particle Bloch orbitals were obtained using Gaussian G09[76] or Quantum Espresso (QE),[77] DFT codes with PBE or PBE0[78] xc functionals, and aug-VTZ basis[79] or plane wave basis set (a kinetic energy plane wave cutoff of 100 Ry), respectively. Brillouin zone sampling meshes ranged from $2 \times 2 \times 1$ to $5 \times 5 \times 1$, consistent with the target real-space supercell sizes used within real-space $\Gamma$-point QMC computations (direct $\Gamma - \Gamma$ transition). All computations used norm-conserving Burkatzki–Filippi–Dolg (BFD) effective core potentials (ECPs).[79]

(ii) Variational Monte Carlo (VMC) optimizations of the parametric Jastrow explicit correlation terms entering $\Psi^{\mathrm{T}}$ used two-particle (electron–electron and electron–nucleus) terms and $2 \times 2$ supercell (QWalk code[80]) or up to three-particle terms (electron–electron, electron–nucleus, and electron–electron–nucleus) within the $3 \times 3$ supercell (QMCPACK[81]).

(iii) FNDMC total energies, corresponding to $\Psi^{\mathrm{T}}$ of ground-states and single-electron VBM-CBM-promoted states, were obtained from supercells containing $\kappa = 4, 9, 16$ (QWalk) or $\kappa = 9, 16, 25$ (QMCPACK) unit cells with VMC-optimized ground-state Jastrows, a time step of 0.01 a.u., and T-moves approximation for the treatment of ECPs.[82]

(iv) Finite size effects were suppressed by linear extrapolations of the series of production results to the thermodynamic limit by taking $1/\kappa \to 0$, where $\kappa$ is the total number of unit cells

present in the simulation supercell. We have verified that misfit of the ground state and promoted state FNDMC total energies normalized to $\kappa$ amounts to 0.002 a.u. in thermodynamic limit so that the total energy consistency condition was not enforced.[25]

The computations of the two sets of the FNDMC results for a series of FG supercells using different codes and setups, QWalk (Gaussian basis sets, Coulomb interaction, two-particle Jastrows, and a vacuum size of 40 Å) and QMCPACK [plane waves, model periodic Coulomb (MPC) interaction,[83] three-particle Jastrows, and a vacuum size of 20 Å], show consistency over the overlapping system sizes ($3 \times 3$ and $4 \times 4$). Therefore, we rule out some of the possible method biases: one-particle basis set bias, slab-model vacuum size, and modified electron interaction.

Additional tests confirming robustness of the chosen production QMC setup for total energy differences were performed as well. Time step error tested by considering 0.01 a.u. vs 0.005 a.u. resulted in a difference of the order of error bars $\sim 0.1 \pm 0.1$ eV in energy differences. Shape effects of one-particle orbitals were ruled out by considering the hybrid xc functional (PBE vs PBE0 in a $4 \times 4$ supercell within QMCPACK), and the results were comparable within the error bar ($6.11 \pm 0.05$ eV vs $6.03 \pm 0.06$ eV). Similarly, CBM orbital replacement by the equivalent orbital from DFT computation using triplet spin multiplicity resulted in no detectable bias within FNDMC energy differences. BFD ECPs transferability was checked vs a new generation of correlation-consistent ccECPs:[84] in a $4 \times 4$ supercell, the promotion energy differences were indistinguishable within the statistical error ($6.11 \pm 0.05$ eV vs $6.12 \pm 0.1$ eV). The Ewald summation consistency test for our 2D FG slab model was tested by considering slab-modified Ewald interaction (Yeh–Berkowitz[85]) within the appropriately adapted QWalk code; no deviation from to the usual 3D Ewald formulation was observed for promotion energy differences within the statistical error of $\sim 0.06$ eV.

## III. RESULTS: GW AND BSE

In this section, we present refined and extrapolated GW quasiparticle gap values, significantly improving upon the previous calculations.[5,14] The currently available best GW values rely on an old generation PAW potentials and do not consider the converged cutoff and/or vacuum size and/or sufficient Brillouin zone integrations and spread between 6.98 eV and 8.28 eV,[5] depending on input sets of orbitals and level of GW calculations (e.g., 7.01 eV,[7] 6.99 eV, and 7.82 eV[14]).

Here, using the new generation of GW-optimized PAW potentials, we obtained ultimate convergence of the simulation parameters, namely, an inter-sheet distance $L_z \to \infty$ and k-point grid ($N_k \to \infty$). The number of bands $N_{\mathrm{B}}$ and energy cutoff in GW calculation $E_{\mathrm{cut}}^{\mathrm{GW}}$ were investigated in detail (Fig. 1) and determined the production setup: $E_{\mathrm{cut}}^{\mathrm{GW}} = 400$ eV and $N_{\mathrm{B}} = 1152$. Subsequently, the effect of inter-sheet distance $L_z$ was investigated for various k-point grids. Because of the nonlocal nature of the GW approximation, the quasiparticle gaps depend on this parameter and keep on increasing as $1/L_z$. The slope of the corresponding linear fit significantly differs for various k-point grids (Fig. 2); extrapolations to zero $1/L_z$ yield quasiparticle gaps of
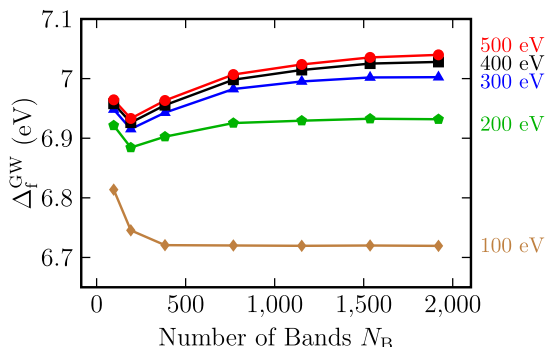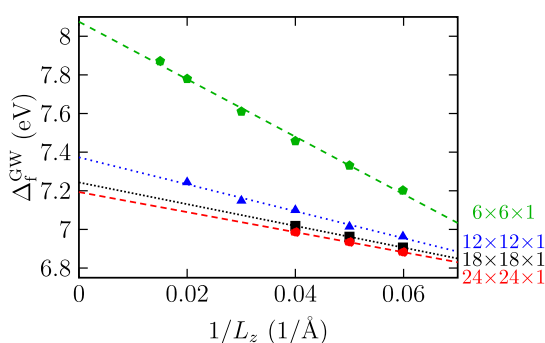
**FIG. 1**. Quasiparticle bandgaps of single-layer FG depending on the number of bands included, calculated using the GW@PBE method with different dielectric matrix cutoffs (100 eV–500 eV), showing the false convergence behavior of the bandgap when a small cutoff energy is used. $12 \times 12 \times 1$ k-point grids, $L_z = 20$ Å, and plane wave cutoff $E_{cut} = 600$ eV were used.

8.08 eV, 7.37 eV, 7.24 eV, and 7.19 eV for $6 \times 6 \times 1$, $12 \times 12 \times 1$, $18 \times 18 \times 1$, and $24 \times 24 \times 1$ k-point grid, respectively. Finally, the quasiparticle bandgap for a full k-point grid ($N_k \to \infty$) was obtained using extrapolation of quasiparticle gap values obtained in Fig. 2 ($1/L_z \to 0$; Fig. 3). The final production value of the quasiparticle gap obtained by the GW method is $\Delta_f^{GW} = 7.14$ eV. The agreement of the above-mentioned unconverged value of 7.01 eV[7] vs our converged result may be attributed to the fortuitous bias cancellation.

For completeness, we calculated the optical gap (position of the first excitonic peak) by the BSE method. Taking all extrapolations of the relevant parameters into account, we obtain $\Delta_{opt}^{BSE} = 5.21$ eV. The binding energy of the first exciton in turn amounts to $E_b^{BSE} = 1.92$ eV.

Finally, we provide an exciton wave function analysis showing contributions of the respective orbitals around VBM maximum and CBM minimum in k-space. The wave function of the $\lambda$-th exciton is expressed in an electron–hole product basis as



**FIG. 2**. Quasiparticle bandgaps of a single-layer of FG depending on inter-sheet distance $L_z$ for various k-point grids. Linear extrapolations for $1/L_z \to 0$ are included as lines.
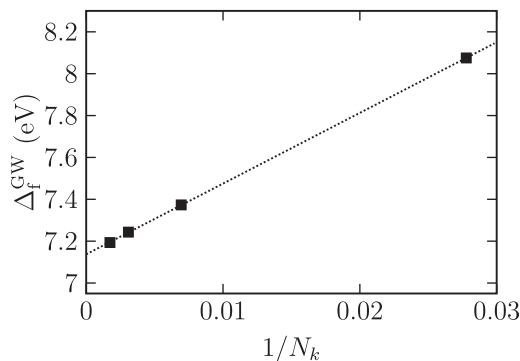


**FIG. 3**. Quasiparticle bandgaps of single-layer FG depending on the k-point grid ($N_k = N_{k_x} \times N_{k_y} \times N_{k_z}$).

$\sum_{cvk} A_{cvk}^\lambda \phi_{ck} \phi_{vk}$. The eigenstate corresponding to the first bright (doubly degenerate) exciton in FG is visualized in Fig. 4 by plotting circles with $|A_{cvk}^1|$ radius into the band structures.[86] Pairs of large circles visible in Fig. 4 represent electron–hole pairs, which contribute the most to the wave function of the first excitonic peak $E_{exc}^1$. It turns out that region close to the $\Gamma$ point (for the highest occupied band and lowest unoccupied band) dominates, whereas other regions of the Brillouin zone provide only negligible contributions to the studied first excitonic state. This salient feature of the FG electronic structure indicates that the nodal surface of $\Psi^T$ of its first excitonic state will likely be well approximated by the
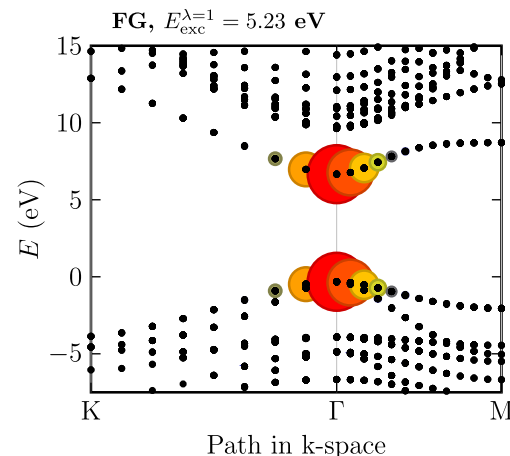


**FIG. 4**. Electronic band structure of FG from GW calculation (black dots) and all $|A_{cvk}^\lambda|$ coefficients from BSE (represented by radius of colored circles) visually show which electron–hole pairs contribute to the first excitonic peak, i.e., to a particular BSE eigenstate $\lambda = 1$. The Fermi energy is set to zero.

multideterminant expansions within restricted active-space consisting of one-particle states in the vicinity of doubly degenerate VBM and CBM in $k$-space (two electrons in three orbitals).

## IV. RESULTS: QMC

The FNDMC production results from both considered codes, QWalk and QMCPACK, are reported in Tables I and II, respectively. Note that the presented FNDMC total energy differences ($\Delta_f^{FN}$) approximate fundamental gap $\Delta_f$ although they were obtained by promotion approach based on two total energies [Eq. (4), elaborated in Sec. II C] instead of the conventional approach based on three total energies [Eq. (1)]. The results agree very well for the overlapping system sizes ($3 \times 3$ and $4 \times 4$), ruling out biases possibly coming from electron interaction modification (Coulomb vs MPC interaction), Jastrow (two-particle vs three-particle), or slab vacuum size (20 Å vs 40 Å).

Linear extrapolations of the QWalk data for sizes ranging from $2 \times 2$–$4 \times 4$ (Table I) to the thermodynamic limit lead to the gaps 6.5 $\pm$ 0.1 eV (three-point) and 6.9 $\pm$ 0.1 eV (using two latter points), respectively, whereas the latter value is more reliable, since, the first point corresponding to $2 \times 2$ supercell appears to be overly influenced by the pronounced size effects.

Linear extrapolations of the FNDMC data obtained from QMCPACK (Table II) to the $1/\kappa \to 0$ limit lead to the gaps 6.9 $\pm$ 0.1 eV (two-point and sizes $3 \times 3$ and $4 \times 4$, which well agrees vs the corresponding QWalk value) and 7.1 $\pm$ 0.1 eV (2-point and sizes $4 \times 4$ and $5 \times 5$), respectively. Linear fit for the full set leads to $\Delta_f^{FN}$ = 7.0 $\pm$ 0.1 eV, which is our best linear-fit FNDMC estimate of the desired quantity for FG. The quadratic three-point fit of the same results leads to the value of 7.1 $\pm$ 0.1 eV that is, within the statistical uncertainty, same as for the QWalk data.

Finally, we have evaluated promotion energy from the ground state to the triplet state (Table II; $T_1$) in order to verify the

**TABLE I**. FNDMC results from QWalk/G09 with PBE orbitals: a time step of 0.01 a.u., two-center Jastrow, 1$e$ VBM-CBM promotion, BFD ECPs, and 40 Å vacuum.

| Size | $\Delta_f^{FN}$ (eV) |
|---|---|
| $2 \times 2$ | $4.99 \pm 0.06$ |
| $3 \times 3$ | $5.67 \pm 0.09$ |
| $4 \times 4$ | $6.20 \pm 0.12$ |

**TABLE II**. Production FNDMC results from QMCPACK/QE with PBE orbitals, MPC interaction for electrons: a time step of 0.01 a.u., three-particle Jastrow, 1$e$ VBM-CBM promotion, BFD ECPs, and 20 Å vacuum.

| Size | $\Delta_f^{FN}$ (eV) |
|---|---|
| $3 \times 3$ | $5.51 \pm 0.07$ |
| $4 \times 4$ | $6.11 \pm 0.05$ |
| $5 \times 5$ | $6.51 \pm 0.08$ |
| $4 \times 4$ $T_1$ | $6.08 \pm 0.06$ |

magnitude of $K_{12}$ [Eq. (22)] contribution to $E_b$ (expected to vanish in the thermodynamic limit). It turns out that already for a finite supercell of size $4 \times 4$, the exchange contribution is negligible (0.03 $\pm$ 0.1 eV, well below our target accuracy standard).

## V. DISCUSSION

The results from the two presented GW and FNDMC methods provide independent, state-of-the-art result in a strikingly similar fundamental gap estimates,

$$\Delta_f^{GW} = 7.14 \text{ eV},$$

and

$$\Delta_f^{FN} = 7.1 \pm 0.1 \text{ eV}.$$

We conclude that such an excellent agreement of the two complementary benchmark methods leaves only very little room for further significant corrections at this accuracy level, and we believe that our results settle an ultimate reference value for an ideal freestanding FG sheet

$$\Delta_f^{theor} \approx 7.1 \pm 0.1 \text{ eV}.$$

Additional BSE computations enable us to ascertain the best available theoretical estimate for an optical gap to

$$\Delta_{opt}^{theor} \approx 5.2 \pm 0.1 \text{ eV}.$$

It is interesting to observe that FG belongs to the class of materials exhibiting universal scaling of exciton binding energy and fundamental gap,[87] which predicts $E_b \approx \Delta_f/4$ (1.78 eV vs our value of 1.92 eV). On the other hand, this value is at the upper bound of experiments that report a lower optical gap value ~3 eV to 5 eV. We must conclude that additional significant effects, beyond the scope of our study of an ideal FG at zero temperature, are likely to be responsible for the remaining discrepancy. The most probable candidates that would cause midgap states and lower optical absorption energies include structural imperfections such as vacancies[5,6] and contaminants.[3] In addition, multilayer effects[10] and termination group effects[1,12,88] cannot be ruled out either. Zero point energy and finite-temperature effects may also cause significant bandgap renormalization, as demonstrated for covalent systems such as diamond[89] and hexagonal BN,[90] and thus leave room for further FG studies.

## VI. CONCLUSIONS

The reference value of the fundamental gap of fluorographene was estimated by the state-of-the-art quantum *ab initio* methods: GW and FNDMC. Both approaches have been pushed to their limits independently and have arrived at the benchmark value of $\Delta_f^{theor} \approx 7.1 \pm 0.1$ eV for a freestanding material sheet free of defects at zero temperature, making little room for further corrections at the 0.1 eV accuracy level. The Bethe–Salpeter equation determined the first exciton stabilization of $E_b^{BSE}$ = 1.92 eV so that our best optical gap estimate amounts to $\Delta_{opt}^{theor} \approx 5.2 \pm 0.1$ eV. In addition, we pointed out a possibility to extract approximations to $\Delta_f$ from neutral single-reference Bloch-orbital FNDMC computations of promotion gaps in finite small-to-medium supercell sizes (vs the actual exciton size) extrapolated to the thermodynamic limit. Such an approach is appreciable since only two total energy FNDMC computations of neutral systems are required to obtain reasonable estimates of the fundamental gap. The alternative involves the usual

three total energies that involve charged states and that can typically exhibit further complications such as more profound finite size effects.

## SUPPLEMENTARY MATERIAL

See the supplementary material for details on the derivation of Coulomb and exchange integrals in 1D and 2D with Bloch orbitals in the thermodynamic limit [Eqs. (28) and (29)].

## ACKNOWLEDGMENTS

## DATA AVAILABILITY

The data that support the findings of this study are available within the article and its supplementary material.

## REFERENCES

[1] R. R. Nair, W. Ren, R. Jalil, I. Riaz, V. G. Kravets, L. Britnell, P. Blake, F. Schedin, A. S. Mayorov, S. Yuan, M. I. Katsnelson, H.-M. Cheng, W. Strupinski, L. G. Bulusheva, A. V. Okotrub, I. V. Grigorieva, A. N. Grigorenko, K. S. Novoselov, and A. K. Geim, Small 6, 2877 (2010).

[2] R. Zbořil, F. Karlický, A. B. Bourlinos, T. A. Steriotis, A. K. Stubos, V. Georgakilas et al., Small 6, 2885 (2010).

[3] F. Karlický, K. Kumara Ramanatha Datta, M. Otyepka, and R. Zbořil, ACS Nano 7, 6434 (2013).

[4] M. Dubecký, E. Otyepková, P. Lazar, F. Karlický, M. Petr, K. Čépe, P. Banáš, R. Zbořil, and M. Otyepka, J. Phys. Chem. Lett. 6, 1430 (2015).

[5] F. Karlický and M. Otyepka, J. Chem. Theory Comput. 9, 4155 (2013).

[6] S. Yuan, M. Rösner, A. Schulz, T. O. Wehling, and M. I. Katsnelson, Phys. Rev. Lett. 114, 047403 (2015).

[7] W. Wei and T. Jacob, Phys. Rev. B 87, 115431 (2013).

[8] K. S. Thygesen, 2D Mater. 4, 022004 (2017).

[9] F. Karlický and J. Turoň, Carbon 135, 134 (2018).

[10] B. Wang, J. R. Sparks, H. R. Gutierrez, F. Okino, Q. Hao, Y. Tang, V. H. Crespi, J. O. Sofo, and J. Zhu, Appl. Phys. Lett. 97, 141915 (2010).

[11] K.-J. Jeon, Z. Lee, E. Pollak, L. Moreschini, A. Bostwick, C.-M. Park, R. Mendelsberg, V. Radmilovic, R. Kostecki, T. J. Richardson, and E. Rotenberg, ACS Nano 5, 1042 (2011).

[12] V. Mazánek, O. Jankovský, J. Luxa, D. Sedmidubský, Z. Janoušek, F. Šembera, M. Mikulics, and Z. Sofer, Nanoscale 7, 13646 (2015).

[13] L. Hedin, Phys. Rev. 139, A796 (1965).

[14] F. Karlický and M. Otyepka, Ann. Phys. 526, 408 (2014).

[15] J. C. Grossman, M. Rohlfing, L. Mitas, S. G. Louie, and M. L. Cohen, Phys. Rev. Lett. 86, 472 (2001).

[16] K. Foyevtsova, J. T. Krogel, J. Kim, P. R. C. Kent, E. Dagotto, and F. A. Reboredo, Phys. Rev. X 4, 031003 (2014).

[17] A. Benali, L. Shulenburger, N. A. Romero, J. Kim, and O. A. von Lilienfeld, J. Chem. Theory Comput. 10, 3417 (2014).

[18] L. K. Wagner, Phys. Rev. B 92, 161116 (2015).

[19] H. Zheng and L. K. Wagner, Phys. Rev. Lett. 114, 176401 (2015).

[20] T. Frank, R. Derian, K. Tokár, L. Mitas, J. Fabian, and I. Štich, Phys. Rev. X 9, 011018 (2019).

[21] R. J. Hunt, B. Monserrat, V. Zólyomi, and N. D. Drummond, Phys. Rev. B 101, 205115 (2020).

[22] D. M. Ceperley, J. Stat. Phys. 63, 1237 (1991).

[23] L. Mitas, Phys. Rev. Lett. 96, 240402 (2006).

[24] W. M. C. Foulkes, R. Q. Hood, and R. J. Needs, Phys. Rev. B 60, 4558 (1999).

[25] C. A. Melton and L. Mitas, Phys. Rev. B 102, 045103 (2020).

[26] W. M. C. Foulkes, L. Mitas, R. J. Needs, and G. Rajagopal, Rev. Mod. Phys. 73, 33 (2001).

[27] J. Kolorenč and L. Mitas, Rep. Prog. Phys. 74, 026502 (2011).

[28] E. Ertekin, L. K. Wagner, and J. C. Grossman, Phys. Rev. B 87, 155210 (2013).

[29] R. J. Hunt, M. Szyniszewski, G. I. Prayogo, R. Maezono, and N. D. Drummond, Phys. Rev. B 98, 075122 (2018).

[30] Y. Yang, V. Gorelov, C. Pierleoni, D. M. Ceperley, and M. Holzmann, Phys. Rev. B 101, 085115 (2020).

[31] M. Ditte and M. Dubecký, Phys. Rev. Lett. 123, 156402 (2019).

[32] J. P. Perdew, R. G. Parr, M. Levy, and J. L. Balduz, Jr., Phys. Rev. Lett. 49, 1691 (1982).

[33] W. Yang, Y. Zhang, and P. W. Ayers, Phys. Rev. Lett. 84, 5172 (2000).

[34] P. Mori-Sanchez, A. J. Cohen, and W. Yang, Phys. Rev. Lett. 102, 066403 (2009).

[35] J. P. Perdew, W. Yang, K. Burke, Z. Yang, E. K. U. Gross, M. Scheffler, G. E. Scuseria, T. M. Henderson, I. Y. Zhang, A. Ruzsinszky, H. Peng, J. Sun, E. Trushin, and A. Görling, Proc. Natl. Acad. Sci. U.S.A. 114, 2801 (2017).

[36] E. J. Baerends, O. V. Gritsenko, and R. van Meer, Phys. Chem. Chem. Phys. 15, 16408 (2013).

[37] H. Şahin, M. Topsakal, and S. Ciraci, Phys. Rev. B 83, 115432 (2011).

[38] G. Kresse and D. Joubert, Phys. Rev. B 59, 1758 (1999).

[39] P. E. Blöchl, Phys. Rev. B 50, 17953 (1994).

[40] D. Nabok, A. Gulans, and C. Draxl, Phys. Rev. B 94, 035118 (2016).

[41] J. P. Perdew, K. Burke, and M. Ernzerhof, Phys. Rev. Lett. 77, 3865 (1996).

[42] M. Shishkin and G. Kresse, Phys. Rev. B 74, 035101 (2006).

[43] M. Kolos and F. Karlický, Phys. Chem. Chem. Phys. 21, 3999 (2019).

[44] D. Y. Qiu, F. H. da Jornada, and S. G. Louie, Phys. Rev. Lett. 111, 216805 (2013).

[45] B.-C. Shih, Y. Xue, P. Zhang, M. L. Cohen, and S. G. Louie, Phys. Rev. Lett. 105, 146401 (2010).

[46] G. Strinati, Phys. Rev. B 29, 5718 (1984).

[47] S. Albrecht, L. Reining, R. Del Sole, and G. Onida, Phys. Rev. Lett. 80, 4510 (1998).

[48] T. Ketolainen, N. Macháčová, and F. Karlický, J. Chem. Theory Comput. 16, 5876 (2020).

[49] J. B. Anderson, J. Chem. Phys. 63, 1499 (1975).

[50] P. J. Reynolds, D. M. Ceperley, B. J. Alder, and W. A. Lester, J. Chem. Phys. 77, 5593 (1982).

[51] C. J. Umrigar, M. P. Nightingale, and K. J. Runge, J. Chem. Phys. 99, 2865 (1993).

[52] L. Mitas, E. L. Shirley, and D. M. Ceperley, J. Chem. Phys. 95, 3467 (1991).

[53] A. Lüchow, Wiley Interdiscip. Rev.: Comput. Mol. Sci. 1, 388 (2011).

[54] B. M. Austin, D. Y. Zubarev, and W. A. Lester, Chem. Rev. 112, 263 (2012).

[55] M. A. Morales, R. Clay, C. Pierleoni, and D. M. Ceperley, Entropy 16, 287 (2014).

[56] L. K. Wagner, Int. J. Quantum Chem. 114, 94 (2014).

[57] M. Dubecký, L. Mitas, and P. Jurečka, Chem. Rev. 116, 5188 (2016).

[58] L. K. Wagner and D. M. Ceperley, Rep. Prog. Phys. 79, 094501 (2016).

[59] J. W. Moskowitz, K. E. Schmidt, M. A. Lee, and M. H. Kalos, J. Chem. Phys. 77, 349 (1982).

[60] F. Schautz and C. Filippi, J. Chem. Phys. 120, 10931 (2004).

[61] P. M. Zimmerman, J. Toulouse, Z. Zhang, C. B. Musgrave, and C. J. Umrigar, J. Chem. Phys. **131**, 124103 (2009).

[62] M. Dubecký, R. Derian, L. Mitas, and I. Štich, J. Chem. Phys. **133**, 244301 (2010).

[63] L. Zhao and E. Neuscamman, Phys. Rev. Lett. **123**, 036402 (2019).

[64] M. A. Morales, J. McMinis, B. K. Clark, J. Kim, and G. E. Scuseria, J. Chem. Theory Comput. **8**, 2181 (2012).

[65] R. C. Clay and M. A. Morales, J. Chem. Phys. **142**, 234103 (2015).

[66] D. Ceperley, G. V. Chester, and M. H. Kalos, Phys. Rev. B **16**, 3081 (1977).

[67] R. Jastrow, Phys. Rev. **98**, 1479 (1955).

[68] E. Mostaani, B. Monserrat, N. D. Drummond, and C. J. Lambert, Phys. Chem. Chem. Phys. **18**, 14810 (2016).

[69] E. J. Baerends, Phys. Chem. Chem. Phys. **19**, 15639 (2017).

[70] A. Szabo and N. S. Ostlund, *Modern Quantum Chemistry* (Dover, New York, 1989).

[71] L. Mitáš and R. M. Martin, Phys. Rev. Lett. **72**, 2438 (1994).

[72] A. Bande, A. Lüchow, F. D. Sala, and A. Görling, Chem. Phys. Lett. **124**, 114114 (2006).

[73] K. M. Rasch and L. Mitas, Phys. Rev. B **92**, 045122 (2015).

[74] A. Annaberdiyev, G. Wang, C. A. Melton, M. C. Bennett, and L. Mitas (to be published).

[75] M. Dubecký, R. Derian, L. Horváthová, M. Allan, and I. Štich, Phys. Chem. Chem. Phys. **13**, 20939 (2011).

[76] M. J. Frisch *et al.*, Gaussian 09, Gaussian, Inc., Wallingford, CT, 2009.

[77] P. Giannozzi, S. Baroni, N. Bonini, M. Calandra, R. Car, C. Cavazzoni, D. Ceresoli, G. L. Chiarotti, M. Cococcioni, I. Dabo, A. Dal Corso, S. de Gironcoli, S. Fabris, G. Fratesi, R. Gebauer, U. Gerstmann, C. Gougoussis, A. Kokalj, M. Lazzeri, L. Martin-Samos, N. Marzari, F. Mauri, R. Mazzarello, S. Paolini, A. Pasquarello, L. Paulatto, C. Sbraccia, S. Scandolo, G. Sclauzero, A. P. Seitsonen, A. Smogunov, P. Umari, and R. M. Wentzcovitch, J. Phys.: Condens. Matter **21**, 395502 (2009).

[78] C. Adamo and V. Barone, J. Chem. Phys. **110**, 6158 (1999).

[79] M. Burkatzki, C. Filippi, and M. Dolg, J. Chem. Phys. **126**, 234105 (2007).

[80] L. K. Wagner, M. Bajdich, and L. Mitas, J. Comput. Phys. **228**, 3390 (2009), http://www.qwalk.org/.

[81] J. Kim *et al.*, J. Phys.: Condens. Matter **30**, 195901 (2018), http://qmcpack.org/.

[82] M. Casula, Phys. Rev. B **74**, 161102(R) (2006).

[83] N. D. Drummond, R. J. Needs, A. Sorouri, and W. M. C. Foulkes, Phys. Rev. B **78**, 125106 (2008).

[84] G. Wang, A. Annaberdiyev, C. A. Melton, M. C. Bennett, L. Shulenburger, and L. Mitas, J. Chem. Phys. **151**, 144110 (2019).

[85] I.-C. Yeh and M. L. Berkowitz, J. Chem. Phys. **111**, 3155 (1999).

[86] M. Bokdam, T. Sander, A. Stroppa, S. Picozzi, D. D. Sarma, C. Franchini, and G. Kresse, Sci. Rep. **6**, 28618 (2016).

[87] Z. Jiang, Z. Liu, Y. Li, and W. Duan, Phys. Rev. Lett. **118**, 266401 (2017).

[88] J. T. Robinson, J. S. Burgess, C. E. Junkermeier, S. C. Badescu, T. L. Reinecke, F. K. Perkins, M. K. Zalalutdniov, J. W. Baldwin, J. C. Culbertson, P. E. Sheehan, and E. S. Snow, Nano Lett. **10**, 3001 (2010).

[89] F. Giustino, S. G. Louie, and M. L. Cohen, Phys. Rev. Lett. **105**, 265501 (2010).

[90] H. Mishra and S. Bhattacharya, Phys. Rev. B **99**, 165201 (2019).

# Supplementary Material 5

## PAPER

# Optical gaps and excitons in semiconducting transition metal carbides (MXenes)†

Tomi Ketolainen [ID] and František Karlický [ID] *

We use time-dependent density functional theory together with the HSE06 hybrid functional to investigate the optical and excitonic properties of two-dimensional transition metal carbides, MXenes. We determine reliable optical gaps, optical absorbance spectra, and exciton features for a set of eight semiconducting MXenes. The optical gaps of $Sc_2CF_2$, $Cr_2CF_2$, $Cr_2C(OH)_2$, and anti-ferromagnetic $Mn_2CO_2$ (1.9–2.3 eV) lie in the energy region of visible (VIS) light. $Sc_2C(OH)_2$, $Ti_2C$, $Ti_2CO_2$, and ferro-magnetic $Mn_2CO_2$ with smaller optical gaps (0.4–1.2 eV) well absorb solar radiation, including VIS light. Moreover, $Ti_2C$ and ferromagnetic $Mn_2CO_2$ show high monolayer absorbance of 10–20% in the 1–3 eV energy range. Finally, we analyse the excitons in MXenes and find that the first bright excitons of Sc- and Ti-based MXenes are strongly localized in $k$-space while the corresponding excitons of Cr- and Mn-based systems are delocalized.

## 1 Introduction

A new group of two-dimensional (2D) materials termed MXenes has attracted a lot of attention recently.[1–3] The MXenes generally consist of layers of transition metal (TM), carbon, and nitrogen atoms. After the synthesis process, the MXenes are usually functionalised with oxygen atoms, fluorine atoms, or hydroxyl groups.[4,5] Furthermore, mixing of different atoms and functional groups on the surfaces of MXenes is energeti-cally favourable, which has been shown in previous studies.[6,7] The surface termination of MXenes affects their electronic and optical properties remarkably.[4,5,8] In addition, the properties of MXenes can be modified by doping or forming heterostructures.[9,10] Due to the promising physical and chemical properties, the MXenes could be utilised in several applications including optical devices and energy storage.[2,3,11–13]

The optical properties of MXenes have been discussed in some computational studies and review articles.[8,14–18] However, the previous computational studies of the optical absorption spectra of MXenes have been performed using density functional theory (DFT) with generalised-gradient approximation and hybrid density functionals. If one focuses on a reliable description of the optical properties of 2D systems, proper inclusion of electron–hole (exciton) effects is necessary.[19] Such effects can be essential in semiconducting

*Department of Physics, Faculty of Science, University of Ostrava, 30. dubna 22, 701 03 Ostrava, Czech Republic. E-mail: frantisek.karlicky@osu.cz; Tel: +420 553 46 2155*

† Electronic supplementary information (ESI) available. See DOI: 10.1039/d2tc00246a

and insulating 2D materials, as we have shown recently.[20,21] Traditional DFT calculations are therefore unsatisfactory and many-body methods beyond DFT are needed. The many-body perturbational GW approximation for the electron self-energy[22] followed by a subsequent solution of the Bethe-Salpeter equation (BSE)[23] is a preferred method. However, such methods are demanding and almost unfeasible for larger unit cells. We therefore use approximate inclusion of electron–electron and electron–hole effects *via* time-dependent density functional theory[24] (TD-DFT) built over hybrid density functionals. We have shown recently that this approach (TD-HSE06) is very successful for a broad set of 2D materials.[25] In addition, TD-DFT together with the so-called Bootstrap kernel has been shown to be a suitable method for describing the excitonic properties of 2D materials qualitatively.[26,27]

The goal of our work is to provide reasonable optical gaps and absorbance spectra for various semiconducting MXenes using the TD-HSE06 method. We choose an important group of MXenes, transition metal carbides, containing 3d TM atoms and we consider structures functionalised with fluorine, oxygen, and hydroxyl groups. Following this choice, the resulting semi-conducting compounds are namely $Sc_2CF_2$, $Sc_2C(OH)_2$, $Ti_2C$, $Ti_2CO_2$, $Cr_2CF_2$, $Cr_2C(OH)_2$, and $Mn_2CO_2$. These particular MXenes are investigated because they create a complete set of semiconducting MXenes containing relatively light (3d) elements (other combinations are metallic). Therefore, the calculations of our systems do not include the spin–orbit coupling and are computationally not so demanding. We examine both the effects of TM atoms and surface functionalisation on the optical absor-bance spectra of MXenes. Besides the absorbance spectrum calculations, we compute the electronic band gaps for our set of

This journal is © The Royal Society of Chemistry 2022

*J. Mater. Chem. C*, 2022, **10**, 3919–3928 | 3919

MXenes and perform analysis of the excitonic wave functions for a few materials. In this work, the MXene systems (with the exception of Ti$_2$C) have uniform functionalisation, which means that each MXene is functionalised with the same types of surface atoms or chemical groups.

The structure of this article is as follows. A short description of the methods is given in Section 2. The results from the optical absorbance calculations are presented in Section 3. Moreover, we discuss the magnetic ground states, electronic band gaps, optical gaps, and excitonic wave function properties of MXenes in Section 3. The main conclusions are summarised in Section 4.

## 2 Computational methods

The optical absorbance spectra of MXenes are computed by using the Vienna *ab initio* simulation package (VASP) based on DFT.[28,29] The plane waves in the VASP code package are constructed with the projector augmented-wave method.[30] To describe exchange–correlation effects, the PBE density functional[31] and the HSE06 hybrid density functional[32] are used in the calculations. The exchange–correlation energy of the HSE06 hybrid functional can be expressed as

$$E_{xc}^{HSE06} = \alpha E_x^{HF,SR}(\omega) + (1 - \alpha)E_x^{PBE,SR}(\omega) + E_x^{PBE,LR}(\omega) + E_c^{PBE} \quad (1)$$

where $E_x^{HF,SR}$ is the short-range Hartree–Fock exchange, $E_x^{PBE,SR}$ is the short-range component of the PBE density functional, $E_x^{PBE,LR}$ is the corresponding long-range component of the PBE density functional, and $E_c$ denotes the correlation energy of PBE. In eqn (1), $\alpha$ and $\omega$ are the exact exchange and screening parameters, respectively. In the HSE06 hybrid functional, the corresponding values are $\alpha = 0.25$ and $\omega = 0.2$ Å$^{-1}$.

The optical absorption spectrum in the PBE and HSE06 calculations is given by the imaginary part of the dielectric function that can be expressed as a sum of interband transitions.[33] Furthermore, we compute the optical absorption spectrum using TD-DFT along with the HSE06 hybrid functional.[25,34] The basic idea of this TD-HSE06 method is to replace the local exchange–correlation kernel by a non-local one. Then the optical absorption spectrum can be computed by solving the Casida's equation. According to our recent work,[25] the matrix equation in the TD-HSE06 method is similar to the BSE but the screened interaction $W$ is replaced by one-quarter of the non-local screened exchange term with a fixed screening parameter $\omega$. The TD-HSE06 method makes it possible to describe excitons in the optical spectra and can be regarded as an approximation of the BSE with the perfect accuracy for the 2D materials.[25] After computing the energy-dependent dielectric function (a broadening of 0.1 eV is used), we can determine the actual optical absorbance that can be written as[35]

$$A(E) = \frac{E\varepsilon_2(E)\Delta z}{\hbar c} \quad (2)$$

where $E$ is the energy of the photon, $\varepsilon_2$ is the imaginary part of the dielectric function, $\Delta z$ is the height of the computational unit cell, $\hbar$ is the reduced Planck's constant, and $c$ is the speed of light. We use the absorbance term instead of the $A$ symbol in all plots and figures.

The computational unit cells are obtained from the C2DB database.[17] Part of the structures have magnetic ground states and we carry out spin-polarized calculations for these systems. We set the cut-off energy of the plane waves to 500 eV. A $\Gamma$-centered 24 × 24 × 1 $k$-point grid is used in the spectrum calculations. The choice of the $k$-point mesh is explained in Section 3.2. In the TD-DFT calculations with the HSE06 functional, we set the numbers of occupied and unoccupied states so that we can describe the optical absorbance spectra accurately enough for photon energies up to 5 eV (see Section 3.2 and Table S1, ESI†). We do not consider spin–orbit coupling as this effect is quite small in our selection of MXenes.

## 3 Results and discussion

### 3.1 Magnetic states of MXenes

Finding the correct magnetic states of MXenes is also essential and the magnetic states depend on the TM atoms and surface functionalisation of the systems. We evaluate the data of the C2DB database[17] in order to select correct ground states. The ground states of Sc$_2$CF$_2$, Sc$_2$C(OH)$_2$, and Ti$_2$CO$_2$ are found to be non-magnetic. The other considered materials (Ti$_2$C, Cr$_2$CF$_2$, Cr$_2$C(OH)$_2$, and Mn$_2$CO$_2$) have antiferromagnetic ground states. According to the C2DB database, the previous systems with the magnetic ground states can also have ferromagnetic structures. However, the MXenes in this study with ferromagnetic states are metallic excluding Mn$_2$CO$_2$ that can also have a ferromagnetic state with semiconducting properties. Thus, we study the optical absorbance of antiferromagnetic MXenes that are semiconducting excluding Mn$_2$CO$_2$ for which we determine the optical absorbance spectrum also when the system is ferromagnetic.

The magnetic moments of the TM atoms in the MXenes with magnetic ground states have been calculated with the VASP code package and are listed in Table 1. In the antiferromagnetic systems, one TM atom has a positive magnetic moment whereas the magnetic moment of the other TM atom in the unit cell is negative. However, the magnitudes of the magnetic moments of both TM atoms are equally large (*i.e.*, the net magnetic moment of the unit cell is zero) and reporting only one value for each magnetic moment is sufficient. In the

**Table 1** Magnetic moments of semiconducting MXenes M$_2$CT$_2$ (M = Ti, Cr, Mn, and T = F, O, OH) computed with the PBE and HSE06 functionals. The magnetic moments are presented for the TM atoms in the antiferromagnetic (AFM) and ferromagnetic (FM) systems. The magnetic state is shown after the chemical formula. The unit of the magnetic moments is the Bohr magneton $\mu_B$

|  | PBE | HSE06 |
|---|---|---|
| Ti$_2$C (AFM) | 0.757 | 0.967 |
| Cr$_2$CF$_2$ (AFM) | 2.585 | 3.008 |
| Cr$_2$C(OH)$_2$ (AFM) | 2.468 | 2.949 |
| Mn$_2$CO$_2$ (AFM) | 2.718 | 3.183 |
| Mn$_2$CO$_2$ (FM) | 2.844 | 3.171 |

**3920** | *J. Mater. Chem. C*, 2022, **10**, 3919–3928

This journal is © The Royal Society of Chemistry 2022

ferromagnetic system, the magnetic moments of both TM atoms are equal. The difference between the total energies of antiferromagnetic and ferromagnetic $Mn_2CO_2$ systems is important in the determination of the magnetic ground state. The total energy difference for the two magnetic structures can be written as $\Delta E = E_{AFM} - E_{FM}$, where $E_{AFM}$ and $E_{FM}$ are the total energies of the antiferromagnetic and ferromagnetic systems. The total energy differences calculated by PBE and HSE06 for the $Mn_2CO_2$ system are $-0.013$ and $0.018$ eV, respectively. Thus, the ground state of $Mn_2CO_2$ is antiferromagnetic in the PBE calculation and ferromagnetic in the HSE06 calculation. A previous study has shown that the total energy difference $\Delta E$ for $Mn_2CO_2$ is $-0.056$ eV when the PBE density functional is used.[36] This value is in quite good agreement with our result. On the other hand, the ground state of $Mn_2CO_2$ has been found to be ferromagnetic in a recent calculation.[37] The recent work has, however, been based on a different geometrical structure. In conclusion, both structures (antiferromagnetic and ferromagnetic) are relevant, close in energy, and studied further.

The magnetic moment calculated by PBE for the Ti atom in $Ti_2C$ is $0.757\mu_B$. This value is similar to the previous values $(0.54-0.92\mu_B)$ found before.[38-41] In a study by Khazaei *et al.*,[4] the ground states of $Cr_2CF_2$ and $Cr_2C(OH)_2$ are found to be ferromagnetic whereas the ground states of the same systems in this work are antiferromagnetic. Consequently, the magnetic moments of ref. 4 are different from the values we have obtained. The optimised atomic structures of $Cr_2CF_2$ and $Cr_2C(OH)_2$ in ref. 4 are similar to our geometries because the functional groups (F and OH) are located at equivalent sites both in the systems of ref. 4 and in the MXenes that we have investigated. Thus, the different magnetic state in the previous investigation may be related to different calculation parameters. However, a comparison between the magnetic moments of the previous study and the present work shows that magnitudes of the magnetic moments are similar in both studies. The magnetic moments of the Cr atoms of $Cr_2CF_2$ and $Cr_2C(OH)_2$ investigated in ref. 4 are $2.71$ and $2.24\mu_B$, respectively. These values have been computed using the PBE functional. In our work, the magnetic moments of the Cr atoms of $Cr_2CF_2$ (see Table 1) are a little smaller than the value obtained in the previous work.[4] The other magnetic moments calculated for the Cr atoms of $Cr_2C(OH)_2$ in Table 1 are larger than the results of the preceding study.

We also determine the magnetic moments with the HSE06 hybrid functional in addition to the usual PBE calculations. The magnetic moments of the TM atoms are always larger when the HSE06 hybrid functional is used instead of the PBE functional. A similar enhancement has been found in the studies of the magnetic moments of Mn dopants in a $MoS_2$ monolayer (ref. 42) and in calculations for Fe atoms in bulk Fe (ref. 43). The amount of exact exchange in the HSE06 hybrid functional is possibly too large for metallic systems, which results in the overestimation of the exchange splitting.[43,44] We assume that similar overestimation of the exchange splitting can also explain the enhanced HSE06 magnetic moments of magnetic semiconducting MXenes.

## 3.2 Accuracy of the optical absorbance spectrum

The optical absorbance spectra of MXenes are computed using the PBE functional, HSE06 hybrid functional, and TD-HSE06 method. To determine the optical absorbance spectra precisely, it is important to examine the influence of various parameters of the DFT calculations on the absorbance spectra and/or make a comparison to reference calculations (*e.g.* BSE). Our previous investigation has shown that the $k$-point grid affects the accuracy of the absorbance spectra significantly.[25] The optimal values of the other parameters including the cut-off energy and the number of bands have been determined and we also use the optimal parameters found in ref. 25 in this work.

We compute the absorbance spectra for $Sc_2CF_2$ and $Ti_2CO_2$ with different $k$-point grids. The results from these convergence studies are displayed in Fig. S1 and S2 in ESI.† The spectra calculated by the PBE and HSE06 functionals do not change so much when the number of $k$-points is increased. Computing the optical absorbance spectra for $Sc_2CF_2$ with the TD-HSE06 method shows that the spectra converge fast with respect to the $k$-point grid. On the other hand, the TD-HSE06 calculations seem to require a dense $k$-point grid in the case of $Ti_2CO_2$. A $24 \times 24 \times 1$ $k$-point grid results in a converged absorbance spectrum. Therefore, we use the $24 \times 24 \times 1$ $k$-point grid in our absorbance spectrum calculations.

We showed in previous work TD-HSE06 as an approximate method with reasonable accuracy for a broad set of materials compared to reference $G_0W_0$ + BSE.[25] To explicitly confirm the TD-HSE06 approximation for present materials, we carefully performed $G_0W_0$ + BSE calculations on a selected MXene ($Sc_2CF_2$) and compared obtained absorbance to that one from TD-HSE06 calculations (Fig. 1, see details on $G_0W_0$ + BSE calculations in ESI,† Fig. S3). The approximate TD-HSE06 optical gap value of $2.31$ eV is good (w.r.t. $G_0W_0$ + BSE optical gap of $2.14$ eV, *i.e.*, $0.17$ eV difference), and the shape of the absorbance curve is similar despite the fact that absolute absorbance is lower in the TD-HSE06 case. Further, our TD-HSE06 optical gap of $1.20$ eV for $Ti_2CO_2$ is in excellent agreement with $1.26$ eV from $G_0W_0$ + BSE.[45] Finally, a simple test on the number of occupied or unoccupied bands for the TD-HSE06 absorption curve is provided in Fig. S4 (ESI†).

## 3.3 Optical absorbance spectra, gaps, and excitons of MXenes

The optical absorbance spectrum curves for Sc-, Ti-, Cr-, and Mn-based MXenes are presented in Fig. 2–5, respectively. In Fig. 2–4, the influence of the surface functionalisation on the optical absorbance spectra can be seen. However, Fig. 5 is different from the other spectrum figures and presents the effect of the magnetic state on the optical absorbance of $Mn_2CO_2$.

Studying the absorbance spectra in Fig. 2–5 reveals that the spectrum curves resemble those of the previous study where the TD-HSE06 method has been used to compute the optical absorbance spectra for conventional 2D materials.[25] The TD-HSE06 curves in Fig. 2–5 are located between the PBE and HSE06 curves. Some new peaks appear in the TD-HSE06 spectra
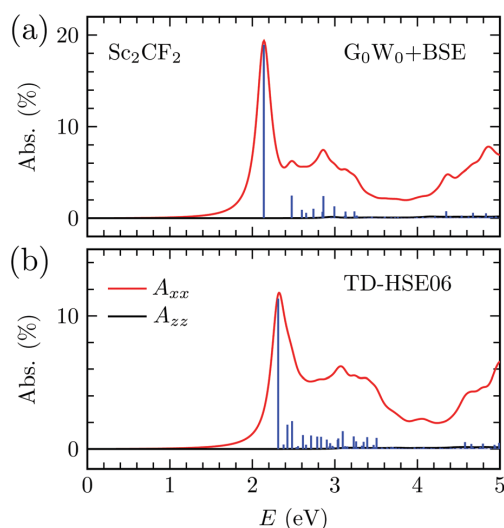
This journal is © The Royal Society of Chemistry 2022

*J. Mater. Chem. C*, 2022, **10**, 3919–3928 | **3921**

Fig. 1 Direct comparison of optical absorbance $A$ ($A_{xx} = A_{yy}$ and $A_{zz}$ components) for $Sc_2CF_2$ computed with (a) $G_0W_0$ + BSE and (b) TD-HSE06 methods. Particular excitonic states are shown using vertical blue lines. See Fig. S1 and S3 (ESI†) for the technical setup and the convergence properties of the spectra from both methods.
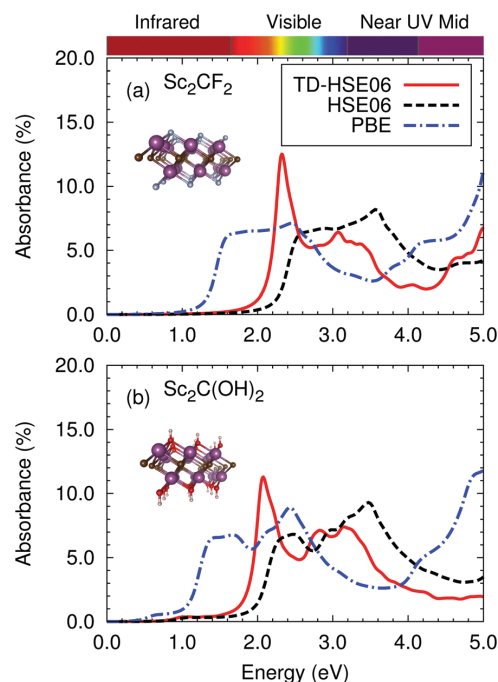


Fig. 2 Optical absorbance of Sc carbides calculated by three different approaches. The absorbance spectra computed with the PBE functional, HSE06 functional, and TD-HSE06 method are displayed for (a) $Sc_2CF_2$ and (b) $Sc_2C(OH)_2$. The color bar on the top shows the actual electromagnetic spectrum of the energy region investigated in our work. The insets in the panels show the atomic structures of the MXenes.

especially above the optical gap and these peaks represent excitons. The small peaks are the most prominent in the TD-HSE06 curve of $Ti_2CO_2$ above the optical gap. Furthermore, the first sharp peaks representing the first excitons in the TD-HSE06 spectra are often significantly higher than the corresponding peaks in the PBE and HSE06 spectra. An advantage of the TD-HSE06 method is the possibility to describe excitons that cannot be seen in the absorbance spectra computed by using standard exchange–correlation functionals.[25]

The electronic band gaps and optical gaps of the MXenes studied in our work are presented in Table 2. In this table, the magnetic states and the location of the minimum direct electronic band gaps in the Brillouin zone are also shown. The electronic band gaps (the gaps that may also be indirect) computed by the PBE functional vary between 0.18 and 1.07 eV as shown in Table 2. The corresponding values given by the HSE06 functional are significantly larger (in the range 0.32–3.24 eV) than the PBE values. Because we are interested in the optical gaps where vertical transitions are important, we also determine the minimum direct band gaps for all materials using both the PBE and HSE06 functionals. Comparing our HSE06 values with the corresponding values in the C2DB database regarding the minimum direct gaps shows that our band gaps are reasonable but our values sometimes differ from the C2DB ones especially when the HSE06 values of the direct band gaps are larger than 1 eV. The minimum direct gaps are located at the $\Gamma$ point or at a point that is close to the $\Gamma$ point (with the exception of $Sc_2CF_2$) as shown in Table 2. However, the location of the minimum direct gap sometimes changes when the HSE06 hybrid functional is used instead of the PBE

functional, which occurs, e.g., in the case of the ferromagnetic ground state of $Mn_2CO_2$.

Our calculations also show that the first excitation energies calculated by the TD-HSE06 method are usually close to the minimum direct gaps determined by using the HSE06 hybrid functional. However, the HSE06 value of the minimum direct gap for $Cr_2CF_2$ is significantly larger than the TD-HSE06 excitation energy (see Table 2). This difference can also be seen in the absorbance spectrum in Fig. 4a.

The accuracy of the band gap calculations seems to decrease when materials with wide band gaps are considered, which can be found by examining the values in Table 2. However, another study by Khazaei et al.[4] shows that the PBE band gaps of $Sc_2CF_2$ and $Sc_2C(OH)_2$ are 1.03 and 0.45 eV, respectively. Furthermore, the same study shows that the band gap computed with the PBE functional for $Ti_2CO_2$ is 0.24 eV. For $Ti_2CO_2$, a band gap of 0.92 eV is obtained when the calculation is carried out with HSE06 functional.[8] According to another computational study by Zhang et al.,[46] the values of the PBE and HSE06 band gaps of $Ti_2CO_2$ are 0.26 and 0.90 eV, respectively. The GW band gap computed in ref. 46 for $Ti_2CO_2$ is 1.15 eV. In addition, the TD-HSE06 optical gap of $Ti_2CO_2$ in this study corresponds to the first absorption peak in the TD-HSE06 spectrum in a recent study.[47] The systems in ref. 8, 4 and 46 probably have
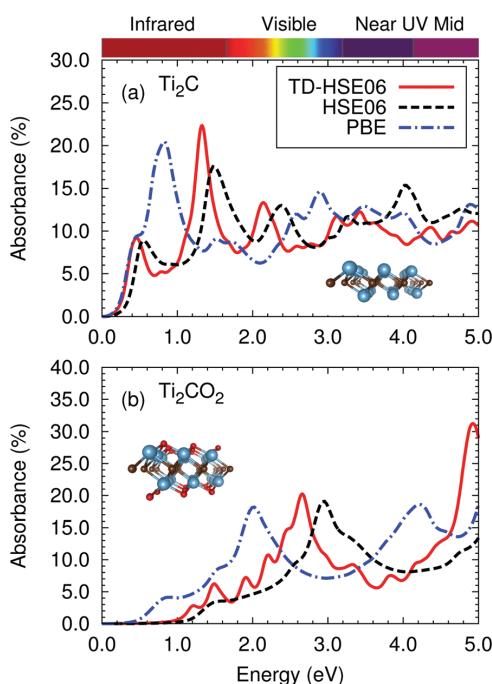
Fig. 3 Optical absorbance of Ti carbides calculated by the PBE functional, HSE06 functional, and TD-HSE06 method. The spectrum curves are presented for (a) $Ti_2C$ and (b) $Ti_2CO_2$. See Fig. 2 for other details.
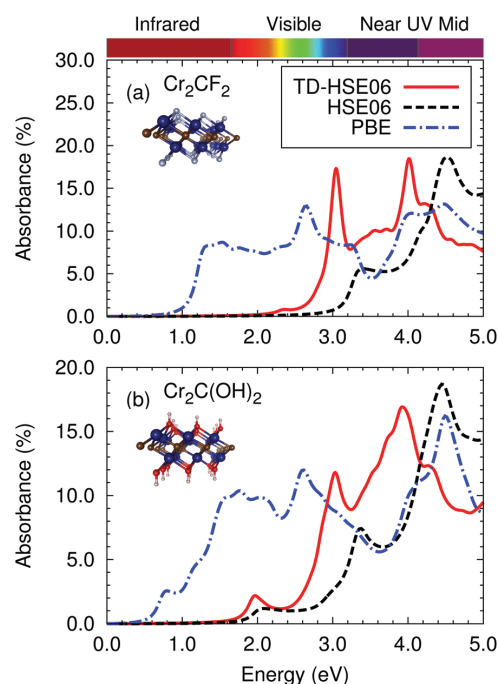


Fig. 4 Optical absorbance spectra computed by the PBE functional, HSE06 functional, and TD-HSE06 method for (a) $Cr_2CF_2$ and (b) $Cr_2C(OH)_2$. See Fig. 2 for other details.

non-magnetic ground states and also have electronic band gaps that are in good agreement with those obtained in our work. We note for completeness that our direct quasiparticle GW gap of $Sc_2CF_2$ (obtained in Section 3.2) is $E_{g,GW}^{d,min} = 2.82$ eV, indirect ($\Gamma \to M$) gap is $E_{g,GW} = 2.33$ eV, and optical gap is $E_{exc}^{BSE} = 2.14$ eV from BSE. Therefore, this is the first indication of the importance of excitonic effects in semiconducting MXenes: the binding energy of the first bright exciton in $Sc_2CF_2$ is $E_b = E_{g,GW}^{d,min} - E_{exc}^{BSE} = 0.68$ eV.

Surface functionalisation and the types of the TM atoms in the MXenes affect the electronic band gaps and optical gaps, which can also be stated by examining the results in Table 2. The MXenes functionalised with F atoms have higher excitation energies than those of MXenes functionalised with OH groups. The TD-HSE06 excitation energy computed for $Sc_2CF_2$ is 2.31 eV whereas the corresponding value for $Sc_2C(OH)_2$ is 0.92 eV. Similarly, the first excitation energy of $Cr_2CF_2$ is higher than the same value determined for $Cr_2C(OH)_2$ although the difference is not so significant as in the case of Sc-based carbides. Furthermore, the first excitation energies computed by the TD-HSE06 method for MXenes with light TM atoms are a little lower than the corresponding values of MXenes consisting of heavy TM atoms. As shown in the TD-HSE06 spectra of $Sc_2C(OH)_2$ and $Cr_2C(OH)_2$ in Fig. 2 and 4, the absorption peaks become broader when the MXenes are functionalised with OH groups instead of F atoms.

Excitons in the TD-HSE06 spectra can be analysed by studying the $A_{vck}^S$ coefficients of electron–hole pairs in the $S$-th exciton

wave function. It can be written in the electron–hole product basis as[21]

$$\sum_{vck} A_{vck}^S |c\mathbf{k}\rangle |v\mathbf{k}\rangle \tag{3}$$

where the $A_{vck}^S$ coefficients are the amplitudes of electron–hole pairs, $|c\mathbf{k}\rangle$ denote electron states, and $|v\mathbf{k}\rangle$ denote hole states. The $\mathbf{k}$ vectors describe Bloch wavevectors in eqn (3). In this equation, the $v$ and $c$ symbols are the indices of the valence and conduction bands, respectively. The band structures and the first bright excitons of $Sc_2CF_2$, $Ti_2CO_2$, $Cr_2CF_2$, and antiferromagnetic $Mn_2CO_2$ are shown in Fig. 6. The $A_{vck}^S$ coefficients are visualised by circles in the band structure plots in Fig. 6 and show which electron–hole pairs contribute to particular TD-HSE06 eigenstates $S$.

The optical absorbance spectrum computed by the TD-HSE06 method for $Sc_2CF_2$ has a sharp peak representing the first bright exciton at 2.31 eV as presented in Fig. 2a. Moreover, the degeneracy of the first excitonic peak is two ($E_{exc}^2 = E_{exc}^3$; the first exciton with the energy $E_{exc}^1 = 2.30$ eV is dark). Inspecting the amplitudes of the excitonic eigenstates shows that the first bright exciton in the TD-HSE06 spectrum of $Sc_2CF_2$ is contributed by electron–hole pairs from the region near the $M$-point of the first Brillouin zone, which can be seen in Fig. 6a. The same is valid for higher bright excitonic states as shown in Fig. S5 (ESI†). In addition, only valence and conduction bands are important
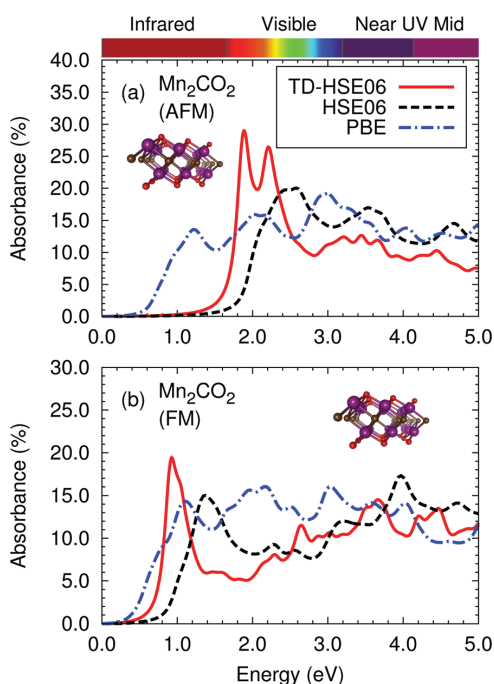
Fig. 5 Optical absorbance spectra determined for (a) antiferromagnetic (AFM) and (b) ferromagnetic (FM) $Mn_2CO_2$ using the PBE functional, HSE06 functional, and TD-HSE06 method. See Fig. 2 for other details.

for the exciton description. In the TD-HSE06 spectrum of $Sc_2C(OH)_2$, the first excitonic peaks are remarkably smaller than the first peak in the TD-HSE06 curve of $Sc_2CF_2$. The TD-HSE06 spectrum of $Sc_2C(OH)_2$ in Fig. 2b has two doubly degenerate excitonic states at 0.92 and 0.97 eV. Performing an analysis of the amplitudes of the four lowest excitonic states for $Sc_2C(OH)_2$ indicates that the excitons are the most remarkable close to the $\Gamma$-point. Therefore, the first excitons of Sc-based MXenes are mainly localised in $k$-space near the points where the smallest direct gaps of these materials are.

Examining the first bright excitons at 1.20 eV in the TD-HSE06 spectrum of $Ti_2CO_2$ (see Fig. 6b and Fig. S6, ESI†) indicates that these excitons are contributed from the $\Gamma$-point in $k$-space. The other bright high-energy excitons responsible for important peaks in the spectrum of Fig. 3b (doubly degenerate energies $E_{exc}^6 = E_{exc}^7 = 1.47$ eV, $E_{exc}^{29} = E_{exc}^{30} = 1.89$ eV and $E_{exc}^{284} = E_{exc}^{285} = 2.66$ eV) are still rather localised, although the high-energy excitons move farther in the $\Gamma \rightarrow K$ and $\Gamma \rightarrow M$ directions to higher interband differences.
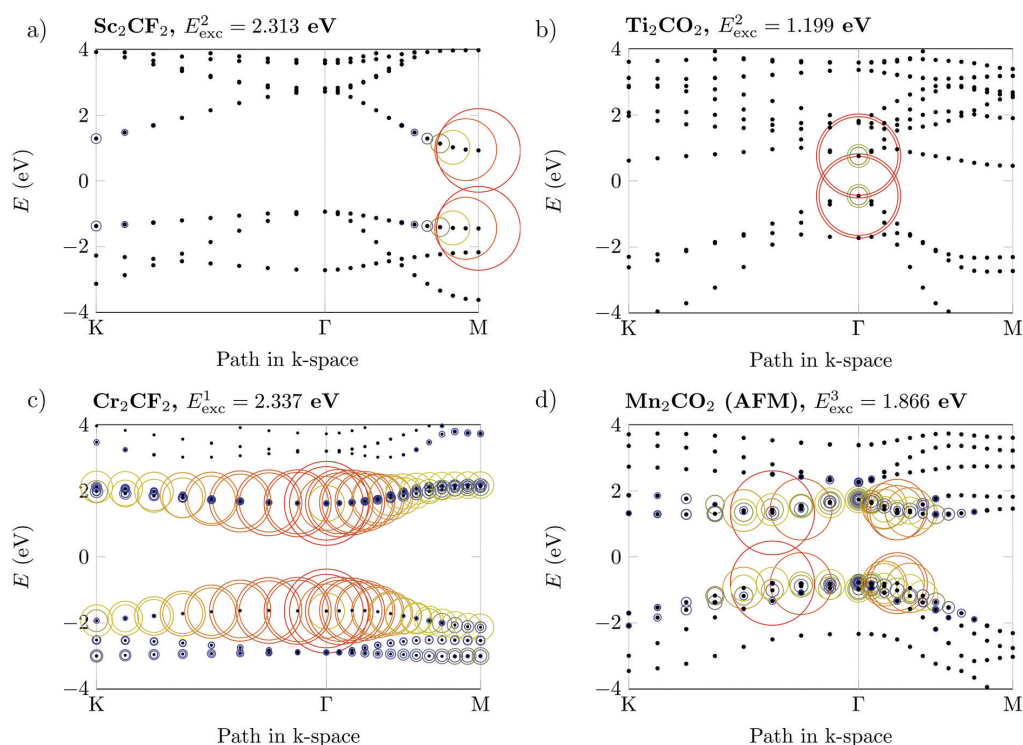
The exciton amplitudes in the TD-HSE06 spectra of $Cr_2CF_2$ and $Cr_2C(OH)_2$ behave differently compared with the excitons in MXenes with Sc and Ti atoms. For example, the amplitudes of the two excitons in $Cr_2CF_2$ at 2.34 and 3.04 eV in Fig. 4a have the largest values close to the $\Gamma$-point but decrease very slowly in the neighbourhood of the $\Gamma$-point (see Fig. 6c and Fig. S7, ESI†). Therefore, the whole Brillouin zone and more bands (at least six) are required for the right description of such delocalised excitons. These excitons are also doubly degenerate. The amplitude of the exciton at 1.95 eV in the TD-HSE06 spectrum of $Cr_2C(OH)_2$ shown in Fig. 4b is also the highest near the $\Gamma$-point and remains quite high in the $\Gamma$-point region in $k$-space. Thus, the first excitons of Cr-based MXenes are contributed broadly from the whole $k$-space with the maxima at the points where the minimum direct gaps are.

The last system for which an analysis of the exciton amplitudes is performed is the antiferromagnetic structure of $Mn_2CO_2$ (see Fig. 6d). The first bright excitons at 1.87 eV ($E_{exc}^3 = E_{exc}^4$) are more localised in $k$-space than Cr-based systems but a large piece of the Brillouin zone and many bands (at least seven) are still important. The properties of other excitons that have larger energies than the energy of the first bright exciton (and significantly contribute to the dominant peak of Fig. 5a; doubly degenerate energies $E_{exc}^7 = E_{exc}^8 = 1.90$ eV, $E_{exc}^{15} = E_{exc}^{16} = 1.97$ eV and $E_{exc}^{39} = E_{exc}^{40} = 2.00$ eV) are presented in Fig. S6 (ESI†). The amplitudes of these other excitons are also similar to those of the first exciton in antiferromagnetic $Mn_2CO_2$. Ferromagnetic $Mn_2CO_2$ includes excitons, which embody similar behaviour.

The radius (delocalization) of the first exciton in real space is clearly indicated by the $k$-point grid necessary for reliable

Table 2 Magnetic states, electronic band gaps, and optical gaps of MXenes. The unit of the energy in this table is eV. The magnetic state (NM = non-magnetic, AFM = antiferromagnetic, and FM = ferromagnetic) is shown for each material in the second column. The standard band gap is denoted by $E_g$ and is indirect in some cases. The band gaps $E_g^{d,min}$ and $E_{g,C2DB}^{d,min}$ denote the minimum direct electronic band gaps of this work and the C2DB database, respectively. The location of $E_g^{d,min}$ is presented in the third column. The $\Gamma^*$ symbol denotes a point that is close to the $\Gamma$ point in the first Brillouin zone. The first excitation energies $E_{exc}$ computed by the TD-HSE06 method are shown in the last column

| | | | PBE | | | HSE06 | | | TD-HSE06 |
|---|---|---|---|---|---|---|---|---|---|
| | Magnetic state | Location of $E_g^{d,min}$ | $E_g$ | $E_g^{d,min}$ | $E_{g,C2DB}^{d,min}$ | $E_g$ | $E_g^{d,min}$ | $E_{g,C2DB}^{d,min}$ | $E_{exc}$ |
| $Sc_2CF_2$ | NM | M | 1.00 | 1.42 | 1.43 | 1.86 | 2.37 | 2.55 | 2.31 |
| $Sc_2C(OH)_2$ | NM | $\Gamma$ | 0.51 | 0.51 | 0.42 | 0.92 | 0.92 | 0.95 | 0.92 |
| $Ti_2C$ | AFM | $\Gamma^*$ | 0.18 | 0.32 | 0.27 | 0.32 | 0.40 | 0.33 | 0.38 |
| $Ti_2CO_2$ | NM | $\Gamma$ | 0.25 | 0.50 | 0.64 | 0.91 | 1.21 | 1.99 | 1.20 |
| $Cr_2CF_2$ | AFM | $\Gamma^*$ | 1.07 | 1.22 | 1.28 | 3.24 | 3.25 | 2.96 | 2.34 |
| $Cr_2C(OH)_2$ | AFM | $\Gamma$ | 0.44 | 0.71 | 0.76 | 1.72 | 1.86 | 1.62 | 1.86 |
| $Mn_2CO_2$ | AFM | $\Gamma^*$ | 0.67 | 0.70 | 0.74 | 1.54 | 1.96 | 2.41 | 1.87 |
| $Mn_2CO_2$ | FM | $\Gamma/\Gamma^*$ | 0.29 | 0.33 | 0.36 | 0.52 | 0.99 | 1.24 | 0.91 |

3924 | J. Mater. Chem. C, 2022, 10, 3919–3928

This journal is © The Royal Society of Chemistry 2022

**Fig. 6** Electronic band structures from HSE06 calculations (black dots) and all $|A^S_{vck}|$ coefficients from eqn (3) (represented by the radii of coloured circles; red = maximum, yellow = middle, grey = minimum) for the first bright exciton in (a) $Sc_2CF_2$, (b) $Ti_2CO_2$, (c) $Cr_2CF_2$, and (d) antiferromagnetic $Mn_2CO_2$. The radii of circles are normalised so that the maximum radius is the same in all plots. The Fermi energy is set to zero. We note that in both AFM cases (c and d), bands corresponding to spin up and spin down are almost the same around the Fermi level, and thus it is not possible to distinguish them (see also Tables S2 and S3, ESI†).

calculation of optical gap value (and similarly for higher excitons and convergence of higher optical transitions). An $n \times n$ grid in reciprocal space can only be used to map an exciton wave function within a real-space $n \times n$ supercell.
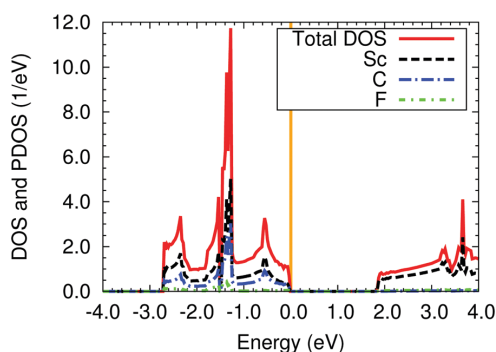


**Fig. 7** Total DOS and PDOS calculated by PBE for $Sc_2CF_2$. The PDOS is shown for the Sc, C, and F atoms. The vertical solid orange line denotes the Fermi level.

Therefore, too coarse grid will impose artificial confinement on the exciton and thus increase its predicted binding energy. The first exciton wave function of $Ti_2CO_2$ or $Sc_2CF_2$, for instance, had a relatively large radius, covering an area lesser than a $12 \times 12$ supercell in real space. For the corresponding $k$-grid, the position of the first exciton peak is converged (Fig. S1–S3, ESI†), however, our attempts with a coarse $6 \times 6 \times 1$ $k$-grid showed biased results. This was reported also in the literature[45] when one can see approximately $10 \times 10$ size of supercell containing wavefunction of the $Ti_2CO_2$ first exciton. However, the wave functions of the higher-energy peaks were more spread out and therefore the whole spectrum converged more slowly with increasing grid size.

We also examine the total density of states (DOS) of $Sc_2CF_2$ and projected density of states (PDOS) of the Sc, C, and F atoms in $Sc_2CF_2$. The results from our DOS and PDOS calculations are shown in Fig. 7. The Sc and C states contribute to the total DOS below the Fermi level significantly while the the PDOS of F states is negligible in the energy region considered in this work. Moreover, the PDOS of Sc states is larger than that computed for the C and F atoms above the band gap. We also report charge distributions on atoms of considered MXenes
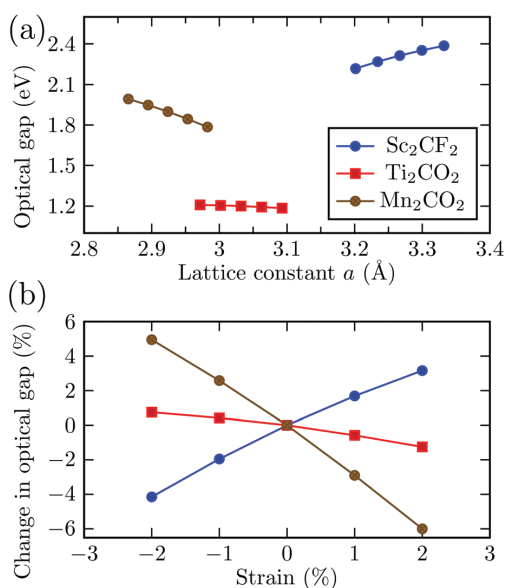
Fig. 8 Influence of the strain on the optical band gap for Sc$_2$CF$_2$, Ti$_2$CO$_2$, and Mn$_2$CO$_2$ (AFM): (a) optical gap as a function of the lattice constant $a$, (b) the same data in terms of the relative change of the optical gap *versus* the strain (both in %; 0% means the equilibrium value).

(Table S4 in ESI†). Interestingly, various metal atoms and termination groups significantly change the charge on inner carbon atoms from $-1.2e$ (in Mn-based MXenes) to $-1.9e$ (in Ti$_2$C).

Reliable prediction of the optical gap values and absorbance curves is important for the design of MXenes in photonics devices.[3] We showed that TD-HSE06 is predictive in this sense,[25] and we, therefore, can formulate some basic conclusions concerning a considered set of MXenes. We focus on comparison for photon energies in the 1–3 eV range, which is of essential relevance for photovoltaics.[35] It is worth noting that the TD-HSE06 optical gaps of Sc$_2$CF$_2$, Cr$_2$CF$_2$, Cr$_2$C(OH)$_2$, and anti-ferromagnetic Mn$_2$CO$_2$ (1.9–2.3 eV) are in the visible light energy region. That can be a useful property of insulating materials in (nano) electronics. On the other hand, the solar radiation absorption is not very effective because the important energy region is not fully covered, and possible photoabsorption devices would have low efficiency (namely, in Cr-based systems). However, antiferromagnetic Mn$_2$CO$_2$ has an absorbance of $A \approx$ 10–25% for photon energies in the 2–3 eV range (see Fig. 5a). Sc$_2$C(OH)$_2$, Ti$_2$C, Ti$_2$CO$_2$, and ferromagnetic Mn$_2$CO$_2$ are much more suitable in this context because of full compatibility with solar radiation flux. Mainly Ti$_2$C and ferromagnetic Mn$_2$CO$_2$ are ideal absorbers: the absorbance is $A \approx$ 10–20% in 1–3 eV energy range (Fig. 3a and 5b) only with 2.3 and 4.4 Å monolayer thickness, respectively. This means significantly better performance than $A \approx$ 5–10% in the MoS$_2$ case[35] with a thickness of 3.1 Å. We, therefore, consider Mn$_2$CO$_2$ MXene as a very interesting and promising material. Its magnetic properties (and possible antiferromagnetic-

ferromagnetic switching) and excellent absorption efficiency suggest Mn$_2$CO$_2$ as an ideal photonics material.

It was shown that mechanical strain is a prominent approach to modulate the electronic properties.[45,48–53] These effects are important because changes in the band structures can also affect the optical properties of MXenes. Further, slightly different geometrical parameters can be a reason for small differences between the obtained band gaps and the ones available in the literature (see above). Therefore, we applied biaxial strain (from $-2$% compression to 2% tension) on selected simple MXenes, namely Sc$_2$CF$_2$, Ti$_2$CO$_2$, and antiferromagnetic Mn$_2$CO$_2$. We define strain as $(a - a_0)/a_0$, where $a_0$ and $a$ are the lattice constants of the original cell and the cell with strain, respectively. The effect of strain on the optical gap is visible in Fig. 8 (absolute values of lattice constants and the optical gap in panel (a), while relative differences in panel (b)). The change in the gap is quite small in the case of Ti$_2$CO$_2$, but significant (up to $-6$% corresponding to strain of 2%) in the case of Sc$_2$CF$_2$ and Mn$_2$CO$_2$. While tension leads to an increase in the optical gap of Sc$_2$CF$_2$, the optical gap of Ti$_2$CO$_2$ and Mn$_2$CO$_2$ is decreasing. A decrease of the direct gap of Ti$_2$CO$_2$ (and optical gap) with increasing strain is in contrast with increasing the indirect gap. This behavior was observed also in literature.[45,49] For larger strains, it can be used for the realization of an indirect-to-direct band gap transition.

We must note that additional non-negligible effects, far beyond the scope of our study of ideal MXenes at zero temperature, could be responsible for slight spectrum shape changes and gaps shifts. For example, the inclusion of electron–phonon coupling allows for evaluating zero-point band-gap renormalization and temperature-dependent properties. We have shown recently on a different 2D nitrogen phosphide material[54] that some changes (of the order of 0.1 eV) can occur. For wide-gap semiconductors like hexagonal BN (ref. 55), finite-temperature effects can cause significant band gap renormalization. On the other hand, we artificially include broadening by temperature using the energy/wavelength-independent value of Lorentzian broadening (0.1 eV, see Section 2).

## 4 Conclusions

The optical and excitonic properties of eight semiconducting transition metal carbides (MXenes) have been investigated using DFT and TD-DFT in this work. Our results show that excitonic effects can often be seen as clear peaks in the absorbance spectra and a proper description of the excitons requires using many-body methods. The use of TD-DFT together with the HSE06 hybrid functional makes it possible to describe the excitonic states of MXenes in a reasonable way. The optical gaps determined by the TD-HSE06 method for four MXenes (Sc$_2$CF$_2$, Cr$_2$CF$_2$, Cr$_2$C(OH)$_2$, and antiferromagnetic Mn$_2$CO$_2$) are found to be in the visible light energy region. Sc$_2$C(OH)$_2$, Ti$_2$C, Ti$_2$CO$_2$, and ferromagnetic Mn$_2$CO$_2$ embody smaller optical gaps and absorb the solar electromagnetic radiation efficiently (with the highest absorbance $A \approx$ 10–20%

3926 | *J. Mater. Chem. C*, 2022, **10**, 3919–3928

This journal is © The Royal Society of Chemistry 2022

in the case of $Ti_2C$ and ferromagnetic $Mn_2CO_2$). The properties of the considered MXenes determine them as good candidates for excitonic solar cells and for building useful van der Waals heterostructures.

The surface functionalisation has a marked effect on the electronic band gaps, which influence the widths of the optical gaps. Fluorine-functionalised MXenes have wider optical gaps than those of OH-functionalised MXenes. In addition, the electronic band gaps and optical gaps seem to be wider when the atomic numbers of MXenes increase. The magnetic moments of the TM atoms in MXenes with magnetic ground states are relatively large and are over $2\mu_B$ per atom in most magnetic MXenes examined in this work. An analysis of the first bright excitons shows that Sc- and Ti-based systems include excitons composed of electron–hole pairs localised in $k$-space near the minimum direct gap positions while the Cr- and Mn-based MXenes exhibit delocalisation of contributions to excitons.

## Conflicts of interest

There are no conflicts to declare.

## Acknowledgements

## References

1 M. Naguib, O. Mashtalir, J. Carle, V. Presser, J. Lu, L. Hultman, Y. Gogotsi and M. W. Barsoum, *ACS Nano*, 2012, **6**, 1322–1331.

2 M. Naguib, V. N. Mochalin, M. W. Barsoum and Y. Gogotsi, *Adv. Mater.*, 2014, **26**, 992–1005.

3 K. Hantanasirisakul and Y. Gogotsi, *Adv. Mater.*, 2018, **30**, 1804779.

4 M. Khazaei, M. Arai, T. Sasaki, C.-Y. Chung, N. S. Venkataramanan, M. Estili, Y. Sakka and Y. Kawazoe, *Adv. Funct. Mater.*, 2013, **23**, 2185–2192.

5 J. L. Hart, K. Hantanasirisakul, A. C. Lang, B. Anasori, D. Pinto, Y. Pivak, J. T. van Omme, S. J. May, Y. Gogotsi and M. L. Taheri, *Nat. Commun.*, 2019, **10**, 522.

6 R. Ibragimova, M. J. Puska and H.-P. Komsa, *ACS Nano*, 2019, **13**, 9171–9181.

7 R. Ibragimova, P. Erhart, P. Rinke and H.-P. Komsa, *J. Phys. Chem. Lett.*, 2021, **12**, 2377–2384.

8 H. Zhang, G. Yang, X. Zuo, H. Tang, Q. Yang and G. Li, *J. Mater. Chem. A*, 2016, **4**, 12913–12920.

9 E. Balcı, Ü. Ö. Akkus and S. Berber, *J. Mater. Chem. C*, 2017, **5**, 5956–5961.

10 Z. Guo, N. Miao, J. Zhou, B. Sa and Z. Sun, *J. Mater. Chem. C*, 2017, **5**, 978–984.

11 B. Anasori, M. R. Lukatskaya and Y. Gogotsi, *Nat. Rev. Mater.*, 2017, **2**, 16098.

12 J. Pang, R. G. Mendes, A. Bachmatiuk, L. Zhao, H. Q. Ta, T. Gemming, H. Liu, Z. Liu and M. H. Rummeli, *Chem. Soc. Rev.*, 2019, **48**, 72–133.

13 C. Zhan, W. Sun, Y. Xie, D.-E. Jiang and P. R. C. Kent, *ACS Appl. Mater. Interfaces*, 2019, **11**, 24885–24905.

14 G. R. Berdiyorov, *AIP Adv.*, 2016, **6**, 055105.

15 M. Khazaei, A. Ranjbar, M. Arai, T. Sasaki and S. Yunoki, *J. Mater. Chem. C*, 2017, **5**, 2488–2503.

16 K. Xiong, P. Wang, G. Yang, Z. Liu, H. Zhang, S. Jin and X. Xu, *Sci. Rep.*, 2017, **7**, 15095.

17 S. Haastrup, M. Strange, M. Pandey, T. Deilmann, P. S. Schmidt, N. F. Hinsche, M. N. Gjerding, D. Torelli, P. M. Larsen, A. C. Riis-Jensen, J. Gath, K. W. Jacobsen, J. J. Mortensen, T. Olsen and K. S. Thygesen, *2D Mater.*, 2018, **5**, 042002.

18 M. Khazaei, A. Mishra, N. S. Venkataramanan, A. K. Singh and S. Yunoki, *Curr. Opin. Solid State Mater. Sci.*, 2019, **23**, 164–178.

19 M. Bernardi, C. Ataca, M. Palummo and J. C. Grossman, *Nanophotonics*, 2017, **6**, 479–493.

20 F. Karlický and J. Turoň, *Carbon*, 2018, **135**, 134–144.

21 M. Kolos and F. Karlický, *Phys. Chem. Chem. Phys.*, 2019, **21**, 3999–4005.

22 L. Hedin, *Phys. Rev.*, 1965, **139**, A796–A823.

23 E. E. Salpeter and H. A. Bethe, *Phys. Rev.*, 1951, **84**, 1232–1242.

24 C. A. Ullrich, *Time-Dependent Density-Functional Theory*, Oxford University Press, New York, 2012.

25 T. Ketolainen, N. Macháčová and F. Karlický, *J. Chem. Theory Comput.*, 2020, **16**, 5876–5883.

26 S. Sharma, J. K. Dewhurst, A. Sanna and E. K. U. Gross, *Phys. Rev. Lett.*, 2011, **107**, 186401.

27 Y. Suzuki and K. Watanabe, *Phys. Chem. Chem. Phys.*, 2020, **22**, 2908–2916.

28 G. Kresse and J. Furthmüller, *Comput. Mater. Sci.*, 1996, **6**, 15–50.

29 G. Kresse and J. Furthmüller, *Phys. Rev. B: Condens. Matter Mater. Phys.*, 1996, **54**, 11169–11186.

30 P. E. Blöchl, *Phys. Rev. B: Condens. Matter Mater. Phys.*, 1994, **50**, 17953–17979.

31 J. P. Perdew, K. Burke and M. Ernzerhof, *Phys. Rev. Lett.*, 1996, **77**, 3865–3868.

32 A. V. Krukau, O. A. Vydrov, A. F. Izmaylov and G. E. Scuseria, *J. Chem. Phys.*, 2006, **125**, 224106.

33 M. Gajdoš, K. Hummer, G. Kresse, J. Furthmüller and F. Bechstedt, *Phys. Rev. B: Condens. Matter Mater. Phys.*, 2006, **73**, 045112.

34 J. Paier, M. Marsman and G. Kresse, *Phys. Rev. B: Condens. Matter Mater. Phys.*, 2008, **78**, 121201(R).

35 M. Bernardi, M. Palummo and J. C. Grossman, *Nano Lett.*, 2013, **13**, 3664–3670.

36 J. He, P. Lyu and P. Nachtigall, *J. Mater. Chem. C*, 2016, **4**, 11143–11149.

37 X. Zhang, T. He, W. Meng, L. Jin, Y. Li, X. Dai and G. Liu, *J. Phys. Chem. C*, 2019, **123**, 16388–16392.

38 Y. Xie and P. R. C. Kent, *Phys. Rev. B: Condens. Matter Mater. Phys.*, 2013, **87**, 235441.

39 P. Chakraborty, T. Das, D. Nafday, L. Boeri and T. Saha-Dasgupta, *Phys. Rev. B*, 2017, **95**, 184106.

40 P. Lv, Y.-L. Li and J.-F. Wang, *Phys. Chem. Chem. Phys.*, 2020, **22**, 11266–11272.

41 K. Luo, X.-H. Zha, Q. Huang, C.-T. Lin, M. Yang, S. Zhou and S. Du, *RSC Adv.*, 2020, **10**, 44430–44436.

42 A. Ramasubramaniam and D. Naveh, *Phys. Rev. B: Condens. Matter Mater. Phys.*, 2013, **87**, 195201.

43 Y.-R. Jang and B. D. Yu, *J. Magnetics*, 2011, **16**, 201.

44 J. Paier, M. Marsman, K. Hummer, G. Kresse, I. C. Gerber and J. G. Ángyán, *J. Chem. Phys.*, 2006, **124**, 154709.

45 Y.-m. Ding, X. Nie, H. Dong, N. Rujisamphan and Y. Li, *Nanoscale Adv.*, 2020, **2**, 2471–2477.

46 Y. Zhang, W. Xia, Y. Wu and P. Zhang, *Nanoscale*, 2019, **11**, 3993–4000.

47 J. Cui, Q. Peng, J. Zhou and Z. Sun, *Nanotechnology*, 2019, **30**, 345205.

48 S. Zhao, W. Kang and J. Xue, *Appl. Phys. Lett.*, 2014, **104**, 133106.

49 X.-F. Yu, J.-B. Cheng, Z.-B. Liu, Q.-Z. Li, W.-Z. Li, X. Yang and B. Xiao, *RSC Adv.*, 2015, **5**, 30438–30444.

50 X.-H. Li, X.-Y. Su and R.-Z. Zhang, *Appl. Surf. Sci.*, 2019, **491**, 276–285.

51 X.-H. Li, X.-Y. Su, R.-Z. Zhang, C.-H. Xing and Z.-L. Zhu, *J. Phys. Chem. Solids*, 2020, **137**, 109218.

52 X.-H. Li, R.-Z. Zhang and H.-L. Cui, *ACS Omega*, 2020, **5**, 18403–18410.

53 Y. Lee, S. B. Cho and Y.-C. Chung, *ACS Appl. Mater. Interfaces*, 2014, **6**, 14724–14728.

54 M. Kolos, L. Cigarini, R. Verma, F. Karlický and S. Bhattacharya, *J. Phys. Chem. C*, 2021, **125**, 12738–12757.

55 H. Mishra and S. Bhattacharya, *Phys. Rev. B*, 2019, **99**, 165201.

# Supplementary Material 6

Check for updates

# DFTB investigations of the electronic and magnetic properties of fluorographene with vacancies and with adsorbed chemical groups†

Taoufik Sakhraoui [ID] and František Karlický [ID] *

The electronic and magnetic properties of fluorographene (CF) in the presence of F-vacancy defects and/or chemical groups ($-OH$, $-CN$, or $-NH_2$) were computationally investigated within the framework of the density functional tight-binding (DFTB) method. The current method parameterization allowed us to perform accurate electronic structure calculations (at the *ab initio* level of many-body methods in the particular case of CF) for hundreds of atoms in the computational cell. We show that the F-vacancy and/or chemical groups influence the magnetic structure, which depends on the number of defects and their distribution between the two sides of the graphene plane. Interestingly, we pointed out a possibility of imprinting local magnetism not only *via* F-vacancy and $-OH$ combinations, but also using F-vacancies and $-CN$ or $-NH_2$ groups. In such structures, the magnetic ordering and the total magnetic moments depend on their adsorption sites and their presence in the same or on opposite sides of the graphene plane. We devote particular attention to the interacting chemical group with the F-vacancies. The interaction between the adsorbed chemical group and the unpaired spins associated with the F-vacancies in CF gives rise to interesting magnetic structures. Finally, the zigzag-like direction is shown as the most preferred for the defluorination of CF. Stable ferrimagnetic zigzag chains with interesting properties are considered to be basic magnetic features in perturbed CF. Our work provides new guidelines for engineering multifunctional spintronic components using CF as a base material. We believe, in particular, that the magnetism is predominantly controlled by the F-vacancies, and the ferromagnet can ideally be regulated *via* the adsorption of a chemical group on a defective CF supercell.

## 1 Introduction

Graphene, a single layer of carbon atoms arranged in a hexagonal structure, has attracted the most attention of researchers because of its fascinating structural and electronic properties as well as its promising applications in modern semiconducting devices.[1–3] However, its zero band gap is a major drawback, making it an inappropriate material for use in logical devices. Therefore, several ways have been explored to open its band gap, which allows combining the advantages of graphene and modern electronic devices.[4] Chemical functionalization[5,6] is a promising way to open the band gap of graphene, where different radicals, such as oxygen,[7] hydrogen,[8,9] or fluorine[10,11] atoms, are adsorbed on the graphene surface. When radicals are adsorbed on the graphene surface they form covalent bonds with the carbon atoms and the hybridization is converted from sp$^2$ to sp$^3$. Both

experimental and theoretical studies have demonstrated that the chemical modification of graphene sheets using F adatoms (fluorination) leads to opening of the band gap[12–16] of graphene.

Fluorographene (CF) is an important example of a stoichiometric covalently modified graphene derivative with insulating properties (with fundamental and optical gaps of 7.1 and 5.2 eV, respectively[17]). Several experimental techniques are known for the preparation of CF: mechanical,[12,18] chemical,[14,19,20] and thermal[21] exfoliation of fluorographite or the fluorination of graphene.[13,22,23] During the experimental preparation of CF, various structural defects, such as vacancies,[10,23,24] contaminants,[16] and termination group effects,[12,13,19] are introduced. F-vacancies (missing fluorine atoms) are supposed to be very important and occur naturally in the process of the fluorination of graphene.[23] Besides, such point defects can induce paramagnetism[25] or trigger the reactivity of fluorographene.[26]

In theoretical simulations, the most common method for the description of structural defects and their electronic structure is the well-known density functional theory (DFT). As standard DFT underestimates the band gap of fluorographene, at least hybrid density functionals or preferentially many-body methods

*Department of Physics, Faculty of Science, University of Ostrava, 701 03 Ostrava, Czech Republic. E-mail: frantisek.karlicky@osu.cz*

**3312** | *Phys. Chem. Chem. Phys.*, 2022, **24**, 3312–3321

This journal is © the Owner Societies 2022

should be used for electronic structure calculations.[17,24,27] However, advanced electronic structure theories are more computationally demanding and limited supercell sizes must be studied: only 3 × 3 CF supercells were used at the hybrid DFT level to study point defects in CF[24] or for the magnetic properties of hydroxofluorographene.[28] By contrast, Yuan *et al.*[10] studied the effect of the presence of structural disorder on the electronic structure and optical properties of fluorinated graphene using an empirical large-scale tight-binding (TB) model fitted to an accurate many-body (GW) band structure. This approach enabled the simulation of systems on the scale of micrometers and the authors showed that different types of structural disorders (C-vacancies, simple F-vacancies, F-vacancy clusters, *etc.*) introduce defect states within the band gap.[10] However, introducing other chemical elements into the this model is problematic as new fitting and reference calculations are needed.

Therefore, motivated by indications of the suitability of TB-based methods for fluorographene-based systems and with a wish to be simultaneously more general and more accurate than TB, we test here the semi-empirical "intermediate"-level method. The so-called self-consistent charge density functional tight-binding method (SCC-DFTB) is an approximate method, which is parameterized from DFT.[29,30] Thus, it helps the study of large systems with hundreds of atoms (we finally use a 9 × 9 CF supercell) and achieves a good compromise between computational efficiency and accuracy. The DFTB method has been used extensively in the modeling of carbon- and graphene-based materials.[31–33] The corresponding results were shown to be in good agreement with more sophisticated methods in the determination of equilibrium geometries, energies, and vibrational modes.[34–37] Based on the very encouraging development of the DFTB approach, we aim to investigate the influence of defects on the electronic structure and magnetic properties of CF. We justify the validity of the DFTB parametrization for pure CF and subsequently investigate the effects of substitutional doping of CF with chemical groups on its electronic and magnetic properties. Our theoretical study shows that when some F atoms are removed, CF becomes a magnetic material and that substituents induce magnetism in the system.

# 2 Computational details

We used the chair configuration of CF because previous first-principles calculations have shown that it is energetically more favorable than other possible conformers.[38,39] The structural optimization and ground-state properties of CF were performed using the spin-polarized self-consistent charge density (SCC-DFTB) method[40] as implemented in the DFTB+ software package.[41,42] This method provides a good compromise between accuracy and computational efficiency, which was proved in the description of molecular and condensed matter systems.[32] Moreover, this method was previously applied for the simulation of various carbon-based materials, in reasonable agreement with experimental data and high-level theoretical methods.[31,43]

After some preliminary tests, we used the pbc-0-3 set[44] from the DFTB Slater–Koster integrals table downloaded from http://www.dftb.org as developed for solids and surfaces. Charge transfers were taken into account through the incorporation of a self-consistency scheme for Mulliken charges based on the second-order expansion of the Kohn–Sham energy in terms of charge-density fluctuations. Self-consistent charges were calculated to a tolerance of $10^{-6}$ a.u. Levels were filled using the Fermi distribution for a system at 300 K. The Broyden method was used for charge mixing. Reciprocal space was represented by a special $k$-point scheme with a Gamma-centered 12 × 12 × 1 Monkhorst–Pack grid[45] for the unit cell ($C_2F_2$). The structures were relaxed without any symmetry constraints. In addition, structures were fully optimized under periodic boundary conditions by using a conjugate gradient algorithm until the residual forces were below $5 \times 10^{-4}$ a.u. We used a vacuum space of 30 Å to avoid direct interactions between adjacent super-cells. In our simulations, we used fully fluorinated graphene as the reference system. Then, to study the effect of F-vacancies and the substitution of a F atom by a chemical group we used a 9 × 9 CF supercell ($C_{162}F_{162}$; Fig. S1, ESI†) and a $\Gamma$-point only setup.

# 3 Results and discussions

## 3.1 Performance of DFTB method for fluorographene

Before the use of any approximate method (such as DFTB) on a certain set of systems, the confirmation of reliable results for some simple representative sample is needed. Here, unperturbed fluorographene (with the $C_2F_2$ unit cell) is a natural choice. Furthermore, we believe that the right DFTB parametrization will be projected onto the reasonable description of large supercells. The calculated geometrical parameters of pristine CF from DFTB are given in Table 1 together with the available experimental and theoretical DFT values. There is a nice agreement between our results and the experimental data. Moreover, the deviations from the DFT-PBE value are low, which ensures the reliability of the present DFTB computations for geometries.

For the discussion of the electronic properties, the band structure of CF and the corresponding density of states are depicted in Fig. 1. It can be seen that the calculations performed using DFTB show a comparable trend to the DFT calculations.[24,27] CF modeled using DFTB is still a wide band gap semiconductor with a direct gap at the $\Gamma$ point. Furthermore, DFT-PBE calculations are known to underestimate the value of the

**Table 1** Summary of CF geometrical parameters (lattice constant $a$, bond lengths $d$ and bond angles) obtained from the DFTB method combined with pbc-0-3 parameters compared with available theoretical and experimental data

| | $a$ (Å) | $d_{C-C}$ (Å) | $d_{C-F}$ (Å) | $\hat{C}\hat{C}\hat{C}$ (°) | $\hat{F}\hat{C}\hat{C}$ (°) |
|---|---|---|---|---|---|
| DFTB | 2.61 | 1.58 | 1.39 | 111.1 | 107.7 |
| DFT-PBE[27] | 2.60 | 1.58 | 1.38 | 110.9 | 108.0 |
| Expt.[46] | 2.60–2.61 | 1.58 | 1.36 | 111.0 | 108.0 |

This journal is © the Owner Societies 2022

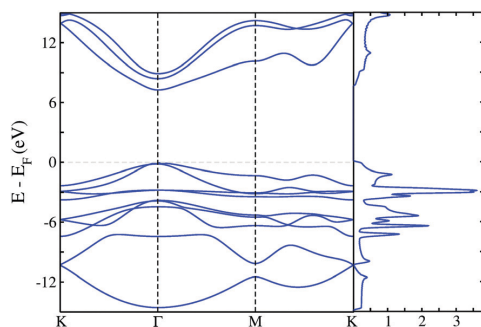*Phys. Chem. Chem. Phys.*, 2022, **24**, 3312–3321 | **3313**

Fig. 1 Electronic band structure (left) and density of states (right) from DFTB calculations combined with pbc-0-3 parameters and corresponding to pristine CF. The Fermi level ($E_F$) is set to zero.
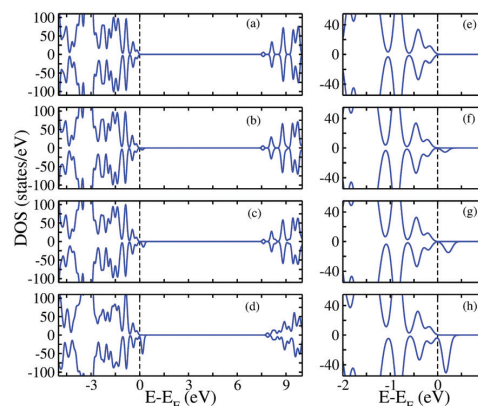


Fig. 2 Electronic density of states of (a) pristine fluorographene and fluorographene containing (b) a point-defect (F-vacancy), (c) a tri-vacancy and (d) a line-defect. (e)–(h) Expanded versions of (a)–(d) in the vicinity of the Fermi level. $9 \times 9$ CF supercells were used in all calculations.

fundamental band gaps (only $\sim 3$ eV in CF),[24,27] which is surprisingly retrieved by current DFTB parametrization. In particular, the present semiempirical DFTB simulations in combination with pbc-0-3 parameters provide a realistic description of the electronic band gap of CF of $E_{gap}^{DFTB}$ = 7.12 eV, which is in excellent agreement with the recent benchmark calculation of the fundamental band gap of fluorographene by Dubecký et al.[17] They found a value of $7.1 \pm 0.1$ eV using two independent approaches, i.e., many-body GW and fixed-node diffusion Monte Carlo (FNDMC) methods. The above results indicate that the high-quality Slater–Koster parameters used for DFTB and our subsequent results on perturbed fluorographene supercells should be of GW/FNDMC quality the concerning electronic properties.

### 3.2 Defects in fluorographene

Defects in CF are naturally produced during the preparation process (see also Section 1). The missing F (as one of the most important defects[10,23–26]) can be the origin of magnetism in the system through leaving an unsaturated dangling bond on the carbon atom, which generates an unpaired electron. The localized state is characterized by an unpaired spin. Therefore, this localized state creates a defect level in the gap and induces spin-polarization in the system. We investigate how different kinds of F-vacancy defects affect the magnetic and electronic properties of CF. We identify the defect levels from the density of states shown in Fig. 2, where it can be seen that defects create states close to the Fermi level. These states almost did not affect the area of the large electronic band gap, which is preserved (cf. Fig. 2(a) vs. Fig. 2(b)–(d)). Then we plot the corresponding spin density distribution in Fig. 3. We consider the case of a single F-vacancy, a tri-vacancy, and a line defect in CF; more types of F-vacancies are presented in the ESI† (including a bigger cluster, an armchair direction defect, and a zigzag direction defect). The structure is relaxed after the vacancies are created. To evaluate the stability of these vacancies, we calculated their vacancy formation energies (see Table S1, ESI†). The calculated formation energy for the point defect (5.32 eV) is in good agreement with DFT calculations from ref. 47. To the best of
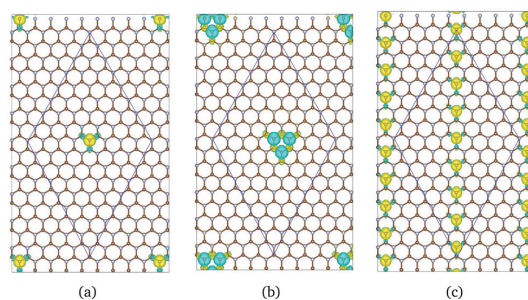


Fig. 3 Distribution of spin densities with the isosurface = $\pm 1 \times 10^{-3}$ atomic units for (a) a point-defect (F-vacancy), (b) a trivacancy, and (c) a line-defect using a $9 \times 9$ supercell for CF. Yellow and cyan indicate positive and negative isosurfaces, respectively. Supercells are depicted by the blue lines.

our knowledge, there are no available data for other types of vacancies considered in the present study.

We plot the spin density distributions for the single F-vacancy in Fig. 3(a), where the difference in charge density between the majority and minority spin occurs only around the vacancy and, thus, the magnetic moment is localized. The defect level appears close to the vicinity of the Fermi level, resulting in a magnetic moment of about 0.97 $\mu_B$. The F-vacancy induces spin-density redistribution and the defect levels have a significant influence on the atoms around the vacancy site. It is clearly seen that the induced magnetic moments are localized on non-fluorinated C atoms, while the fluorinated C atoms and F atoms do not carry any magnetic moments.

Tri-vacancies also form a magnetic configuration, since creating more F-defects involves the breaking of other bonds and induces more magnetization to the system ($m_{tot}$ = 2.99 $\mu_B$). We can see from Fig. 3(b) that the polarized electrons are

3314 | Phys. Chem. Chem. Phys., 2022, 24, 3312–3321

This journal is © the Owner Societies 2022

mainly localized at the non-fluorinated C atoms. The $p_z$ orbitals of F atoms also make a small contribution to the magnetism close to the non-fluorinated C atoms and the fluorinated C atoms make no contributions to the magnetic moments. Moreover, a line defect on CF is another vacancy-type that we considered (Fig. 3(c)). We can see that the appearance of magnetism is due to the empty $p_z$ orbitals of non-fluorinated C atoms, just as with semi-fluorinated graphene.[48]

Based on our analysis (see also Fig. S2 and S3, ESI†), polarized electrons are mainly located at the non-fluorinated C atoms and no magnetic moments are near to the fluorinated C atoms. Therefore, 2p electrons in the non-fluorinated carbon play an important role in magnetism. Yuan *et al.*[10] claimed that the presence of fluorine vacancies, fluorine vacancy clusters, and fluorine armchair and zigzag clusters introduced defect states within the band gap. We have shown that the defect states induce further magnetism on CF. In all cases we showed that magnetic moments couple ferromagnetically (FM) and that the magnetism is independent of the concentration of the vacancies although it is mediated by the unpaired electrons that exist in the fluorographene only. We note that different magnetic orderings are possible too, see Section 3.4.

### 3.3 Adsorption of chemical groups on fluorographene in the position of the F defect

It was shown that it is possible to introduce magnetism in CF by substitution of the defect with a chemical group.[28] Thus, it is not necessary to substitute atoms with transition metal atoms. Recently, the –OH group was identified as an effective $sp^3$-type candidate for inducing robust magnetic moments.[28,49] Here we consider the adsorption of different chemical groups at the position of the F-vacancy. The groups that we have considered are hydroxyl (–OH), nitrile (–CN), and amine (–NH$_2$). Our models are plotted in Fig. 4.

We discuss the effects of the adsorption of a chemical group on the magnetic properties of fluorographene. Through the adsorption of the chemical group, both the chemical group and the CF supercell were changed from non-magnetic (NM) to magnetic matter. However, the magnetic moment of the total system was offset since each component showed the opposite sign. The rearrangement of the under-coordinated carbon atom (caused by the removal of a single fluorine atom) after the adsorption of a chemical group leads to the elimination of the dangling bond (all carbon atoms are of $sp^3$ type). As a result, the magnetic up and down moments are quenched after adsorption of the chemical group, while the magnetic behavior (antiferromagnetic (AFM) alignment) is still well-preserved.

To clarify the changes in the magnetic properties, the spin density of the total system is also presented in Fig. 4. As mentioned above, the different spin density distributions are likely to occur *via* adsorption of the –OH, –CN, and –NH$_2$ chemical groups. The spin density is strongly localized on the chemical group. For –CN adsorption, more remarkable changes in the spin density distributions are observed. The directions of the spin state around the chemical group are opposite. Therefore, their total magnetic moments are equal to zero
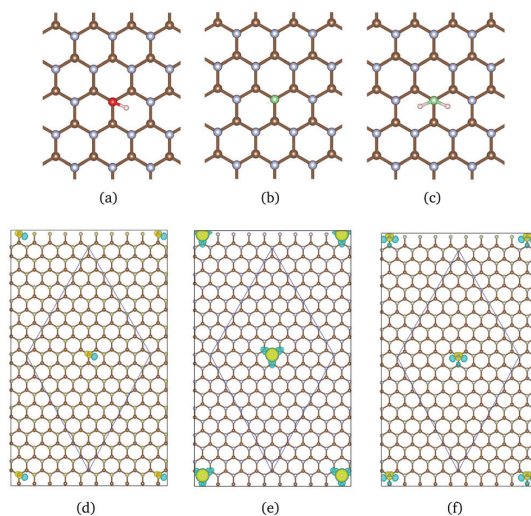


**Fig. 4** Optimized structural models of substitution of the F atom in CF by (a) –OH, (b) –CN, and (c) –NH$_2$ chemical groups. (d)–(f) Corresponding distribution of spin densities with the isosurface = $\pm 2 \times 10^{-4}$ atomic units. Yellow and cyan indicate positive and negative isosurfaces, respectively. Supercells are depicted by the blue lines.

(the antiferromagnetic state). Since the adsorption of a chemical group induces a complete spin polarization on C, this condition can be applied to spintronic devices such, as spin valves, to obtain a giant magnetoresistance effect by changing the electrical resistance.

### 3.4 Systematic study

**3.4.1 Interaction of a single F-vacancy with a F-vacancy/chemical group.** It is interesting to explore the variation in magnetic moments with systems having more than a single F-vacancy. In fact, the interaction of an existing F-vacancy with another F-vacancy or with a chemical group in a CF compound can give rise to a significant magnetic moment. Fig. 5a represents the supercell used to study the interaction of a F-vacancy with another F-vacancy or a chemical group on the CF supercell with the corresponding energies in Fig. 5b. The second created F-vacancy or the adsorbed chemical group is expected at six possible sites (labeled by rings 1–6 in Fig. 5a; the other positions on specific rings are always symmetry-equivalent) and they are created either on the same side (rings 2, 5, and 6) or on the opposite side (rings 1, 3, and 4) of the carbon plane with respect to the fixed F-vacancy. We examine the relative energy ($E - E_0$) for every case as the energetic difference between the total energy of the created F-vacancy or adsorbed chemical group and the total energy of the most stable position ($E_0$) of them for every case.

We found that the interaction of the F-vacancy/chemical group at the first nearest-neighbor shells is strong, meaning that the F-vacancy/chemical group is very local. The second introduced F-vacancy likes to be present close and on the opposite side to the present F-vacancy, and the chemical group
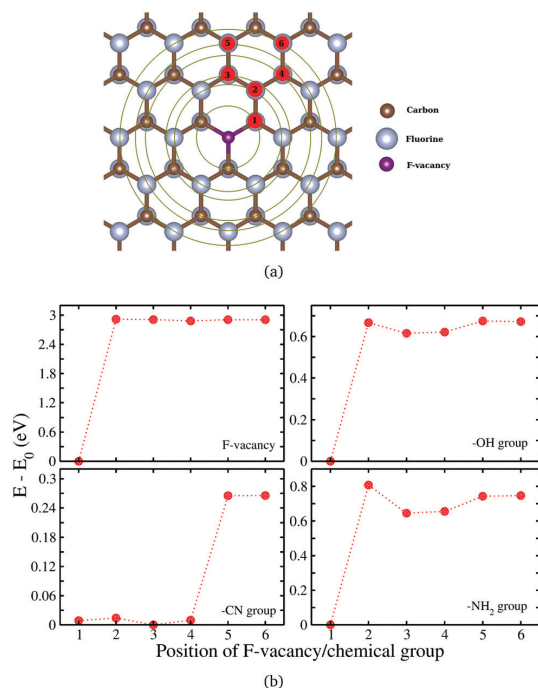
This journal is © the Owner Societies 2022

*Phys. Chem. Chem. Phys.*, 2022, **24**, 3312–3321 | **3315**

(a)



(b)

**Fig. 5** (a) Structure of the interacting F-vacancy and −OH, −CN, and −NH$_2$ groups with a single F-vacancy on the CF supercell, where circles display the possible sites (labeled with numbers) for the second F-vacancy or the adsorption site of the chemical group. Ring 1 represents the nearest neighbors (equivalent positions because of symmetry), ring 2 represents the second nearest neighbors, *etc*. The fixed F-vacancy is in violet. Rings 2, 5, and 6 are on the same side of the existing F-vacancy and rings 1, 3, and 4 are on the opposite side. (b) Corresponding relative energies. Zero energy corresponds to the energy $E_0$ of the most favorable position.

favors being adsorbed on the opposite side from the present F-vacancy. We carefully checked the energetics and magnetic ground-state case of two vacancies in close positions (*i.e.*, *ortho*-, *meta*-, and *para*-configurations as located on rings no. 1, 2, and 3 of Fig. 5a, respectively). The direct comparison of DFTB and DFT AFM, FM, and NM states (Table S2, ESI,† both in a 5 × 5 supercell) provides the same energy order and strong preference of the NM *ortho*-configuration (first ring) followed by AFM (close to FM) configurations in the third and second ring.

Furthermore, the presence of a chemical group nearby the F-vacancy is shown to produce the FM configuration with a total magnetic moment of about 1 $\mu_B$, which indicates the possibility of tuning the magnetization in CF *via* substitution of a F atom by a chemical group in the presence of a F-vacancy. The highest value of the total magnetic moment is found when the chemical group is adsorbed very close to the existing F-vacancy with a magnetic moment of 1.000, 0.998, and 0.999 $\mu_B$ for −CN, −OH, and −NH$_2$, respectively, decreasing slowly with increasing distance from the F-vacancy (*e.g.*, to 0.86 $\mu_B$ for ring no. 5 in the −NH$_2$ case, Table 2). It is worth noting that the relative energy differences corresponding to the different positions of the −OH

**Table 2** Total magnetic moments (in $\mu_B$) of CF containing a single F-vacancy interacting with another F-vacancy (second column) or chemical group (columns 3–5). The considered positions are explained in Fig. 5

| Ring no. | F-vacancy | −CN group | −OH group | −NH$_2$ group |
| --- | --- | --- | --- | --- |
| 1 | 0 (NM) | 1.000 | 0.998 | 0.999 |
| 2 | 1.998 | 0.976 | 0.985 | 0.943 |
| 3 | 1.998 | 0.976 | 0.945 | 0.912 |
| 4 | 1.997 | 0.975 | 0.921 | 0.925 |
| 5 | 1.996 | 0.976 | 0.972 | 0.859 |
| 6 | 2.000 | 0.976 | 0.965 | 0.879 |

and −NH$_2$ groups are not big, up to 0.8 eV, *i.e.*, the total energies are similar in magnitude (Fig. 5b). Moreover, both the first and third neighboring positions of the −CN group are essentially preferred: almost 0.27 eV energy difference corresponds to different −CN positions.

Fig. 6 displays the spin densities of the most stable positions for the interacting F-vacancy with −OH, −CN, or −NH$_2$ chemical groups. The calculated results show that the total magnetic moment arises mainly from the surrounding C and F atoms. The chemical groups that are bonded close to the F-vacancy display FM coupling to the vacancy. In all structures, an FM coupling is clearly visible.

**3.4.2 Interaction of a double F-vacancy with a F-vacancy/ chemical group.** Introducing a third F-vacancy or chemical group in the CF supercell influences the total magnetic moment. We have investigated various possible topological configurations for interacting a double F-vacancy with a F-vacancy/chemical group. The position of the double F-vacancy was chosen according to the previous paragraph. The first neighbor of the fixed single F-vacancy was shown to be the most stable according to the previous paragraph. We take this situation as a reference (violet color in Fig. 7a) to study the interaction of a double F-vacancy with a third F-vacancy or chemical group. We adopt the same strategy for the study of the evaluation of the stability of the third created F-vacancy or adsorbed chemical group on various sites in the presence of a double fixed F-vacancy. The topological
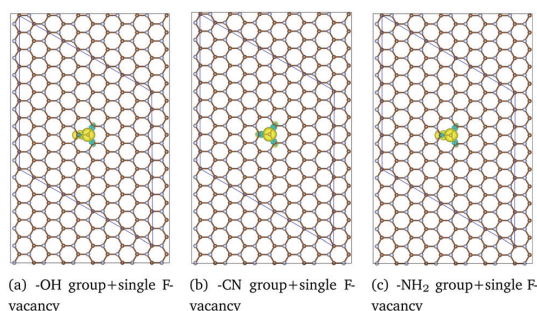


(a) -OH group+single F-vacancy  (b) -CN group+single F-vacancy  (c) -NH$_2$ group+single F-vacancy

**Fig. 6** Distribution of spin densities of CF in the presence of an interacting F-vacancy or chemical group (−OH, −CN or −NH$_2$) with a single F-vacancy in the most favorable positions with the isosurface = ±2 × 10$^{-4}$ atomic units for the (a) −OH, (b) −CN and (c) −NH$_2$ group in the first ring. Yellow and cyan indicate positive and negative isosurfaces, respectively. Supercells are depicted by the blue lines.
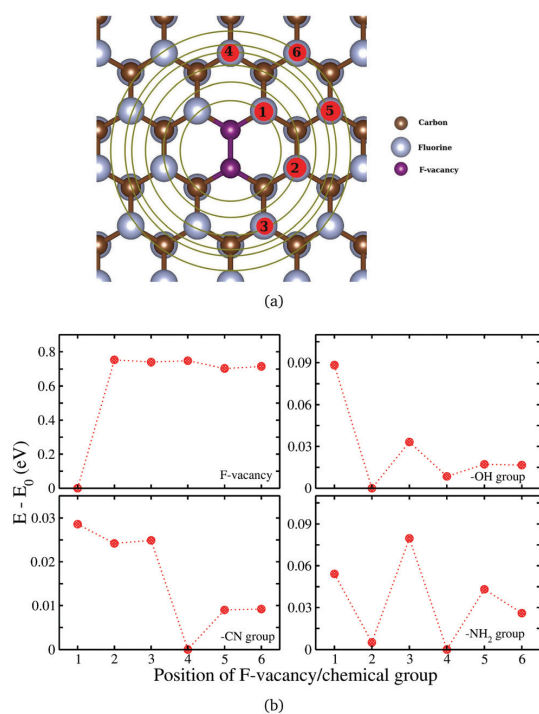
**3316** | *Phys. Chem. Chem. Phys.*, 2022, **24**, 3312–3321

This journal is © the Owner Societies 2022

Fig. 7 (a) CF supercell in the presence of an interacting F-vacancy or −OH, −CN, and −NH₂ groups with a double F-vacancy, where the circles display the possible sites (labeled with numbers) for the third F-vacancy or the adsorbed chemical group. The fixed double F-vacancy is in violet. (b) Corresponding relative energies. Zero energy corresponds to the energy $E_0$ of the most favorable position.

configurations of the structure are shown in Fig. 7a (again, a particular ring includes all symmetry-equivalent positions).

The third introduced F-vacancy prefers to be created in the first ring on the opposite side to the closest F-vacancy, while the chemical group likes to be adsorbed on the second and the fourth rings. The energy range between the different positions (possibilities) is about 0.8 eV for the created F-vacancy and less than 0.1 eV for the adsorbed chemical group, indicating that the adsorption of the chemical group in the presence of a double F-vacancy can occur on all sites.

The interaction of a double F-vacancy with another F-vacancy tends to ferrimagnetic (FiM) ordering with a magnetic moment of about 1 $\mu_B$. However, the interaction with a chemical group is non-magnetic. In Fig. 11b, we plot the spin density distribution of a interacting double F-vacancy with a F-vacancy. A significant portion of the spin density is localized around the three F-vacancies and between them, with two of them being coupled antiferromagnetically and the FM configuration with a total magnetic moment of 1 $\mu_B$ is caused by the unpaired electron of the third introduced F-vacancy.

**3.4.3 Interaction of a triple F-vacancy with a F-vacancy/ chemical group.** We investigated various possibilities for the interaction of a F-vacancy/chemical group with a triple fixed

F-vacancy. The positions are chosen according to the previous paragraph. The CF supercell containing a triple fixed F-vacancy and the corresponding relative energies are shown in Fig. 8. Numbers from 1 to 6 represent the different possibilities studied in the present work and we note that we followed the same methodology explained in the previous two paragraphs (only because of the complexity do we omit the drawing of equivalent positions in Fig. 8a). Position no. 3 (the zigzag direction) is slightly more energetically preferred over position no. 2 (the armchair direction) created by the F-vacancy, while the chemical groups are adsorbed on the second or fourth sites. The created F-vacancy gives rise to a magnetic moment of about 2 $\mu_B$ when created at positions 1, 4, 5, and 6. However, at positions 2 and 3 an NM structure is shown (see also Table 3). Moreover, according to Table 3, the structures of the interacting triple F-vacancy with a chemical group (–OH, –CN, or NH₂) have a magnetic moment of 0.99 $\mu_B$.

In Fig. 9 we plot the distribution of spin densities for the identified most stable position of the interacting F-vacancy/ chemical group with the triple fixed F-vacancy. We notice that the different spin density distributions are likely to occur for the adsorbed groups and contributions are only induced at their nearest atoms. The spin density was strongly localized on
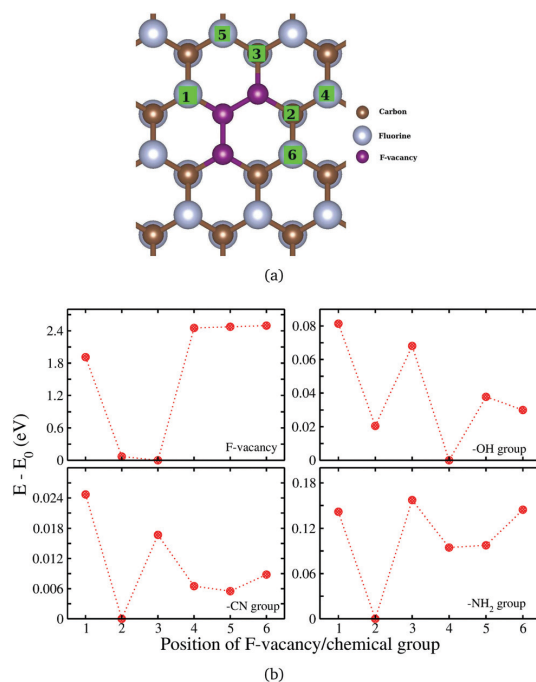


Fig. 8 (a) CF supercell in the presence of an interacting F-vacancy or −OH, −CN, or −NH₂ groups with a triple fixed F-vacancy, where the numbers display the possible sites for the fourth introduced F-vacancy or the adsorbed chemical group. The fixed triple F-vacancy is in violet. (b) Corresponding relative energies. Zero energy corresponds to the energy $E_0$ of the most favorable position.

This journal is © the Owner Societies 2022

*Phys. Chem. Chem. Phys.*, 2022, **24**, 3312–3321 | **3317**

**Table 3** Total magnetic moments (in $\mu_B$) of CF containing a triple F-vacancy interacting with another F-vacancy (second column) or chemical group (columns 3–5)

| Ring no. | F-vacancy | –CN group | –OH group | –NH$_2$ group |
|----------|-----------|-----------|-----------|---------------|
| 1 | 2.00 | 0.99 | 0.99 | 0.99 |
| 2 | NM | 0.99 | 0.99 | 0.99 |
| 3 | NM | 0.99 | 0.99 | 0.99 |
| 4 | 1.99 | 0.99 | 0.99 | 0.99 |
| 5 | 1.99 | 0.99 | 0.99 | 0.99 |
| 6 | 2.00 | 0.99 | 0.99 | 0.99 |

the adsorbed chemical group and the created F-vacancies. The adsorption of a chemical group led to local polarization of the system. In addition, when the F-vacancies are not distributed equally on both sides they show an FM state.

Finally, we note that the bulk of the band gap ($\sim 7$ eV) was similar for all studied configurations (as in Fig. 2), *i.e.*, we studied various magnetic configurations, which induced rather small perturbations in the CF electronic structure.

### 3.5 Defluorination path

From Section 3.4.3, we noticed that the zigzag-direction is expected to be more preferred for the defluorination of fluorographene. To gain further understanding of the mechanism for the defluorination of fluorographene, we go further in our investigations by studying the interaction of 2, 3, 4, 5, and 6 F-vacancies. We start by considering the interaction of a single F-vacancy with another F-vacancy. The most stable configuration was chosen for studying the interaction of a double F-vacancy with a F-vacancy. Moreover, we follow the same reasoning as for the rest. Different spin orientations were considered as shown in ESI,† Table S3. The topological configurations of the structure are shown in the ESI,† Fig. S4 with the corresponding total magnetic moments listed in ESI,† Table S3. The ordering of spins of the localized states is defined by the distance to the defects and the distribution of those sites on both sides of the graphene plane. We show that the preferential "zigzag"-direction evolution during defluorination is likely to occur as represented in Fig. 10.



(a) -CN group+three F-vacancies

(b) -OH group+three F-vacancies

(c) -NH$_2$ group+three F-vacancies
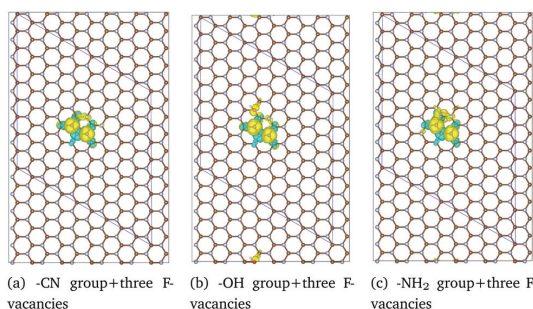
**Fig. 9** Distribution of spin densities of the CF in the presence of interacting (a) –CN, (b) –OH and (c) –NH$_2$ groups with a triple fixed F-vacancy for the most stable positions with the isosurface = $\pm 3 \times 10^{-4}$ atomic units. Spin-up and spin-down densities are shown in yellow/cyan. Supercells are depicted by the blue lines.
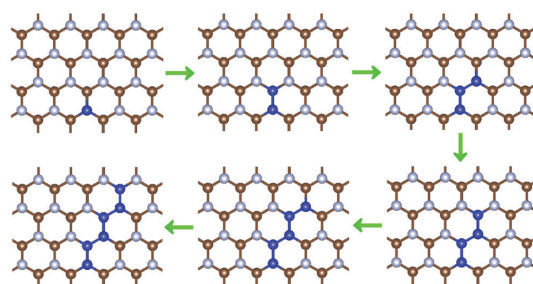


**Fig. 10** Defluorination path on fluorographene. The preferred defluorination pathway is the zigzag direction as shown in blue. The reader may refer to the ESI† for more details.

This result may be confirmed *via* an experimental study. Moreover, depending on the number and the position of the F-vacancies and their distribution around the graphene cell, the NM, FM, AFM and ferrimagnetic (FiM) ordering are possibilities. For the most stable positions, the NM structure is preferred for an even number, while FiM alignment is favored for an odd number of F-vacancies; *e.g.*, in the case of three F-vacancies on CF, the local magnetic moments on each of the vacancies are 0.54, −0.11, and 0.54 $\mu_B$, and for five F-vacancies they are 0.37, −0.08, 0.43, −0.08, and 0.37 $\mu_B$, *etc.*, see ESI,† Table S4. An AFM ordering is shown for some less stable positions.

We note that we come to the same conclusion as in the work of Tucek *et al.*,[47] in which the authors claimed that the defluorination pathways follow a zigzag direction by using a $3 \times 3$ supercell. In our study, we considered a $9 \times 9$ supercell, which is a very big supercell. We show that the introduced F-vacancy prefers to be created close to the existing/fixed F-vacancies following a zigzag direction. Moreover, such results may strengthen the validity of the computational models based on the DFTB formalism for the fluorographene system. We calculated the magnetic moments on the C atoms in zigzag chains of F-vacancies (from three to nine F-vacancies) using the DFTB and DFT methods (see Table S4 and Fig. S5, ESI†). Direct comparison of the $9 \times 9$ supercell used in DFTB and the $7 \times 7$ supercell used in DFT provided magnetic moments on C sites that were in perfect agreement (as collected in Table S4, ESI†).

The respective spin densities of the three, five, seven, and nine F-vacancies on fluorinated graphene formed into zigzag chains are listed in Fig. 11. The spin densities are mainly located at the non-fluorinated carbon atoms. Vacancies in the same sub-lattice show the same spin direction, which is opposite to the F-vacancy on the opposite side, leading to a magnetic alignment due to the odd number of F-defects, and the spin density is distributed along the zigzag-direction. It is worthy of note that for odd numbers of F-vacancies, there is always one unpaired electron in sum and a total magnetic moment of 1 $\mu_B$ per unit cell; however, the ground state is always ferrimagnetic (FiM; *i.e.*, the local magnetic moments on the C-sites in one sub-lattice are larger in magnitude than in another sub-lattice). For unit cells containing an even number of F-vacancies, the complete pairing of electrons produces no net magnetic moment
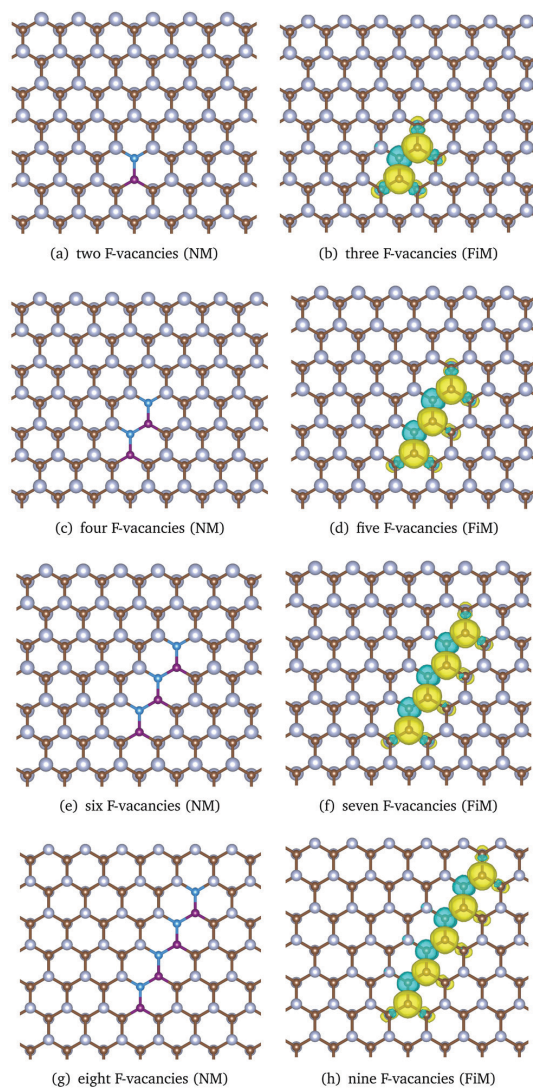
**3318** | *Phys. Chem. Chem. Phys.*, 2022, **24**, 3312–3321

This journal is © the Owner Societies 2022

(a) two F-vacancies (NM)

(b) three F-vacancies (FiM)

(c) four F-vacancies (NM)

(d) five F-vacancies (FiM)

(e) six F-vacancies (NM)

(f) seven F-vacancies (FiM)

(g) eight F-vacancies (NM)

(h) nine F-vacancies (FiM)

**Fig. 11** Isosurfaces of the spin density difference when (a)–(h) two–nine F-vacancies are introduced on CF following the zigzag-direction. The range of isovalues is set at $8 \times 10^{-4}$ atomic units. The yellow and cyan hypersurfaces show contours of positive and negative magnetization density, respectively. The violet and blue colors refer to F-vacancies on opposite sides of the carbon plane.

in the unit cell because, in the zigzag-direction, the F-vacancies are adjacent to one another.

Finally, we checked the stability of the zigzag chains with respect to the back-adsorption of fluorine atoms. If the zigzag ferromagnetic chain is attacked by one fluorine atom, the resulting state is dependent on the C-site position, which is achieved. Whereas the division into two sub-chains with an odd number of empty C-sites leads to two ferrimagnetic entities (the total magnetic moment of the supercell is 0 or 2 $\mu_B$), in the

case of two sub-chains with an even number of empty C-sites this results in two non-magnetic sub-chains (see example in ESI† Fig. S6). Ferrimagnetic zigzag chains, therefore, seem like an important stable magnetic motif in perturbed fluorographene. Interestingly, it is quite easy to control the magnetic state, *via* the length of the F-vacancy chains. Or switch on/off the magnetic ordering *via* the absorption/desorption of fluorine atoms.

# 4 Conclusions

In this paper, we discussed the effect of F-vacancies and the substitution of a F atom with a chemical group (–OH, –CN, or –NH$_2$) using the DFTB method. We show that defects in CF materials have a pronounced impact on the local magnetic properties, while the electronic properties are not significantly changed. First, we considered several vacancy configurations, such as a single F-vacancy, a trivacancy, and line vacancy defects, then we substitutes a F atom with a chemical group, and finally we examined the magnetic properties of the inter-acting F-vacancy/chemical group with the F-vacancy on CF with several possible adsorption sites. The created F-vacancies like to be located close to the fixed vacancies and show non-magnetic (NM), ferromagnetic (FM) or antiferromagnetic (AFM) ordering depending on their number.

It is possible to tune the magnetic structure of the CF by creating an interacting F-vacancy or adsorbed chemical group with the existing F-vacancy. Moreover, our results show that a substitutional chemical group is an effective way to modulate the electronic and magnetic properties of the CF monolayer, which may be used for spintronics and other potential applications. Moreover, we show that the zigzag-like direction is most preferred for defluorination and NM, FM, AFM and ferrimagnetic (FiM) structures result, depending on the number of F-vacancies and their distribution around the fluorographene cell. Ferrimagnetic zigzag chains are a basic stable magnetic motif in perturbed fluorographene and can be driven by F-atom desorption/adsorption. These findings may open a new venue in the field of spintronics in CF-based 2D materials.

On the other hand, we conclude that studies performed at the DFTB level of theory are sufficiently accurate for the description of fluorographene, fluorographene with defects, and magnetism in fluorographene at much lower costs. The description is reliable despite being an approximate method with a set of parametrized computational models that require careful para-metrization before application. The computational efficiency of DFTB enables us to consider systems with hundreds of atoms.

# Conflicts of interest

There are no conflicts to declare.

# Acknowledgements

This journal is © the Owner Societies 2022

*Phys. Chem. Chem. Phys.*, 2022, **24**, 3312–3321 | **3319**

# References

1 K. S. Novoselov, A. K. Geim, S. V. Morozov, D. Jiang, Y. Zhang, S. V. Dubonos, I. V. Grigorieva and A. A. Firsov, *Science*, 2004, **306**, 666–669.

2 A. K. Geim and K. S. Novoselov, *Nat. Mater.*, 2007, **6**, 183–191.

3 A. H. Castro Neto, F. Guinea, N. M. R. Peres, K. S. Novoselov and A. K. Geim, *Rev. Mod. Phys.*, 2009, **81**, 109–162.

4 F. Schwierz, *Nat. Nanotechnol.*, 2010, **5**, 487–496.

5 F. Schedin, A. K. Geim, S. V. Morozov, E. W. Hill, P. Blake, M. I. Katsnelson and K. S. Novoselov, *Nat. Mater.*, 2007, **6**, 652–655.

6 T. Wehling, M. Katsnelson and A. Lichtenstein, *Chem. Phys. Lett.*, 2009, **476**, 125–134.

7 Ž. Šljivančanin, A. S. Milošević, Z. S. Popović and F. R. Vukajlović, *Carbon*, 2013, **54**, 482–488.

8 J. L. Cheng, C. Salazar and J. E. Sipe, *Phys. Rev. B: Condens. Matter Mater. Phys.*, 2013, **88**, 045438.

9 S. Putz, M. Gmitra and J. Fabian, *Phys. Rev. B: Condens. Matter Mater. Phys.*, 2014, **89**, 035437.

10 S. Yuan, M. Rösner, A. Schulz, T. O. Wehling and M. I. Katsnelson, *Phys. Rev. Lett.*, 2015, **114**, 047403.

11 H. Sahin, M. Topsakal and S. Ciraci, *Phys. Rev. B: Condens. Matter Mater. Phys.*, 2011, **83**, 115432.

12 R. R. Nair, W. Ren, R. Jalil, I. Riaz, V. G. Kravets, L. Britnell, P. Blake, F. Schedin, A. S. Mayorov, S. Yuan, M. I. Katsnelson, H.-M. Cheng, W. Strupinski, L. G. Bulusheva, A. V. Okotrub, I. V. Grigorieva, A. N. Grigorenko, K. S. Novoselov and A. K. Geim, *Small*, 2010, **6**, 2877–2884.

13 J. T. Robinson, J. S. Burgess, C. E. Junkermeier, S. C. Badescu, T. L. Reinecke, F. K. Perkins, M. K. Zalalutdniov, J. W. Baldwin, J. C. Culbertson, P. E. Sheehan and E. S. Snow, *Nano Lett.*, 2010, **10**, 3001–3005.

14 R. Zbořil, F. Karlický, A. B. Bourlinos, T. A. Steriotis, A. K. Stubos, V. Georgakilas, K. Šafářová, D. Jančík, C. Trapalis and M. Otyepka, *Small*, 2010, **6**, 2885–2891.

15 F. Karlický, R. Zbořil and M. Otyepka, *J. Chem. Phys.*, 2012, **137**, 034709.

16 F. Karlický, K. Kumara Ramanatha Datta, M. Otyepka and R. Zbořil, *ACS Nano*, 2013, **7**, 6434–6464.

17 M. Dubecký, F. Karlický, S. Minárik and L. Mitas, *J. Chem. Phys.*, 2020, **153**, 184706.

18 Y. Yang, G. Lu, Y. Li, Z. Liu and X. Huang, *ACS Appl. Mater. Interfaces*, 2013, **5**, 13478–13483.

19 V. Mazánek, O. Jankovský, J. Luxa, D. Sedmidubský, Z. Janoušek, F. Šembera, M. Mikulics and Z. Sofer, *Nanoscale*, 2015, **7**, 13646–13655.

20 E. Bordes, J. Szala-Bilnik and A. Padua, *Faraday Discuss.*, 2018, **206**, 61–75.

21 O. Jankovský, V. Mazánek, K. Klímová, D. Sedmidubský, J. Kosina, M. Pumera and Z. Sofer, *Chem. – Eur. J.*, 2016, **22**, 17696–17703.

22 K.-J. Jeon, Z. Lee, E. Pollak, L. Moreschini, A. Bostwick, C.-M. Park, R. Mendelsberg, V. Radmilovic, R. Kostecki, T. J. Richardson and E. Rotenberg, *ACS Nano*, 2011, **5**, 1042–1046.

23 B. Wang, J. Wang and J. Zhu, *ACS Nano*, 2014, **8**, 1862–1870.

24 F. Karlický and M. Otyepka, *J. Chem. Theory Comput.*, 2013, **9**, 4155–4164.

25 R. R. Nair, M. Sepioni, I.-L. Tsai, O. Lehtinen, J. Keinonen, A. V. Krasheninnikov, T. Thomson, A. K. Geim and I. V. Grigorieva, *Nat. Phys.*, 2012, **8**, 199–202.

26 M. Medved', G. Zoppellaro, J. Ugolotti, D. Matochová, P. Lazar, T. Pospíšil, A. Bakandritsos, J. Tuček, R. Zbořil and M. Otyepka, *Nanoscale*, 2018, **10**, 4696–4707.

27 F. Karlický and M. Otyepka, *Ann. Phys.*, 2014, **526**, 408–414.

28 J. Tuček, K. Holá, A. B. Bourlinos, P. Błoński, A. Bakandritsos, J. Ugolotti, M. Dubecký, F. Karlický, V. Ranc, K. Čépe, M. Otyepka and R. Zbořil, *Nat. Commun.*, 2017, **8**, 14525.

29 M. Elstner, D. Porezag, G. Jungnickel, J. Elsner, M. Haugk, T. Frauenheim, S. Suhai and G. Seifert, *Phys. Rev. B: Condens. Matter Mater. Phys.*, 1998, **58**, 7260–7268.

30 T. Frauenheim, G. Seifert, M. Elsterner, Z. Hajnal, G. Jungnickel, D. Porezag, S. Suhai and R. Scholz, *Phys. Status Solidi B*, 2000, **217**, 41–62.

31 A. Enyashin and A. Ivanovskii, *Chem. Phys. Lett.*, 2013, **576**, 44–48.

32 H. Manzano, A. N. Enyashin, J. S. Dolado, A. Ayuela, J. Frenzel and G. Seifert, *Adv. Mater.*, 2012, **24**, 3239–3245.

33 E. Posenitskiy, M. Rapacioli, B. Lepetit, D. Lemoine and F. Spiegelman, *Phys. Chem. Chem. Phys.*, 2019, **21**, 12139–12149.

34 A. A. Artyukh, I. A. Mikhailov and L. A. Chernozatonskii, *JETP Lett.*, 2018, **107**, 66–71.

35 T. O. Wehling, B. Grundkötter-Stock, B. Aradi, T. Frauenheim and T. Niehaus, *Phys. Rev. B: Condens. Matter Mater. Phys.*, 2014, **90**, 085422.

36 P. Wagner, V. V. Ivanovskaya, M. Melle-Franco, B. Humbert, J.-J. Adjizian, P. R. Briddon and C. P. Ewels, *Phys. Rev. B: Condens. Matter Mater. Phys.*, 2013, **88**, 094106.

37 S. Irle, G. Zheng, Z. Wang and K. Morokuma, *J. Phys. Chem. B*, 2006, **110**, 14531–14545.

38 D. K. Samarakoon, Z. Chen, C. Nicolas and X.-Q. Wang, *Small*, 2011, **7**, 965–969.

39 O. Leenaerts, H. Peelaers, A. D. Hernández-Nieves, B. Partoens and F. M. Peeters, *Phys. Rev. B: Condens. Matter Mater. Phys.*, 2010, **82**, 195409.

40 M. Elstner, D. Porezag, G. Jungnickel, J. Elsner, M. Haugk, T. Frauenheim, S. Suhai and G. Seifert, *Phys. Rev. B: Condens. Matter Mater. Phys.*, 1998, **58**, 7260–7268.

41 B. Aradi, B. Hourahine and T. Frauenheim, *J. Phys. Chem. A*, 2007, **111**, 5678–5684.

42 B. Hourahine, B. Aradi, V. Blum, F. Bonafé, A. Buccheri, C. Camacho, C. Cevallos, M. Y. Deshaye, T. Dumitrică,

**3320** | *Phys. Chem. Chem. Phys.*, 2022, **24**, 3312–3321

This journal is © the Owner Societies 2022

A. Dominguez, S. Ehlert, M. Elstner, T. van der Heide, J. Hermann, S. Irle, J. J. Kranz, C. Köhler, T. Kowalczyk, T. Kubař, I. S. Lee, V. Lutsker, R. J. Maurer, S. K. Min, I. Mitchell, C. Negre, T. A. Niehaus, A. M. N. Niklasson, A. J. Page, A. Pecchia, G. Penazzi, M. P. Persson, J. Řezáč, C. G. Sánchez, M. Sternberg, M. Stöhr, F. Stuckenberg, A. Tkatchenko, V. W.-Z. Yu and T. Frauenheim, *J. Chem. Phys.*, 2020, **152**, 124101.

43 A. Enyashin, V. Bamburov and A. Ivanovskii, *Dokl. Phys. Chem.*, 2012, **442**, 1–4.

44 C. Köhler and T. Frauenheim, *Surf. Sci.*, 2006, **600**, 453–460.

45 H. J. Monkhorst and J. D. Pack, *Phys. Rev. B: Solid State*, 1976, **13**, 5188–5192.

46 Y. Sato, K. Itoh, R. Hagiwara, T. Fukunaga and Y. Ito, *Carbon*, 2004, **42**, 2897–2903.

47 J. Tuček, K. Holá, G. Zoppellaro, P. Błoński, R. Langer, M. Medved', T. Susi, M. Otyepka and R. Zbořil, *ACS Nano*, 2018, **12**, 12847–12859.

48 Y. Ma, Y. Dai, M. Guo, C. Niu, L. Yu and B. Huang, *Nanoscale*, 2011, **3**, 2301–2306.

49 D. Matochová, M. Medved', A. Bakandritsos, T. Steklý, R. Zbořil and M. Otyepka, *J. Phys. Chem. Lett.*, 2018, **9**, 3580–3585.

This journal is © the Owner Societies 2022

*Phys. Chem. Chem. Phys.*, 2022, **24**, 3312–3321 | **3321**

# Supplementary Material 7

## PAPER

Check for updates

# The electronic and optical properties of III−V binary 2D semiconductors: how to achieve high precision from accurate many-body methods†

Miroslav Kolos [ID] and František Karlický [ID] *

Seven hexagonal 2D materials consisting of elements of the IIIA and VA groups (BN, BP, BAs, AlN, GaN, GaP, and GaAs) were theoretically studied using first-principles methods. Simultaneous convergence in all principal parameters of the accurate many-body perturbational GW approach and the subsequent Bethe−Salpeter equation (BSE) was necessary to achieve precise fundamental and optical gaps, exciton binding energies, and absorbance spectra. Various convergence rates of studied properties in the case of different materials were visualized and explained. Benchmark calculations show several 2D materials from this set that strongly absorb in the visible and ultraviolet parts of the spectra, and therefore can be promising materials for (opto)electronic applications.

## 1 Introduction

Layered hexagonal materials are promising for new electronics applications. Accurate theoretical estimations of the optical and electronic properties of these materials with good precision are needed to consider the usability of these materials in new modern devices. We made a set of benchmark calculations of 2D hexagonal materials made from IIIA and VA group elements by making seven combinations of atoms from rows 2–4 in these groups. Our set of 2D materials is boron nitride (BN), boron phosphide (BP), boron arsenide (BAs), aluminum nitride (AlN), gallium nitride (GaN), gallium phosphide (GaP), and gallium arsenide (GaAs). These materials are semiconductors/insulators with an electronic band gap range of *ca.* 1.6 eV to 7 eV and with mostly strong excitonic effects. These materials are promising in (opto)electronics with the possibility of tuning their band gaps, for instance, by making vdW heterostructures with another 2D material.[1–4] Except for BN, which has been studied intensely in many studies (including many-body methods used[5–16]), there are only rare theoretical estimations of the electronic and optical properties of these materials[5,16–23] (we summarized the available values in Table 1), so we assume there is immense importance in doing such studies. On the experimental side, measurements on free-standing monolayers are not yet fully established, and currently cannot provide

reliable optical/fundamental gaps for applications and for cross-validating the existing theoretical estimations. We explicitly mention some experimental band gap measurements concerning materials (or material-based heterostructures) from this set: a BN/graphite indirect electronic gap of $6.8 \pm 0.2$ eV[24] and an optical gap of 6.1 eV;[24] an AlN electronic gap of $9.2 \pm 0.1$ eV;[25] a GaN/Al$_{0.65}$Ga$_{0.35}$N optical gap of 4.79 eV;[26] and a MoS$_2$/GaN electronic gap of 3.4 eV.[27]

To obtain accurate electronic properties from theoretical *ab initio* calculations, it is crucial to correctly treat the electron–electron interaction using many-body methods, such as computationally demanding GW perturbation theory. Moreover, in particular for 2D materials, it is essential to distinguish between the optical and electronic band gaps because of the intense excitonic binding energy. To calculate the excitonic effects (electron–hole interaction), one needs to solve the Bethe–Salpeter equation (BSE). These methods can give the required properties comparable to the experiment. However, to achieve precise results using GW and BSE calculations, a careful convergence study of various parameters must be

*Department of Physics, Faculty of Science, University of Ostrava, 30. dubna 22, 701 03, Ostrava, Czech Republic. E-mail: frantisek.karlicky@osu.cz; Tel: +420 553 46 2155*

**Table 1** Available quasiparticle gaps from GW calculations $E_{\text{gap}}^{\text{GW}}$, optical gaps from BSE calculations $E_{\text{gap}}^{\text{BSE}}$ and exciton binding energies $E_{\text{b}}^{\text{exc}}$ of III−V binary 2D semiconductors

| Material | $E_{\text{gap}}^{\text{GW}}$ | $E_{\text{gap}}^{\text{BSE}}$ | $E_{\text{b}}^{\text{exc}}$ |
|---|---|---|---|
| BN | 6.7–7.74[5–16] | 5.02–5.81[6–9,16] | 1.6–2.71[6–9,16] |
| BP | 1.67[17] | | |
| AlN | 5.19–5.80[5,16,18,19] | 4.02[18,19] 4.60[16] | 1.90–2.05[16,18,19] |
| GaN | 4.10–4.55[5,16,18,20–22] | 3.10–3.46[16,18,20,21] | 1.20–1.38[16,18,21] |
| GaAs | 2.95[23] | 1.85[23] | 1.10[23] |

This journal is © the Owner Societies 2022

*Phys. Chem. Chem. Phys.*, 2022, **24**, 27459–27466 | **27459**

performed.[28–36] Here, we provide the following for all considered hexagonal III–V binary 2D semiconductors: the benchmark values of fundamental and optical gaps, exciton binding energies, and precise absorbance spectra. In addition, we rationalize and visualize the convergence rate of studied properties depending on various numerical parameters such as the density of $k$-point sampling, the basis set size, or the vacuum layer thickness in the direction perpendicular to the 2D material.

## 2 Methods

The Vienna *ab initio* simulation package (VASP)[37] implementing the projector augmented wave (PAW) method[37,38] is used in all calculations. GW sets of PAWs are used with the s and p electrons explicitly treated for all elements excluding Ga, where the d electrons were explicitly included in the calculations (for specific PAW potentials used, see Table S1, ESI†). Atomic positions are relaxed using density functional theory (DFT) implementing the Perdew, Burke, and Ernzerhof (PBE) density functional[39] using the conjugate gradient algorithm until the change in forces is less than $10^{-3}$ eV Å$^{-1}$, an electronic step condition for the SCF convergence is $10^{-7}$ eV, and the cut-off energy of the plane-wave basis set is $E_{cut} = 800$ eV. The lattice vibrational frequencies are calculated using the PBE density functional and the finite displacement method with a displacement of 0.01 Å in the Phonopy program.[40]

For electronic properties, we use the GW approximation (based on Green's function $G$ and the screened Coulomb potential $W$) with input orbitals $|n\boldsymbol{k}\rangle$ from PBE. That is, quasiparticle energies $\varepsilon_{n\boldsymbol{k}}^{GW}$ are calculated as first-order corrections to the DFT single-particle energies $\varepsilon_{n\boldsymbol{k}}$

$$\varepsilon_{n\boldsymbol{k}}^{QP,0} = \varepsilon_{n\boldsymbol{k}} + Z_{n\boldsymbol{k}}\mathrm{Re}[\langle n\boldsymbol{k}|T + V_{n-e} + V_H + \Sigma(G, W; \varepsilon_{n\boldsymbol{k}})|n\boldsymbol{k}\rangle - \varepsilon_{n\boldsymbol{k}}]$$
(1)

where $n$ is the band index, $\boldsymbol{k}$ is the Bloch vector, $Z$ is the normalization factor,[41] $T$ is the kinetic energy operator, $V_{n-e}$ is the potential of the nuclei, and $V_H$ is the Hartree potential. Henceforth, the corresponding single-shot energies are referred to as $G_0W_0$. The quasiparticle gap is computed as $E_{gap}^{indir} = \varepsilon_{CBM}^{QP} - \varepsilon_{VBM}^{QP}$, where the CBM stands for the conduction band minimum and the VBM stands for the valence band maximum, respectively. The break condition for the electronic step is an energy difference of $1 \times 10^{-7}$ eV and the energy cut-off is $E_{cut} = 600$ eV. Excitonic effects are accounted for by the Bethe–Salpeter equation,[42] which corresponds to the excitonic equation (eigenvalue problem)[43–45]

$$\left(\varepsilon_{c\boldsymbol{k}}^{QP} - \varepsilon_{v\boldsymbol{k}}^{QP}\right)A_{cv\boldsymbol{k}}^S + \sum_{c'v'\boldsymbol{k'}}[2\langle c\boldsymbol{k}v\boldsymbol{k}|\nu|c'\boldsymbol{k'}v'\boldsymbol{k'}\rangle - \langle c\boldsymbol{k}c'\boldsymbol{k'}|W|v\boldsymbol{k}v'\boldsymbol{k'}\rangle]A_{c'v'\boldsymbol{k'}}^S$$
$$= E_{exc}^S A_{cv\boldsymbol{k}}^S$$
(2)

where $c$ and $v$ represent the band indexes of the conduction and valence bands, respectively. The $A_{vc\boldsymbol{k}}^S$ values are obtained by diagonalization of eqn (2) and correspond to the amplitudes of
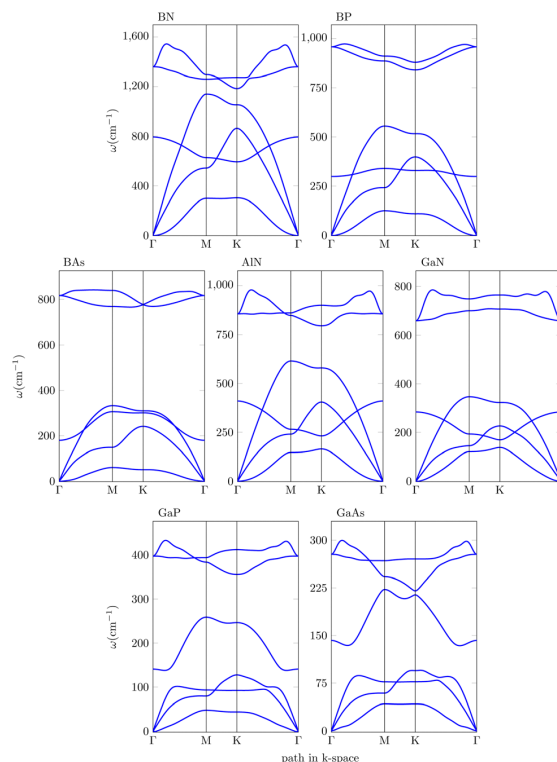


**Fig. 1** Lattice vibration dispersion along the Brillouin zone of seven materials.

a free electron–hole pair configuration composed of the electron state $|c\boldsymbol{k}\rangle$ and the hole state $|v\boldsymbol{k}\rangle$; the $E_{exc}^S$ values are eigenenergies corresponding to exciton excitation energies (with optical gap $E_{opt}^{gap} \equiv E_{exc}^S$), and $\nu$ is the Coulomb kernel, $1/|\boldsymbol{r} - \boldsymbol{r'}|$. After computing the energy-dependent dielectric function, we determine the actual optical absorbance[1] $A(E) = 1 - \exp(-\varepsilon_{im}(E)EL_z/\hbar c)$, where $\varepsilon_{im}$ is the imaginary part of the dielectric function, $E$ is the energy of the photon, $L_z$ is the height of the computational unit cell, $\hbar$ is the reduced Planck constant and $c$ is the speed of light.

## 3 Results and discussion

The studied materials have a hexagonal planar structure, but two materials from this set, GaP and GaAs, have a buckled out-of-plane structure, as shown in a previous study[46] with buckling heights of $h = 0.41$ Å and $h = 0.59$ Å, respectively. The optimized $a$ lattice constants are collected in Table 2 and are in the range from 2.511 Å (BN) to 4.054 Å (GaAs). The phonon spectra of optimized geometries are shown in Fig. 1, and the corresponding supercell sizes necessary for phonon calculations are reported in Table S2 (ESI†). The buckled structures (GaP and GaAs) are distinguished by clearly separated low-frequency acoustic phonon branches (up to $\sim 130$ cm$^{-1}$) from optical phonon branches (bottom of Fig. 1), while the lowest optical

**27460** | *Phys. Chem. Chem. Phys.*, 2022, **24**, 27459–27466

This journal is © the Owner Societies 2022

**Table 2** Accurate values of indirect gaps $E_{\text{gap}}^{\text{indir}}$, direct gaps $E_{\text{gap}}^{\text{dir}}$, optical gaps $E_{\text{gap}}^{\text{opt}}$, exciton binding energy $E_{\text{b}}^{\text{exc}} = E_{\text{gap}}^{\text{dir}} - E_{\text{gap}}^{\text{opt}}$ (all in eV), $a$ lattice constant (in Å; optimised using the PBE functional), and the type of the structure (P stands for planar and B stands for buckled) of seven materials. The positions of indirect and direct band gaps in the Brillouin zone are in brackets

| Material | $E_{\text{gap}}^{\text{indir}}$ | $E_{\text{gap}}^{\text{dir}}$ | $E_{\text{gap}}^{\text{opt}}$ | $E_{\text{b}}^{\text{exc}}$ | $a$ | Type |
|---|---|---|---|---|---|---|
| BN | $6.94_{(K \Rightarrow \Gamma)}$ | $7.64_{(K)}$ | 5.39 | 2.25 | 2.511 | P |
| BP | $1.89_{(K \Rightarrow K)}$ | $1.89_{(K)}$ | 1.23 | 0.66 | 3.214 | P |
| BAs | $1.58_{(K \Rightarrow K)}$ | $1.58_{(K)}$ | 1.04 | 0.54 | 3.390 | P |
| AlN | $5.61_{(K \Rightarrow \Gamma)}$ | $6.30_{(\Gamma)}$ | 4.36 | 1.94 | 3.125 | P |
| GaN | $4.22_{(K \Rightarrow \Gamma)}$ | $4.60_{(\Gamma)}$ | 3.27 | 1.33 | 3.252 | P |
| GaP | $3.26_{(K \Rightarrow \Gamma)}$ | $3.57_{(K)}$ | 2.46 | 1.11 | 3.916 | B |
| GaAs | $2.50_{(K \Rightarrow \Gamma)}$ | $2.61_{(\Gamma)}$ | 1.94 | 0.67 | 4.054 | B |

phonon branch crosses the acoustic ones in planar structures. We also attempted to obtain a buckled structure in all other studied free-standing materials, but had no success in finding local/global buckled minima. In contrast, we were able to find energy minima corresponding to the planar structures of GaP and GaAs, which were not dynamically stable and energetically less favorable than the buckled ones. We note that the unstable free-standing structures/conformers can be stabilized by strain[47] or a support (such as 2D buckled GaN prepared *via* migration-enhanced encapsulated growth; graphene/2D GaN/SiC[48]).

Since many-body calculations serve here as a reference, we emphasize that the VASP plane-wave $G_0W_0$ calculations based on PAWs can be considered highly accurate. PAW-$G_0W_0$ calculations were validated in ref. 49 for a larger set of materials using the all-electron full-potential linearized-augmented plane wave (FLAPW) method, which is regarded as an established reference method in condensed matter physics. Therefore, additional numerical uncertainties due to pseudization in the VASP can be ruled out. Taking into account several previous studies comparing GW calculation levels with experimental studies[28,30,31] and, in particular, comparing GW and Quantum Monte Carlo,[34,36] we believe that the most suitable GW level to describe the electronic and optical properties of our class of materials is its first iteration $G_0W_0$ if it perfectly converges toward the number of bands included in the calculation, the GW energy cut-off, and $k$-point sampling. We, however, show differences in electronic band gaps for two materials (wide gap BN and narrow gap BP) between single-shot $G_0W_0$ and subsequent iterations of G ($G_iW_0$) and G and W ($G_iW_i$) in Fig. S1 (ESI†). It should be noted from this picture that one can obtain an overestimated band gap of nearly 20% (BP $G_3W_3$ *vs.* $G_0W_0$). Moreover, for 2D materials, due to long-range Coulomb interactions, it is necessary to be aware of the vacuum space in the out-of-plane direction (the spatial separation $L_z$ between the 2D sheets). Another parameter that we emphasized that needs to be checked in the GW/BSE calculation is the number of frequency grid points used to construct the dielectric function.

We set our target precision of band gaps to 0.05 eV for each of the aforementioned parameters, marked as a gray bar in Fig. 2 and 3. The suitability of each parameter setting was also
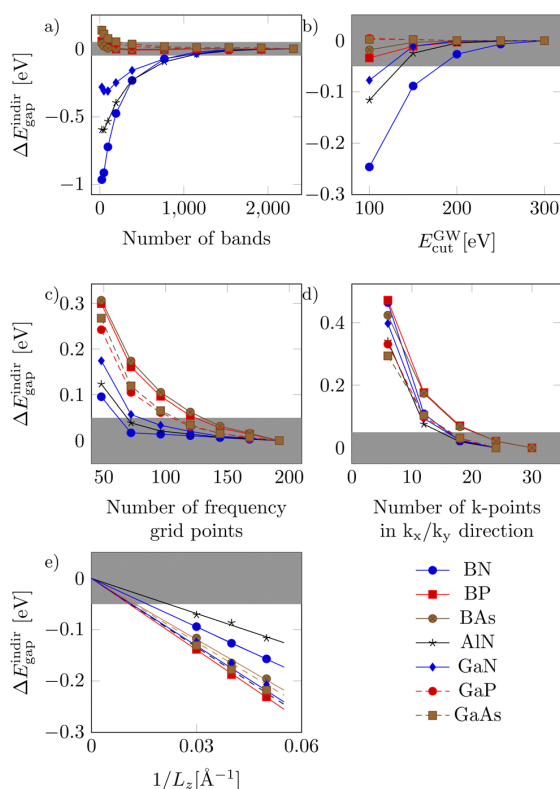


**Fig. 2** Representative differences of indirect $G_0W_0$ band gaps ($\Delta E_{\text{gap}}^{\text{indir}}$) from the converged values of seven 2D materials with respect to the (a) number of bands, (b) GW energy cut-off $E_{\text{cut}}^{\text{GW}}$, (c) number of frequency grid points for the GW calculation, and (d) number of $k$-points in $x$ and $y$ directions. (e) Extrapolation of $\Delta E_{\text{gap}}^{\text{indir}}$ to the infinite height of the computational cell ($L_z \to \infty$). Grey bars show regions within the target $\pm$ 0.05 eV threshold.

checked by the visual control of the parameter convergence to prevent biased results. Note that the GW basis for the response function ($E_{\text{cut}}^{\text{GW}}$) and the number of bands included in the calculation are linked and their mutual influence is also checked. The final recommended parameters differ for each material and are shown in Table S2 in the ESI.† The final setting of the number of bands included in the calculations was between 192 and 1152 (see (*a*) panels in Fig. 2 and 3), the energy cut-off for GW calculations was in the range of 150 to 200 eV (see (*b*) panels in Fig. 2 and 3), the number of frequency grid points for GW/BSE calculations was set to 144 for all materials (see (*c*) panels in Fig. 2 and 3) and the number of $k$-points for electronic and optical gaps was set to 18 × 18 × 1 except BP and BAs where the 24 × 24 × 1 grid was used (see (*d*) panels in Fig. 2 and 3). These red pre-final calculations were performed with a vacuum space of 25 Å. Finally, extrapolations to the infinite height of the computational cell ($L_z \to \infty$, *i.e.* $1/L_z \to 0$) were performed using three values of $L_z = 33.33$, 25 and 20 Å (Fig. 2e and 3e). The ultimate values of the indirect, direct, and optical gaps are reported in Table 2.

This journal is © the Owner Societies 2022

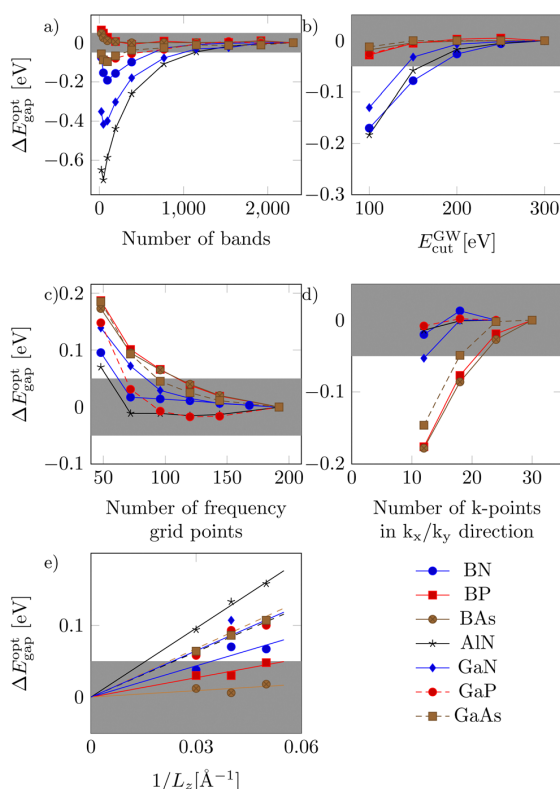*Phys. Chem. Chem. Phys.*, 2022, **24**, 27459–27466 | **27461**

Fig. 3 Representative differences of optical band gaps from the BSE calculations $\Delta E_{\text{gap}}^{\text{opt}}$ from the converged values of seven 2D materials with respect to parameters as shown in Fig. 2.
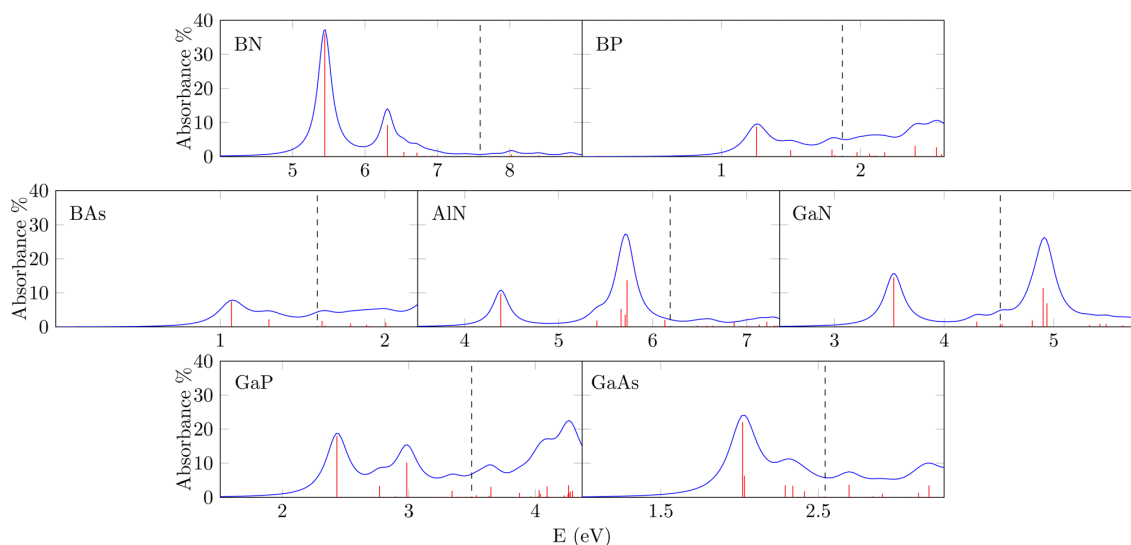
imaginary part of the dielectric function and non-extrapolated spectra, see Fig. S3, ESI†). Namely, the final spectra of Fig. 4 are $L_z$-corrected spectra (i.e., the energy shift from Fig. 3e, corresponding to the used k-grid of Table S2, ESI,† was applied).

We observed some general trends concerning parameter convergence and optical properties in this set of materials. For the two direct materials, BP and BAs, in contrast to other indirect materials, we observed a much stronger sensitivity to the k-point sampling and a lower sensitivity to the number of virtual bands included in the calculation and energy cut-off in the GW calculations. These direct materials show much lower absorbance than all indirect materials. The reason for the slow convergence of optical gaps with respect to the k-point sampling of these two materials can be explained by the localization of the first bound exciton. We demonstrate it in Fig. 5, where we plotted the excitonic probability density by fixing the hole position of the first excitons for BAs in contrast to BN.[51] We used k-point grids of 18 × 18 × 1 and 30 × 30 × 1 for BN and BAs, respectively. The first BN exciton is much more localized with an exciton size of ca. 10 real unit cells. On the other hand, the first BAs exciton is very delocalized, and one needs a supercell size larger than 20 real unit cells to ensure the wave function fade-out on the border of the supercell (Fig. 5). We remind here that the delocalization (radius) of the exciton in real space is indicated by the k-point density necessary for the reliable calculation of the optical gap value (Fig. 3d). An exciton wave function covering a $n \times n$ real-space supercell can be reasonably mapped at least by the $n \times n$ grid in the reciprocal space. Therefore, the artificial confinement of the exciton by a too coarse grid will lead to a biased optical gap (and will untruly increase the predicted binding energy of the exciton). We demonstrate such a bad calculation in the ESI† (18 × 18 × 1 k-point grid for BAs; cf. non-zero probability density of the first exciton in the whole supercell (Fig. S4, ESI†) vs. corresponding non-converged optical gap of Fig. 3d). The same is valid for higher excitons and, therefore, the convergence of higher optical transitions (and subsequently whole absorption spectra) can be of different rates (slower in our case, i.e. requiring a denser k-grid, see discussion above).

Interestingly, all the nitrides are more sensitive to the number of bands and the GW cut-off energy of the electronic band gap. We see the same trend for the optical gap, except for BN in the number of bands. Therefore, we conducted a convergence study for several sets of plane-wave energy cut-off $E_{\text{cut}}$ of BN, but it does not show an impact of this parameter (Fig. S5, ESI†). We also visually checked (Fig. 6 for BN and AlN, visually different cases) the charge densities corresponding to the valence and conduction bands in specific k-points of the location of the direct band gap (see Fig. S6 and S7, ESI† for all materials). The valence state is always localized near the VA elements (N, P, and As). While the valence state in BN, BP, BAs, and GaP is of the $p_z$-like orbital character, in AlN, GaN, and GaAs the valence state is localized in-plane. We assume that such valence bands, because of their location in the plane, will not be much influenced by other layers in the prospective bulk material. To strengthen our assumption, we plotted the

We can deduce from Fig. 2 and 3 that one can easily obtain the biased values of electronic and optical properties up to several tenths of eV despite using state-of-the-art GW/BSE methods. The relative errors of the gaps in Table 2 can therefore be up to 30% from a single parameter (BAs k-point case) and the target precision in many-body calculations can be challenging. In contrast, the standard DFT methods are considered as well established, quite precise, and reproducible in many different codes[50] with the default setup; however, they are often inaccurate for band gap predictions. Therefore, we consider the values in Table 2 as benchmarks for the 2D materials considered and as values that solve discrepancies in the values from the previous literature (Table 1). For two 2D materials (BAs and GaP), many-body gaps are provided for the first time.

Achieving the precise absorbance spectra from the BSE calculations is more challenging than optical band gaps because one needs converged results within a range of several eV. The most problematic parameter is the k-point sampling (see Fig. S2, ESI†); therefore, the denser k-point grid was used for the correct optical spectra, namely 30 × 30 × 1 for BP and BAs and 24 × 24 × 1 for GaN, GaP, and GaAs. With these settings, we achieved the precise absorption spectra in Fig. 4 up to the energy of the direct band gap (alternatively, for the

27462 | Phys. Chem. Chem. Phys., 2022, **24**, 27459–27466

This journal is © the Owner Societies 2022

Fig. 4 Accurate absorbance spectra $A^{xx}$ (%) of seven 2D materials, with oscillator strengths (red, arbitrary units) from BSE. The black dashed lines are fundamental direct gaps. $L_z$ = 25 Å is used in calculations, and graphs are subsequently shifted by the energy difference between $L_z$ = 25 and ∞ calculations (Fig. 3e). The smearing width of 0.04 eV is used.
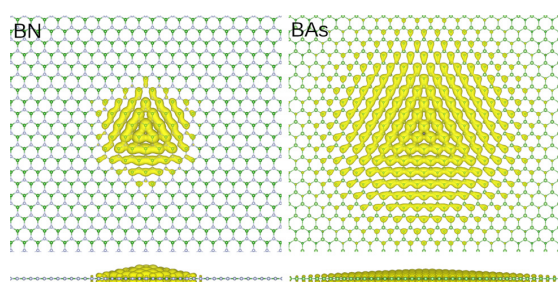


Fig. 5 Top and side views of the isosurface of the first bound exciton with a fixed hole for BN (left) and BAs (right) plotted with the same level of isosurface.
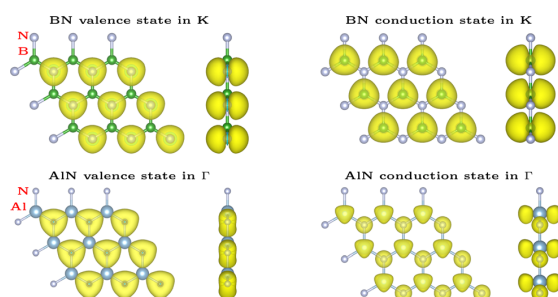


Fig. 6 Charge density distributions (with a level of 0.01) of the highest valence and lowest conduction states in specific $k$-points of the direct gap location for BN and AlN from the PBE calculations.

$z$-direction extrapolation of direct gaps for all non-buckled materials (Fig. S8, ESI†). From this figure, it is obvious that

materials with a $p_z$-like orbital character of the valence bands (BN, BP, and BAs) are more sensitive to the thickness of the vacuum layer than materials with the valence state localized in-plane (AlN and GaN). In addition, note that all the out-of-plane valence states are located at the $K$ point of the BZ, and, on the other hand, the in-plane ones are located at the $\Gamma$ point. The conduction state is localized on IIIA elements in boron materials, and in all other materials, both elements contribute to the conduction state.

The type of electronic band gaps of BP and BAs is direct, and for both materials, the band gap is located in the highly symmetric $K$ point in the first Brillouin zone. All other materials are indirect, with the valence band maximum (VBM) located at the $K$ point and the conduction band minimum (CBM) located at the $\Gamma$ point of the first Brillouin zone. The direct band gaps are for BN and GaP located at the $K$ point and for AlN, GaN and GaAs at the $\Gamma$ point of the first Brillouin zone. This set of materials provides the linear scaling of the exciton binding energy with respect to the electronic band gap shown in previous studies[52,53] with the fit equation $E_b^{exc}$ = 0.291$E_{gap}^{dir}$ + 0.043 (see Fig. 7).

The optical spectra arise from the different number of excitonic transitions with different localizations and strengths. Although in all nitrides the spectra in the studied region consist of two dominant peaks, which are separated and where the first peak originates from just one transition (double-degenerate), the spectra of all other materials are more spread in energy (Fig. 4). Note that the excitonic transitions in this figure are represented by red lines. The first exciton is always bright and double-degenerate in all materials. The following one is then bright and double-degenerate in all of the materials studied except AlN, where the second exciton is dark and does not

This journal is © the Owner Societies 2022

Phys. Chem. Chem. Phys., 2022, **24**, 27459–27466 | **27463**
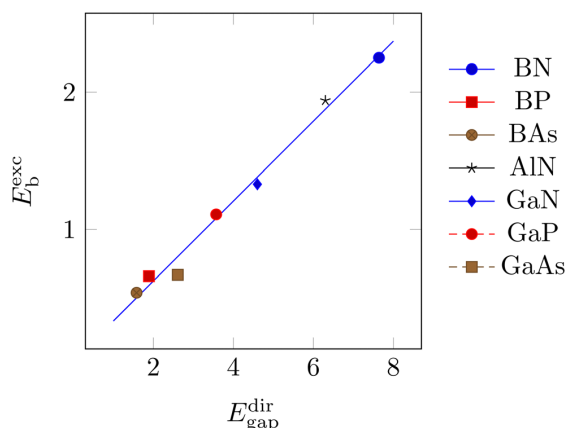
**Fig. 7** Excitonic binding energy $E_b^{exc}$ as a function of the fundamental direct gap $E_{gap}^{dir}$. The linear fit function $E_b^{exc} = 0.291 \times E_{gap}^{dir} + 0.043$ is added.

degenerate. It should be noted that the second double-degenerate exciton in GaAs is only 0.011 eV different from the

first one, and therefore, the first GaAs exciton can be roughly understood as a four-time degenerate.

The exciton wave function of the $S$-th exciton is expressed in an electron–hole product basis as $\sum_{vck} A_{vck}^S |ck\rangle |vk\rangle$. For a better understanding of the nature of the first optical transitions of each material and which the region of the Brillouin zone is essential for the optical gap (and the corresponding exciton wave function), the eigenstate corresponding to the first exciton from the generalized BSE eigenvalue problem of eqn (2) is visualized in Fig. 8 by plotting circles with the $|A_{vck}^S|$ radius of the band structure.[54] The pairs of large circles visible in Fig. 8 represent the electron–hole pairs, which contribute the most to the first excitonic peak. The locations of these contributions differ in materials. In AlN, GaN, and GaAs, it is located at the $\Gamma$ point of the Brillouin zone and in all other materials it is located in the vicinity of the $K$ point. The main contribution, therefore, grows dominantly from the location of the direct electronic band gap of all materials.

The reliable prediction of optical gap values and absorbance curves is important for the design of 2D materials in photonics
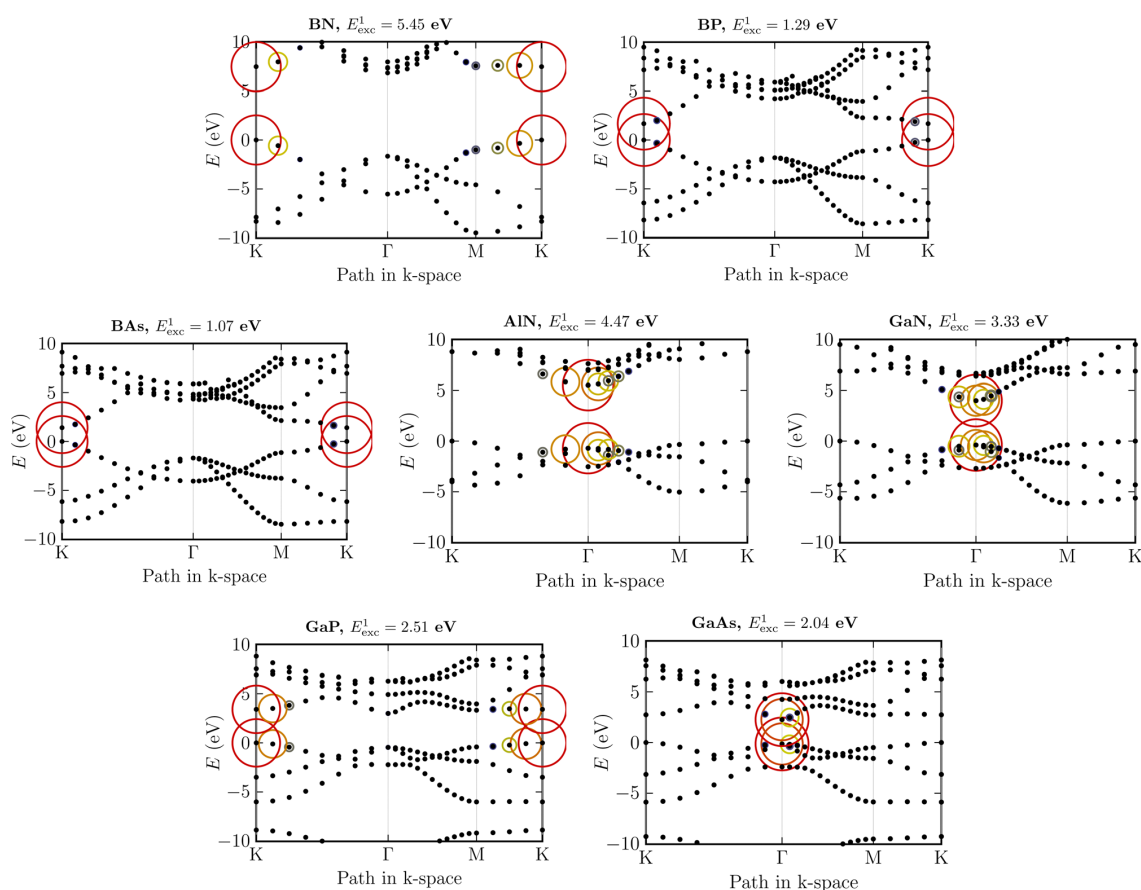


**Fig. 8** $G_0W_0$ band structures (black dots) of seven materials and $|A_{vck}^S|$ coefficients (coloured circles) from eqn (2), which shows the weight of contributions to the first excitonic peak by its radius.

and electronic devices. Most of the studied materials show relatively high absorbance values (notice 0–40% values on the $y$-axis of Fig. 4) if one takes into account that we consider the one-atomic-thickness of materials (2D materials). Moreover, some of the considered 2D materials have broad peaks and strong absorbance in the visible part of the spectra; however, only BP and BAs absorb from 1 eV. Both are very good absorbers: the absorbance is $A \approx$ 5–10% in the energy range of 1–3 eV (Fig. 4 and Fig. S3, ESI†), which is of essential relevance for photovoltaics.[55] This indicates comparable performance to $A \approx$ 5–10% in the $MoS_2$ case[55] with a thickness of 3.1 Å. On the other hand, BN and AlN are wide-gap indirect semiconductors (indirect gaps of 6.9 and 5.6 eV, respectively). The studied seven 2D hexagonal materials consisting of IIIA and VA group elements are therefore a very property-rich set of materials and promising to be incorporated into various devices, including vdW heterostructures or interfaces, suitable for optical applications.

## 4 Conclusions

We provided the benchmark values of electronic band gaps, optical gaps, excitonic binding energies, and absorbance spectra for seven hexagonal III–V binary 2D semiconductors. In particular, using sophisticated many-body methods (GW and BSE) beyond the density functional theory, which were proved as accurate in many previous studies, we cautiously converged technical settings to obtain the best precision. The convergence rates of studied properties concerning various numerical parameters (such as the density of $k$-point sampling, the basis set size, or the vacuum layer thickness in the direction perpendicular to the 2D material) were material-dependent, which we visualized and rationalized. The dispersion of the gaps provided by many-body methods (using various input settings) can be significantly larger than the dispersion of results produced from the standard density functional theory. In other words, it is more challenging to achieve the high precision of such accurate methods than to be precise at the level of DFT, which is, however, inaccurate for band gaps and spectra. Several 2D materials from our set show intense exciton binding energies and high absorbance values in the visible and UV spectra; therefore, suitability for optoelectronic applications was confirmed.

## Conflicts of interest

There are no conflicts to declare.

## Acknowledgements

## References

1 T. Ketolainen, N. Macháčová and F. Karlický, *J. Chem. Theory Comput.*, 2020, **16**, 5876–5883.

2 W. Xia, L. Dai, P. Yu, X. Tong, W. Song, G. Zhang and Z. Wang, *Nanoscale*, 2017, **9**, 4324–4365.

3 K. S. Novoselov, A. Mishchenko, A. Carvalho and A. H. Castro Neto, *Science*, 2016, **353**, aac9439.

4 A. K. Geim and I. V. Grigorieva, *Nature*, 2013, **499**, 419–425.

5 M. S. Prete, A. Mosca Conte, P. Gori, F. Bechstedt and O. Pulci, *Appl. Phys. Lett.*, 2017, **110**, 012103.

6 R. Hunt, B. Monserrat, V. Zólyomi and N. Drummond, *Phys. Rev. B*, 2020, **101**, 205115.

7 I. Guilhon, M. Marques, L. Teles, M. Palummo, O. Pulci, S. Botti and F. Bechstedt, *Phys. Rev. B*, 2019, **99**, 161201.

8 H. Mishra and S. Bhattacharya, *Phys. Rev. B*, 2019, **99**, 165201.

9 F. Ferreira, A. Chaves, N. Peres and R. Ribeiro, *J. Opt. Soc. Am. B*, 2019, **36**, 674.

10 L. Wirtz, A. Marini and A. Rubio, *Phys. Rev. Lett.*, 2006, **96**, 126104.

11 F. A. Rasmussen, P. S. Schmidt, K. T. Winther and K. S. Thygesen, *Phys. Rev. B*, 2016, **94**, 155406.

12 J. C. G. Henriques, G. B. Ventura, C. D. M. Fernandes and N. M. R. Peres, *J. Phys.: Condens. Matter*, 2019, **32**, 025304.

13 T. Galvani, F. Paleari, H. P. Miranda, A. Molina-Sánchez, L. Wirtz, S. Latil, H. Amara and F. Ducastelle, *Phys. Rev. B*, 2016, **94**, 125303.

14 K. Mengle and E. Kioupakis, *APL Mater.*, 2019, **7**, 021106.

15 Z. Rukelj and V. Despoja, *New J. Phys.*, 2020, **22**, 063052.

16 M. S. Prete, D. Grassano, O. Pulci, I. Kupchak, V. Olevano and F. Bechstedt, *Sci. Rep.*, 2020, **10**, 10719.

17 D. Hoat, M. Naseri, N. T. Binh, T. V. Vu, J. Rivas-Silva, M. M. Obeid and G. H. Cocoletzi, *Phys. B*, 2021, **603**, 412757.

18 D. Wines, F. Ersan and C. Ataca, *ACS Appl. Mater. Interfaces*, 2020, **12**, 46416–46428.

19 D. Vahedi Fakhrabad, N. Shahtahmasebi and M. Ashhadi, *Superlattices Microstruct.*, 2015, **79**, 38–44.

20 C. Attaccalite, A. Nguer, E. Cannuccia and M. Grüning, *Phys. Chem. Chem. Phys.*, 2015, **17**, 9533–9540.

21 H. Shu, X. Niu, X. Ding and Y. Wang, *Appl. Surf. Sci.*, 2019, **479**, 475–481.

22 A. Onen, D. Kecik, E. Durgun and S. Ciraci, *Phys. Rev. B*, 2016, **93**, 085431.

23 H. Mishra and S. Bhattacharya, *Phys. Rev. B*, 2020, **101**, 155132.

24 R. J. P. Roman, F. J. R. Costa, A. Zobelli, C. Elias, P. Valvin, G. Cassabois, B. Gil, A. Summerfield, T. S. Cheng, C. J. Mellor, P. H. Beton, S. V. Novikov and L. F. Zagonel, *2D Mater.*, 2021, **8**, 044001.

25 P. Wang, T. Wang, H. Wang, X. Sun, P. Huang, B. Sheng, X. Rong, X. Zheng, Z. Chen, Y. Wang, D. Wang, H. Liu, F. Liu, L. Yang, D. Li, L. Chen, X. Yang, F. Xu, Z. Qin, J. Shi, T. Yu, W. Ge, B. Shen and X. Wang, *Adv. Funct. Mater.*, 2019, **29**, 1902608.

26 A. Aiello, Y. Wu, A. Pandey, P. Wang, W. Lee, D. Bayerl, N. Sanders, Z. Deng, J. Gim, K. Sun, R. Hovden, E. Kioupakis, Z. Mi and P. Bhattacharya, *Nano Lett.*, 2019, **19**, 7852–7858.

This journal is © the Owner Societies 2022

*Phys. Chem. Chem. Phys.*, 2022, **24**, 27459–27466 | **27465**

27 Z. Zhang, Q. Qian, B. Li and K. J. Chen, *ACS Appl. Mater. Interfaces*, 2018, **10**, 17419–17426.

28 M. Kolos and F. Karlický, *Phys. Chem. Chem. Phys.*, 2019, **21**, 3999–4005.

29 J. Klimeš, M. Kaltak and G. Kresse, *Phys. Rev. B: Condens. Matter Mater. Phys.*, 2014, **90**, 075125.

30 B.-C. Shih, Y. Xue, P. Zhang, M. L. Cohen and S. G. Louie, *Phys. Rev. Lett.*, 2010, **105**, 146401.

31 D. Y. Qiu, F. H. da Jornada and S. G. Louie, *Phys. Rev. Lett.*, 2013, **111**, 216805.

32 F. Karlický and J. Turoň, *Carbon*, 2018, **135**, 134–144.

33 A. Gulans, *J. Chem. Phys.*, 2014, **141**, 164127.

34 M. Dubecký, F. Karlický, S. Minárik and L. Mitas, *J. Chem. Phys.*, 2020, **153**, 184706.

35 M. Kolos, L. Cigarini, R. Verma, F. Karlický and S. Bhattacharya, *J. Phys. Chem. C*, 2021, **125**, 12738–12757.

36 M. Dubecký and F. Karlický, to be published.

37 G. Kresse and D. Joubert, *Phys. Rev. B: Condens. Matter Mater. Phys.*, 1999, **59**, 1758–1775.

38 P. Blöchl, *Phys. Rev. B: Condens. Matter Mater. Phys.*, 1994, **50**, 17953–17979.

39 J. P. Perdew, K. Burke and M. Ernzerhof, *Phys. Rev. Lett.*, 1996, **77**, 3865–3868.

40 A. Togo and I. Tanaka, *Scr. Mater.*, 2015, **108**, 1–5.

41 M. Shishkin and G. Kresse, *Phys. Rev. B: Condens. Matter Mater. Phys.*, 2006, **74**, 035101.

42 H. Bethe and E. Salpeter, *Phys. Rev.*, 1951, **82**, 309–310.

43 G. Strinati, *Phys. Rev. B: Condens. Matter Mater. Phys.*, 1984, **29**, 5718–5726.

44 M. Rohlfing and S. G. Louie, *Phys. Rev. B: Condens. Matter Mater. Phys.*, 2000, **62**, 4927–4944.

45 F. Fuchs, C. Rödl, A. Schleife and F. Bechstedt, *Phys. Rev. B: Condens. Matter Mater. Phys.*, 2008, **78**, 085103.

46 H. S. S. Ahin, S. Cahangirov, M. Topsakal, E. Bekaroglu, E. Akturk, R. T. Senger and S. Ciraci, *Phys. Rev. B: Condens. Matter Mater. Phys.*, 2009, **80**, 155453.

47 M. Kolos, R. Verma, F. Karlický and S. Bhattacharya, *J. Phys. Chem. C*, 2022, **126**, 14931–14959.

48 Z. Y. Al Balushi, K. Wang, R. K. Ghosh, R. A. Vilá, S. M. Eichfeld, J. D. Caldwell, X. Qin, Y.-C. Lin, P. A. DeSario, G. Stone, S. Subramanian, D. F. Paul, R. M. Wallace, S. Datta, J. M. Redwing and J. A. Robinson, *Nat. Mater.*, 2016, **15**, 1166–1171.

49 D. Nabok, A. Gulans and C. Draxl, *Phys. Rev. B*, 2016, **94**, 035118.

50 K. Lejaeghere, G. Bihlmayer, T. Björkman, P. Blaha and S. Blügel, *et al.*, *Science*, 2016, **351**, aad3000.

51 Calculated by the Yambo code using Quantum Espresso DFT input. Scissor-corrected PBE band structure (without GW input) was used for BSE, with a scissor operator obtained from VASP calculations.

52 J.-H. Choi, P. Cui, H. Lan and Z. Zhang, *Phys. Rev. Lett.*, 2015, **115**, 066403.

53 Z. Jiang, Z. Liu, Y. Li and W. Duan, *Phys. Rev. Lett.*, 2017, **118**, 266401.

54 M. Bokdam, T. Sander, A. Stroppa, S. Picozzi, D. Sarma, C. Franchini and G. Kresse, *Sci. Rep.*, 2016, **6**, 28618.

55 M. Bernardi, M. Palummo and J. C. Grossman, *Nano Lett.*, 2013, **13**, 3664–3670.

**27466** | *Phys. Chem. Chem. Phys.*, 2022, **24**, 27459–27466

This journal is © the Owner Societies 2022

# Supplementary Material 8

# Benchmarking fundamental gap of Sc$_2$C(OH)$_2$ MXene by many-body methods

Matúš Dubecký,[1,2] 🆔 Stanislav Minárik,[2] 🆔 and František Karlický[1,a)] 🆔

AFFILIATIONS

[1] Department of Physics, University of Ostrava, 30. dubna 22, 701 03 Ostrava, Czech Republic
[2] ATRI, Slovak University of Technology in Bratislava, J. Bottu 25, 917 24 Trnava, Slovakia

[a)] Author to whom correspondence should be addressed: frantisek.karlicky@osu.cz

ABSTRACT

Sc$_2$C(OH)$_2$ is a prototypical non-magnetic member of MXenes, a promising transition-metal-based 2D material family, with a direct bandgap. We provide here a benchmark of its fundamental gap $\Delta$ obtained from many-body GW and fixed-node diffusion Monte Carlo methods. Both approaches independently arrive at a similar value of $\Delta \sim 1.3$ eV, suggesting the validity of both methods. Such a bandgap makes Sc$_2$C(OH)$_2$ a 2D semiconductor suitable for optoelectronic applications. The absorbance spectra and the first exciton binding energy (0.63 eV), based on the Bethe–Salpeter equation, are presented as well. The reported results may serve to delineate experimental uncertainties and enable selection of reasonable approximations such as density functional theory functionals, for use in modeling of related MXenes.

*Published under an exclusive license by AIP Publishing.* https://doi.org/10.1063/5.0140315

## I. MOTIVATION

In recent decades, 2D materials[1–5] became an important topic of material research due to the rich possibilities regarding their physical, electrical, chemical, and optical properties, enriching the possibilities provided by conventional bulk materials. Flexible and transparent electronics technology has stimulated the search for new semiconducting 2D materials with a direct bandgap, suitable for assembly of low-dimensional optoelectronic components.[6] After initial attempts such as MoS$_2$[7,8] or phosphorene[9,10] that were somewhat limited (e.g., by strong dependency of the bandgap on the number of layers and chemical degradation problems at ambient conditions), the MXene material family has attracted attention due to the versatility and tunability of the individual material properties by selection of the appropriate precursor MAX phase.[11–13] It turned out that many MXenes are metallic, while the semiconducting ones show an indirect bandgap.[14–18] Theoretically predicted direct-bandgap semiconducting MXenes have been hard to prepare experimentally.[15]

Some of the theoretically considered MXenes, such as the Sc-based Sc$_2$CF and Sc$_2$C(OH)$_2$, were found promising for their stability and revealed direct bandgaps of 0.9–1.9 eV at density functional theory (DFT) level of theory.[17,19,20] Although experimental realization of these materials still depends on future progress in synthesis, partial success has been recently reported for the OH-based system.

In particular, ScC$_x$OH[15] has been synthesized, taking an important step forward toward production of standalone Sc$_2$C(OH)$_2$ 2D MXene material. In this work, the freestanding Sc$_2$C(OH)$_2$ monolayer is considered due to its importance as a possible direct 2D MXene semiconductor[17] that has a chance to be synthesized in the near future, and due to the lack of reference data for this system beyond the DFT level of theory.

The goal of the present study is a non-empirical reference many-body estimation of the Sc$_2$C(OH)$_2$ fundamental gap (or quasiparticle gap), defined as

$$\Delta = I - A = E_{N-1} + E_{N+1} - 2E_N, \tag{1}$$

where $I$ is a first ionization potential, and $A$ is an electron affinity of the solid, and $E_{N(\pm 1)}$ is the total energy of $N(\pm 1)$-electron ground state. To this end, we employ two independent, state-of-the-art, complementary many-body approaches, recently proved to provide consistent $\Delta$ in 2D materials such as fluorographene:[21] The GW many-body perturbation theory,[22] and the real-space, continuum fixed-node diffusion Monte Carlo (FNDMC) method that gained traction in material science in the recent decade.[23–35] It is interesting to observe that, again,[21] both independent and complementary benchmark-level approaches reach a remarkable agreement for $\Delta$ in the considered 2D material, suggesting the validity of both approaches for prediction of this quantity, leaving only little room

for its further possible corrections at the 0.1 eV energy scale. We also provide absorbance spectra and estimate of an optical gap $(\Delta_{opt})$ of the $Sc_2C(OH)_2$ monolayer, based upon our high accuracy GW inputs and the Bethe–Salpeter equation[36] (BSE), to settle the first exciton binding energy $(E_b)$ in this MXene material.

## II. MODELS AND METHODS

### A. $Sc_2C(OH)_2$ model

The slab model of $Sc_2C(OH)_2$ (Fig. 1) was obtained from the C2DB database[14] of 2D materials. Atomic positions, as well as unit cell parameters, were reoptimized, to find the nearest local minimum on the DFT potential energy surface, using the HSE06[37] xc functional, a $12 \times 12 \times 1$ k-point mesh sampling the first Brillouin zone (BZ), a plane-wave cutoff energy of 450 eV, and the Vienna *Ab initio* Simulation Package (VASP) software package.[38] The unit cell contained 7 atoms, corresponding to a single stoichiometric unit of the material and 15 Å of vacuum. The HSE06 unit cell parameters were found to differ by ~0.6% vs the initial Perdew–Burke–Ernzerhof (PBE) unit cell.[14] For the final atomic positions and unit cell parameters, see the supplementary material.

The HSE06 bandgap of this model was found to be 0.85 eV, consistent with the previously reported value[14] (0.95 eV, using the PBE structure) to within 0.1 eV.

### B. GW and BSE

The VASP software package implementing the projector augmented-wave (PAW) method[39,40] was used in all GW, BSE, and underlying DFT calculations. The VASP plane-wave calculations based on PAWs can be considered highly accurate from a comparison of their results vs all-electron calculations[41] so that the pseudopotential construction error is ruled out.

The GW approximation used for computations of $\Delta$ is based on the Green's function ($G$) method and the screened Coulomb potential ($W$). The electron self-energy $\Sigma$ uses orbitals $\phi_{nk}(\mathbf{r})$ from DFT and PBE xc functional[42] as an input. The quasi-particle energies $\epsilon_{nk}^{GW}$ were calculated as first-order corrections to the DFT single-particle energies $\epsilon_{nk}$,

$$\epsilon_{nk}^{GW} = \epsilon_{nk} + Z_{nk}\text{Re}\left[\langle \phi_{nk}|\hat{T} + \hat{V}_{n-e} + \hat{V}_H + \Sigma(G, W; \epsilon_{nk})|\phi_{nk}\rangle - \epsilon_{nk}\right], \quad (2)$$
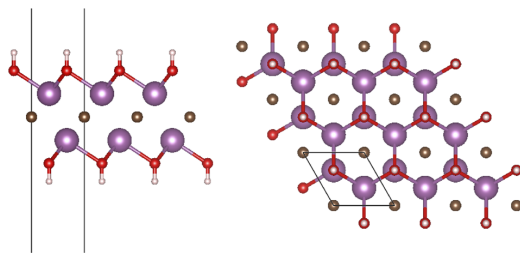


**FIG. 1.** Sketch of the $Sc_2C(OH)_2$ model used in production calculations of the fundamental gap $\Delta$. Left panel–side view; right panel–top view. Color code: Sc, violet; C, brown; O, red; H, white. The thin black lines indicate the unit cell.

where $Z_{nk}$ is the normalization factor,[43] $\hat{T}$ the kinetic energy operator, $\hat{V}_{n-e}$ the potential energy between electrons and nuclei, and $\hat{V}_H$ the Hartree potential energy. The quasiparticle gap was computed as $\Delta^{GW} = \epsilon_{CBM}^{GW} - \epsilon_{VBM}^{GW}$, where CBM stands for conduction band minimum, and VBM denotes the valence band maximum.

Recently, it was shown that on layered hexagonal boron nitride,[44] monolayer $MoS_2$,[45] and bulk ZnO,[46] the single-shot GW method with PBE orbitals provides $\Delta$ extremely well comparable to experiment, so, there is no necessity to go beyond by iterating $G$ or $W$. In order to reach the desired accuracy of our calculations, we used the PAWs designed for GW computations, a plane-wave cutoff energy $E_{cut}$ = 500 eV, and a strict electronic-step convergence criterion ($1 \times 10^{-7}$ eV). The presented production results were carefully converged with respect to the technical parameters that may possibly affect the accuracy, including the plane-wave cutoff energy, the number of bands in GW, the frequency grid size, the size of the vacuum region in the simulation cell, and the size of the k-point mesh.[47]

For insulating the materials with the occupied valence bands ($v$ index) and completely unoccupied conduction bands ($c$), the BSE can be rewritten as an eigenvalue problem[48,49]

$$(\epsilon_{ck}^{GW} - \epsilon_{vk}^{GW})A_{cvk}^\lambda + \sum_{c'v'k'}\left[2\langle\phi_{ck}\phi_{vk}|\nu|\phi_{c'k'}\phi_{v'k'}\rangle\right.$$
$$\left. - \langle\phi_{ck}\phi_{c'k'}|W|\phi_{vk}\phi_{v'k'}\rangle\right]A_{c'v'k'}^\lambda = E_{exc}^\lambda A_{cvk}^\lambda, \quad (3)$$

where $\nu$ is the Coulomb kernel, $1/|\mathbf{r} - \mathbf{r}'|$, the eigenvectors $A_{cvk}^\lambda$ correspond to the amplitudes of the free electron–hole pair configurations composed of electron states $|\phi_{ck}\rangle$ and hole states $|\phi_{vk}\rangle$, and the eigenenergies $E_{exc}^\lambda$ correspond to the excitation energies (with $\Delta_{opt}^{BSE} \equiv E_{exc}^{\lambda=1}$).

The (positive) exciton binding energy was finally estimated as $E_b = \Delta^{GW} - \Delta_{opt}^{BSE}$.

After computing the energy-dependent dielectric function, given the complex dielectric function $\epsilon^{\alpha\beta}(E) = \epsilon_1^{\alpha\beta}(E) + i\epsilon_2^{\alpha\beta}(E)$, various linear optical properties can be calculated as the absorbance

$$A^{\alpha\beta}(E) = 1 - \exp(-\epsilon_2^{\alpha\beta}(E)EL_z/\hbar c), \quad (4)$$

where $\alpha, \beta \in \{x, y, z\}$ denotes the matrix element indices, and $L_z$ is the height of the computational unit cell.[50]

### C. FNDMC

FNDMC is a stochastic many-body real-space projector quantum Monte Carlo (QMC) method[51–54] that can be applied to systems with hundreds of valence electrons. The method has been increasingly popular in electronic structure calculations of molecules and extended systems due to its low-order central processing unit (CPU) cost scaling, massive parallelism, accuracy, and, versatility.[30,55–63] For a Hamiltonian $\hat{H}$, the FNDMC imaginary time projection extracts the exact ground state component that has a non-zero overlap with the supplied antisymmetric trial state $\Psi_T$, i.e.,

$$\Psi^{FN} = \lim_{\tau\to\infty}\exp[-\tau(\hat{H} - E_T)]\Psi_T, \quad (5)$$

where $E_T$ is a total energy offset that keeps the norm of $\Psi^{FN}$ asymptotically constant. The superscript FN indicates that $\Psi^{FN}$ and $\Psi_T$

share the same fixed node $\gamma = \{\mathbf{R}; \Psi_T(\mathbf{R}) = 0\}$, and $\mathbf{R}$ is a $3N$ dimensional position vector of $N$ simulated electrons. FNDMC simulation provides a stochastic estimate of the total energy, $E^{FN} \pm \frac{\sigma}{\sqrt{K}}$, where $\sigma$ is a local energy dispersion, and $K$ is the number of independent samples. $E^{FN}$ is an upper bound to the exact total energy of a ground state[64] of $\hat{H}$, having the same symmetry as $\Psi_T$. The total energy bias depends quadratically on the inaccuracy of $\gamma$.[54] In order to simulate an excited state, one may intentionally pick the appropriate $\Psi_T$ orthogonal to the lower state/s.[65–69]

$\Psi_T$ may be sophisticated enough to marginalize the FN bias as much as possible.[70,71] Practical FNDMC computations, nevertheless, rely on computationally efficient forms such as the widely used the Slater–Jastrow trial wave functions,[72] $\Psi_T = \Psi_S J$, where $\Psi_S$ is a single Slater determinant, and $J$ is a parametric, explicitly correlated, positive-definite Jastrow term.[73] $\Psi_T$ is variationally improved within the variation Monte Carlo (VMC) and then serves as an input to the FNDMC calculations. One of the key FNDMC ingredients to account for accurate $\Delta$ seems to be the ability to correctly describe the total energy $E(N)$ dependency on the fractional system charge $N$, namely, the piecewise-linear $E(N)$ with derivative discontinuities of $\frac{\partial E(N)}{\partial N}$ at integer $N$,[74] conditions known to hold for exact solutions.[75–77]

In systems with translational symmetry, FNDMC computations of $\Delta^{FN}$ may use two strategies—either directly apply Eq. (1) that involves charged states and pronounced size-effects or the so-called *promotion approach*[21,29] involving the total energy differences of neutral states. The latter approach can be employed if $\Psi_T$ can be constructed such that its node is invariant upon action of translation operators corresponding to the unit cell, i.e., if $\Psi_T$ transforms as a one-dimensional irreducible representation of the translation-symmetry subgroup of the symmetry group of the Hamiltonian. The translation symmetry-constrained variation principle for excited states then applies (see Ref. 65 for rigorous details). It guarantees that the FNDMC total energy of the promoted state within the supercell does not drop (by translation symmetry breaking) below the variation bounds given by the nodal surface, constructed in such a way that it strictly obeys the translation symmetry of the unit cell. The promoted state (within a supercell) then remains extended within the FNDMC simulation, i.e., it corresponds to an electron promotion into the (fully extended) conduction band (in contrast to an optical gap and localized electron–hole pair formation that would result if the simulation was able to break the translation symmetry). In this case, the electron–hole interaction would be non-zero within a finite supercell, but, it rigorously diminishes with the supercell size to zero in the thermodynamic limit.[21,29,65] An example of $\Psi_T$ where this principle applies is the Slater–Jastrow wave function with a node fixed by a Slater determinant of real Bloch orbitals. In this work, we are interested in the direct bandgap of a material in a $\Gamma$-point, i.e., the Slater determinant of real Bloch orbitals can be constructed for all the considered supercells. We can thus benefit from the use of a promotion approach that relies on the total energy differences involving neutral states only.[21,29]

The antisymmetric parts of our $\Psi_T$, with the nodes that satisfy the translation symmetry-constrained variation principle, were obtained by constructing the Slater determinants of real Bloch orbitals, each individually strictly obeying the periodicity of the unit cell. For a series of supercell sizes, labeled $s$, we evaluate

$\Delta^{FN}(s) = E^*(s) - E_0(s)$, where $E_0$ corresponds to a ground-state, and $E^*$ corresponds to a promoted state, achieved by using $\Psi_S^* = a_{CBM}^\dagger a_{VBM} \Psi_S$ (in $\Psi_T^*$), where a single electron was promoted from the CBM to the VBM orbital at the $\Gamma$-point. The series of $\Delta^{FN}(s)$ is then extrapolated to the thermodynamic limit to obtain $\Delta^{FN} \equiv \Delta^{FN}(\infty)$, i.e., a direct FNDMC bandgap estimate at the $\Gamma$-point. The extrapolation effectively removes the finite-size effects and diminishes the residual electron–hole interactions to zero.[21]

The production QMC computations of $\Delta$ in $Sc_2C(OH)_2$ consisted of multiple stages[78] involving the following (mostly usual) steps:

(i) One-particle DFT-based Bloch orbitals in a unit cell were obtained using Quantum Espresso,[79] a plane wave DFT code, with a PBE[42] xc functional and a steep plane-wave cutoff energy of 400 Ry. The nuclei were represented by the correlation-consistent effective core potentials, ccECPs.[80] The BZ sampling used $12 \times 12 \times 1$ k-points. The spin-restricted Kohn–Sham orbitals (used in $\Psi_T$ below) were obtained from computations using the pre-defined occupation number vector $\vec{\lambda}_{opt} = [\ldots, 2, 2, 1, 1, 0, 0, \ldots]$. This was found by minimization of the FNDMC total energy for the ground-state and 1-electron promoted state, in a $3 \times 3$ supercell, with respect to a single parameter $q$ that defines a parametric (restricted open-shell) occupation vector $\vec{\lambda} = [\ldots, 2, 2, 2 - q, q, 0, 0, \ldots]$ and determines the VBM and CBM occupation numbers within the DFT orbital production run. Such a minimization of the 1-electron effective Hamiltonian determining the improved node[81] was found important in order to avoid bias toward the (here, suboptimal) ground-state. Interestingly, both considered states individually minimized the FNDMC total energy for $q = 1$. The FNDMC bandgap computed with the usual setting (using $\vec{\lambda}_0$ corresponding to $q = 0$) resulted in $\Delta_{3\times3}^{FN}(\vec{\lambda}_0) = 3.43$ eV, while the optimization of the FNDMC total energies led to $\Delta_{3\times3}^{FN}(\vec{\lambda}_{opt}) = 1.34$ eV. Similarly, in the $4 \times 4$ supercell, the FNDMC total energies for $q = 1$ were verified to be lower than those corresponding to $q = 0$ in both, ground- and promoted-states, respectively.

(ii) Variational Monte Carlo (VMC) optimizations of the parametric, explicit correlation $J$ entering $\Psi_T$, using the QMCPACK[82] code, which used up to three center terms (electron–electron, electron–nucleus, and electron–electron–nucleus), were performed in the ground-state and the $3 \times 3$ supercell.

(iii) The FNDMC total energies, corresponding to $\Psi_T$ and the promoted-states $\Psi_T^*$, with $J$ from step (ii), were individually obtained for the $3 \times 3$, $4 \times 4$, and, $5 \times 5$ supercell sizes (in multiples of unit cell), with an imaginary timestep of 0.01 a.u., and a T-moves approximation for the treatment of ECPs.[83] All FNDMC simulations reported within this work used standard occupation numbers, i.e., $[\ldots, 2, 2, 0, 0, \ldots]$ and $[\ldots, 2, 1, 1, 0, \ldots]$, for the ground-state and the promoted-state, respectively.

(iv) The finite size effects[84] and residual electron–hole interactions (see above) were suppressed by linear extrapolations of the series of the production results (for supercells ranging from

3 × 3 to 5 × 5 unit cells) to the thermodynamic limit vs the number of unit cells in the supercell.

(v) Particle number fluctuations between unit cells were evaluated within the 3 × 3 and 4 × 4 supercells (using at least 200 k FNDMC production-run walkers), in order to verify that FNDMC simulations using $\Psi_T^*$ remained fully extended within the supercells, thus ruling out translation symmetry breaking and localized exciton state formation within the considered supercells.

## III. RESULTS AND DISCUSSION

### A. GW and BSE

The production estimate of $\Delta^{GW}$ was obtained by careful convergence of the relevant simulation parameters, including the number of bands $N_B$, the plane-wave cutoff energy used in the GW calculation, $E_{cut}^{GW}$; the number of frequency grid points, $N_\omega$; the inter-sheet distance along the z-direction, $L_z$, and the k-point sampling of 2D BZ in the xy-direction.

The convergence characteristics of $\Delta^{GW}$ on the number of bands $N_B$ and $E_{cut}^{GW}$ is reported in Fig. 2. Note that low $E_{cut}^{GW}$ may lead to false convergence behavior (insensitivity to $N_B$), as observed for $E_{cut}^{GW}$ = 100 eV. Reasonable tradeoff between CPU cost and convergence is only achieved for highest $E_{cut}^{GW}$ and large $N_B$. However, the bandgap for the largest $E_{cut}^{GW}$ = 300–400 eV and $N_B$ = 2500–3000 bands seems still not completely converged yet. Therefore, we fitted the values with the hyperbolical function[41,85]

$$\Delta^{GW}(N_B) = \frac{A}{B + N_B} + \Delta^{GW}(\infty), \quad (6)$$

where $A$, $B$, and $\Delta^{GW}(\infty)$ are parameters of the fit. The fitted curve of highest $E_{cut}^{GW}$ = 400 eV follows the calculated data points very closely (Fig. 2, see also the supplementary material for nonlinear fit parameters and characteristics). This makes us

confident in taking the fit asymptote $\Delta^{GW}(\infty)$ as the bandgap extrapolated to the infinite number of bands limit. The error bar of such a procedure is about ±0.02 eV (see the supplementary material). To avoid extremely demanding GW calculations, we decided to use reasonable production parameters ($E_{cut}^{GW}$ = 300 eV and $N_B$ = 1920) for subsequent calculations and a corresponding *a posteriori* rigid correction to the asymptote, by taking $\Delta^{GW}(\infty) - \Delta^{GW}(N_B^{production})$ = 0.11 eV.
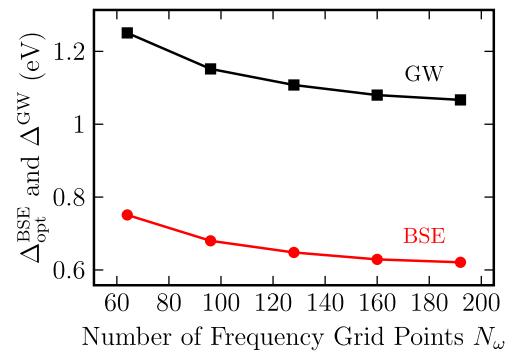
$\Delta^{GW}$ is also sensitive to the number of frequency grid points $N_\omega$ used by the GW method (Fig. 3, black).[47] The production results presented below used $N_\omega$ = 128 and a corresponding *a posteriori* correction of −0.09 eV.

Subsequently, the effect of inter-sheet distance $L_z$[21,47,86–88] was investigated for various k-point grids, and the bias was eliminated by extrapolations of $\Delta^{GW}$ to the thermodynamic limit, by taking $1/L_z \to 0$ and $1/N_k \to 0$, where $N_k$ is the number of k-points in the first 2D BZ (Fig. 4).

The slope $C$ of the corresponding linear fit[86–88]

$$\Delta^{GW}\left(\frac{1}{L_z}\right) = C\frac{1}{L_z} + \Delta^{GW}(0), \quad (7)$$

where $C$ and $\Delta^{GW}(0)$ are fitting parameters, significantly differing for various k-point grids (Fig. 4). In addition, significant deviation from linearity was observed for small values of $L_z$. This was attributed to the significant deformation of the lowest unoccupied orbitals [Fig. 4(a)]. The corresponding $\Delta^{GW}$ values [Fig. 4(a), green square] were, therefore, removed from the fitting procedure [Fig. 4(b)]. The extrapolations to the zero $1/L_z$ limit yielded $\Delta^{GW}$ of 1.60 ± 0.04 eV, 1.41 ± 0.01 eV, and 1.28 ± 0.02 eV, for the 6 × 6 × 1, 12 × 12 × 1, and, 18 × 18 × 1 k-point grids, respectively. Finally, the $\Delta^{GW}$ estimate for a full k-point grid ($N_k \to \infty$) was obtained using extrapolation of the quasiparticle gap values obtained in Fig. 4 (points corresponding to $1/L_z \to 0$ limits for varying k-point meshes). A weighted linear fit was used in Fig. 5, where the weights were $N_k$ values, because the reliability of $\Delta^{GW}$ from Eq. (7) is higher



**FIG. 2.** Quasiparticle bandgaps ($\Delta^{GW}$) of a single-layer of $Sc_2C(OH)_2$ depending on the number of bands included in computations within the GW@PBE method with different dielectric matrix cutoffs ($E_{cut}^{GW}$ = 100–400 eV). The curves and vertical segments show the hyperbolical fits and asymptotes, respectively, corresponding to Eq. (6). The results were obtained with a 12 × 12 × 1 k-point grid, $N_\omega$ = 96, vacuum size $L_z$ = 20 Å, and a plane-wave cut-off energy of $E_{cut}$ = 500 eV.



**FIG. 3.** Quasiparticle bandgaps ($\Delta^{GW}$, black) and optical gaps ($\Delta_{opt}^{BSE}$, red) of single-layer of $Sc_2C(OH)_2$, depending on the number of frequency grid points $N_\omega$. The results were obtained with 12 × 12 × 1 k-point grids, $L_z$ = 20 Å, $N_B$ = 1152, $E_{cut}^{GW}$ = 200 eV, and $E_{cut}$ = 500eV.
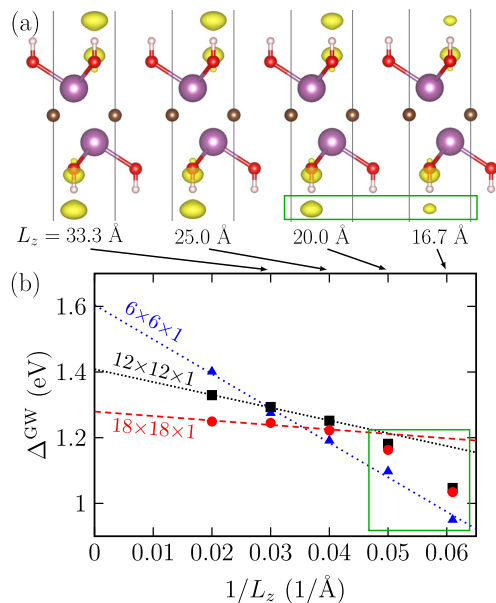
**FIG. 4.** (a) Lowest unoccupied orbitals in $\Gamma$ and (b) quasiparticle bandgaps of a single-layer of $Sc_2C(OH)_2$ depending on inter-sheet distance $L_z$ for (a) $12 \times 12 \times 1$ k-point grid and (b) various k-point grids. Linear extrapolations for $1/L_z \rightarrow 0$ are included as lines. The points in the green box (b) correspond to the deformed orbitals in the green box (a) and were excluded from the fitting procedure. The number of bands $N_B = 1920$, the dielectric matrix cutoff $E_{cut}^{GW} = 300$ eV, $N_\omega = 128$, and plane-wave cut-off $E_{cut} = 500$ eV.
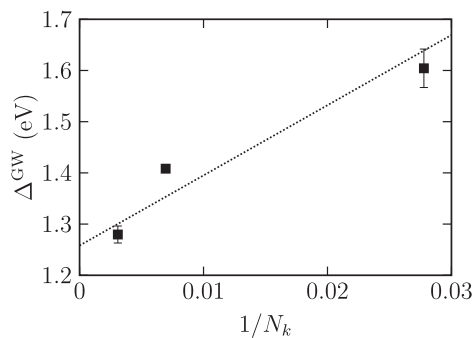


**FIG. 5.** Quasiparticle gaps $\Delta^{GW}$ of single-layer $Sc_2C(OH)_2$ depending on a k-point grid size ($N_k = N_{k_x} \times N_{k_y} \times N_{k_z}$), and the linear fit provides the best guess of $\Delta^{GW}$ for $1/N_k \rightarrow 0$.

if other computational parameters (plane wave cutoff, k-point sampling, and number of bands) are well converged.[87,88] Based on the presented extrapolations ($1.26 \pm 0.10$ eV, see also the supplementary material) and rigid corrections from the paragraph of Eq. (6)

($0.11 \pm 0.02$ eV and $-0.09 \pm 0.02$ eV), we arrive at the final GW production estimate of the quasiparticle gap for $Sc_2C(OH)_2$ MXene sheet of

$$\Delta^{GW} = (1.28 \pm 0.10) \text{ eV},$$

where the uncertainty was evaluated by the standard variance formula for error propagation.

An optical gap (position of the first excitonic peak) obtained by the BSE method was computed by taking all extrapolations of the relevant parameters into account (for $N_\omega$ dependency, see Fig. 3). The current best estimate amounts to $\Delta_{opt}^{BSE} = 0.65 \pm 0.10$ eV. The first exciton binding energy consequently amounts to $E_b^{BSE} = 0.63$ eV—an unusually large value relative to the predicted $\Delta$ (many 2D materials show[89] $E_b \approx \Delta/4$).

Achieving precise absorbance spectra from BSE calculations is more difficult than optical bandgaps because convergence of more states, within range of several eV, is required. First, we choose the number of considered GW bands allowed for optical transitions in the final BSE step to have reliable optical absorbance spectra for photon energies up to 4 eV. Here, 7 occupied and 11 virtual orbitals were
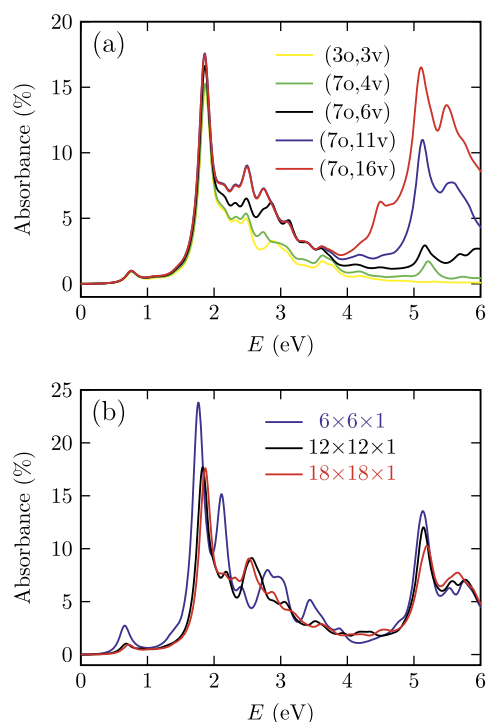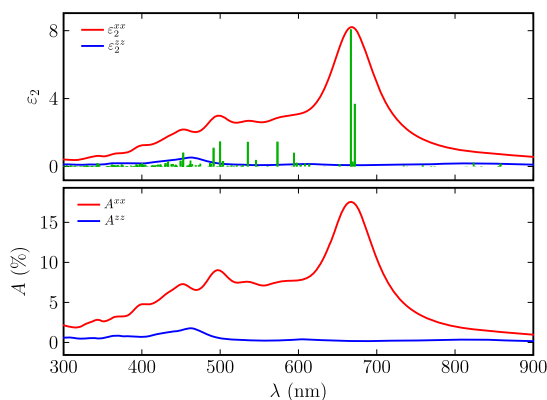


**FIG. 6.** Convergence of optical absorbance spectra $A^{xx} = A^{yy}$ (%) for $Sc_2C(OH)_2$, computed with the GW + BSE method. Dependence of optical absorbance on (a) the number of considered bands in the final BSE step (o = occupied, v = virtual; $L_z = 25$ Å); (b) k-point grid density ($L_z = 33.3$ Å).

sufficient, as follows from Fig. 6(a). Subsequently, the typical most problematic BSE factor, BZ k-point sampling density,[44,45,50,88] was checked. The spectra obtained for the $12 \times 12 \times 1$ and $18 \times 18 \times 1$ k-point grids [Fig. 6(b)] seem to be reasonably similar (although not perfect), both in amplitudes (absorbance values) and peak positions, up to the desired 4 eV. Coarser k-point grids clearly lead to overestimated absorbance, different weights of optical transitions, and peak shifts. The red curve in Fig. 6(b) can be considered as an accurate GW + BSE-based prediction of the $Sc_2C(OH)_2$ absorbance spectrum in the energy range 0–4 eV. Absorbance $A$, within the photovoltaics-relevant photon energy window[90] (1.5–3 eV), amounts to $A \approx 5$–15%. $Sc_2C(OH)_2$, with its ~6.9 Å thickness, is, therefore, expected to be a good solar light absorber, with similar performance as the $MoS_2$ monolayer (3.1 Å thick) showing $A \approx 5$–10%.[90]

For completeness, we also present the imaginary part of the dielectric function and absorbance as a function of wavelength in Fig. 7. The production GW + BSE curves are displayed in the near ultraviolet and visible regions and serve for comparison with future experimental measurements not yet available. We note that our choice of the coordinate system (the material lies in the $xy$ plane, see also Fig. 1) implies zero off-diagonal and nonzero diagonal elements of the above-mentioned tensors. $Sc_2C(OH)_2$ is highly anisotropic: e.g., the $\varepsilon_2^{zz}$ element of the dielectric matrix (corresponding to absorption spectra of $Sc_2C(OH)_2$ for light polarization perpendicular to the surface plane) is zero or very small in the whole wavelength region of Fig. 7.

Finally, we comment on the first exciton wave function, expressed in an electron–hole product basis as $\sum_{cvk} A_{cvk}^{\lambda} \phi_{ck} \phi_{vk}$ for the first ($\lambda = 1$) doubly degenerate exciton state, which is essential for $\Delta_{opt}$. The $|A_{cvk}^1|$ coefficients in Eq. (3) correspond to the contribution of the electron–hole pair configuration in the specific band and k-point to the exciton wave function. These contributions, projected onto the quasiparticle band structure,[91] are depicted by circles, with a size proportional to $|A_{cvk}^1|$ in Fig. 8. Clearly, only
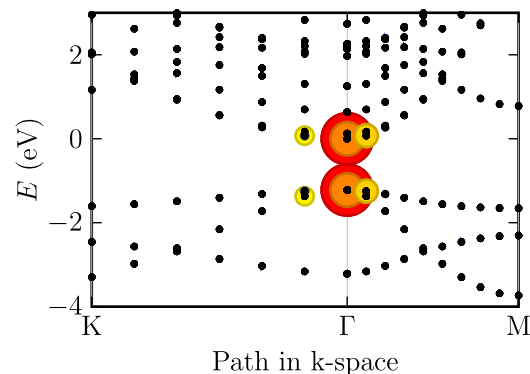


**FIG. 8.** Quasiparticle (GW) band structure of $Sc_2C(OH)_2$ (black dots) and all $|A_{cvk}^{\lambda}|$ coefficients from BSE (represented by the radius of the colored circles) visually show which electron–hole pairs contribute to the first excitonic peak, i.e., to a particular BSE eigenstate $\lambda = 1$. The Fermi energy is set to zero.

the highest occupied band and the lowest unoccupied band in the k-space region very close to the $\Gamma$ point contribute to the first excitonic state. Other regions of the BZ and other bands provide only negligible contributions to the first excitonic state. The $A_{cvk}^1$ coefficient distribution in $Sc_2C(OH)_2$ resembles the case of insulating fluorographene.[21]

## B. FNDMC

Several validation computations were performed within FNDMC to rule out biases that may possibly stem from various method settings and inputs such as the shape of orbitals (well possible in transition-metal containing systems[81]), vacuum size of the periodic slab model, and finite time step.

The computations of the two sets of $\Delta^{FN}$, using restricted PBE and HSE06 orbitals in $\Psi_T$, revealed consistency over all considered supercell sizes ($3 \times 3$ to $5 \times 5$), as well as for the value extrapolated to the thermodynamic limit, to about $0.05 \pm 0.1$ eV. PBE was thus selected as a less computationally demanding method for production of orbitals entering $\Psi_T$.

The timestep error was tested within the $3 \times 3$ supercell by considering two timestep values (0.01 a.u. and 0.005 a.u.). The difference in $\Delta^{FN}(3 \times 3)$ was of the order of $0.1 \pm 0.1$ eV, and the larger value was observed for the smaller timestep. The effect of vacuum size was verified by additional computation of $\Delta$ in the supercell with $2L_z$, where $L_z = 20$ Å is the original size of the supercell in the z-direction, used in all FNDMC computations. The results of the $3 \times 3$ supercell revealed a shift by $0.1 \pm 0.1$ eV. Although timestep error and vacuum-size correction were indistinguishable from noise, they were both positive. It is well possible that our production FNDMC value may be underestimated by ~0.2 ± 0.14 eV. These effects (timestep bias and vacuum-size bias) were accounted for by taking into account a systematic bias correction of ±0.14 eV in the statistical error bar of the production FNDMC bandgap estimate (taking MC sampling and finite-size extrapolation biases into account) below.



**FIG. 7.** Imaginary part of the dielectric function $\epsilon_2^{\alpha\beta}$ (and corresponding oscillator strengths) and the absorbance $A^{\alpha\beta}$ of $Sc_2C(OH)_2$, calculated by the GW + BSE in the near ultraviolet and visible regions, as a function of wavelength.

Particle number differences from the charge neutrality (zero) projected onto the individual unit cells, examined for the $3 \times 3$ and $4 \times 4$ supercells, confirm that the simulated FNDMC states, including the promoted states, remained fully translation-invariant (Table I). Promoted-states charge distributions were found to be statistically indistinguishable from charge neutrality, and, from the translation-invariant distributions sampled by the individual ground-states, no traces of charge localization within the considered supercells were detected whatsoever. Note that the localized exciton state formation would induce charge redistribution and translation symmetry breaking within the supercell of the promoted state, where the center would exhibit systematic charge accumulation and the corners would show the corresponding charge depletion that was not observed. The (neutral) FNDMC energy differences reported below, therefore, unambiguously correspond to the fundamental (quasiparticle) gap estimates (see arguments in Sec. II C).

The production FNDMC $\Delta^{FN}(s)$ results are summarized in Table II. The best available linear extrapolation of $\Delta^{FN}(s)$ from the production data (Table II) for the considered supercell sizes amounts to $\Delta^{FN}(\infty) = 1.30 \pm 0.14$ eV. The best available FNDMC-based estimate of a fundamental gap of $Sc_2C(OH)_2$, produced within the current work, thus amounts to

$$\Delta^{FN} = (1.3 \pm 0.2) \text{ eV.}$$

**TABLE I.** FNDMC particle number differences from charge neutrality (in units of elementary charge) for ground-state (GS) and promoted-state (PS) simulations within the $3 \times 3$ and $4 \times 4$ supercells, projected onto the individual unit cells of the given supercell in the xy-plane. Standard deviations $\sigma$ of the sampled distributions and $1\sigma$ error bars ($\pm$) for the individual entries are reported above each dataset.

| $3 \times 3$ GS | $\sigma = 2.28$ | $\pm 4.8 \times 10^{-3}$ | |
|---|---|---|---|
| $6.428 \times 10^{-3}$ | $-2.008 \times 10^{-3}$ | $-4.599 \times 10^{-3}$ | |
| $1.619 \times 10^{-2}$ | $-1.170 \times 10^{-2}$ | $1.501 \times 10^{-2}$ | |
| $8.449 \times 10^{-3}$ | $-1.586 \times 10^{-2}$ | $-1.191 \times 10^{-2}$ | |
| $3 \times 3$ PS | $\sigma = 2.29$ | $\pm 4.5 \times 10^{-3}$ | |
| $-1.669 \times 10^{-2}$ | $1.633 \times 10^{-2}$ | $4.299 \times 10^{-3}$ | |
| $6.913 \times 10^{-3}$ | $-6.082 \times 10^{-3}$ | $-1.703 \times 10^{-3}$ | |
| $-2.012 \times 10^{-3}$ | $5.540 \times 10^{-3}$ | $-6.586 \times 10^{-3}$ | |
| $4 \times 4$ GS | $\sigma = 2.28$ | $\pm 5.5 \times 10^{-3}$ | |
| $2.440 \times 10^{-2}$ | $-1.459 \times 10^{-2}$ | $-1.257 \times 10^{-2}$ | $-1.892 \times 10^{-2}$ |
| $-1.061 \times 10^{-2}$ | $9.353 \times 10^{-3}$ | $-4.380 \times 10^{-4}$ | $2.825 \times 10^{-2}$ |
| $-9.847 \times 10^{-3}$ | $-1.890 \times 10^{-2}$ | $1.869 \times 10^{-3}$ | $-5.786 \times 10^{-3}$ |
| $6.604 \times 10^{-3}$ | $8.431 \times 10^{-3}$ | $2.439 \times 10^{-2}$ | $-1.164 \times 10^{-2}$ |
| $4 \times 4$ PS | $\sigma = 2.29$ | $\pm 5.1 \times 10^{-3}$ | |
| $-1.546 \times 10^{-3}$ | $-2.007 \times 10^{-2}$ | $1.205 \times 10^{-2}$ | $1.909 \times 10^{-2}$ |
| $-6.365 \times 10^{-3}$ | $8.354 \times 10^{-3}$ | $2.397 \times 10^{-2}$ | $-1.742 \times 10^{-3}$ |
| $3.365 \times 10^{-3}$ | $-1.539 \times 10^{-2}$ | $8.710 \times 10^{-3}$ | $1.710 \times 10^{-3}$ |
| $-7.555 \times 10^{-3}$ | $-1.563 \times 10^{-2}$ | $4.292 \times 10^{-3}$ | $-1.330 \times 10^{-2}$ |

**TABLE II.** Production FNDMC fundamental gaps $\Delta^{FN}(s)$ for varying supercell sizes $s$ obtained with PBE orbitals corresponding to the optimized occupation vector $\vec{\lambda}_{opt}$ (see Sec. II C), timestep of 0.01 a.u., three-center Jastrow terms, single electron VBM–CBM promotion approach, and ccECPs. The value for the thermodynamic ($\infty$) limit was obtained by linear extrapolation of $\Delta^{FN}(s)$ for all $s$.

| Size ($s$) | $\Delta^{FN}(s)$ (eV) |
|---|---|
| $3 \times 3$ | $1.34 \pm 0.04$ |
| $4 \times 4$ | $1.31 \pm 0.09$ |
| $5 \times 5$ | $1.32 \pm 0.11$ |
| $\infty$ | $1.30 \pm 0.14$ |

This value is statistically indistinguishable from all the finite-size bandgap values (Table II), indicating small, if not negligible, size effects within the (neutral) FNDMC simulations. This result also shows a very good agreement with the $\Delta^{GW}$ reported above, within the error bars.

## IV. SUMMARY

Benchmark non-empirical many-body GW and FNDMC-based estimates of $\Delta$ were presented for a freestanding monolayer of $Sc_2C(OH)_2$—a prototypical, non-magnetic MXene with a direct bandgap. Careful elimination of biases from several methods, stemming from various technical settings, turned out essential to reach the convergence for the unusual sensitivity of $\Delta$ to technical parameters in both complementary methods used—GW and FNDMC alike. The converged individual fundamental gap estimates reached $\Delta^{GW} = 1.28 \pm 0.1$ eV and $\Delta^{FN} = 1.30 \pm 0.2$ eV. Remarkable consistency of our $\Delta$ estimates for a freestanding $Sc_2C(OH)_2$ monolayer, based on the non-empirical, many-body FNDMC and GW methods, suggests that benchmark accuracy has been achieved by both methods, and further corrections of this quantity at the 0.1 eV energy scale are not expected. Our final estimate of the $Sc_2C(OH)_2$ fundamental gap, based on GW and FNDMC, is

$$\Delta \approx (1.29 \pm 0.2) \text{ eV.}$$

The first exciton binding energy of a freestanding $Sc_2C(OH)_2$ monolayer, based on the Bethe–Salpeter equation, amounts to 0.63 eV. This value is unusually high, almost reaching $E_b \approx \Delta/2$. Therefore, unlike in many other 2D materials, it seems that $E_b$ in $Sc_2C(OH)_2$ does not exhibit universal scaling of the exciton binding energy[89] with $\Delta$ (following $E_b \approx \Delta/4$). In addition, the absorbance spectra and dielectric function were provided as a prediction for future reference.

## SUPPLEMENTARY MATERIAL

See the supplementary material for the $Sc_2C(OH)_2$ model structure used in the reported computations, details on the non-linear fitting of quasi-particle gaps with respect to the number of bands and plane-wave cutoff, and uncertainty evaluations with respect to the number of bands and the number of k-points, respectively.

## ACKNOWLEDGMENTS

## AUTHOR DECLARATIONS

### Conflict of Interest

The authors have no conflicts to disclose.

### Author Contributions

**Matúš Dubecký**: Conceptualization (equal); Data curation (equal); Formal analysis (equal); Funding acquisition (equal); Investigation (equal); Methodology (equal); Project administration (equal); Validation (equal); Visualization (equal); Writing – original draft (equal); Writing – review & editing (equal). **Stanislav Minárik**: Formal analysis (supporting); Investigation (supporting); Methodology (supporting); Writing – review & editing (supporting). **František Karlický**: Conceptualization (equal); Data curation (equal); Formal analysis (equal); Funding acquisition (equal); Investigation (equal); Methodology (equal); Project administration (equal); Resources (equal); Supervision (equal); Visualization (equal); Writing – original draft (equal); Writing – review & editing (equal).

## DATA AVAILABILITY

The data that support the findings of this study are available within the article and its supplementary material.

## REFERENCES

[1] S. Das, J. A. Robinson, M. Dubey, H. Terrones, and M. Terrones, Annu. Rev. Mater. Res. **45**, 1 (2015).

[2] M. Pykal, P. Jurečka, F. Karlický, and M. Otyepka, Phys. Chem. Chem. Phys. **18**, 6351 (2016).

[3] M. Zeng, Y. Xiao, J. Liu, K. Yang, and L. Fu, Chem. Rev. **118**, 6236 (2018).

[4] E. C. Ahn, npj 2D Mater. Appl. **4**, 17 (2020).

[5] K. Khan, A. K. Tareen, M. Aslam, R. Wang, Y. Zhang, A. Mahmood, Z. Ouyang, H. Zhang, and Z. Guo, J. Mater. Chem. C **8**, 387 (2020).

[6] K. Nomura, H. Ohta, A. Takagi, T. Kamiya, M. Hirano, and H. Hosono, Nature **432**, 488 (2004).

[7] K. F. Mak, C. Lee, J. Hone, J. Shan, and T. F. Heinz, Phys. Rev. Lett. **105**, 136805 (2010).

[8] K. F. Mak and J. Shan, Nat. Photonics **10**, 216 (2016).

[9] L. Li, Y. Yu, G. J. Ye, Q. Ge, X. Ou, H. Wu, D. Feng, X. H. Chen, and Y. Zhang, Nat. Nanotechnol. **9**, 372 (2014).

[10] J. D. Wood, S. A. Wells, D. Jariwala, K.-S. Chen, E. Cho, V. K. Sangwan, X. Liu, L. J. Lauhon, T. J. Marks, and M. C. Hersam, Nano Lett. **14**, 6964 (2014).

[11] M. W. Barsoum, Prog. Solid State Chem. **28**, 201 (2000).

[12] M. Naguib, M. Kurtoglu, V. Presser, J. Lu, J. Niu, M. Heon, L. Hultman, Y. Gogotsi, and M. W. Barsoum, Adv. Mater. **23**, 4248 (2011).

[13] Q. Tao, P. Helmer, L. Jouffret, M. Dahlqvist, J. Lu, J. Zhou, and J. Rosen, Cryst. Growth Des. **20**, 7640 (2020).

[14] S. Haastrup, M. Strange, M. Pandey, T. Deilmann, P. S. Schmidt, N. F. Hinsche, M. N. Gjerding, D. Torelli, P. M. Larsen, A. C. Riis-Jensen, J. Gath, K. W. Jacobsen, J. Jørgen Mortensen, T. Olsen, and K. S. Thygesen, 2D Mater. **5**, 042002 (2018).

[15] J. Zhou, X.-H. Zha, M. Yildizhan, P. Eklund, J. Xue, M. Liao, P. O. A. Persson, S. Du, and Q. Huang, ACS Nano **13**, 1195 (2019).

[16] A. Bhat, S. Anwer, K. S. Bhat et al., npj 2D Mater. Appl. **5**, 61 (2021).

[17] T. Ketolainen and F. Karlický, J. Mater. Chem. C **10**, 3919 (2022).

[18] T. Sakhraoui and F. Karlický, ACS Omega **7**, 42221 (2022).

[19] M. Khazaei, M. Arai, T. Sasaki, C.-Y. Chung, N. S. Venkataramanan, M. Estili, Y. Sakka, and Y. Kawazoe, Adv. Funct. Mater. **23**, 2185 (2013).

[20] X. Kuangwei, W. Peihong, Y. Guang, L. Zhongfei, Z. Haijun, J. Shaowei, and X. Xin, Sci. Rep. **7**, 15095 (2017).

[21] M. Dubecký, F. Karlický, S. Minárik, and L. Mitas, J. Chem. Phys. **153**, 184706 (2020).

[22] L. Hedin, Phys. Rev. **139**, A796 (1965).

[23] L. Horváthova, M. Dubecký, L. Mitas, and I. Štich, Phys. Rev. Lett. **109**, 053001 (2012).

[24] E. Ertekin, L. K. Wagner, and J. C. Grossman, Phys. Rev. B **87**, 155210 (2013).

[25] K. Foyevtsova, J. T. Krogel, J. Kim, P. R. C. Kent, E. Dagotto, and F. A. Reboredo, Phys. Rev. X **4**, 031003 (2014).

[26] A. Benali, L. Shulenburger, N. A. Romero, J. Kim, and O. A. von Lilienfeld, J. Chem. Theory Comput. **10**, 3417 (2014).

[27] L. K. Wagner, Phys. Rev. B **92**, 161116 (2015).

[28] H. Zheng and L. K. Wagner, Phys. Rev. Lett. **114**, 176401 (2015).

[29] T. Frank, R. Derian, K. Tokár, L. Mitas, J. Fabian, and I. Štich, Phys. Rev. X **9**, 011018 (2019).

[30] R. J. Hunt, M. Szyniszewski, G. I. Prayogo, R. Maezono, and N. D. Drummond, Phys. Rev. B **98**, 075122 (2018).

[31] Y. Yang, V. Gorelov, C. Pierleoni, D. M. Ceperley, and M. Holzmann, Phys. Rev. B **101**, 085115 (2020).

[32] R. J. Hunt, B. Monserrat, V. Zólyomi, and N. D. Drummond, Phys. Rev. B **101**, 205115 (2020).

[33] D. Wines, K. Saritas, and C. Ataca, J. Chem. Phys. **153**, 154704 (2020).

[34] C. A. Melton and L. Mitas, Phys. Rev. B **102**, 045103 (2020).

[35] X. Huang, H. Zhang, and X.-L. Cheng, Int. J. Quantum Chem. **121**, e26643 (2021).

[36] E. E. Salpeter and H. A. Bethe, Phys. Rev. **84**, 1232 (1951).

[37] J. Heyd, G. E. Scuseria, and M. Ernzerhof, J. Chem. Phys. **124**, 219906 (2006).

[38] G. Kresse and J. Furthmüller, Phys. Rev. B **54**, 11169 (1996).

[39] P. E. Blöchl, Phys. Rev. B **50**, 17953 (1994).

[40] G. Kresse and D. Joubert, Phys. Rev. B **59**, 1758 (1999).

[41] D. Nabok, A. Gulans, and C. Draxl, Phys. Rev. B **94**, 035118 (2016).

[42] J. P. Perdew, K. Burke, and M. Ernzerhof, Phys. Rev. Lett. **77**, 3865 (1996).

[43] M. Shishkin and G. Kresse, Phys. Rev. B **74**, 035101 (2006).

[44] M. Kolos and F. Karlický, Phys. Chem. Chem. Phys. **21**, 3999 (2019).

[45] D. Y. Qiu, F. H. da Jornada, and S. G. Louie, Phys. Rev. Lett. **111**, 216805 (2013).

[46] B.-C. Shih, Y. Xue, P. Zhang, M. L. Cohen, and S. G. Louie, Phys. Rev. Lett. **105**, 146401 (2010).

[47] M. Kolos and F. Karlický, Phys. Chem. Chem. Phys. **24**, 27459 (2022).

[48] G. Strinati, Phys. Rev. B **29**, 5718 (1984).

[49] S. Albrecht, L. Reining, R. Del Sole, and G. Onida, Phys. Rev. Lett. **80**, 4510 (1998).

[50] T. Ketolainen, N. Macháčová, and F. Karlický, J. Chem. Theory Comput. **16**, 5876 (2020).

[51] J. B. Anderson, J. Chem. Phys. **63**, 1499 (1975).

[52] P. J. Reynolds, D. M. Ceperley, B. J. Alder, and W. A. Lester, J. Chem. Phys. **77**, 5593 (1982).

[53] C. J. Umrigar, M. P. Nightingale, and K. J. Runge, J. Chem. Phys. **99**, 2865 (1993).

[54] L. Mitas, E. L. Shirley, and D. M. Ceperley, J. Chem. Phys. **95**, 3467 (1991).

[55] W. M. C. Foulkes, L. Mitas, R. J. Needs, and G. Rajagopal, Rev. Mod. Phys. **73**, 33 (2001).

[56] J. Kolorenč and L. Mitas, Rep. Prog. Phys. **74**, 026502 (2011).

# Supplementary Material 9

# Oxygen-terminated Ti₃C₂ MXene as an excitonic insulator

View Online    Export Citation    CrossMark

Nilesh Kumar (iD) and František Karlický[a] (iD)

**AFFILIATIONS**

Department of Physics, Faculty of Science, University of Ostrava, 30. dubna 22, 701 03 Ostrava, Czech Republic

**Note:** This paper is part of the APL Special Collection on MXenes - Physics and Devices.
[a]Author to whom correspondence should be addressed: frantisek.karlicky@osu.cz

**ABSTRACT**

Excitonic insulators originate from the formation of bound excitons (electron–hole pairs) in semiconductors and provide a solid-state platform for quantum many-boson physics. We determined the excitonic insulator phase of $Ti_3C_2O_2$ monolayer from its indirect quasiparticle band structure and from the precise evaluation of the relative value of the fundamental bandgap vs the momentum-indirect excitonic binding energy. The excitonic insulator is stable over the $\pm 4\%$ range of compressive and tensile biaxial strain. The energy region relevant for the optical absorption is strongly strain-dependent.

Published under an exclusive license by AIP Publishing. https://doi.org/10.1063/5.0143313

MXenes, a family of recent two-dimensional (2D) carbides, nitrides, and carbonitrides, embody various interesting properties promising for technical applications.[1–3] Since the first experimentally prepared MXene monolayer, $Ti_3C_2$,[4] more than 20 MXenes were synthesized, and tens of others were theoretically predicted.[5–7] All reported MXenes were terminated by –O, –OH, –F, or Cl on the surface, and Ti-based ones are, therefore, labeled as $Ti_3C_2T_x$, where T is the terminal atom or group. In general, the metallic behavior of $Ti_3C_2T_x$ was observed.[8] Despite the exact composition of terminal groups is typically not under control, here, we focus on stoichiometric oxygen-terminated monolayer $Ti_3C_2O_2$. Oxygen termination should be theoretically the most stable,[9] useful properties of $Ti_3C_2O_2$ were predicted,[10] and we presently discovered its unusual nature by many-body methods.

Some many-body effects, as properties of excitons–electron (e) and hole (h) pairs interacting by Coulomb force, are significantly amplified in 2D materials due to reduced dielectric screening.[11] The binding energy of excitons is one or two orders larger in magnitude than in the corresponding bulk analogs (and is in eV scale, e.g., 2D III–V binary semiconductors[12] or graphene derivatives[13]). 2D MXene's properties are sensitive to composition, termination, or external conditions (pressure, support, solvent, etc.) and provide a rich set of its phases: metals, semiconductors,[14] ferromagnets, antiferromagnets,[15] or topologic insulators.[16] Here, we focus on $Ti_3C_2O_2$, where we indicate that the binding energy of excitons overcomes the fundamental gap, giving rise to a new phase: excitonic

insulator (EI). The EI phenomena in 2D materials were discovered very recently for monolayer $WSe_2$, moiré $WS_2/WSe_2$, or bulk $MoS_2$ under pressure.[17–19] We demonstrate by the first-principles many-body perturbation theory that it not only occurs in $Ti_3C_2O_2$ for equilibrium geometry but is also more pronounced by biaxial strain. We note that the mechanical strain on MXenes is possible to realize experimentally.[20,21]

In *ab initio* calculations, the Bethe–Salpeter equation (BSE), computed on top of an accurate band structure, including quasiparticle corrections in GW approximation, is considered the state-of-the-art approach to model excitons. The GW fundamental gaps, based on Green's function (G) method and screened Coulomb potential (W), were also recently confirmed as very accurate for MXenes by direct comparison with the independent stochastic many-body fixed-node diffusion Monte Carlo method.[22] The VASP software package implementing the projector augmented-wave (PAW) method[23,24] was used in all GW, BSE, and underlying density functional theory (DFT) calculations. The electron self-energy $\Sigma$ uses orbitals $\phi_{nk}(\mathbf{r})$ from DFT and PBE xc functional as an input. The quasiparticle energies $\varepsilon_{nk}^{GW}$ were calculated as first-order corrections to the DFT single-particle energies $\varepsilon_{nk}$. The quasiparticle gap was computed as $\Delta^{GW} = \varepsilon_{CBM}^{GW} - \varepsilon_{VBM}^{GW}$, where CBM stands for conduction band minimum and VBM denotes valence band maximum. For insulating materials with occupied valence bands ($v$ index) and completely unoccupied conduction bands ($c$), the BSE can be rewritten as an eigenvalue problem[25]

$$\left(\varepsilon_{ck}^{\mathrm{GW}} - \varepsilon_{vk}^{\mathrm{GW}}\right)A_{cvk}^{\lambda} + \sum_{c'v'k'}[2\langle\phi_{ck}\phi_{vk}|\nu|\phi_{c'k'}\phi_{v'k'}\rangle$$

$$-\langle\phi_{ck}\phi_{c'k'}|W|\phi_{vk}\phi_{v'k'}\rangle]A_{c'v'k'}^{\lambda} = E_{\mathrm{exc}}^{\lambda}A_{cvk}^{\lambda}, \qquad (1)$$

where $\nu$ is the Coulomb kernel, $1/|\boldsymbol{r} - \boldsymbol{r'}|$, the eigenvectors $A_{cvk}^{\lambda}$ correspond to the amplitudes of free electron–hole pair configurations composed of electron states $|\phi_{ck}\rangle$ and hole states $|\phi_{vk}\rangle$, and the eigenenergies $E_{\mathrm{exc}}^{\lambda}$ correspond to the excitation energies (with optical gap $\Delta_{\mathrm{opt}}^{\mathrm{BSE}} \equiv E_{\mathrm{exc}}^{\lambda}$, for $\lambda$ from first nonzero transition, i.e., first bright exciton). The (positive) exciton binding energy was finally estimated as $E_{\mathrm{b}} = \Delta^{\mathrm{GW,dir}} - \Delta_{\mathrm{opt}}^{\mathrm{BSE}}$, where the "dir" index denotes direct gap. All methods are described in detail in the supplementary material.

The determination of the EI phase is mostly quantitative rather than qualitative, i.e., it depends on the relative value of the fundamental bandgap vs the excitonic binding energy. Therefore, accurate numerical simulations are essential. To reach the desired accuracy of our calculations, we used PAW potentials designed for GW computations, plane wave cutoff energy $E_{\mathrm{cut}} = 500$ eV, and strict electronic-step convergence criterion ($1 \times 10^{-7}$ eV). It is more challenging to achieve high precision of such accurate GW+BSE methods than to be precise at the level of DFT,[12] which is, however, inaccurate for band gaps and spectra. The presented production results were, therefore, converged carefully with respect to the technical parameters that may affect the accuracy, including plane wave cutoff energy for the dielectric matrix, number of unoccupied bands in the calculation, frequency grid size, the size of the vacuum region in the simulation cell, and the size of the k-point mesh. All details are described, and graphs are provided in the supplementary material. Final production results were obtained using $N_B = 480$ bands, $N_\omega = 192$ frequency grid points, $L_z = 20$ Å computation cell height, $E_{\mathrm{cut}}^{\mathrm{GW}} = 200$ eV GW energy cutoff, and $18 \times 18 \times 1$ k-point grid.

First, we optimized the lattice structure of 12 different conformers of $Ti_3C_2O_2$ monolayer because in some MXenes, more energetically close conformers/phases can coexist.[26] Here, the most stable conformer contains the oxygen in the hollow site, see optimized structure in Fig. 1. The second conformer is ~1.8 eV above the lowest one and will not be contained in real samples (see the supplementary material for evaluation of all conformers). The most stable $Ti_3C_2O_2$ belongs to the P-6m2 space group with a space group number of 187. Such $Ti_3C_2O_2$ monolayer is dynamically stable because all the phonon modes are positive in phonon band dispersion,[9] and constant temperature *ab initio* molecular dynamics simulations did not change the structure (see the supplementary material). The initial PBE DFT

electronic structure calculations indicate $Ti_3C_2O_2$ monolayer as conductive indirect $\Gamma \rightarrow M$ material, however, with 0.54 eV direct bandgap located near the center of the $\Gamma$–M segment in the Brillouin zone. More realistic hybrid calculation opened the gap as expected: we obtained values of 0.35 and 1.31 eV for indirect and direct bandgaps, respectively. More importantly, after convergence of all mentioned parameters mentioned earlier[12] and justified in the Supporting Information, we obtained the fundamental quasiparticle indirect and direct gap values of $\Delta^{\mathrm{GW,ind}} = 0.15$ and $\Delta^{\mathrm{GW,dir}} = 1.15$ eV, respectively. Quasiparticle band structure from GW calculation displayed in Fig. 2(a) documents that indirect character ($\Gamma \rightarrow M$) is preserved.

Using BSE [Eq. (1)] on top of GW, we calculated optical excitations and determined the optical gap, which corresponds to the position of the first bright excitonic peak. After necessary testing of important technical parameters convergence (see the supplementary material for k-grid, etc.), we obtained a final optical gap of 0.96 eV. The corresponding binding energy of the first bright exciton is $E_{\mathrm{b}} = 0.19$ eV. On the other hand, the first bright bound exciton at 0.96 eV is of low intensity in the absorbance spectra, see the subplot of Fig. 2(b). The dominant exciton in the spectra at 1.24 eV is a resonant one (slightly above the direct gap of 1.15 eV). Furthermore, from the imaginary part $\varepsilon_2$ of energy-dependent dielectric function $\varepsilon(E) = \varepsilon_1(E) + i\varepsilon_2(E)$, we calculated the optical absorbance[27] $A(E) = 1 - \exp[-\varepsilon_2 E L_z/\hbar c]$, where $E$ is the energy, $L_z$ is the inter-sheet distance, $\hbar$ is the reduced Planck's constant, and $c$ is the speed of light. In the visible part of the spectra (1.5–3 eV), the obtained absorbance is around 10%. The highest absorbance around 26% is located at 3.3 eV in the near ultraviolet region [Fig. 2(b)]. We also comment on the first bright exciton wave function (here $\lambda = 3$), which is essential for $\Delta^{\mathrm{opt}}$, expressed in an electron-hole product basis as $\sum_{cvk} A_{cvk}^{\lambda}\phi_{ck}\phi_{vk}$. Pairs of large circles at the M point and between the $\Gamma$ and M points in Fig. 2(a) represent the electron–hole pairs, significantly contributing to the wave function of the first bright exciton in $Ti_3C_2O_2$. Only the valence band (VB) and conduction band (CB) are important. The dominant exciton at 1.24 eV is composed of pairs between VB-1 and CB in the M point.

Electronic properties are also sensitive to external pressure,[28] and, e.g., $Ti_2CO_2$ monolayer substantially changes its properties by metal/semiconductor and indirect/direct transitions.[15,29] We, therefore, studied the effect of biaxial strain (from −6% to 6%) on the electronic and optical properties of $Ti_3C_2O_2$ monolayer. Figure 3(a) showed the variation in fundamental gap $\Delta$ (direct and indirect) and optical gap $\Delta_{opt}$ under the biaxial strain. At −6% compressive strain, the system showed metallic behavior, but when we changed the strain from −6% to −2%, the indirect fundamental gap increased until the
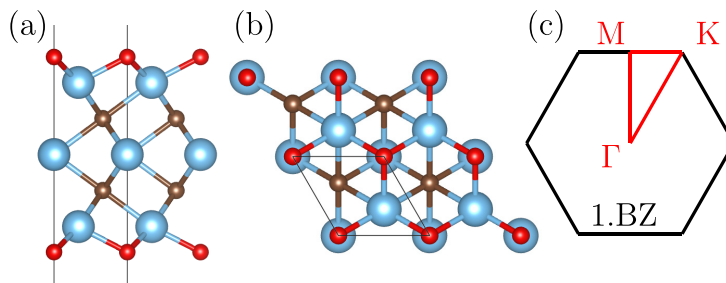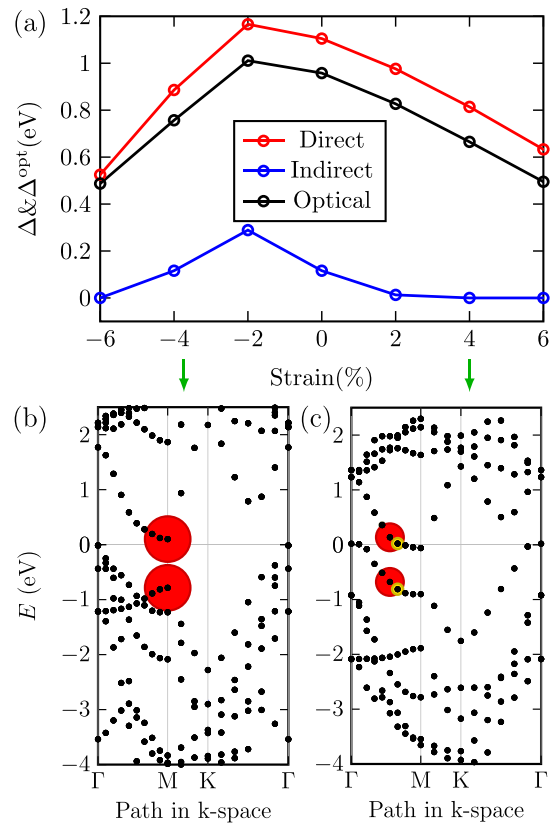


**FIG. 1.** The $Ti_3C_2O_2$ geometrical structure used in present calculations. (a) Side view; (b) top view. Ti, blue; C, brown; and O, red. The thin black lines indicate the unit cell. (c) Sketch of the first Brillouin zone (1.BZ) and high-symmetry points $\Gamma$, M, and K in reciprocal space.
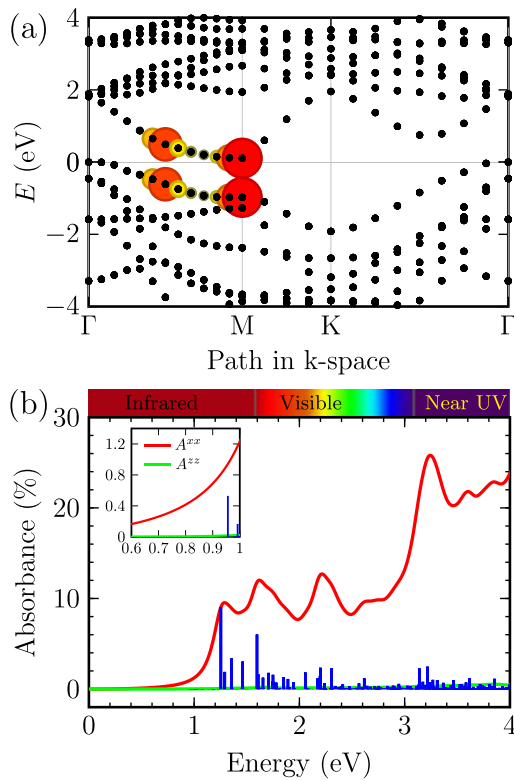
FIG. 2. (a) Quasiparticle (GW) band structure of $Ti_3C_2O_2$ (black dots), and all $|A^\lambda_{cvk}|$ coefficients from BSE (represented by the radius of the colored circles) visually show which electron–hole pairs contribute to the first excitonic peak, i.e., to a particular BSE eigenstate $\lambda = 3$. The top of the valence band is set to zero. (b) Absorbance spectra $A$ ($A_{xx} = A_{yy}$ and $A_{zz}$ components) form BSE for $Ti_3C_2O_2$ monolayer. Particular excitonic states are shown using vertical blue lines. The first excitonic peak is very weak and is depicted in the subplot.



FIG. 3. (a) Variation of fundamental quasiparticle gap (both minimal direct and indirect) and optical gap of $Ti_3C_2O_2$ as a function of biaxial strain. (b) Selected quasiparticle (GW) band structures of $Ti_3C_2O_2$ (black dots) corresponding to -4% (left) and +4% (right) strain. $|A^\lambda_{cvk}|$ coefficients from BSE as in Fig. 2 are added. The top of the valence band is set to zero.

maximum value of 0.29 eV. Furthermore, we noticed metallic behavior again for +4% tensile strain. On the other hand, the direct fundamental gap increased from 0.52 to 1.17 eV (maximum value) when we decreased the biaxial strain from -6% to −2%, and furthermore, the gap decreased back when we increased the tensile strain. Finally, the optical gap $\Delta_{opt}$ showed an analogous trend [Fig. 3(a)]. For −2% strain, we found the maximum value of both minimal direct and optical gaps. As we noticed, the metallic behavior of $Ti_3C_2O_2$ monolayer was observed for compressive strain lesser or equal to −6% and tensile strain larger or equal to 4%. Corresponding deformed quasiparticle electronic structures under +4% and −4% biaxial strains are plotted in Figs. 3(b) and 3(c), respectively. For −4% compressive strain, one can observe the dominant contribution to excitonic wavefunction from CB and VB in the M point [the region of minimal direct gap location; Fig. 3(b)], the large direct gap (∼0.8 eV), small indirect gap (∼0.1 eV), and the binding energy of the first bright exciton slightly exceeding indirect gap. In the +4% tensile strain case, the location of

the direct gap is near the center of the Γ–M path in the Brillouin zone [with maximal excitonic contribution; Fig. 3(c)], and zero indirect gap is smaller than the binding energy of the first bright exciton (∼0.1 eV).

We, therefore, remind the case, where the quasiparticle gap is smaller than the binding energy of the first bright exciton. Such a phenomenon is called the excitonic insulator (EI). However, the band structure shows that the $Ti_3C_2O_2$ monolayer has a small indirect bandgap [Fig. 2(a)]. Then, the criterion for an EI should be that the binding energy of the corresponding momentum-indirect exciton overcomes the indirect bandgap. We, therefore, performed additional calculations of excitons in $Ti_3C_2O_2$ with the inclusion of exciton momentum $\mathbf{q}$ along the ΓM direction. The whole situation is documented in Fig. 4 (purple curve). The calculations clearly show that the excitation energies are rapidly decreasing, going to slightly negative values with a minimal value for $\mathbf{q} = \Gamma M$ and are, therefore, relevant for the ground state of the system. The condition of the exciton insulator is fulfilled for $Ti_3C_2O_2$: $E^{ind}_b = 0.12 - (-0.03) = 0.15\,eV > \Delta^{ind} = 0.12\,eV$, where "ind" index
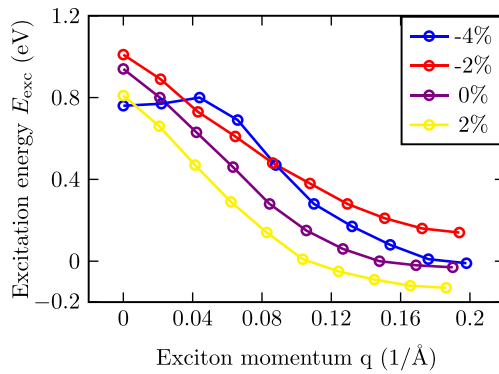
**FIG. 4.** Excitation energy of the MXene $Ti_3C_2O_2$ monolayer with exciton momentum **q** along $\Gamma$ to M path. BSE data (circles) are calculated for several strains (legend), and solid lines are guides to the eye. The M point position in units of $\text{Å}^{-1}$ shifts with the strain.

denotes "indirect" word. As the EI phase can be connected with charge density wave (CDW) states like the case of 1T-TiSe$_2$ transition-metal dichalcogenide,[30] we also tried to investigate the possible CDW phase. However, we did not obtain any indication of the hypothetical CDW phase existence at the DFT level (see the supplementary material for details). A high energy barrier probably exists for CDW formation. The CDW phase would be the ground state only when the excitonic energy gain can overcome this energy barrier.

This example greatly documents the paradox of the exciton insulator nature: quasiparticle band structure indicates indirect semimetal [Fig. 3(c)] with significant minimal direct gap resulting in the significant optical gap [Fig. 3(a)]. The nonzero momentum-indirect exciton binding energy then fulfills the condition of exciton insulator, and the global situation is accomplished by weak oscillator weights of lowest excitons resulting in a big effective optical gap (Fig. 5) in absorbance. The similar behavior is valid for other presented strains in Fig. 4 (with exception of −2%), while calculations of indirect-momentum excitons for zero/negative indirect-gapped cases were complicated due to numerical instability of the Fermi level position. The $Ti_3C_2O_2$ monolayer is, therefore, a reliable candidate for an excitonic insulator under various conditions. Another essential difference between compressive and tensile strain impact is the character of the first excitonic peak. For the tensile strain (similar to the equilibrium geometry), the lowest excitonic transition is of very weak intensity, i.e., the global shape of the absorbance spectra is almost not influenced by such transitions. On the contrary, when an increasing compressive strain is applied, the first exciton transition becomes very strong, and the low-energy peak becomes dominant for the global spectra shape. The situation is reported in Fig. 5, where the position of the first excitonic peak is always indicated by the black arrow. In other words, the first excitonic peak position is roughly decreasing if one applies both tensile and compressive strain. However, the oscillator weights are significantly redistributed. If the compressive strain is applied, a strong absorbance region (10%–30%) is available for the whole energy region (0–4 eV) with the maximum in the infrared part, while the application of tensile strain induces the "effective optical gap" up to 2 eV (almost zero signal,
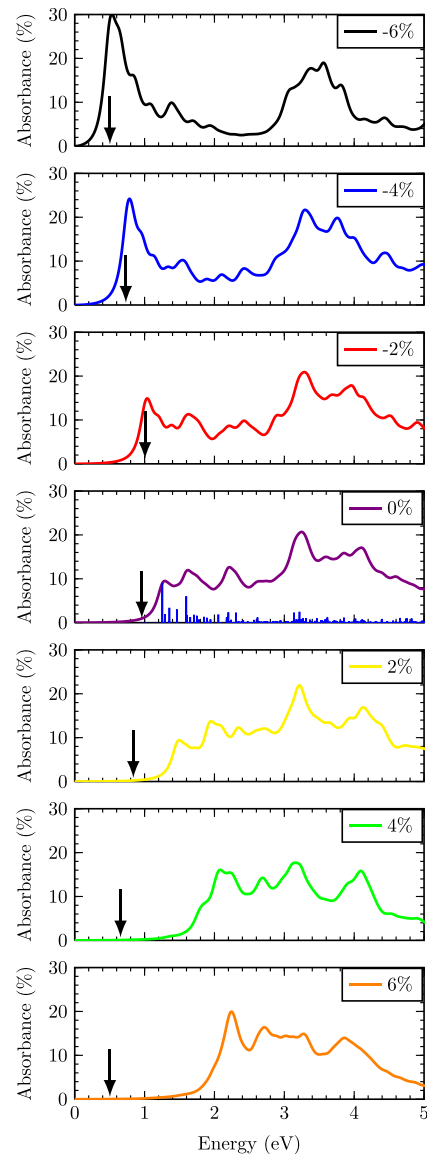


**FIG. 5.** Optical absorbance spectra $A^{xx} = A^{yy}$ (%) for $Ti_3C_2O_2$ computed with the GW+BSE method depended on biaxial strain. The position of the first optical excitation $\Delta_{opt}$ is labeled by the black arrow.

see Fig. 5). Due to excitons, the strain can significantly change the absorbance properties of $Ti_3C_2O_2$ excitonic insulator.

In summary, we bring evidence of $Ti_3C_2O_2$ monolayer excitonic insulator (EI) in equilibrium and under stress. The electronic phase transitions cannot be typically experimentally disentangled, making

direct proof of the EI existence a nontrivial problem. This is why *ab initio* numerical simulations are the key instruments to be used. Standard density functional theory (DFT) does not include a description of the electron–electron and electron–hole (exciton) interactions, and accurate many-body methods beyond DFT are, therefore, necessary for the analysis. Here, we determine the EI phase of $Ti_3C_2O_2$ monolayer from its indirect quasiparticle band structure character and from the precise evaluation of the relative value of the fundamental bandgap vs the momentum-indirect excitonic binding energy.

See the supplementary material for computational details, more details on the geometrical structure and stability, the convergence of electronic and optical properties, and properties under strain.

## AUTHOR DECLARATIONS
### Conflict of Interest

The authors have no conflicts to disclose.

### Author Contributions

**Nilesh Kumar:** Data curation (equal); Formal analysis (equal); Investigation (lead); Methodology (supporting); Visualization (lead); Writing – original draft (lead); Writing – review & editing (supporting). **Frantisek Karlicky:** Conceptualization (lead); Data curation (equal); Formal analysis (equal); Funding acquisition (lead); Investigation (supporting); Methodology (lead); Project administration (lead); Supervision (lead); Visualization (supporting); Writing – original draft (supporting); Writing – review & editing (lead).

## DATA AVAILABILITY

The data that support the findings of this study are available within the article and its supplementary material.

## REFERENCES

[1]B. Anasori, M. R. Lukatskaya, and Y. Gogotsi, "2D metal carbides and nitrides (MXenes) for energy storage," Nat. Rev. Mater. **2**, 16098 (2017).

[2]K. Hantanasirisakul and Y. Gogotsi, "Electronic and optical properties of 2D transition metal carbides and nitrides (MXenes)," Adv. Mater. **30**, 1804779 (2018).

[3]Y. Gogotsi and B. Anasori, "The rise of MXenes," ACS Nano **13**, 8491–8494 (2019).

[4]M. Naguib, M. Kurtoglu, V. Presser, J. Lu, J. Niu, M. Heon, L. Hultman, Y. Gogotsi, and M. W. Barsoum, "Two-dimensional nanocrystals produced by exfoliation of $Ti_3AlC_2$," Adv. Mater. **23**, 4248–4253 (2011).

[5]*2D Metal Carbides and Nitrides (MXenes)*, edited by B. Anasori and Y. Gogotsi (Springer, Switzerland, 2020).

[6]B. Anasori and Y. Gogotsi, "MXenes: Trends, growth, and future directions," Graphene 2D Mater. **7**, 75–79 (2022).

[7]K. R. G. Lim, M. Shekhirev, B. C. Wyatt, B. Anasori, Y. Gogotsi, and Z. W. Seh, "Fundamentals of MXene synthesis," Nat. Synthesis **1**, 601–614 (2022).

[8]S. J. Kim, H.-J. Koh, C. E. Ren, O. Kwon, K. Maleski, S.-Y. Cho, B. Anasori, C.-K. Kim, Y.-K. Choi, J. Kim, Y. Gogotsi, and H.-T. Jung, "Metallic $Ti_3C_2T_x$ MXene gas sensors with ultrahigh signal-to-noise ratio," ACS Nano **12**, 986–993 (2018).

[9]T. Hu, M. Hu, B. Gao, W. Li, and X. Wang, "Screening surface structure of mxenes by high-throughput computation and vibrational spectroscopic confirmation," J. Phys. Chem. C **122**, 18501–18509 (2018).

[10]M. Ashton, R. G. Hennig, and S. B. Sinnott, "Computational characterization of lightweight multilayer MXene Li-ion battery anodes," Appl. Phys. Lett. **108**, 023901 (2016).

[11]A. Chernikov, T. C. Berkelbach, H. M. Hill, A. Rigosi, Y. Li, B. Aslan, D. R. Reichman, M. S. Hybertsen, and T. F. Heinz, "Exciton binding energy and non-hydrogenic Rydberg series in monolayer $WS_2$," Phys. Rev. Lett. **113**, 076802 (2014).

[12]M. Kolos and F. Karlický, "The electronic and optical properties of III–V binary 2D semiconductors: How to achieve high precision from accurate many-body methods," Phys. Chem. Chem. Phys. **24**, 27459–27466 (2022).

[13]F. Karlický and J. Turoň, "Fluorographane $C_2FH$: Stable and wide band gap insulator with huge excitonic effect," Carbon **135**, 134–144 (2018).

[14]T. Ketolainen and F. Karlický, "Optical gaps and excitons in semiconducting transition metal carbides (MXenes)," J. Mater. Chem. C **10**, 3919–3928 (2022).

[15]T. Sakhraoui and F. Karlický, "Electronic nature transition and magnetism creation in vacancy-defected $Ti_2CO_2$ MXene under biaxial strain: A DFTB + U study," ACS Omega **7**, 42221–42232 (2022).

[16]A. Champagne and J.-C. Charlier, "Physical properties of 2D MXenes: From a theoretical perspective," J. Phys. Mater. **3**, 032006 (2020).

[17]Z. Zhang, E. C. Regan, D. Wang, W. Zhao, S. Wang, M. Sayyad, K. Yumigeta, K. Watanabe, T. Taniguchi, S. Tongay *et al.*, "Correlated interlayer exciton insulator in heterostructures of monolayer $WSe_2$ and Moiré $WS_2/WSe_2$," Nat. Phys. **18**, 1214–1220 (2022).

[18]L. Ma, P. X. Nguyen, Z. Wang, Y. Zeng, K. Watanabe, T. Taniguchi, A. H. MacDonald, K. F. Mak, and J. Shan, "Strongly correlated excitonic insulator in atomic double layers," Nature **598**, 585–589 (2021).

[19]S. S. Ataei, D. Varsano, E. Molinari, and M. Rontani, "Evidence of ideal excitonic insulator in bulk $MoS_2$ under pressure," Proc. Natl. Acad. Sci. U. S. A. **118**, e2010110118 (2021).

[20]A. Lipatov, H. Lu, M. Alhabeb, B. Anasori, A. Gruverman, Y. Gogotsi, and A. Sinitskii, "Elastic properties of 2D $Ti_3C_2T_x$ mxene monolayers and bilayers," Sci. Adv. **4**, eaat0491 (2018).

[21]B. C. Wyatt, A. Rosenkranz, and B. Anasori, "2D MXenes: Tunable mechanical and tribological properties," Adv. Mater. **33**, 2007973 (2021).

[22]M. Dubecký, S. Minárik, and F. Karlický, "Benchmarking fundamental gap of $Sc_2C(OH)_2$ MXene by many-body methods," J. Chem. Phys. **158**, 054703 (2023).

[23]P. E. Blöchl, "Projector augmented-wave method," Phys. Rev. B **50**, 17953–17979 (1994).

[24]G. Kresse and D. Joubert, "From ultrasoft pseudopotentials to the projector augmented-wave method," Phys. Rev. B **59**, 1758–1775 (1999).

[25]S. Albrecht, L. Reining, R. Del Sole, and G. Onida, "Ab initio calculation of excitonic effects in the optical spectra of semiconductors," Phys. Rev. Lett. **80**, 4510–4513 (1998).

[26]M. Khazaei, M. Arai, T. Sasaki, C.-Y. Chung, N. S. Venkataramanan, M. Estili, Y. Sakka, and Y. Kawazoe, "Novel electronic and magnetic properties of two-dimensional transition metal carbides and nitrides," Adv. Funct. Mater. **23**, 2185–2192 (2013).

[27]T. Ketolainen, N. Macháčová, and F. Karlický, "Optical gaps and excitonic properties of 2d materials by hybrid time-dependent density functional theory: Evidences for monolayers and prospects for van der Waals heterostructures," J. Chem. Theory Comput. **16**, 5876–5883 (2020).

[28]N. Kumar, R. Chaurasiya, and A. Dixit, "Strain tailored thermodynamic stability, electronic transitions, and optoelectronic properties of iii (In, Ga and Al)-nitride monolayers," Nanotechnology **33**, 045202 (2022).

[29]Y-m Ding, X. Nie, H. Dong, N. Rujisamphan, and Y. Li, "Many-body effects in an MXene $Ti_2CO_2$ monolayer modified by tensile strain: GW-BSE calculations," Nanoscale Adv. **2**, 2471–2477 (2020).

[30]H. Cercellier, C. Monney, F. Clerc, C. Battaglia, L. Despont, M. G. Garnier, H. Beck, P. Aebi, L. Patthey, H. Berger, and L. Forró, "Evidence for an excitonic insulator phase in $1T − TiSe_2$," Phys. Rev. Lett. **99**, 146403 (2007).

# Supplementary Material 10

# Excitons, optical spectra, and electronic properties of semiconducting Hf-based MXenes

Nilesh Kumar,[1] [ID] Miroslav Kolos,[1] [ID] Sitangshu Bhattacharya,[2,a)] [ID] and František Karlický[1,b)] [ID]

AFFILIATIONS

[1] Department of Physics, Faculty of Science, University of Ostrava, 30. dubna 22, 701 03 Ostrava, Czech Republic

[2] Electronic Structure Theory Group, Department of Electronics and Communication Engineering, Indian Institute of Information Technology-Allahabad, Allahabad, Uttar Pradesh 211015, India

Note: This paper is part of the JCP Special Topic on Light-matter Interaction at the Nano and Molecular Scale.
a) Electronic mail: sitangshu@iiita.ac.in
b) Author to whom correspondence should be addressed: frantisek.karlicky@osu.cz

ABSTRACT

Semiconducting MXenes are an intriguing two-dimensional (2D) material class with promising electronic and optoelectronic properties. Here, we focused on recently prepared Hf-based MXenes, namely, $Hf_3C_2O_2$ and $Hf_2CO_2$. Using the first-principles calculation and excited state corrections, we proved their dynamical stability, reconciled their semiconducting behavior, and obtained fundamental gaps by using the many-body GW method (indirect 1.1 and 2.2 eV; direct 1.4 and 3.5 eV). Using the Bethe–Salpeter equation, we subsequently provided optical gaps (0.9 and 2.7 eV, respectively), exciton binding energies, absorption spectra, and other properties of excitons in both Hf-based MXenes. The indirect character of both 2D materials further allowed for a significant decrease of excitation energies by considering indirect excitons with exciton momentum along the Γ-M path in the Brillouin zone. The first bright excitons are strongly delocalized in real space while contributed by only a limited number of electron–hole pairs around the M point in the k-space from the valence and conduction band. A diverse range of excitonic states in $Hf_3C_2O_2$ MXene lead to a 4% and 13% absorptance for the first and second peaks in the infrared region of absorption spectra, respectively. In contrast, a prominent 28% absorptance peak in the visible region appears in $Hf_2CO_2$ MXene. Results from radiative lifetime calculations indicate the promising potential of these materials in optoelectric devices requiring sustained and efficient exciton behavior.

*Published under an exclusive license by AIP Publishing.* https://doi.org/10.1063/5.0197238

## I. INTRODUCTION

In recent years, the exploration of two-dimensional (2D) monolayers and their derivatives has captivated the attention of researchers due to their remarkable potential in the realm of electrical and optoelectronic applications. The groundbreaking properties exhibited by graphene have inspired scientific inquiry into novel 2D materials possessing finite bandgaps. Among these, 2D MXenes have emerged as a distinct class of materials exhibiting extraordinary characteristics and versatile applications in nanotechnology.[1–3] MXenes are a unique and intriguing material class belonging to the family of 2D transition metal carbides, nitrides, or carbonitrides. MXenes represent $M_{n+1}X_nT_x$, where M is a transition metal (such as titanium, scandium, or hafnium), X is carbon and/or nitrogen, $n$ is the number of layers ($n \leq 4$), and T denotes surface functional groups.

MXenes were first discovered in 2011 by Naguib *et al.* ($Ti_3C_2T_x$), and more than 20 MXenes have been synthesized until now.[4] Following these experimental syntheses, many other MXene compositions have been predicted theoretically.[5,6] 2D semiconducting MXenes have a tunable bandgap that can be adjusted by changing the transition metal, surface functionalization (T = O, F, OH, Cl, ...), strain, defects, or intercalated species.[7–10] This tunability enables customized band topologies, making semiconducting MXenes highly valuable for various electronic device applications.[11,12]

Experimental preparation of MXenes is often realized from the corresponding layered materials, MAX phases, where A is an A group (mostly IIIA and IVA) element. Al-containing MAX phases $Hf_2AlC$ and $Hf_3AlC_2$ were experimentally synthesized too.[13] However, the subsequent preparation of Hf-containing MXene from the MAX phase was not yet done and the transition metal Hf was iden-

tified as more inclined to form a different family of layered ternary and quaternary transition metal carbides beyond the MAX phases (as $Hf_3Al_3C_5$, $Hf_3Al_4C_6$, $Hf_2Al_4C_5$, or $Hf_2[Al(Si)]_4C_5$).[14] In 2017, Zhou *et al.*[15] experimentally prepared 2D Hf-based MXenes $Hf_3C_2T_x$ by selective etching of a layered parent $Hf_3[Al(Si)]_4C_6$ compound. Such MXenes were determined to be flexible, conductive, and good candidates for anode materials for metal–ion intercalation. Furthermore, theoretical findings of the Ref. [15] predicted the metallic behavior with good electrical conductivity for $Hf_3C_2T_2$ MXenes with T = O, F, and OH, particularly highlighting the robustness of $Hf_3C_2O_2$ with a superior mechanical strength of 417 GPa value of elastic constant. In addition, Zha *et al.*[16] claimed using the density functional theory (DFT) calculations $Hf_3C_2O_2$ MXene as a semi-metal or conductor (depending on the DFT level). Finally, $Hf_3C_2O_2$ was also suggested to be a promising material for electronic devices modulated by strain because DFT calculations predicted a transition between semi-metals and semi-conductors induced by strain.[17] On the other hand, the moderate and tunable gap of MXene $Hf_2CO_2$ made itself a unique 2D semiconductor.[12,18,19]

In the realm of previous computational studies, there are various investigations on the electronic and optical properties of MXenes, which have primarily relied on generalized-gradient approximation (GGA) to density functional theory (DFT) and other higher levels of density functionals (as hybrids). To reconcile unclarities mainly in $Hf_3C_2O_2$ electronic properties (we finally assigned here the material as a semiconductor, analogically to the $Ti_3C_2O_2$ case[10]), there is a necessity to study the material in more detail. DFT is generally suitable to study the structure, the trends in composition, or the impact of strain in 2D materials.[20,21] However, the reason for going beyond DFT is that DFT does not inherently include the effects of excitons (electron–hole pairs), which are crucial in understanding the optical properties of 2D materials.[22,23] To overcome these limitations and obtain more accurate electronic and optical properties, it is necessary to consider more advanced many-body methods. Many-body perturbation theory, GW approximation for the self-energy calculation,[24] and subsequent GW+BSE (Bethe–Salpeter equation),[25,26] including excitonic effects, are preferred computational methods, recently shown as precise-performing for different MXenes in comparison to another independent and demanding stochastic many-body method.[27]

In this study, we focus our attention on semiconducting oxygen-terminated Hf-based MXenes and we carefully describe them using the many-body perturbation theory. Both Hf-based MXenes, $Hf_3C_2O_2$ and $Hf_2CO_2$, contain heavy 5d elements, so it was also demanded to include the spin–orbit coupling (SOC) in the calculations. We present their accurate electronic and optical properties (including absorptance spectra and a radiative lifetime of exciton), and we describe their indirect nature.

## II. COMPUTATIONAL METHODS

For ground-state calculations, geometrical conformers of 2D-MXenes were prepared following our previous work on the $Ti_3C_2O_2$ case[10] (see a set of highly symmetric structures in Figs. S1 and S2 in the supplementary material). Vacuum space was added along the out-of-plane axis (z-direction), leading to the *c* lattice constant of 22.5 and 19.6 Å for $Hf_3C_2O_2$ and $Hf_2CO_2$, respectively,

preventing interlayer interactions. Density functional theory (DFT) calculations were performed using the Quantum ESPRESSO (QE) package,[28] utilizing a fully relativistic norm-conserving pseudopotential[29] enabling spin–orbit coupling (SOC). A Perdew–Burke–Ernzerhof (PBE) exchange–correlation functional[30] within the generalized gradient approximation (GGA) to DFT was used, and a kinetic cutoff energy of 70 Ry ensured accurate ground-state calculations. The convergence behavior of the kinetic energy cutoff is plotted in Fig. S3 of the supplementary material. A set of $24 \times 24 \times 1$ k-mesh grid was used for the structure relaxation without using any constraint through the force and total energy minimization with respect to all atomic positions and unit cell parameters. A self-consistency convergence threshold of $1 \times 10^{-8}$ Ry was used in the calculations. Self-consistent and non-self-consistent calculations were performed, incorporating non-collinear spin–orbit interactions. To confirm the dynamic stability of both Hf-based MXenes, phonon band dispersion calculations were performed using density functional perturbation theory (DFPT) on a $10 \times 10 \times 1$ **q**-grid and a threshold $1 \times 10^{-15}$ Ry. A non-analytical part (using dielectric matrix and Born effective charges) was included.

Excited state corrections were computed via the many-body perturbation theory (MBPT) YAMBO code (version 5.1.0),[31,32] employing the GW approximation to include quasiparticle self-energy corrections. A converged value of 70 Ry of cutoff energy is used in the sum of the exchange self-energy. The converged value 14 Ry of screening cutoff energy is used to calculate the polarization function in GW calculations. A total of 300 polarization bands were utilized, comprising 56 bands for $Hf_3C_2O_2$ and 40 bands for $Hf_2CO_2$, all of which represent the filled electronic states up to the Fermi level in the respective materials. These bands were employed to calculate the irreducible polarization response function. The GW calculations utilized a random integration method[33] with $1 \times 10^6$ **q** points and a truncated Coulomb potential.[34,35] Box-like Coulomb cutoff geometries of 21.98 and 19.09 Å were applied in the z-direction to the sheet for $Hf_3C_2O_2$ and $Hf_2CO_2$, respectively. Utilizing Kohn–Sham wavefunctions and GW quasiparticle energies, we computed the linear response optical spectra employing the time-independent Bethe–Salpeter equation (BSE). The exchanged and screened cutoffs are used at the converged value of 30 and 3 Ry to build up the exchange electron–hole attractive and repulsive kernels in the BSE matrix. Tamm–Dancoff approximation is used, incorporating the resonant matrix element into the BSE Hamiltonian. The BSE matrix was solved using the diagonalization method, where the obtained poles corresponded to optical transition energies. The BSE can be written as an eigenvalue problem for insulating materials possessing occupied valence bands (v) and entirely unoccupied conduction bands (c),[36,37]

$$(\varepsilon_{ck}^{GW} - \varepsilon_{vk}^{GW})A_{cvk}^{\lambda} + \sum_{c'v'k'} [2\langle\phi_{ck}\phi_{vk}|v|\phi_{c'k'}\phi_{v'k'}\rangle - \langle\phi_{ck}\phi_{c'k'}|W|\phi_{vk}\phi_{v'k'}\rangle]A_{c'v'k'}^{\lambda} = E_{\lambda}A_{cvk}^{\lambda}, \quad (1)$$

where $v$ is the Coulomb kernel, $1/|\mathbf{r} - \mathbf{r}'|$, the eigenvectors $A_{cvk}^{\lambda}$ correspond to the amplitudes of free electron–hole pair configurations composed of electron states $|\phi_{ck}\rangle$ and hole states $|\phi_{vk}\rangle$), and the eigenenergies $E_{\lambda}$ correspond to the excitation energies (with

optical gap $\Delta_{opt} \equiv E_\lambda$, for $\lambda$ from first nonzero transition, i.e., first bright exciton). The exciton binding energy was finally estimated as $E_b = \Delta_{GW,dir} - \Delta_{opt,dir}$, where "dir" index denotes the direct gap.

Indeed, in our GW+BSE calculations employing a truncated Coulomb potential, the spectra were obtained in terms of macroscopic polarizability $\alpha$, a well-defined quantity intimately linked to absorption spectra. For a 2D system, $\alpha$ is expressed in units of length and is defined as[38,39]

$$\alpha(\omega) = -\lim_{\mathbf{q}\to 0} \frac{L}{4\pi q^2} \chi_{00}(\mathbf{q},\omega),$$ (2)

where $\chi_{00}(\mathbf{q},\omega)$ is the non-interacting density response function or irreducible polarizability and $L$ is the length of the computational cell in the $z$-direction.

The dielectric function ($\varepsilon$) is extracted from this macroscopic polarizability ($\alpha = \alpha_1 + i\alpha_2$) using the following equations:[40]

$$\varepsilon(E) = \left(1 + 4\pi\frac{\alpha_1}{L}\right) + i4\pi\frac{\alpha_2}{L}$$ (3)

and $\varepsilon(E) = \varepsilon_1(E) + i\varepsilon_2(E)$, where $\varepsilon_1(E)$ and $\varepsilon_2(E)$ are the real and imaginary part of the dielectric function. The absorptance is calculated using the relation[37] $A(E) = 1 - \exp[-\varepsilon_2 EL/\hbar c]$, where $E$ is the energy of incoming photon, $\hbar$ is the reduced Planck constant, and $c$ is the speed of light.

Additionally, we determine the exciton radiative lifetime $\tau_\lambda^0$ utilizing the following relation (in SI units):[41]

$$\tau_\lambda^0 = \frac{\varepsilon_0 \hbar^2 c}{e^2 E_\lambda} \frac{A_{uc}}{\mu_\lambda^2},$$ (4)

where $A_{uc}$ is the area of the unit cell, $\varepsilon_0$ is the vacuum permittivity, $E_\lambda$ is the exciton energy related to Eq. (1), $e$ is the elementary charge, and $\mu_\lambda^2 = |\sum_{cv\mathbf{k}} A_{cv\mathbf{k}}^\lambda \langle \phi_{c\mathbf{k}}|\mathbf{r}|\phi_{v\mathbf{k}}\rangle|^2/N_k$ is the $\lambda$-exciton intensity[42] given by the linear combination of the square of the transition matrix elements between electron–hole pairs with the excitonic weights $A_{cv\mathbf{k}}^\lambda$ [from Eq. (1)] divided by the number of k-points.[41,43,44] The average radiative lifetime $\langle\tau_\lambda^T\rangle$ of an exciton in state $\lambda$ at temperature $T$ is given by[43]

$$\langle\tau_\lambda^T\rangle = \frac{3}{4}\tau_\lambda^0 \frac{2M_\lambda c^2}{E_\lambda^2} k_B T,$$ (5)

where $M_\lambda$ is the exciton mass, $k_B$ is the Boltzmann constant, and zero-momentum approximation $E_\lambda(q) \approx E_\lambda(q = 0)$ is used.[41]

## III. RESULTS AND DISCUSSION

### A. Structural properties and stability

First, we refined the lattice structure of 12 possible high-symmetry conformers of the $Hf_3C_2O_2$ unit cell and corresponding 8 conformers of the $Hf_2CO_2$ unit cell, as these MXenes can have energetically comparable phases.[18] Information about the optimization of all $Hf_3C_2O_2$ and $Hf_2CO_2$ conformers is mentioned in the supplementary material in Tables S1 and S2, respectively, and the optimized structures of the conformers are plotted in Figs. S1 and S2, respectively. The most stable conformer (A2) of both $Hf_3C_2O_2$ and $Hf_2CO_2$ MXenes contains the oxygen atom at the hollow site. The second energetically favorable conformers, i.e., A4 and B2 for
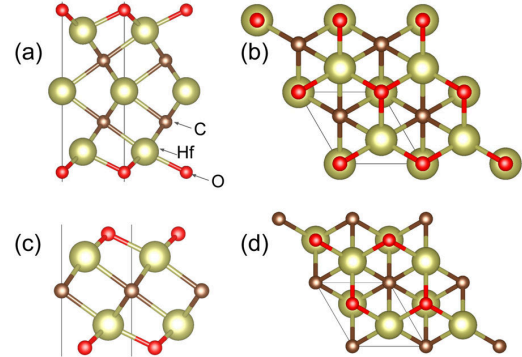


**FIG. 1.** (a) and (c) The side and (b) and (d) top view of the energetically most favorable conformers of (a) and (b) $Hf_3C_2O_2$ and (c) and (d) $Hf_2CO_2$ MXenes. The black line defines the unit cell.

$Hf_3C_2O_2$ and $Hf_2CO_2$, respectively, are significantly energetically higher (1.11 and 0.64 eV above the lowest conformers A2) and therefore not expected to be present in real samples due to their higher energy state. Figure 1 shows the side and top views of the most stable optimized structures (A2) used in the subsequent calculations.

Both favorable structures of $Hf_3C_2O_2$ and $Hf_2CO_2$ MXenes exhibit hexagonal configurations. The $Hf_3C_2O_2$ structure of Fig. 1 has a $D_{3h}$ (−62 m) symmetry, while $Hf_2CO_2$ has a $D_{3d}$ (−3 m) symmetry. The primary distinction between $D_{3h}$ and $D_{3d}$ point groups is the presence (or lack) of certain symmetry elements, namely, the horizontal mirror plane (h) in $D_{3h}$ and the vertical mirror plane (d) in $D_{3d}$. The optimized in-plane lattice constant is 3.26 Å, the same for both $Hf_3C_2O_2$ and $Hf_2CO_2$ MXenes. This implies that these compounds have an equivalent area of the unit cell, which indicates that they may have comparable densities and atomic configurations along the crystallographic directions. In $Hf_3C_2O_2$, the Hf–C bond lengths range from 2.32 to 2.34 Å, reflecting the variation in bonding distances within the material. Additionally, the Hf–O bond length in $Hf_3C_2O_2$ is 2.10 Å, while in $Hf_2CO_2$, the Hf–C bond length is 2.34 Å, indicating a consistent bonding distance between Hf and C atoms. The Hf–O bond length in $Hf_2CO_2$ matches that of $Hf_3C_2O_2$ at 2.10 Å.

We also computed the phonon band structures using density functional perturbation theory (DFPT) for both Hf-based MXenes, employing a $24 \times 24 \times 1$ k-mesh grid. The resulting phonon band structures depicted in Fig. 2 reveal positive frequencies throughout the Brillouin zone (BZ). This stability signifies that the crystal lattice vibrations are secure and devoid of spontaneous deformations or phase transitions.

### B. Electronic band structures and charge analysis from DFT

In our study, we first calculated the ground-state DFT electronic band structures of both Hf-based MXenes using the $30 \times 30 \times 1$ k-mesh grid, plotted in Fig. 3 (blue line). Given the substantial presence of hafnium (Hf) atoms, we conducted comprehensive spin–orbit coupling (SOC) calculations to account for
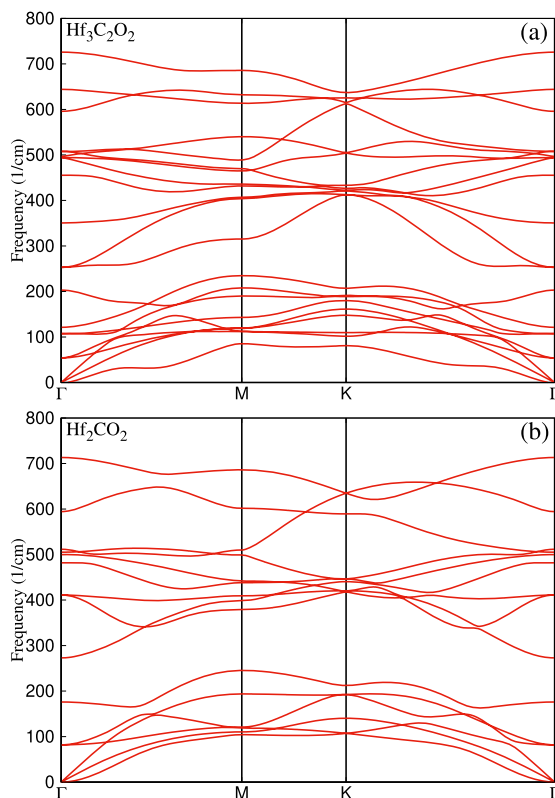
**FIG. 2.** Phonon band structures of (a) $Hf_3C_2O_2$ and (b) $Hf_2CO_2$ MXenes.
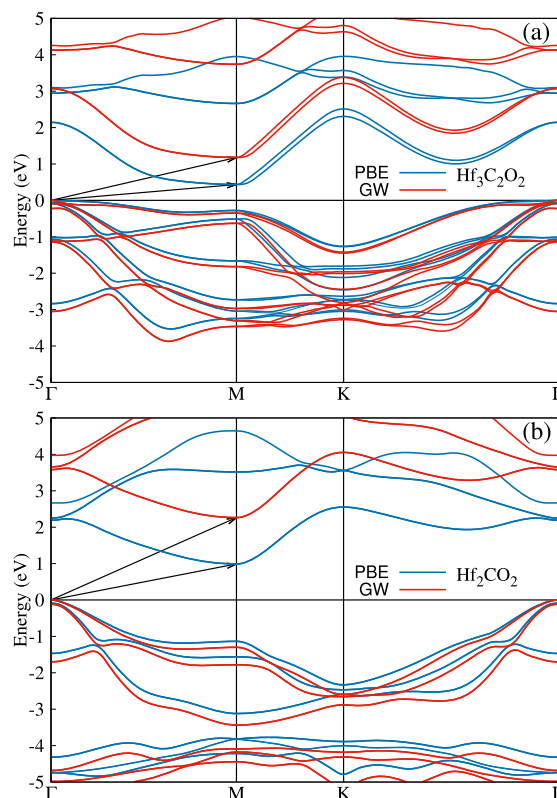


**FIG. 3.** DFT (blue lines) and quasiparticle GW (red lines) band structures of (a) $Hf_3C_2O_2$ and (b) $Hf_2CO_2$ MXenes with included spin–orbit coupling (SOC). Black arrows highlight indirect gaps. The Fermi level is set to zero.

relativistic effects. The DFT electronic band structures are also calculated without SOC consideration, plotted in Fig. S4 of the supplementary material. The significant influence of SOC was evident mainly in $Hf_3C_2O_2$, as indicated by the observed energy band splitting in the electronic band structure around the K point (Figure S4). We determined the DFT indirect bandgaps of 0.43 and 0.99 eV between the high-symmetry points Γ (the top of the valence band) and M (the bottom of the conduction band) for $Hf_3C_2O_2$ and $Hf_2CO_2$, respectively. The corresponding direct bandgaps of 0.71 and 2.12 eV were located in the high-symmetry point M (considering SOC; Fig. 3). The absence of a shift in the positions of the valence band maximum (VBM) and conduction band minimum (CBM) due to SOC is a notable observation in both Hf-based MXenes and indicates that SOC did not significantly affect the bandgap in these systems. The observed degeneracy in the energy bands at the Γ point implies that specific electronic states at this high-symmetry point have identical energies, even when considering SOC. For $Hf_2CO_2$ MXene, the DFT results are in good agreement with previously reported values.[17,19] Both Hf-based MXenes exhibited a non-magnetic semiconducting behavior.

In the case of $Hf_3C_2O_2$, the Bader charge analysis reveals a notable electron loss in the Hf atoms, with the central atom losing ~1.88 electrons and the other two Hf atoms each losing around 2.23 electrons as shown in Table S3 of the supplementary material. This electron deficit indicates the high oxidation states in transition metals within MXene structures. Concurrently, the carbon atoms in $Hf_3C_2O_2$ each gain about 1.92 electrons. Like the carbon atoms, the terminal oxygen atoms also exhibit an increase in electron density, each gaining about 1.25 electrons, indicating their involvement in substantial bonding interactions with the Hf atoms.

Shifting the focus to $Hf_2CO_2$, the Bader charges indicate a similar trend of electron distribution. Here, the Hf atoms lose ~2.25 electrons when incorporated into the $Hf_2CO_2$ structure, further corroborating their higher oxidation state as detailed in Table S3 of the supplementary material. This electron loss aligns with the behavior typically observed in transition metals in MXene materials. The carbon atom gains about two electrons in this structure, pointing to a reduced state. The terminal oxygen atoms in $Hf_2CO_2$, such as their counterparts in $Hf_3C_2O_2$, gain roughly 1.25 electrons each.

27 March 2024 10:49:10

## C. Electronic and optical properties from many-body methods

To address the issue of inaccuracy in the results of standard DFT calculations and obtain precise results for the electronic bandgap and other material properties, employing the many-body methods GW becomes imperative. We included the quasi-particle (QP) self-energy corrections on top of the ground-state DFT calculations. Meticulous convergence of computational parameters, including cutoff energies, screening cutoff, polarization bands, G-vector grid, and k-mesh grid, was paramount to ensure the accuracy and reliability of electronic properties in GW calculations (Figs. S5–S7). Long-range interactions, the presence of Rydberg states, complex dielectric screening, discretization errors, and the need to balance between localized and delocalized electronic states all contribute to the slow convergence of the fundamental quasi-particle bandgaps in 2D materials with a truncated Coulomb potential.[38] We also obtained the convergence of the fundamental quasi-particle bandgaps with different k-mesh grids ($N_k$), plotted in Fig. 4. The information regarding the convergence of the fundamental quasi-particle gap (direct gap $\Delta_{\mathrm{GW,dir}}$ and indirect gap $\Delta_{\mathrm{GW,ind}}$) with the k-mesh grid for MXenes $Hf_3C_2O_2$ and $Hf_2CO_2$
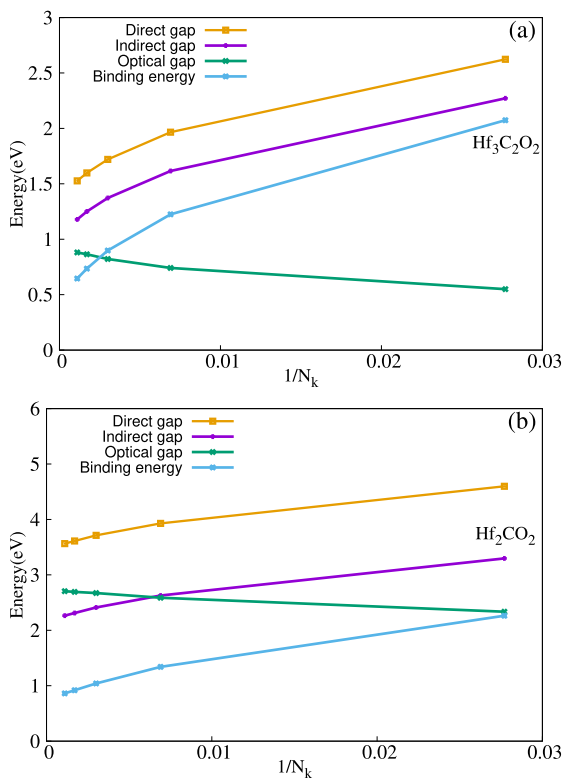


**FIG. 4.** Convergence behavior of quasiparticle gap, optical gap, and binding energy with k-mesh grid ($N_k = N_{k_x} \times N_{k_y} \times N_{k_z}$) in the case of (a) $Hf_3C_2O_2$ and (b) $Hf_2CO_2$ MXenes.

is mentioned in Table S4 of the supplementary material too. We see slow convergence of electronic bandgaps concerning the k-point grid, especially for $Hf_3C_2O_2$, with the same behavior for the optical gap. The converged values of all fundamental properties are not easy to obtain even with a $30 \times 30 \times 1$ k-mesh grid. To ensure more precise gaps, we extrapolated the values from the best k-grids;[27] see also Fig. S8 of the supplementary material for details (this procedure corrected gaps for ≤0.11 eV). A similar trend (slow gap convergence with $N_k$) was observed for BAs and BP monolayers[45] or in $Sc_2C(OH)_2$ MXene[27] and was associated with the delocalization of first bound exciton. A detailed discussion on this topic is presented in the subsequent paragraphs of this paper.

The calculated GW band structures with SOC are plotted in Fig. 3. We obtained an indirect bandgap of 1.08 eV and a direct bandgap of 1.42 eV for $Hf_3C_2O_2$ MXene, while we obtained an indirect bandgap of 2.18 eV and a direct bandgap of 3.48 eV for $Hf_2CO_2$ MXene (all reported values are extrapolated ones, following Fig. S8). The GW indirect bandgap is located between Γ and M high-symmetry points, while the minimum direct bandgap is noticed at high-symmetry point M.

Using BSE [Eq. (1)] on the top of the GW method, we calculated the optical gap $\Delta_{\mathrm{opt}}$, which corresponds to the position of the first bright excitonic peak, and absorption spectra for both $Hf_3C_2O_2$ and $Hf_2CO_2$ MXenes. The convergence of optical gap $\Delta_{\mathrm{opt}}$ and the binding energy $E_b$ with the k-mesh grid are also visible in Fig. 4 and mentioned in Table S4 and Fig. S8 of the supplementary material. We obtained the converged value of $\Delta_{\mathrm{opt}}$ of 0.91 and 2.72 eV and the binding energy $E_b$ of the first bright exciton of 0.51 and 0.76 eV for $Hf_3C_2O_2$ and $Hf_2CO_2$, respectively.

In our investigation of optical absorption spectra, a meticulous convergence of various calculation parameters was crucial for accurate results. Notably, the choice of the k-mesh grid, the number of bands included in BSE, and other parameters in the BSE significantly impacted the precision of the absorption spectra.[10,27,45] The converged values 3 and 30 Ry of screening cutoff and exchange cutoff, respectively, were used to obtain the accurate absorption spectra (see also Figs. S9 and S10 of the supplementary material). The convergence of the imaginary part of the macroscopic polarizability ($\alpha$) concerning k-mesh grids is typically crucial in BSE, and it is plotted in Fig. S11 for both MXenes. Finally, the reliability of the considered energy window for the spectra (the imaginary part of $\alpha$) is given by the number of occupied and virtual bands (o,v) included in the BSE calculation. Based on Fig. S12 of the supplementary material, we used the converged values (12,4) and (6,6) of (o,v) bands for $Hf_3C_2O_2$ and $Hf_2CO_2$, respectively.
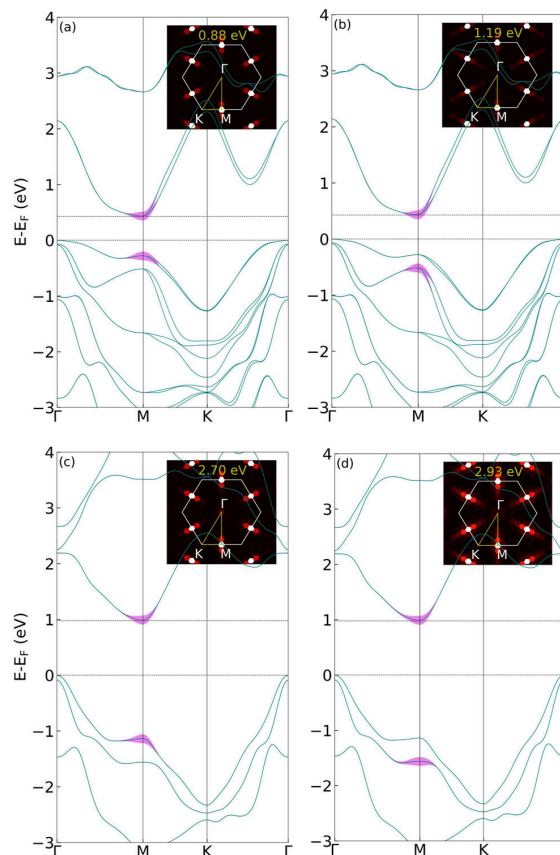
In our study, we observed a rich array of excitonic states contributing to the absorption spectra of $Hf_3C_2O_2$ MXene (Fig. 5). We obtained the absorptance of 4% for the peak corresponding to the first bright optical transition, but specifically, multiple excitons were identified, leading to the absorptance of 13% for the second peak of spectra within the infrared region (0–1.5 eV) of the spectra. The absorption spectra revealed a prominent peak, located at 4.8 eV in the near UV region with a strikingly high absorptance of ~17%. In the case of the $Hf_2CO_2$ monolayer, the first peak is located in the visible part of the spectra (1.5–3 eV) with maximum absorptance around 28%. We identified 5 and 10 dark excitons for $Hf_3C_2O_2$ and $Hf_2CO_2$, respectively, which are located below the prominent first peak in the spectra. For completeness, imaginary $\alpha$ are plotted along

27 March 2024 10:49:10
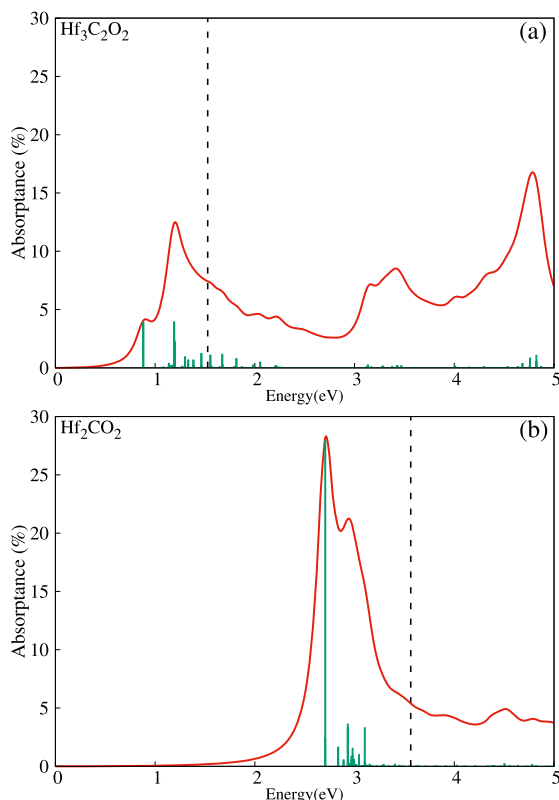
**FIG. 5.** Optical absorption spectra from BSE for (a) $Hf_3C_2O_2$ and (b) $Hf_2CO_2$ MXenes. The black dotted line denotes the direct quasi-particle gap. Oscillator strengths (arbitrary units) are added as green columns.



**FIG. 6.** Exciton weights in (a) and (b) $Hf_3C_2O_2$ and (c) and (d) $Hf_2CO_2$ projected onto the ground-state electronic dispersion. The purple shade (and its vertical thickness) represents the $|A_{cvk}^{\lambda}|$ coefficients [from Eq. (1)], indicating visually which electron–hole pairs contribute to a particular BSE eigenstate: (a) degenerated first-bright exciton with $\lambda = 6$–9 and (b) higher exciton $\lambda = 262, 263$ in $Hf_3C_2O_2$; (c) degenerated first-bright exciton with $\lambda = 9$–12 and (d) higher exciton $\lambda = 35, 36$ in $Hf_2CO_2$. The accompanying subplot in each panel displays the exciton weights within the whole Brillouin zone, not resolving particular bands.

oscillator strengths in Fig. S13 of the supplementary material using the $30 \times 30 \times 1$ k-mesh grid for both $Hf_3C_2O_2$ and $Hf_2CO_2$.

In our detailed analysis of optical transitions and exciton formation, we investigated the excitonic weights $A_{cvk}^{\lambda}$ [from Eq. (1)] because the excitonic wave function is expressed in an electron–hole product basis as $\sum_{cvk} A_{cvk}^{\lambda} \phi_{ck} \phi_{vk}$. The $A_{cvk}^{\lambda}$ coefficients, therefore, help us to identify which electron–hole pairs in the expansion dominantly contribute to the wave function of the particular exciton (labeled by certain $\lambda$). The purple shade in Fig. 6 represents $|A_{cvk}^{\lambda}|$ visualizing the important electron–hole contributions labeled by $c, v$ subscripts (band pairs on the y axis) and by $k$ subscript describing the x axis (missing purple shade means negligible coefficients are not visible in the graph). For the first bright excitons in both $Hf_3C_2O_2$ [Fig. 6(a)] and $Hf_2CO_2$ [Fig. 6(c)], which are consisting of several BSE states $\lambda = 6$–9 ($E^{6-9} = 0.91$ eV) and $\lambda = 9$–12 ($E^{9-12} = 2.72$ eV), respectively, only the valence band and conduction band are important. Moreover, only the area around the high-symmetry M point in the Brillouin zone contributes (visible also in the subplots of Fig. 6). Furthermore, we visualized excitons dominantly responsible for the second significant peaks in the spectra of Fig. 5.

In $Hf_3C_2O_2$, the exciton at 1.2 eV [Fig. 6(b)] is mainly composed of M localized pairs of the conduction band and second valence (VB-1) band. The properties of the bright $Hf_2CO_2$ exciton at 2.9 eV [Fig. 6(d)] are similar.

We also explored the spatial distribution of excitons by fixing the position of the hole within the material and examining the probability of finding the electron in different spatial locations. This approach provided valuable insights into the spatial characteristics of excitonic states.[46,47] By fixing the hole's position and studying the electron's probability distribution, we could distinguish between localized and delocalized excitonic states within the material.[48,49] We focused here on the first bright exciton states in $Hf_3C_2O_2$ (at 0.9 eV) and $Hf_2CO_2$ (at 2.7 eV). These low-energy excitons are,
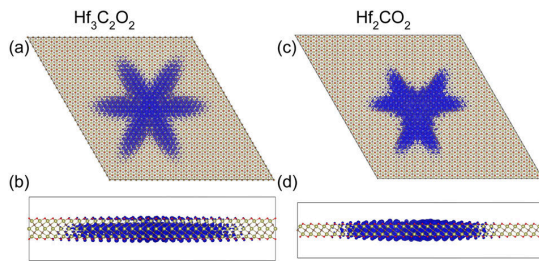
**FIG. 7.** Isosurface (with value of $3 \times 10^{-9}$) for the real space electron probability density of the first bright exciton in (a) and (b) $Hf_3C_2O_2$ and (c) and (d) $Hf_2CO_2$. The hole is located above a carbon atom, 1 Å away in the z-direction in both materials.

in fact, consisting of four degenerated BSE states in both materials. Nevertheless, in $Hf_3C_2O_2$, two are dominant (by the strength), with the other two are dark (strength is negligible) and not influencing the spatial distribution or optical spectrum. $Hf_2CO_2$ is a slightly different situation where from $\lambda = 9\text{–}12$ BSE eigenstates are just $\lambda = 11$ bright and others are more or less dark. For the real-space plot of Fig. 7, we fixed the position of the hole located at the top of the C atom at a distance of 1 Å in the z-direction for both materials.

Our observations show that the wave functions associated with individual BSE eingenstates exhibit a notable deviation from the intrinsic symmetry characteristics of the host materials. Specifically, the electron probability densities within these BSE eingenstates do not conform to a rotationally symmetric distribution. This asymmetry in electron distribution is an intriguing aspect, as it contrasts with the expected behavior based on the material's inherent properties. However, an interesting phenomenon arises when we consider the cumulative effect of the electron probability densities. By aggregating the densities of all parts of excitons in $Hf_3C_2O_2$ and $Hf_2CO_2$, an alignment with the material's native threefold rotational symmetry emerges, as can be seen in subplots of Fig. 6 and Fig. 7. This suggests that while individual BSE states might exhibit asymmetrical properties, their collective behavior can reflect and restore the material's symmetry. Furthermore, the exciton responsible for the first dominant peak in $Hf_3C_2O_2$ spectrum is very delocalized, and we were forced to use at least a $30 \times 30 \times 1$ k-mesh grid. Therefore, we needed a supercell of 30 real unit cells to ensure the wave function fades out on the border of the supercell (Fig. 7). For smaller k-grids/supercells, the artificial confinement of the exciton led to a biased optical gap and untruly increased the predicted binding energy of the exciton (Fig. 4). On the other hand, the first bright exciton in $Hf_2CO_2$ was more localized (cf. isosurfaces of Fig. 7). In our investigation into the variance of the first exciton's spatial extent, we gain insights into the differing rates of convergence of the optical bandgaps in $Hf_3C_2O_2$ and $Hf_2CO_2$ relative to the number of k-points. Building upon the findings discussed in our preceding work,[45] we understand that an exciton with a widespread distribution in real space necessitates a higher number of k-points for accurate characterization. Consequently, the optical bandgaps in $Hf_3C_2O_2$ exhibit a slower convergence concerning the number of k-points compared to $Hf_2CO_2$ (Fig. 4). This slower convergence is attributed

to the broader spatial distribution of the first bright exciton in $Hf_3C_2O_2$, as opposed to the more localized nature of the exciton in $Hf_2CO_2$.

In examining the symmetry of the first bound exciton in both materials, the influence of spin–orbit coupling (SOC) on the degeneracy (splitting of bands), and the respective symmetry groups $D_{3h}$ for $Hf_3C_2O_2$ and $D_{3d}$ for $Hf_2CO_2$, it is evident that these excitons align with the E-type irreducible representations because these are associated with degeneracy. Specifically, for $Hf_3C_2O_2$, the first bright exciton can be associated with the E$'$ and E$''$ representations. Meanwhile, the $Hf_2CO_2$ first bright exciton can correspond to the E$_g$ and E$_u$ representations. The real-space exciton projection for $Hf_3C_2O_2$ [Figs. 7(a) and 7(b)] exhibits vertical plane symmetry, leading to the assignment of the E$'$ group. In contrast, the gerade centrosymmetric nature observed in the $Hf_2CO_2$ exciton projection [Figs. 7(c) and 7(d)] suggests its alignment with the E$_g$ group.

Concerning the indirect nature of both investigated materials (see indirect bands in Fig. 3), we finally performed excitonic BSE
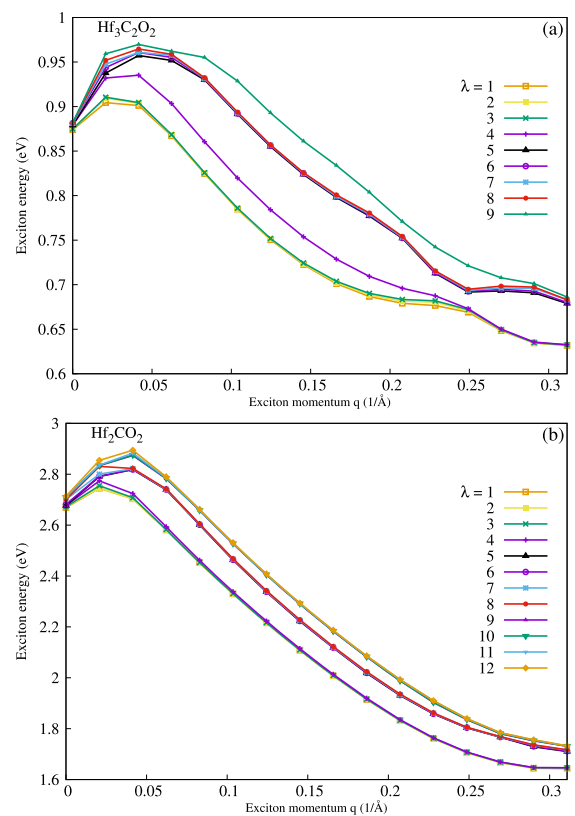


**FIG. 8.** Excitation energy of the (a) $Hf_3C_2O_2$ and (b) $Hf_2CO_2$ MXene with exciton momentum **q** along Γ to the M path.

27 March 2024 10:49:10

**TABLE I.** Zero-temperature $\tau_\lambda^0$ and average room-temperature $\langle\tau_\lambda^{RT}\rangle$ radiative lifetimes of the first bright excitons (all degenerated BSE eigenstates $\lambda$ are included) in $Hf_3C_2O_2$ and $Hf_2CO_2$, where $M_\lambda$ is the mass of exciton and $E_\lambda$ is the extrapolated energy of the first bright excitons.

|  | $Hf_3C_2O_2$ | $Hf_2CO_2$ |
|---|---|---|
| $E_\lambda$ (eV) | 0.91 | 2.72 |
| $\mu_\lambda^2/A_{uc}$ | 0.04 | 0.12 |
| $M_\lambda$ (a.u.) | 2.22 | 0.92 |
| $\tau_\lambda^0$ (ps) | 0.22 | 0.02 |
| $\langle\tau_\lambda^{RT}\rangle$ (ns) | 11.44 | 0.06 |

calculations for the indirect exciton momentum ($\mathbf{q} \neq 0$). In indirect materials, it leads to a decrease in excitation energies, or in extreme cases of excitonic insulator candidates, it can lead to negative excitation energies, i.e., the situation where the binding energy of excitons overcomes the fundamental gap.[10] Here, following the band structure of Fig. 3, we were focused on exciton momentum along $\Gamma M$ direction. The calculations reveal that the exciton energies are (after a slight increase) significantly decreasing, approaching a minimal value to the M point—see Fig. 8. The non-extrapolated excitation energy of 0.88 eV in $Hf_3C_2O_2$ was reduced to 0.68 eV (ca. to 78% of the original value). In the $Hf_2CO_2$ case, the reduction was extreme, from 2.70 to 1.73 eV (ca. to 64% of the original value).

Our last analysis lies in the guess of exciton behavior in time (Table I). Using Eq. (4), we calculated the radiative lifetime $\tau_\lambda^0$ (free from temperature dependency) for the first bright excitons in the $Hf_3C_2O_2$ and $Hf_2CO_2$ MXenes, 0.22 and 0.02 ps, respectively. These lifetimes indicate rapid radiative recombination processes, showing that light emission from these excitonic states is highly efficient. Values of $\tau_\lambda^0$ for $Hf_3C_2O_2$ are comparable with best-known monolayer transition metal dichalcogenides (TMDs) because the radiative exciton lifetime in $MoS_2$, $MoSe_2$, $WS_2$, or $WSe_2$ is of order 0.1–1 ps.[43] On the other hand, the first bright exciton in $Hf_2CO_2$ has a shorter lifetime of one order of magnitude, i.e., comparable with exciton lifetimes in two-dimensional group-III nitrides as BN, AlN, GaN, and InN, which are of 0.01 ps order.[50] For computing the average radiative lifetime $\langle\tau_\lambda^{RT}\rangle$ of exciton at temperature $T$, it was necessary to calculate the exciton mass $M_\lambda$, 2.22 a.u. and 0.92 a.u. for the $Hf_3C_2O_2$ and $Hf_2CO_2$ monolayers, where we sum effective masses of electron and hole[51] in the M point of BZ. At room temperature (300 K) using Eq. (5), the average radiative lifetimes $\langle\tau_\lambda^{RT}\rangle$ of $Hf_3C_2O_2$ and $Hf_2CO_2$ are 11.44 and 0.06 ns. While in Mo- and W-based TMDs, the first bright exciton has $\langle\tau_\lambda^{RT}\rangle$ of tenths of ns, it is much longer in $Hf_3C_2O_2$. This behavior mostly comes from $Hf_3C_2O_2$ first bright exciton energy (0.9 eV) in the infrared region, while first bright exciton energies of TMDs (1.7–2.0 eV)[43] are in the visible region [see also $E_\lambda^2$ in Eq. (5)]. We note that the short average radiative lifetime of the first bright exciton in $Hf_2CO_2$ is rather similar to excitonic lifetimes in monolayer BN, AlN, and GaN (tens of ps).[50] Linear dependence of the average radiative lifetimes with respect to the temperature [Eq. (5)] has a slope of 38.13 and 0.19 ps/K for $Hf_3C_2O_2$ and $Hf_2CO_2$, respectively. The $Hf_3C_2O_2$ value is comparable to that of the beforementioned TMDs.[43]

## IV. CONCLUSIONS

In conclusion, motivated by recent discoveries of Hf-based MXenes, we examined the geometric and optoelectronic properties with many-body methods. We presented a detailed study of the fundamental properties following linear optics of new 2D materials, Hf-based MXenes, $Hf_3C_2O_2$ and $Hf_2CO_2$. Both semiconducting $Hf_3C_2O_2$ and $Hf_2CO_2$ MXenes have an indirect quasiparticle gap of 1.08 and 2.18 eV, respectively. Both $Hf_3C_2O_2$ and $Hf_2CO_2$ MXenes showed strong exciton binding energies of 0.51 and 0.76 eV, respectively. The excitation energies of direct excitons can be significantly decreased by considering indirect excitons with exciton momentum $\mathbf{q} = \Gamma M$. The observed 4% and 13% absorptance in the infrared region and the remarkable 17% peak at 4.8 eV in the near UV region highlight the rich excitonic landscape of MXene $Hf_3C_2O_2$. Additionally, MXene $Hf_2CO_2$ exhibited a significant 28% absorptance peak in the visible spectra. The emission properties of the Hf-based MXenes are illustrated by the radiative lifetimes of the lowest-energy excitons. We observed almost three orders' lifetime difference between three-Hf-layered and two-Hf-layered materials at room temperature: very long-lived (~ 10 ns) excitons in $Hf_3C_2O_2$ (longer than in transition metal dichalcogenides) vs short living (approximately tens of picoseconds) in $Hf_2CO_2$.

## SUPPLEMENTARY MATERIAL

See the supplementary material for the Hf-based MXene structures used in the reported computations, optimization of the conformers, and convergence of the necessary parameters used in DFT, GW, and BSE calculations.

## AUTHOR DECLARATIONS

### Conflict of Interest

The authors have no conflicts to disclose.

### Author Contributions

**Nilesh Kumar**: Formal analysis (supporting); Investigation (lead); Validation (equal); Visualization (lead); Writing – original draft (lead); Writing – review & editing (supporting). **Miroslav Kolos**: Formal analysis (supporting); Investigation (supporting); Resources (supporting); Validation (equal); Writing – original draft

(supporting); Writing – review & editing (equal). **Sitangshu Bhattacharya**: Formal analysis (supporting); Funding acquisition (supporting); Methodology (equal); Project administration (supporting); Resources (supporting); Supervision (equal); Visualization (supporting); Writing – review & editing (supporting). **František Karlický**: Conceptualization (lead); Formal analysis (lead); Funding acquisition (lead); Investigation (supporting); Methodology (equal); Project administration (lead); Resources (lead); Supervision (lead); Validation (equal); Writing – original draft (supporting); Writing – review & editing (lead).

## DATA AVAILABILITY

The data that support the findings of this study are available from the corresponding author upon reasonable request.

## REFERENCES

[1] M. Naguib, V. N. Mochalin, M. W. Barsoum, and Y. Gogotsi, "25th anniversary article: Mxenes: A new family of two-dimensional materials," Adv. Mater. **26**, 992–1005 (2014).

[2] B. Anasori, M. R. Lukatskaya, and Y. Gogotsi, "2D metal carbides and nitrides (MXenes) for energy storage," Nat. Rev. Mater. **2**, 16098 (2017).

[3] Y. Gogotsi and B. Anasori, "The rise of mxenes," ACS Nano **13**, 8491–8494 (2019).

[4] M. Naguib, M. Kurtoglu, V. Presser, J. Lu, J. Niu, M. Heon, L. Hultman, Y. Gogotsi, and M. W. Barsoum, "Two-dimensional nanocrystals produced by exfoliation of $Ti_3AlC_2$," Adv. Mater. **23**, 4248–4253 (2011).

[5] K. R. G. Lim, M. Shekhirev, B. C. Wyatt, B. Anasori, Y. Gogotsi, and Z. W. Seh, "Fundamentals of mxene synthesis," Nat. Synth. **1**, 601–614 (2022).

[6] B. Anasori and Y. Gogotsi, "MXenes: Trends, growth, and future directions," Graphene 2D Mater. **7**, 75–79 (2022).

[7] J. L. Hart, K. Hantanasirisakul, A. C. Lang, B. Anasori, D. Pinto, Y. Pivak, J. T. van Omme, S. J. May, Y. Gogotsi, and M. L. Taheri, "Control of MXenes' electronic properties through termination and intercalation," Nat. Commun. **10**, 522 (2019).

[8] T. Ketolainen and F. Karlický, "Optical gaps and excitons in semiconducting transition metal carbides (MXenes)," J. Mater. Chem. C **10**, 3919–3928 (2022).

[9] T. Sakhraoui and F. Karlický, "Electronic nature transition and magnetism creation in vacancy-defected $Ti_2CO_2$ MXene under biaxial strain: A DFTB + U study," ACS Omega **7**, 42221–42232 (2022).

[10] N. Kumar and F. Karlický, "Oxygen-terminated $Ti_3C_2$ MXene as an excitonic insulator," Appl. Phys. Lett. **122**, 183102 (2023).

[11] H. Kim and H. N. Alshareef, "MXetronics: MXene-enabled electronic and photonic devices," ACS Mater. Lett. **2**, 55–70 (2020).

[12] A. Champagne and J. C. Charlier, "Physical properties of 2D MXenes: From a theoretical perspective," J. Phys. Mater. **3**, 032006 (2020).

[13] T. Lapauw, B. Tunca, T. Cabioc'h, J. Lu, P. O. A. Persson, K. Lambrinou, and J. Vleugels, "Synthesis of MAX phases in the Hf–Al–C system," Inorg. Chem. **55**, 10922–10927 (2016).

[14] Y.-C. Zhou, L.-F. He, Z.-J. Lin, and J.-Y. Wang, "Synthesis and structure–property relationships of a new family of layered carbides in Zr-Al(Si)-C and Hf-Al(Si)-C systems," J. Eur. Ceram. Soc. **33**, 2831–2865 (2013).

[15] J. Zhou, X. Zha, X. Zhou, F. Chen, G. Gao, S. Wang, C. Shen, T. Chen, C. Zhi, P. Eklund, S. Du, J. Xue, W. Shi, Z. Chai, and Q. Huang, "Synthesis and electrochemical properties of two-dimensional hafnium carbide," ACS Nano **11**, 3841–3850 (2017).

[16] X.-H. Zha, J. Zhou, K. Luo, J. Lang, Q. Huang, X. Zhou, J. S. Francisco, J. He, and S. Du, "Controllable magnitude and anisotropy of the electrical conductivity of $Hf_3C_2O_2$ MXene," J. Phys.: Condens. Matter **29**, 165701 (2017).

[17] X.-H. Zha, Q. Huang, J. He, H. He, J. Zhai, J. S. Francisco, and S. Du, "The thermal and electrical properties of the promising semiconductor mxene $Hf_2Co2$," Sci. Rep. **6**, 27971 (2016).

[18] M. Khazaei, M. Arai, T. Sasaki, C.-Y. Chung, N. S. Venkataramanan, M. Estili, Y. Sakka, and Y. Kawazoe, "Novel electronic and magnetic properties of two-dimensional transition metal carbides and nitrides," Adv. Funct. Mater. **23**, 2185–2192 (2013).

[19] Y. Zhang, W. Xia, Y. Wu, and P. Zhang, "Prediction of MXene based 2D tunable band gap semiconductors: GW quasiparticle calculations," Nanoscale **11**, 3993–4000 (2019).

[20] N. Kumar, R. Chaurasiya, and A. Dixit, "Strain tailored thermodynamic stability, electronic transitions, and optoelectronic properties of III (In, Ga and Al)-nitride monolayers," Nanotechnology **33**, 045202 (2021).

[21] N. Kumar, R. Chaurasiya, F. Karlicky, and A. Dixit, "Bandgap engineering and modulation of thermodynamic, and optical properties of III-N monolayers XN (X = In, Ga & Al) by mutual alloying," Phys. Scr. **97**, 095806 (2022).

[22] M. Bernardi, M. Palummo, and J. C. Grossman, "Extraordinary sunlight absorption and one nanometer thick photovoltaics using two-dimensional monolayer materials," Nano Lett. **13**, 3664–3670 (2013).

[23] D. Y. Qiu, F. H. Da Jornada, and S. G. Louie, "Optical spectrum of $MoS_2$: Many-body effects and diversity of exciton states," Phys. Rev. Lett. **111**, 216805 (2013).

[24] L. Hedin, "New method for calculating the one-particle green's function with application to the electron-gas problem," Phys. Rev. **139**, A796 (1965).

[25] E. E. Salpeter and H. A. Bethe, "A relativistic equation for bound-state problems," Phys. Rev. **84**, 1232 (1951).

[26] A. L. Fetter and J. D. Walecka, *Quantum Theory of Many-Particle Systems* (Courier Corporation, 2012).

[27] M. Dubecký, S. Minárik, and F. Karlický, "Benchmarking fundamental gap of $Sc_2C(OH)_2$ MXene by many-body methods," J. Chem. Phys. **158**, 054703 (2023).

[28] P. Giannozzi, O. Andreussi, T. Brumme, O. Bunau, M. Buongiorno Nardelli, M. Calandra, R. Car, C. Cavazzoni, D. Ceresoli, M. Cococcioni *et al.*, "Advanced capabilities for materials modelling with quantum espresso," J. Phys.: Condens. Matter **29**, 465901 (2017).

[29] D. Hamann, "Optimized norm-conserving vanderbilt pseudopotentials," Phys. Rev. B **88**, 085117 (2013).

[30] J. P. Perdew, K. Burke, and M. Ernzerhof, "Generalized gradient approximation made simple," Phys. Rev. Lett. **77**, 3865 (1996).

[31] A. Marini, C. Hogan, M. Grüning, and D. Varsano, "Yambo: An *ab initio* tool for excited state calculations," Comput. Phys. Commun. **180**, 1392–1403 (2009).

[32] D. Sangalli, A. Ferretti, H. Miranda, C. Attaccalite, I. Marri, E. Cannuccia, P. Melo, M. Marsili, F. Paleari, A. Marrazzo *et al.*, "Many-body perturbation theory calculations using the yambo code," J. Phys.: Condens. Matter **31**, 325902 (2019).

[33] O. Pulci, G. Onida, R. Del Sole, and L. Reining, "*Ab Initio* calculation of self-energy effects on optical properties of GaAs(110)," Phys. Rev. Lett. **81**, 5374 (1998).

[34] C. A. Rozzi, D. Varsano, A. Marini, E. K. Gross, and A. Rubio, "Exact Coulomb cutoff technique for supercell calculations," Phys. Rev. B **73**, 205119 (2006).

[35] A. Castro, E. Räsänen, and C. A. Rozzi, "Exact Coulomb cutoff technique for supercell calculations in two dimensions," Phys. Rev. B **80**, 033102 (2009).

[36] S. Albrecht, L. Reining, R. Del Sole, and G. Onida, "*Ab Initio* calculation of excitonic effects in the optical spectra of semiconductors," Phys. Rev. Lett. **80**, 4510 (1998).

[37] T. Ketolainen, N. Macháčová, and F. Karlický, "Optical gaps and excitonic properties of 2D materials by hybrid time-dependent density functional theory: Evidences for monolayers and prospects for van der Waals heterostructures," J. Chem. Theory Comput. **16**, 5876–5883 (2020).

[38] F. A. Rasmussen, P. S. Schmidt, K. T. Winther, and K. S. Thygesen, "Efficient many-body calculations for two-dimensional materials using exact limits for the screened potential: Band gaps of $MoS_2$, *h*-BN, and phosphorene," Phys. Rev. B **94**, 155406 (2016).

[39] A. Guandalini, P. D'Amico, A. Ferretti, and D. Varsano, "Efficient GW calculations in two dimensional materials through a stochastic integration of the screened potential," npj Comput. Mater. **9**, 44 (2023).

[40] A. Molina-Sánchez, G. Catarina, D. Sangalli, and J. Fernandez-Rossier, "Magneto-optical response of chromium trihalide monolayers: Chemical trends," J. Mater. Chem. C **8**, 8856–8863 (2020).

27 March 2024 10:49:10

[41] H.-Y. Chen, M. Palummo, D. Sangalli, and M. Bernardi, "Theory and *ab initio* computation of the anisotropic light emission in monolayer transition metal dichalcogenides," Nano Lett. **18**, 3839–3843 (2018).

[42] 'Strengths' output printed out by a post-processing tool (YPP) included in the Yambo code (version 5.1.0) in eV must be converted to $\mu_\lambda^2$ (in SI units): $\mu_\lambda^2 = \frac{\varepsilon_0 V}{e^2}$ strengths, where $\varepsilon_0$ is the vacuum permittivity, $V$ is the volume of the computational cell, and $e$ is the elementary charge.

[43] M. Palummo, M. Bernardi, and J. C. Grossman, "Exciton radiative lifetimes in two-dimensional transition metal dichalcogenides," Nano Lett. **15**, 2794–2800 (2015).

[44] H.-Y. Chen, V. A. Jhalani, M. Palummo, and M. Bernardi, "*Ab initio* calculations of exciton radiative lifetimes in bulk crystals, nanostructures, and molecules," Phys. Rev. B **100**, 075135 (2019).

[45] M. Kolos and F. Karlický, "The electronic and optical properties of III–V binary 2D semiconductors: How to achieve high precision from accurate many-body methods," Phys. Chem. Chem. Phys. **24**, 27459–27466 (2022).

[46] M. Kolos, L. Cigarini, R. Verma, F. Karlicky, and S. Bhattacharya, "Giant linear and nonlinear excitonic responses in an atomically thin indirect semiconductor nitrogen phosphide," J. Phys. Chem. C. **125**, 12738–12757 (2021).

[47] M. Kolos, R. Verma, F. Karlický, and S. Bhattacharya, "Large exciton-driven linear and nonlinear optical processes in monolayers of nitrogen arsenide and nitrogen antimonide," J. Phys. Chem. C. **126**, 14931–14959 (2022).

[48] A. Chernikov, T. C. Berkelbach, H. M. Hill, A. Rigosi, Y. Li, B. Aslan, D. R. Reichman, M. S. Hybertsen, and T. F. Heinz, "Exciton binding energy and nonhydrogenic rydberg series in monolayer $WS_2$," Phys. Rev. Lett. **113**, 076802 (2014).

[49] P. Cudazzo, L. Sponza, C. Giorgetti, L. Reining, F. Sottile, and M. Gatti, "Exciton band structure in two-dimensional materials," Phys. Rev. Lett. **116**, 066803 (2016).

[50] M. S. Prete, D. Grassano, O. Pulci, I. Kupchak, V. Olevano, and F. Bechstedt, "Giant excitonic absorption and emission in two-dimensional group-III nitrides," Sci. Rep. **10**, 10719 (2020).

[51] C. D. Spataru, S. Ismail-Beigi, R. B. Capaz, and S. G. Louie, "Theory and *Ab Initio* calculation of radiative lifetime of excitons in semiconducting carbon nanotubes," Phys. Rev. Lett. **95**, 247402 (2005).

27 March 2024 10:49:10

# Supplementary Material 11

# Strain-induced changes of electronic and optical properties of Zr-based MXenes

Jiří Kalmár [ID] and František Karlický[a) [ID]

**AFFILIATIONS**

Department of Physics, Faculty of Science, University of Ostrava, 30. dubna 22, 701 03 Ostrava, Czech Republic

**Note:** This paper is part of the special topic, Two-Dimensional Materials and Heterostructures Under Strain.
[a)]**Author to whom correspondence should be addressed:** frantisek.karlicky@osu.cz

## ABSTRACT

Zr-based MXenes recently attracted attention because of its experimental preparation showing temperature stability, mechanical strength, and promising energy, sensoric, and electrochemistry applications. However, necessary theoretical predictions at a precise/predictive level are complicated due to essential excitonic features and strong electron correlation (i.e., a necessity to go beyond standard density functional theory, DFT). Contrary to the prevailing focus on oxygen-terminated MXenes and standard predictions of other Zr-based MXenes as conductors, based on the hybrid DFT and GW many-body perturbational theory, we were able to find seven different semiconductors (five of them for their equilibrium geometry and two others under slight tensile biaxial strain) in the case of two- and three-layered $Zr_2CT_2$ and $Zr_3C_2T_2$ configurations with various terminations (T = O, F, S, Cl). We observed semiconductor-to-conductor transition induced by strain in the majority of such Zr-based MXenes at an experimentally achievable strain range. Furthermore, using the Bethe–Salpeter equation (BSE), we demonstrated that selected semiconducting Zr-based MXenes possess high optical absorption efficiency (20%–30%) in the visible light range, underscoring their potential in photonic applications. The high sensitivity of Zr-based MXenes to external conditions and functionalization combined with the thermal stability makes the materials promising for applications at operational temperatures in electronic and optical technologies.

## I. INTRODUCTION

MXenes, a family of recent two-dimensional (2D) carbides, nitrides, and carbonitrides, embody various interesting properties promising for technical applications.[1–3] Since the first experimentally prepared MXene monolayer, $Ti_3C_2$,[4] more than 20 MXenes were synthesized and tens of others were theoretically predicted.[5–7] All reported MXenes were terminated by some functional groups on the surface (as –O, –OH, –F, or –Cl), MXenes are, therefore, labeled as $M_nC_{n-1}T_x$, where M is metal and T is the terminal atom or group. 2D MXene's properties are sensitive to composition, termination, or external conditions (pressure, support, solvent, etc.) and provide a rich set of its phases: metals, semiconductors,[8] ferromagnets, antiferromagnets,[9] topological insulators,[10] or excitonic insulators.[11]

Here, we are focused on Zr-based MXenes terminated by various groups (O, F, S, Cl) for which the semiconducting behavior could be expected, their electronic and optical properties, and the changes of these properties under biaxial strain. As has been shown recently, the mechanical strain on MXenes can be realized experimentally.[12,13] We note that Zr-based MXenes are a topic of investigation for a few recent studies,[14–18] but these studies are mostly focused on the oxygen-terminated $Zr_2CO_2$ and $Zr_3C_2O_2$ MXenes. It is, therefore, our goal to bring a broader understanding of this family of materials and to bring forward less investigated materials with potential applications.

Recently, $Zr_3C_2T_x$ 2D MXene was experimentally prepared by Zhou *et al.*[19] by a non-traditional method of selectively etching the $Al_3C_3$ layer from the nanolaminated $Zr_3Al_3C_5$ MAX phase under hydrofluoric acid treatment. 2D $Zr_3C_2T_x$ demonstrates an enhanced capability to preserve its two-dimensional characteristics and structural integrity at elevated temperatures in vacuum or argon atmosphere, in comparison to $Ti_3C_2T_x$ MXenes. The difference was explained by a theoretical investigation of binding energy.

Together with predicted mechanical strengths, it is reasonable to expect that the 2D $Zr_3C_2T_x$ MXenes will have promising applications from electrical energy storage, reinforcement fillers for polymers, to sensors and catalysts, especially when used in high-temperature environment.[19] In addition, Zr-MXenes are promising as anode materials of sodium ion batteries.[20]

The zirconium-based MXenes are often predicted as conductors, with the only exception being the $Zr_2CO_2$ MXene.[10,14] A standard tool for the *ab initio* calculations is the density functional theory (DFT), and it has been for years accepted as a reliable and robust computational method. The DFT approach can, however, exhibit inconsistencies in its predictions, such as predicting semiconducting materials as gapless,[21] particularly when applied to complex systems, such as those containing transition metals. These discrepancies often arise due to the different implementation levels of DFT, primarily the diverse density functionals employed.

As has been recently shown, the mechanical biaxial strain can induce indirect to direct semiconductor transitions or can lead to the emergence (or disappearance) of the fundamental bandgap in MXenes.[9,17,22–24] Moreover, due to the change in the bandgap, the optical absorption of materials can be redshifted or blueshifted when the strain is applied. The possibility of tuning the electronic and optical properties of MXenes thus makes this approach highly promising for the design of efficient (opto)electronic devices.

In this paper, we use state-of-the-art methods to reliably determine the electronic and optical properties of Zr-based MXenes in their natural state and under biaxial strain. Many-body perturbation GW method[25] is used to obtain an accurate prediction of the fundamental bandgap of semiconducting MXenes and beyond GW approximation, the complete comprehension of light absorption is achievable by solving the excitonic equation of motion, known as the Bethe–Salpeter equation (BSE).[26] First, we have investigated several possible geometrical conformers of terminated Zr-based MXenes, selected the energetically most favorable ones for corresponding terminal groups, and determined their mechanical stability by analysis of the *ab initio* molecular dynamics (AIMD) simulations. Then, we investigated the changes in band structures under biaxial strain and further selected the most promising conformations. Beyond DFT, we have discovered five semiconducting Zr-based MXenes: $Zr_2CO_2$, $Zr_2CF_2$, $Zr_2CCl_2$, $Zr_3C_2O_2$, and $Zr_3C_2F_2$, with two other semiconducting under a relatively small biaxial strain ($Zr_2CS_2$, $Zr_3C_2Cl_2$). Finally, we have used advanced many-body methods to determine the fundamental bandgap, the optical gap, and the exciton binding energy and their strain-induced changes in these MXenes.

## II. METHODS

Calculations were performed using the periodic density functional theory code Vienna *Ab Initio* Simulation Package (VASP)[27–30] in version 6.3.1. The DFT Kohn–Sham equations have been solved variationally in a plane wave basis set using the projector-augmented-wave (PAW) method.[31] Structural optimization, ground-state calculations, and band structure calculations were done with Perdew–Burke–Ernzerhof (PBE) density functional[32] in generalized gradient approximation (GGA) as well as with meta-GGA Strongly Constrained and Appropriately Normed (SCAN)[33] density functional. Furthermore, for more precise results,

the wave functions from SCAN functional calculations were used for static calculations using more advanced hybrid density functional HSE06.[34] The convergence criterion for the electronic self-consistency cycle was in all cases set to $10^{-6}$ eV/cell, and the structural optimization was stopped if forces were less than $10^{-3}$ eV/Å. The plane wave cutoff energy was set to 500 eV for all calculations uniformly. GW sets of PAWs were used in all calculations with valence electrons being considered for C atoms and termination groups (O, F, S, Cl). For Zr atoms, the semi-core $s$ and $p$ states were added ($4s^2 4p^6 4d^2 5s^2$). For optimizations of the unit cell, k-point grid density $12 \times 12 \times 1$ was used and a denser $18 \times 18 \times 1$ grid was used for subsequent ground-state calculations. In all band structure calculations, the standard k-point path of Γ-M-K-Γ for 2D hexagonal systems was used.

*Ab initio* molecular dynamics (AIMD) was performed on $6 \times 6 \times 1$ supercells at 300 K, using the Andersen thermostat and the time step of 2 fs for a total of 1000 steps. Supercells were generated by the `Phonopy` code.[35]

The quasi-particle energies $\varepsilon_{nk}^{GW}$ were computed as the first-order corrections to the Kohn–Sham energies $\varepsilon_{nk}$ (the so-called $G_0W_0$ variant).[36] The quasi-particle gap was then calculated as $\Delta^{GW} = \varepsilon_{CBM}^{GW} - \varepsilon_{VBM}^{GW}$, where VBM denotes valence band maximum and CBM stands for conduction band minimum. It has been shown that this GW approach can for 2D materials produce very accurate results (when the method is well converged).[37–39] The BSE was then used in an eigenvalue problem form[40] for insulating materials with occupied valence bands ($v$ index) and completely unoccupied conduction bands ($c$ index),

$$(\varepsilon_{ck}^{GW} - \varepsilon_{vk}^{GW})A_{cvk}^\lambda + \sum_{c'v'k'} [2\langle\phi_{ck}\phi_{vk}|v|\phi_{c'k'}\phi_{v'k'}\rangle$$
$$- \langle\phi_{ck}\phi_{c'k'}|W|\phi_{vk}\phi_{v'k'}\rangle]A_{c'v'k'}^\lambda = E_{exc}^\lambda A_{cvk}^\lambda, \quad (1)$$

where $v$ is the Coulomb kernel, $1/|r - r'|$, $W$ is the dynamically screened potential, and the eigenvectors $A_{cvk}^\lambda$ correspond to the amplitudes of free electron–hole pair configurations composed of electron states $|\phi_{ck}\rangle$ and hole states $|\phi_{vk}\rangle$. The eigenenergies $E_{exc}^\lambda$ correspond to the excitation energies (with optical gap $\Delta_{opt}^{BSE} \equiv E_{exc}^\lambda$, for $\lambda$ from first nonzero transition, i.e., first bright exciton). The difference $E_b = \Delta^{GW,dir} - \Delta_{opt}^{BSE}$ is called exciton binding energy, where "dir" index denotes the direct quasiparticle gap.

During the convergence of GW parameters, we observed that the quasiparticle gap and the optical gap converged slowly with increasing height of the computational cell $L_z$. To ensure more credible results, we fitted the values with the linear fit[41–44]

$$\Delta_f^{GW}\left(\frac{1}{L_z}\right) = C\frac{1}{L_z} + \Delta_f^{GW}(0), \quad (2)$$

where $C$ and $\Delta_f^{GW}(0)$ are fitting parameters. The extrapolation to the zero $1/L_z$ limit was then used to form a corresponding *a posteriori* rigid correction by taking $\Delta_f^{GW}(0) - \Delta_f^{GW}(1/L_z)$, where $1/L_z = 0.05$ Å$^{-1}$. Similarly, we fitted the values of the optical gap $\Delta_{opt}^{BSE}$ and formed *a posteriori* correction of $\Delta_{opt}^{BSE}(0) - \Delta_{opt}^{BSE}(1/L_z)$ with the corresponding height of the computational cell. Therefore, all values of the quasiparticle gap and optical gap reported in

26 June 2024 14:24:57

Secs. III B–III C are corrected. The results of convergence calculations for the direct and indirect quasiparticle bandgaps and optical gaps depending on the height of the computational cell $L_z$ can be found in Fig. S1 in the supplementary material. Other GW parameters, for which the values converged sufficiently, were set as follows: the total number of bands $N_B = 768$, the energy cutoff for the response function $E_{cut}^{GW} = 200$ eV, the number of frequency-dependent grid points $N_\omega = 192$, and the $18 \times 18 \times 1$ k-point grid consistent with the rest of the ground-state calculations.

## III. RESULTS AND DISCUSSION

### A. Energetics and stability

We considered eight different high-symmetric configurations for the two-layered $Zr_2CT_2$ MXene and 12 geometries for three-layered $Zr_3C_2T_2$ MXene (see Fig. 1, only the three-layered case is



(a) T1  (b) T2  (c) T3  (d) T4

(e) H1  (f) H2  (g) H3  (h) H4

(i) H′1  (j) H′2  (k) H′3  (l) H′4
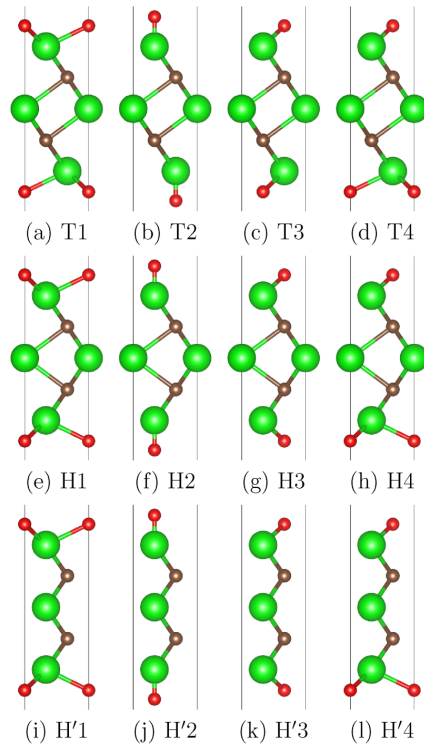
**FIG. 1.** T-, H-, and H′- geometric conformations of $Zr_3C_2T_2$ with varying positions (1–4) of termination groups. Green atoms = Zr, brown = C, red = O, F, S, or Cl. Vertical lines depict the boundaries of the unit cell. Two-layered MXenes $Zr_2CT_2$ then possess the T- and H- geometries accordingly.

shown). The conformations for the two-layered $Zr_2CT_2$ MXene correspond to the T- (trigonal) and H- (hexagonal) structures of transition metal dichalcogenides.[45] For three-layered $Zr_3C_2T_2$ MXene, we consider one trigonal (T) structure of space group $D_{3d}$ and two hexagonal (H, H′) structures of space group $D_{3h}$. The numbers in Fig. 1 then denote the positions of functional groups (O, F, S, Cl): hollow site (1), metal site (2), carbon site (3), and mixed site (4). After optimizing the structures at the level of PBE and SCAN density functionals, we conclude that every MXene, regardless of the layers, has a trigonal T1 ground state. The results for the SCAN functional are collected in Table I. The O- and S-terminated Zr-MXenes have a distinct ground state with the second most favorable conformation being >0.5 eV higher in total energy (similarly as its Ti- and Hf-based analogs[11,46]). This energy difference ensures that the ground-state conformation stays energetically more favorable even at a non-zero temperature and that no switching of phases occurs. For F- and Cl- terminated MXenes, on the other hand, two different conformations must be taken into account as the energy differences between the ground-state and the second most favorable conformations are much smaller (0.002–0.06 eV, see Table I). Therefore, for F- and Cl- terminated MXenes, T1 and T4 configurations are chosen for the two-layered cases, while T1 and H1 configurations are chosen for the three-layered MXenes.

To determine the stability of given systems and to possibly resolve the energetically close isomers, we have conducted *ab initio*

**TABLE I.** Relative energies (in eV) of two-layered ($Zr_2CT_2$) and three-layered ($Zr_3C_2T_2$) Zr-based MXenes in various conformations (Fig. 1) and with changing termination groups (T = O, F, S, Cl) at the level of SCAN density functional.

| | | O | F | S | Cl |
|---|---|---|---|---|---|
| $Zr_2C$ | T1 | 0.00 | 0.00 | 0.00 | 0.00 |
| | T2 | ...[a] | ...[a] | ...[a] | ...[a] |
| | T3 | 2.43 | 0.44 | 1.21 | 0.34 |
| | T4 | 1.03 | 0.06 | 0.51 | 0.06 |
| | H1 | 0.70 | 1.45 | 1.18 | 1.76 |
| | H2 | 8.17 | 4.68 | 6.49 | ...[b] |
| | H3 | 2.95 | 1.99 | 2.23 | 2.06 |
| | H4 | 1.69 | 1.67 | 1.65 | 1.89 |
| $Zr_3C_2$ | T1 | 0.00 | 0.00 | 0.00 | 0.00 |
| | T2 | 7.55 | 2.35 | 4.72 | 2.44 |
| | T3 | 1.91 | 0.71 | 0.94 | 0.45 |
| | T4 | 0.95 | 0.33 | 0.49 | 0.21 |
| | H1 | 0.53 | 0.002 | 0.54 | 0.03 |
| | H2 | 8.11 | ...[b] | 4.89 | 2.50 |
| | H3 | 2.91 | 0.91 | 1.68 | 0.62 |
| | H4 | 1.70 | 0.44 | 1.11 | 0.32 |
| | H′1 | 2.34 | 2.66 | 2.98 | 3.01 |
| | H′2 | 24.26 | ...[b] | ...[b] | 5.77 |
| | H′3 | 4.36 | 3.55 | 3.92 | 3.46 |
| | H′4 | 3.29 | 3.08 | 3.43 | 3.21 |

[a]These systems converged to a more stable T1 configuration during the optimization process.
[b]Conformers have proven to be unstable at the optimization step.

molecular dynamics (AIMD) simulations at 300 K on selected energetically most favorable Zr-based MXenes, as discussed above. The resulting AIMD energy profiles can be seen in Fig. S2 in the supplementary material. No Zr-based MXene transformed into a different conformation or exhibited signs of structural instability that would disrupt the material.
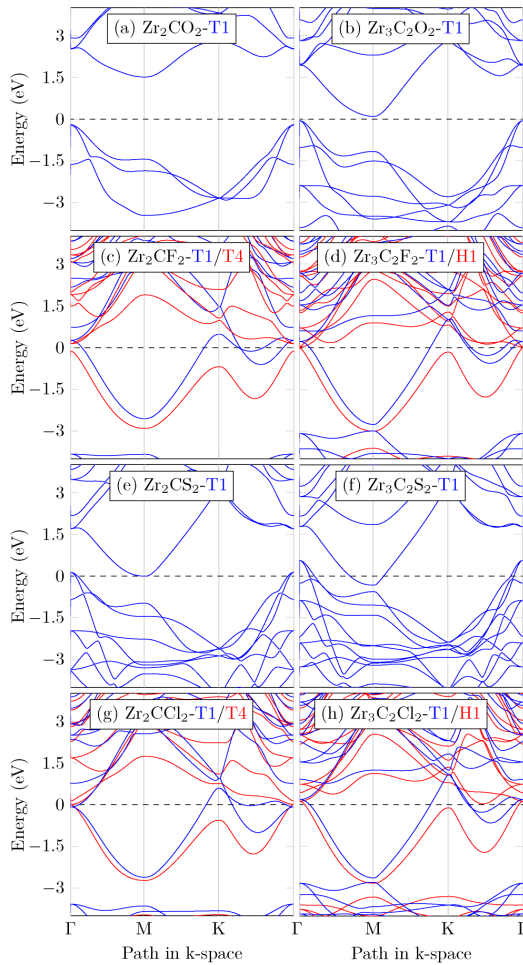
## B. Electronic properties and strain

We performed calculations on Zr-based MXenes with the inclusion of the spin–orbit coupling (SOC), which are important in analogous Hf-based MXenes.[46] The results, however, show that the SOC has only a marginal effect on the total energies and band structures of these MXenes (see Fig. S3 with the $Zr_2CO_2$ MXene in the supplementary material). To lower the computational cost, we performed subsequent calculations without the inclusion of SOC.

Upon analyzing the most favorable conformations, considering two possible structures for F- and Cl- terminated MXenes, some of the SCAN band structures raised a suspicion that the meta-GGA functional might be insufficient for the accurate determination of the band structures and for the evaluation of electronic bandgaps in semiconducting MXenes. Therefore, a set of HSE06 band structures for chosen MXenes is presented in Fig. 2. SCAN band structures can be seen in Fig. S4 in the supplementary material, as well as the comparison of meta-GGA and hybrid band structures in Fig. S5 of the supplementary material. At the level of hybrid density functional, the number of semiconducting cases has risen significantly when compared to the available literature, where only $Zr_2CO_2$ is usually identified as a semiconductor. Here, we show that when conformations energetically close to the ground state are considered, we can identify a total of five semiconducting Zr-based MXenes— $Zr_2CO_2$-T1, $Zr_2CF_2$-T4, $Zr_2CCl_2$-T4, $Zr_3C_2O_2$-T1, and $Zr_3C_2F_2$-H1. Note that the semiconducting conformations for F- and Cl-terminated MXenes are in Figs. 2(c), 2(d), and 2(g) shown in red. The bandgaps for selected semiconducting MXenes obtained with different levels of computational theory (PBE, SCAN, HSE06, and $G_0W_0$@HSE06) are collected in Table II.

The changes in indirect, direct, and $\Gamma$-point electronic bandgap for chosen MXenes under biaxial strain are shown in Fig. 3. MXenes that are missing from this selection exhibited conducting behavior in the full strain range. Each MXene presented in Fig. 3 has been tested in AIMD simulation in the range from $-6\%$ to $+6\%$ biaxial strain to ensure their stability in these regions. Individual band structures and their changes with biaxial strain for every configuration can be seen in Figs. S6–S17 in the supplementary material. The changes in the total energy of given conformations under strain are presented in Fig. S18 of the



**FIG. 2.** HSE06 band structures for Zr-based MXenes $Zr_2CT_2$ and $Zr_3C_2T_2$, where T = O, F, S, Cl. Two band structures for different geometric conformations are presented when the given conformations are energetically very close (<0.07 eV).

**TABLE II.** Bandgaps of semiconducting Zr-based MXenes at different levels of computational theory (in eV). For indirect materials, a value of the direct bandgap is given in parentheses.

|         |     |     | PBE | SCAN | HSE06 | $G_0W_0$[a] |
|---------|-----|-----|-----|------|-------|-------------|
| $Zr_2C$ | O   | T1  | 0.95(1.81) | 1.25(2.11) | 1.73(2.72) | 2.61(3.56) |
|         | F   | T4  | 0.22 | 0.26 | 0.26 | 0.72 |
|         | Cl  | T4  | 0.00[b] | 0.00[b] | 0.01 | 0.25[c] |
| $Zr_3C_2$ | O | T1  | … | … | 0.17(1.27) | 0.61(1.71) |
|         | F   | H1  | … | 0.05 | 0.03 | 0.29 |

[a]For $G_0W_0$, HSE06 wave functions were used, and the reported value assumes *a posteriori* rigid correction due to the height of the computational cell $L_z$.

[b]The zero reported means that the system is a zero-gap semiconductor.

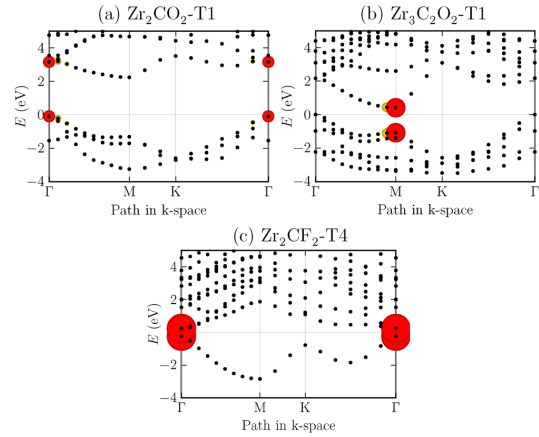[c]The rigid correction was fine-tuned on +2% strained system.
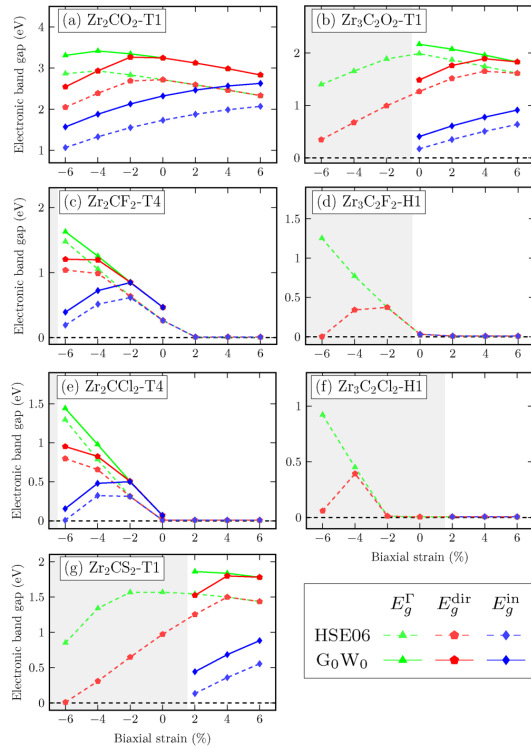
**FIG. 3.** The effect of biaxial strain on the indirect ($E_g^{in}$), direct ($E_g^{dir}$), and $\Gamma$-point ($E_g^{\Gamma}$) electronic bandgap in several Zr-based MXenes. The MXenes, which exhibited conducting behavior in the full strain range, are not shown. For chosen MXenes, two levels of theory are used to model the behavior under biaxial strain (hybrid functional HSE06 and many-body perturbation $G_0W_0$ method). The gray area signifies the biaxial strain beyond which the material lost its indirect bandgap and became conducting at the hybrid density functional level.



**FIG. 4.** Quasiparticle ($G_0W_0$) band structure (black dots) of (a) $Zr_2CO_2$-T1, (b) $Zr_3C_2O_2$-T1, and (c) $Zr_2CF_2$-T4 and all $|A_{cvk}^{\lambda}|$ coefficients from BSE (represented by the radii of the colored circles) visually show which electron–hole pairs contribute to the first bright excitonic peak. The top of the valence band is set to zero.

supplementary material. The detailed analysis of the electronic properties of given Zr-based MXenes and their changes with the biaxial strain are presented in Secs. III B 1–III B 4, with a focus on each termination group separately.

### 1. O-terminated Zr-based MXenes

In an unstrained state the O-terminated two-layered MXene $Zr_2CO_2$ exhibits at levels of PBE, SCAN, HSE06, and $G_0W_0$@HSE06 an indirect bandgap 0.95, 1.25, 1.73, and 2.61 eV, respectively, and a direct bandgap 1.81, 2.11, 2.72, and 3.56 eV, respectively (see Table II). The indirect gap is located between $\Gamma$ and M points in the Brillouin zone, while the minimal direct gap is located in the $\Gamma$ point. This behavior holds at all computational

levels, cf. the $G_0W_0$ band structure in Fig. 4(a) and the HSE06 band structure in Fig. 2(a) (or also the SCAN band structure in Fig. S4a). At the level of PBE density functional, the electronic bandgap of 0.88 eV is usually reported for $Zr_2CO_2$. This result, calculated by Khazaei et al.,[14] differs slightly from our estimation and a possible explanation could arise from the fact that four more inner electrons ($s$ and $p$ states) for Zr atoms were included in self-consistent calculations. Our results are in very good agreement with a different study done by Zha et al., where the electronic configuration for Zr atoms is identical to ours and an indirect bandgap of 0.97 eV is reported for $Zr_2CO_2$.[18]

Results for $Zr_2CO_2$ indicate that a indirect-to-direct semiconductor transition would occur under tensile strain larger than +6% [see Fig. 3(a)]. Under compressive strain, it experiences a decrease of the indirect bandgap, and it is expected to lose its semiconducting properties under large enough compressive strain. These results are consistent with different studies of the effects of strain on $Zr_2CO_2$.[22,23]

With the use of SCAN density functional, the three-layered MXene $Zr_3C_2O_2$ shows conducting behavior in its unstrained state (see Fig. S4b in the supplementary material) but it was suspected that this could be just an artifact of the GGA and meta-GGA bandgap underestimation. This is subsequently proven as with the HSE06 functional the $Zr_3C_2O_2$ MXene exhibits an indirect and direct electronic bandgap of 0.17 and 1.27 eV, respectively [Fig. 2(b)]. Furthermore, with the $G_0W_0$ the bandgap increases and is estimated to be 0.61 eV (indirect between $\Gamma$ and M points) and 1.71 eV (direct in M, Fig. 4). Under compressive strain, the MXene becomes conductive with either density functional used. Under tensile strain, the indirect bandgap increases (the material becomes

semiconducting even at the SCAN level), and the direct band gap is moved to the $\Gamma$ point.

To better understand strain-induced changes in the band structure of $Zr_3C_2O_2$-T1 MXene, we have analyzed partial charge densities of states near the bandgap. These are collected in Fig. S19 in the supplementary material. These representations then reflect well the band structure changes in Fig. S12 in the supplementary material where the top two valence bands degenerate in the $\Gamma$ point but exchange with the increasing tensile strain, and thus we observe the change of $p$-state in the M point. Furthermore, Fig. S20 in the supplementary material shows the projected density of states (PDOS) of $Zr_3C_2O_2$-T1, which underline that Zr-atoms mainly contribute to the conduction states and C-atoms contribute to the valence states.

### 2. F-terminated Zr-based MXenes

The trigonal T1 geometry of the two-layered MXene $Zr_2CF_2$ is energetically more favorable in the full strain range at the meta-GGA level of the theory (see Fig. S18c in the supplementary material). On the other hand, with increasing levels of theory, energy differences between energies of conformations became even smaller: competing T1 and T4 configurations have energy differences of 0.08, 0.06, and 0.03 eV for GGA (PBE), meta-GGA (SCAN), and hybrid (HSE06) DFT method, respectively. Speculatively, a higher, more correlated level of theory (fully beyond the scope of our work, such as random phase approximation or quantum Monte Carlo) could, therefore, lead to the T4 ground state. Unstrained T1 geometry is conducting and this behavior is not changed under any strain, either compressive or tensile (see Fig. S7 of the supplementary material). The trigonal T4 conformer exhibits at the level of the hybrid HSE06 functional a direct bandgap of 0.26 eV which then gets substantially larger (0.72 eV) with the many-body $G_0W_0$ method (and with the correction to $L_z$). The minimal direct gap is located in the $\Gamma$ point and this behavior holds at all computational levels, cf. the $G_0W_0$ band structure in Fig. 4(c) and the HSE06 band structure in Fig. 2(c). Our results agree very well with another study done by Duan *et al.*[16] where the order of conformers is equivalent to ours and the electronic band gap of 0.24 eV is reported for the $Zr_2CF_2$-T4 MXene.

With a compressive strain, the direct bandgap of the T4 conformer becomes even larger up to $-2\%$ strain when the MXene undergoes a transition to an indirect material [see Fig. 3(c)]. From the presented results we can suspect, that beyond $-6\%$ compressive strain the $Zr_2CF_2$-T4 MXene would lose its bandgap and become a conductor.

For the three-layered MXene $Zr_3C_2F_2$, the energy differences between T1 and H1 conformers are very small. At the ground-state SCAN level, the difference is only 0.002 eV (Table I). It is also the only tested MXene that experiences a phase shift under compressive strain (Fig. S18d in the supplementary material). This MXene, as well as $Zr_3C_2O_2$, was the first indication that a higher level density functional needs to be used. With the use of hybrid functional HSE06, the semiconducting hexagonal H1 geometry becomes the ground-state conformation. The energy levels between individual phases (T1 and H1) then get pushed further apart as the H1 geometry is 0.02 eV energetically lower than the T1 geometry.

The T1 geometry exhibits a metallic behavior in the full range of compressive and tensile strain regardless of the method used (Fig. S13 in the supplementary material). The hexagonal H1 geometry has at its unstrained state a small direct bandgap of 0.03 at the hybrid level. Under a relatively small $-2\%$ compressive strain, the $Zr_3C_2F_2$-H1 MXene starts exhibiting conducting behavior [see Fig. 3(d)]. Under tensile strain, the bandgap vanishes to zero (similarly as in the two-layered case) and the H1 conformer stays as a zero-gap semiconductor further on. These near-zero band gaps [which occur under tensile strain in all tested F- and Cl-terminated MXenes, see Figs. 3(c)–3(f)] have proven to be quite challenging when one chooses to use the many-body approach. With valence and conduction bands being so close to the Fermi level, the $G_0W_0$ method can sometimes make a wrong correction and predict that material, claimed as semiconducting at the SCAN or HSE06 level, is conducting. One thus has to be careful in such scenarios, as the wrong initial guess, such as slightly partially occupied bands near the Fermi level, can get magnified and result in the wrong final prediction. In the case of this MXene, the SCAN bandgap of 0.05 eV was with the use of $G_0W_0$@SCAN wrongfully predicted as a conductor. The HSE06 bandgap of 0.03 eV was then successfully corrected to 0.29 eV after the $G_0W_0$@HSE06 computation (taking into account the correction to $L_z$).

### 3. S-terminated Zr-based MXenes

The two-layered MXene $Zr_2CS_2$ exhibits conducting behavior while unstrained. However, the emergence of a non-zero gap can be observed under tensile strain beyond $+2\%$ at the hybrid functional level [see Fig. 3(g)]. The $G_0W_0$@HSE06 approach then suggests that $Zr_2CS_2$ could retain its semiconducting properties even in its unstrained state. However, without the initial semiconducting guess at no strain, we are not able to confirm this hypothesis. Under compressive strain, the MXene retains its conducting properties.

Three-layered $Zr_3C_2S_2$ MXene exhibits conductive behavior in the full strain range and does not show signs that a bandgap could appear (Fig. S15 in the supplementary material).

### 4. Cl-terminated Zr-based MXenes

T1 geometry of the two-layered MXene $Zr_2CCl_2$ remains energetically more favorable (0.03 eV or less) for the full range of compressive and tensile strain (see Fig. S18g in the supplementary material). The hybrid HSE06 density functional then pushes the energy levels closer but the order remains unchanged (and we can speculate on almost identical energies using a higher, more correlated, level of theory). The same holds for the three-layered Cl-terminated MXene $Zr_3C_2Cl_2$.
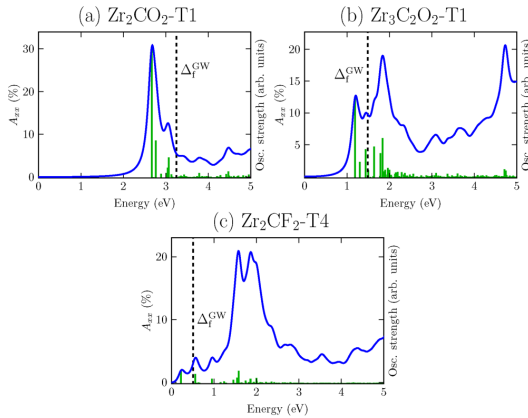
Unstrained $Zr_2CCl_2$-T1 conformer exhibits conducting behavior and this behavior is unchanged under any strain (Fig. S10 in the supplementary material). The T4 geometry has at the level of hybrid density functional a very small direct band gap of 0.01 eV. This bandgap is then increased by the many-body $G_0W_0$ approach to 0.25 eV (after rigid correction to $L_z$). Under tensile strain, the direct bandgap diminishes to near-zero values, as in other halogen-terminated MXenes reported here [Fig. 3(e)].

26 June 2024 14:24:57

Under compressive strain, the MXene behaves similarly to the F-terminated $Zr_2CF_2$-T4 [see Fig. 3(c) and 3(e)]. The direct bandgap increases up to $-2\%$ strain, the material then becomes indirect, and with further strain, the bandgap disappears as the valence band crosses the Fermi level.

The three-layered T1 geometry of the $Zr_3C_2Cl_2$ MXene is metallic in its unstrained state and the behavior is not changed under either compressive or tensile strain (Fig. S16 in the supplementary material). The H1 geometry is also predicted to be conducting in its unstrained state [Fig. 3(f)]. Under a small $+2\%$ tensile strain, we can observe the disappearance of the conducting behavior as there again appears to be a near-zero bandgap at the $\Gamma$ point. Under compressive strain, the $Zr_3C_2Cl_2$ MXene retains its conducting properties.

## C. Optical properties

We provide calculated absorption spectra for three selected Zr-based MXenes, $Zr_2CO_2$-T1, $Zr_3C_2O_2$-T1, and $Zr_2CF_2$-T4, by the GW+BSE many-body approach. The very small bandgap of the remaining semiconducting MXenes made the estimation of the optical gap unreliable. The number of occupied and virtual bands that enter the solution of BSE was chosen to ensure credibility up to a photon energy of 5 eV. The resulting value of optical gap $\Delta_{opt}^{BSE}$ for each MXene is also, similarly as for quasiparticle gap $\Delta_f^{GW}$, corrected by *a posteriori* rigid correction, as discussed in Sec. II. The resulting absorption spectra, paired with corresponding oscillator strengths, can be seen in Fig. 5 with the quasiparticle bandgap marked with a dashed line. The visualized quantity here is the optical absorptance

**TABLE III.** The direct quasiparticle bandgap ($\Delta_f^{GW,dir}$), optical gap ($\Delta_{opt}^{BSE}$), and the exciton binding energy ($E_b$) for three selected Zr-based MXenes.

| | $\Delta_f^{GW,dir}$ | $\Delta_{opt}^{BSE}$ | $E_b$ |
|---|---|---|---|
| $Zr_2CO_2$-T1 | 3.56 | 2.56 | 1.00 |
| $Zr_3C_2O_2$-T1 | 1.71 | 1.09 | 0.62 |
| $Zr_2CF_2$-T4 | 0.72 | 0.20 | 0.52 |

$A(E) = 1 - \exp[-\varepsilon_2 E L_z / \hbar c]$,[47] where $E$ is the energy of incident photon, $\varepsilon_2$ is the imaginary part of dielectric function, $\hbar$ is reduced Planck's constant, and $c$ is speed of light.

For all selected MXenes, we can observe at least partial absorption of the visible range of incoming radiation (1.63–3.26 eV) with exceptionally high efficiency in a range of 20%–30%. Table III collects the many-body results for the three selected MXenes, including the direct quasiparticle gap, optical gap, and their difference in the form of exciton binding energy. The first bright exciton (i.e., first nonzero optical transition) occurs for $\lambda = 2, 4$, and 1 in $Zr_2CO_2$-T1, $Zr_3C_2O_2$-T1, and $Zr_2CF_2$-T4, respectively. The dominant contribution to the corresponding excitonic wave function [expressed in an electron–hole product basis as $\sum_{cvk} A_{cvk}^\lambda \phi_{ck} \phi_{vk}$; see also Eq. (1)] is always from the k-space area sharply located in minimal direct gap position (i.e., $\Gamma$, M, and $\Gamma$ location for $Zr_2CO_2$-T1, $Zr_3C_2O_2$-T1, and $Zr_2CF_2$-T4, respectively). This is visible in Fig. 4 by color circles representing $|A_{cvk}^\lambda|$ as the important electron–hole contributions labeled by $c, v$ subscripts (band pairs on the y-axis; only the valence band and conduction band are important) and by $k$ subscript describing the x-axis (missing color circles on black points means negligible coefficients are not visible in the graph).

It is possible to compare materials based on the relationship between $\Delta_f^{GW}$ and $E_B$ as many 2D semiconductors exhibit linear scaling $E_B \approx \Delta_f / 4$.[48] Both O-terminated MXenes satisfy this scaling within some margin of error. The F-terminated MXene, on the other hand, exceeds this ratio threefold.

To investigate the effect of strain on the optical properties of Zr-based MXenes, we have calculated the optical absorption spectra of the three selected MXenes depending on the biaxial strain. The resulting spectra can be seen in Fig. 6 with the quasiparticle gap and optical gap marked. It can be seen that the optical gap follows a pattern similar to the results collected in Fig. 3. Therefore, no significant change to the exciton binding energy is observed. On the other hand, it is possible to tune the energy/wavelength region of maximal absorption by strain (Fig. 6). The $Zr_2CO_2$-T1 MXene has the highest absorption efficiency in its unstrained state. When tensile or compressive strain is applied, the absorption maxima decreases but remains in the range of 15%–20%. The three-layered $Zr_3C_2O_2$-T1 MXene, on the other hand, shows an increase in absorption when tensile strain is applied. For F-terminated $Zr_2CF_2$-T4, we observe that when the material is compressed, the first optically active exciton is shifted to higher energies (correspondingly with the change in the fundamental bandgap). The bulk of absorption is at the same time shifted to lower energies.
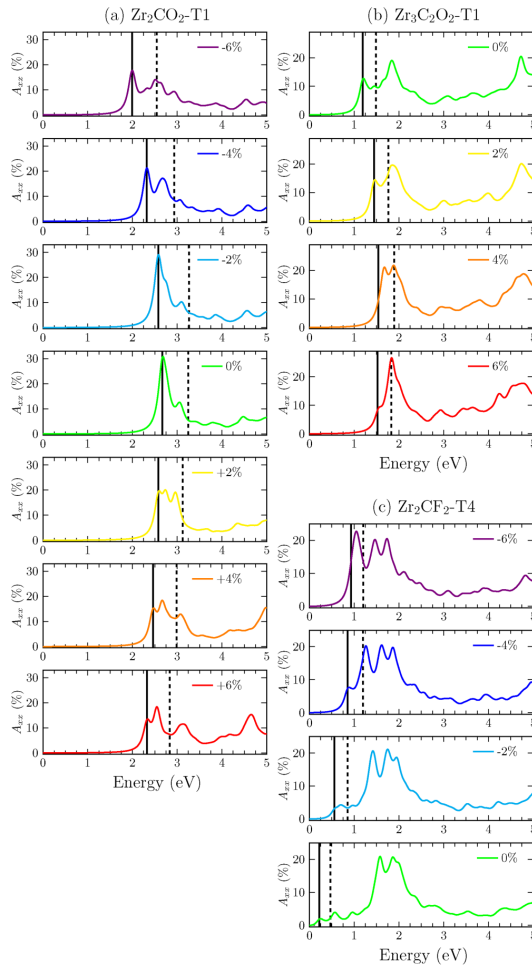


**FIG. 5.** Optical absorption spectra ($A_{xx} = A_{yy}, A_{zz} \approx 0$) for Zr-based MXenes (a) $Zr_2CO_2$-T1, (b) $Zr_3C_2O_2$-T1, and (c) $Zr_2CF_2$-T4 at the level of $G_0W_0$ + BSE and corresponding oscillator strengths. The dashed line in spectra marks the $G_0W_0$ + BSE estimation of the fundamental bandgap $\Delta_f$.

**FIG. 6.** Optical absorption spectra ($A_{xx} = A_{yy}$, $A_{zz} \approx 0$) for Zr-based MXenes (a) $Zr_2CO_2$-T1, (b) $Zr_3C_2O_2$-T1, and (c) $Zr_2CF_2$-T4 computed with the $G_0W_0$ +BSE method depended on biaxial strain. The black solid and dashed lines note the position of the first optically active exciton $\Delta_{opt}^{BSE}$ and the quasiparticle bandgap $\Delta_f^{GW}$, respectively.

## IV. CONCLUSIONS

In this study, we have systematically investigated the strain-induced electronic and optical properties of zirconium-based MXenes, specifically focusing on two- and three-layered configurations of $Zr_2CT_2$ and $Zr_3C_2T_2$ MXenes, where T is a terminal group. Through extensive computational analyses

employing methodologies of density functional theory (DFT) ranging from the Generalized Gradient Approximation (GGA), meta-GGA, to the more sophisticated hybrid functional and many-body single-shot $G_0W_0$ method, we have explored a total of eight highly symmetrical configurations for two-layered and twelve configurations for three-layered Zr-based MXenes, encompassing a variety of terminations including oxygen, fluorine, sulfur, and chlorine.

Our findings reveal that all investigated Zr-based MXenes exhibit, at the meta-GGA level, a trigonal ground state with a second geometry being energetically very close to the ground state in halogen-terminated MXenes. The energy levels of different phases become more closely spaced upon using the hybrid functional, and $Zr_3C_2F_2$ MXene has hexagonal semiconducting ground state. Diverging from the prevailing focus on oxygen-terminated MXenes in the available literature, which predominantly identifies only $Zr_2CO_2$ as semiconducting, our research, particularly at the level of the hybrid functional HSE06, identifies three Zr-based MXenes that are semiconducting in their ground-state conformation: $Zr_2CO_2$, $Zr_3C_2O_2$, $Zr_3C_2F_2$. Moreover, two more MXenes, $Zr_2CF_2$, and $Zr_2CCl_2$, are found to have a semiconducting conformation energetically very close to the ground state, within a margin of less than 0.03 eV at hybrid density functional level (or speculatively the true ground state if using a higher, more correlated, level of theory).

Furthermore, our investigation reveals that additional conducting MXenes ($Zr_2CS_2$, $Zr_3C_2Cl_2$) transition to a semiconducting state under a relatively minor application of tensile biaxial strain, thus expanding the potential catalog of Zr-based MXenes suitable for semiconducting applications. This finding suggests that Zr-based MXenes hold a broader utility in the fabrication of electronic devices than previously recognized. On the other hand, the semiconducting Zr-based MXenes always switch to conducting states under compressive biaxial strain.

Advancing beyond electronic properties, our study also employs the solution of the Bethe–Salpeter equation (BSE) to elucidate the optical absorption spectra, estimate the optical gap, and determine the exciton binding energy for three selected MXenes: $Zr_2CO_2$, $Zr_2CF_2$, and $Zr_3C_2O_2$. The results from this segment of our research highlight the exceptional potential of these MXenes to absorb electromagnetic radiation within the visible photon energy range of 1.63–3.26 eV, demonstrating an unusually high efficiency of 20%–30%.

The thermal stability, the possibility of semiconductor-to-conductor transitions, and the high sensitivity of Zr-based MXenes to external conditions and functionalization are unusually promising combinations. These make the Zr-based MXenes materials promising for device applications at operational temperatures in electronic, sensor, and optical technologies.

## SUPPLEMENTARY MATERIAL

See the supplementary material for computational details, more details on the geometrical structure and stability, the convergence of electronic and optical properties, and properties under strain.

## ACKNOWLEDGMENTS

## AUTHOR DECLARATIONS

### Conflict of Interest

The authors have no conflicts to disclose.

### Author Contributions

**Jiří Kalmár:** Data curation (lead); Formal analysis (equal); Investigation (lead); Visualization (lead); Writing – original draft (lead); Writing – review & editing (supporting). **František Karlický:** Conceptualization (lead);Data curation (supporting); Formal analysis (equal); Funding acquisition (lead); Investigation (supporting); Methodology (lead); Project administration (lead); Resources (lead); Supervision (lead); Validation (lead); Visualization (supporting); Writing – original draft (supporting); Writing – review & editing (lead).

## DATA AVAILABILITY

The data that support the findings of this study are available from the corresponding author upon reasonable request.

## REFERENCES

[1]B. Anasori, M. R. Lukatskaya, and Y. Gogotsi, "2D metal carbides and nitrides (MXenes) for energy storage," Nat. Rev. Mater. **2**, 16098 (2017).

[2]K. Hantanasirisakul and Y. Gogotsi, "Electronic and optical properties of 2D transition metal carbides and nitrides (MXenes)," Adv. Mater. **30**, 1804779 (2018).

[3]Y. Gogotsi and B. Anasori, "The rise of MXenes," ACS Nano **13**, 8491–8494 (2019).

[4]M. Naguib, M. Kurtoglu, V. Presser, J. Lu, J. Niu, M. Heon, L. Hultman, Y. Gogotsi, and M. W. Barsoum, "Two-dimensional nanocrystals produced by exfoliation of $Ti_3AlC_2$," Adv. Mater. **23**, 4248–4253 (2011).

[5]2D Metal Carbides and Nitrides (MXenes), edited by B. Anasori and Y. Gogotsi (Springer, Switzerland, 2020).

[6]B. Anasori and Y. Gogotsi, "MXenes: Trends, growth, and future directions," Graphene 2D Mater. **7**, 75–79 (2022).

[7]K. R. G. Lim, M. Shekhirev, B. C. Wyatt, B. Anasori, Y. Gogotsi, and Z. W. Seh, "Fundamentals of MXene synthesis," Nat. Synthesis **1**, 601–614 (2022).

[8]T. Ketolainen and F. Karlický, "Optical gaps and excitons in semiconducting transition metal carbides (MXenes)," J. Mater. Chem. C **10**, 3919–3928 (2022).

[9]T. Sakhraoui and F. Karlický, "Electronic nature transition and magnetism creation in vacancy-defected $Ti_2CO_2$ MXene under biaxial strain: A DFTB + U study," ACS Omega **7**, 42221–42232 (2022).

[10]A. Champagne and J.-C. Charlier, "Physical properties of 2D MXenes: From a theoretical perspective," J. Phys.: Mater. **3**, 032006 (2020).

[11]N. Kumar and F. Karlický, "Oxygen-terminated $Ti_3C_2$ MXene as an excitonic insulator," Appl. Phys. Lett. **122**, 183102 (2023).

[12]A. Lipatov, H. Lu, M. Alhabeb, B. Anasori, A. Gruverman, Y. Gogotsi, and A. Sinitskii, "Elastic properties of 2D $Ti_3C_2T_x$ MXene monolayers and bilayers," Sci. Adv. **4**, eaat0491 (2018).

[13]B. C. Wyatt, A. Rosenkranz, and B. Anasori, "2D MXenes: Tunable mechanical and tribological properties," Adv. Mater. **33**, 2007973 (2021).

[14]M. Khazaei, M. Arai, T. Sasaki, C. Chung, N. S. Venkataramanan, M. Estili, Y. Sakka, and Y. Kawazoe, "Novel electronic and magnetic properties of two-dimensional transition metal carbides and nitrides," Adv. Funct. Mater. **23**, 2185–2192 (2012).

[15]S. A. Thomas and J. Cherusseri, "Recent advances in synthesis and properties of zirconium-based MXenes for application in rechargeable batteries," Energy Storage **5**, e475 (2023).

[16]X. Duan, B. Zhou, and X. Wang, "Strain tailored electronic structure and magnetic properties of Fe-doped $Zr_8C_4T_8$ (T = F, O) monolayers," Phys. E: Low-Dimens. **145**, 115488 (2023).

[17]H. Zhang, X.-H. Li, R.-Z. Zhang, and H.-L. Cui, "First-principle study of electronic, optical, quantum capacitance, carrier mobility and photocatalytic properties of $Zr_2Co_2$ MXene under uniaxial strain," Vacuum **220**, 112813 (2024).

[18]X.-H. Zha, K. Luo, Q. Li, Q. Huang, J. He, X. Wen, and S. Du, "Role of the surface effect on the structural, electronic and mechanical properties of the carbide MXenes," Eur. Phys. Lett. **111**, 26007 (2015).

[19]J. Zhou, X. Zha, F. Y. Chen, Q. Ye, P. Eklund, S. Du, and Q. Huang, "A two-dimensional zirconium carbide by selective etching of $Al_3C_3$ from nanolaminated $Zr_3Al_3C_5$," Angew. Chem. Int. Ed. **55**, 5008–5013 (2016).

[20]X.-H. Zha, X. Ma, J.-T. Luo, and C. Fu, "Surface potential-determined performance of $Ti_3C_2T_2$ (T = O, F, OH) and $Zr_3C_2T_2$ (T = O, F, OH, S) MXenes as anode materials of sodium ion batteries," Nanoscale **14**, 10549–10558 (2022).

[21]Z. Yang, H. Peng, J. Sun, and J. P. Perdew, "More realistic band gaps from meta-generalized gradient approximations: Only in a generalized Kohn-Sham scheme," Phys. Rev. B **93**, 205205 (2016).

[22]S. A. Khan, B. Amin, L.-Y. Gan, and I. Ahmad, "Strain engineering of electronic structures and photocatalytic responses of MXenes functionalized by oxygen," Phys. Chem. Chem. Phys. **19**, 14738–14744 (2017).

[23]J. Cui, Q. Peng, J. Zhou, and Z. Sun, "Strain-tunable electronic structures and optical properties of semiconducting MXenes," Nanotechnology **30**, 345205 (2019).

[24]Y. Zhang, X.-H. Zha, K. Luo, Y. Qin, X. Bai, J. Xu, C.-T. Lin, Q. Huang, and S. Du, "Theoretical study on the electrical and mechanical properties of MXene multilayer structures through strain regulation," Chem. Phys. Lett. **760**, 137997 (2020).

[25]L. Hedin, "New method for calculating the one-particle Green's function with application to the electron-gas problem," Phys. Rev. **139**, A796–A823 (1965).

[26]H. Bethe and E. Salpeter, "A relativistic equation for bound state problems," Phys. Rev. **84**, 1232–1242 (1951).

[27]G. Kresse and J. Hafner, "Ab initio molecular dynamics for open-shell transition metals," Phys. Rev. B **48**, 13115–13118 (1993).

[28]G. Kresse and J. Furthmüller, "Efficiency of ab-initio total energy calculations for metals and semiconductors using a plane-wave basis set," Comput. Mater. Sci. **6**, 15–50 (1996).

[29]G. Kresse and J. Furthmüller, "Efficient iterative schemes for ab initio total-energy calculations using a plane-wave basis set," Phys. Rev. B **54**, 11169–11186 (1996).

[30]G. Kresse and J. Hafner, "Norm-conserving and ultrasoft pseudopotentials for first-row and transition elements," J. Phys.: Condens. Matter **6**, 8245–8257 (1994).

[31]P. E. Blöchl, "Projector augmented-wave method," Phys. Rev. B **50**, 17953–17979 (1994).

[32]J. P. Perdew, K. Burke, and M. Ernzerhof, "Generalized gradient approximation made simple," Phys. Rev. Lett. **77**, 3865–3868 (1996).

[33]J. Sun, A. Ruzsinszky, and J. P. Perdew, "Strongly constrained and appropriately normed semilocal density functional," Phys. Rev. Lett. **115**, 036402 (2015).

[34]A. V. Krukau, O. A. Vydrov, A. F. Izmaylov, and G. E. Scuseria, "Influence of the exchange screening parameter on the performance of screened hybrid functionals," J. Chem. Phys. **125**, 224106 (2006).

[35]A. Togo and I. Tanaka, "First principles phonon calculations in materials science," Scr. Mater. **108**, 1–5 (2015).

[36]M. Shishkin and G. Kresse, "Implementation and performance of the frequency-dependent *GW* method within the PAW framework," Phys. Rev. B **74**, 035101 (2006).

[37]M. Kolos and F. Karlický, "Accurate many-body calculation of electronic and optical band gap of bulk hexagonal boron nitride," Phys. Chem. Chem. Phys. **21**, 3999–4005 (2019).

[38]M. Dubecký, F. Karlický, S. Minárik, and L. Mitas, "Fundamental gap of fluorographene by many-body GW and fixed-node diffusion Monte Carlo methods," J. Chem. Phys. **153**, 184706 (2020).

[39]M. Kolos and F. Karlický, "The electronic and optical properties of III–V binary 2D semiconductors: How to achieve high precision from accurate many-body methods," Phys. Chem. Chem. Phys. **24**, 27459–27466 (2022).

[40]S. Albrecht, L. Reining, R. Del Sole, and G. Onida, "Ab initio calculation of excitonic effects in the optical spectra of semiconductors," Phys. Rev. Lett. **80**, 4510–4513 (1998).

[41]F. Karlický and J. Turoň, "Fluorographane $C_2FH$: Stable and wide band gap insulator with huge excitonic effect," Carbon **135**, 134–144 (2018).

[42]M. Dubecký, S. Minárik, and F. Karlický, "Benchmarking fundamental gap of $Sc_2C(OH)_2$ MXene by many-body methods," J. Chem. Phys. **158**, 054703 (2023).

[43]N. Berseneva, A. Gulans, A. V. Krasheninnikov, and R. M. Nieminen, "Electronic structure of boron nitride sheets doped with carbon from first-principles calculations," Phys. Rev. B **87**, 035404 (2013).

[44]J.-H. Choi, P. Cui, H. Lan, and Z. Zhang, "Linear scaling of the exciton binding energy versus the band gap of two-dimensional materials," Phys. Rev. Lett. **115**, 066403 (2015).

[45]X. Qian, J. Liu, L. Fu, and J. Li, "Quantum spin Hall effect in two-dimensional transition metal dichalcogenides," Science **346**, 1344–1347 (2014).

[46]N. Kumar, M. Kolos, S. Bhattacharya, and F. Karlický, "Excitons, optical spectra, and electronic properties of semiconducting Hf-based MXenes," J. Chem. Phys. **160**, 124707 (2024).

[47]T. Ketolainen, N. Macháčová, and F. Karlický, "Optical gaps and excitonic properties of 2D materials by hybrid time-dependent density functional theory: Evidences for monolayers and prospects for van der Waals heterostructures," J. Chem. Theory Comput. **16**, 5876–5883 (2020).

[48]Z. Jiang, Z. Liu, Y. Li, and W. Duan, "Scaling universality between band gap and exciton binding energy of two-dimensional semiconductors," Phys. Rev. Lett. **118**, 266401 (2017).

26 June 2024 14:24:57

# Supplementary Material 12

Check for updates

# Mn₂C MXene functionalized by oxygen is a semiconducting antiferromagnet and an efficient visible light absorber†

Jiří Kalmár [ID] and František Karlický [ID] *

Manganese-based MXenes are promising two-dimensional materials due to the broad palette of their magnetic phases and the possibility of experimental preparation because the corresponding MAX phase was already prepared. Here, we systematically investigated geometrical conformers and spin solutions of oxygen-terminated Mn₂C MXene and performed subsequent many-body calculations to obtain reliable electronic and optical properties. Allowing energy-lowering using the correct spin ordering *via* supercell magnetic motifs is essential for the Mn₂CO₂ system. The stable ground-state Mn₂CO₂ conformation is antiferromagnetic (AFM) with zigzag lines of up and down spins on Mn atoms. The AFM nature is consistent with the parent MAX phase and even the clean depleted Mn₂C sheet. Other magnetic states and geometrical conformations are energetically very close, providing state-switching possibilities in the material. Subsequent many-body GW and Bethe–Salpeter equation (BSE) calculations provide indirect semiconductor characteristics of AFM Mn₂CO₂ with a fundamental gap of 2.1 eV (and a direct gap of 2.4 eV), the first bright optical transition at 1.3 eV and extremely strongly bound (1.1 eV) first bright exciton. Mn₂CO₂ absorbs efficiently the whole visible light range and near ultraviolet range (between 10 and 20%).

## 1 Introduction

MXenes, a family of recent two-dimensional (2D) carbides, nitrides, and carbonitrides, embody various interesting properties promising for technical applications. Besides more than 20 MXenes being prepared experimentally, theoretical modeling suggested tens of others and such a tool became necessary in the design of new MXenes and their properties.[1–4] The typical composition of MXenes is $M_{n+1}X_nT_x$ with $1 \leq n \leq 4$ and $x \leq 2$, where M is a transition metal, X is carbon or nitrogen, and T is the surface termination which includes groups 16 and 17 of the periodic table or hydroxyl and imido groups. 2D MXene's properties are sensitive to composition, termination, or external conditions and provide a rich set of its phases: metals, semiconductors,[5] ferromagnets,[6–9] antiferromagnets,[9–13] topological insulators[14] or excitonic insulators[15] with the possibility of magnetization modulation by an electric field[16,17] or lattice defects.[10] Here we focus on less explored manganese-based MXenes as they are extremely interesting for the energetic competition of magnetic states. This MXene subfamily is still rather a

*Department of Physics, Faculty of Science, University of Ostrava, 30. dubna 22, 7013 Ostrava, Czech Republic. E-mail: frantisek.karlicky@osu.cz; Tel: +420 553 46 2155*

† Electronic supplementary information (ESI) available. See DOI: https://doi.org/10.1039/d4cp02264e

hypothetical one, however, it is proposed that $Mn_2CT_x$ MXenes can be prepared experimentally from the already existing parent Mn₂GaC MAX phase[18–21] by exfoliation techniques. Also, other Mn-containing magnetic MAX phases such as (Cr,Mn)₂AlC or (Mo,Mn)₂GaC were prepared.[22,23] Mn-based MXenes are typically predicted as conductors[14,24] and the standard prediction tool for materials modeling, density functional theory (DFT), is robust and generally accepted. However, DFT can sometimes predict different or opposite properties when using its various levels of implementation (mainly various density functionals) for complicated systems (*e.g.* transition metal containing ones). Therefore, when recent works proved that at least one Mn-based MXene, namely oxygen-terminated Mn₂C MXene, is a semiconductor,[5,25–27] the need for a deeper understanding of the systems grew. In addition, the standard generalized gradient approximation (GGA) of DFT showed antiferromagnetic (AFM) behavior of Mn₂CO₂, while recent (higher level) hybrid DFT calculations predicted the ferromagnetic (FM) phase.[5] Moreover, if magnetism is properly treated, magnetic motifs larger than a unit cell should be considered too.[28] Finally, we showed recently the unusually high absorptance in Mn₂CO₂ of $A \approx 10\text{–}20\%$ in the visible 1–3 eV range[5] (however, in a simple unit cell using time-dependent DFT), so the material would also be interesting technologically.

The uncertainties mentioned, the complicated magnetism, the existence of geometric and magnetic conformers, and the

This journal is © the Owner Societies 2024

*Phys. Chem. Chem. Phys.*, 2024, **26**, 19733–19741 | 19733

close energetic levels of the corresponding various electronic states should be reconciled by systematical study and more accurate methods (including many-body methods). Especially, if the material is expected to be an excellent absorber and possibly an easy switch between FM and AFM phases, both are technologically promising for device applications. We therefore used state-of-the-art methods to discover the right nature of $Mn_2CO_2$ and reliably determine its promising properties. Many-body perturbation theory mimics experiments like ARPES and EELS in that the former precisely captures the same single-particle spectral function. Within this framework in the GW approximation,[29] the light absorption can be fully understood through the solution of the excitonic equation of motion, the Bethe–Salpeter equation (BSE).[30] Firstly, we systematically investigated many different spin solutions and geometrical conformers of $Mn_2CO_2$, determined the ground state, and confirmed its stability using phonon analysis and molecular dynamics. Then, we used well-converged advanced many-body methods to determine the fundamental gap, optical gap, and exciton binding energy. Finally, we determined the optical properties and classified $Mn_2CO_2$ as an efficient absorber of the visible and near ultraviolet (UV) part of the sun spectrum.

# 2 Computational methods

All calculations have been performed using the periodic density functional theory code Vienna Ab initio Simulation Package (VASP)[31–34] in versions 6.2.1 and 6.3.0. The spin-polarized DFT Kohn–Sham equations have been solved variationally in a plane-wave basis set using the projector-augmented-wave (PAW) method.[35] For structural optimization, ground-state calculations, and band structure calculations the Perdew–Burke–Ernzerhof (PBE) density functional[36] in the generalized gradient approximation (GGA) was used as well as the *meta*-GGA Strongly Constrained and Appropriately Normed (SCAN)[37] density functional. Later, an advanced hybrid density functional HSE06 was used to further compare energetically close solutions. The convergence criterion for the electronic self-consistency cycle was in all cases set to $10^{-7}$ eV per cell and the structural optimization converged within $10^{-2}$ eV Å$^{-1}$. The plane-wave cutoff energy was set to 500 eV for all calculations uniformly. GW sets of PAWs were used in all calculations and only valence electrons were considered for C and O atoms ($2s^2 2p^2$ and $2s^2 2p^4$, respectively) but the semi-core s and p states were added for Mn atoms ($3s^2 3p^6 3d^5 4s^2$).[38] For a standard unit cell, $12 \times 12 \times 1$ and $24 \times 24 \times 1$ k-point grids were used for relaxation and ground-state calculation, respectively. For subsequent magnetic $2 \times 2$ supercells, the grid was changed to $6 \times 6 \times 1$ and $12 \times 12 \times 1$, respectively, to maintain a constant k-point grid density. In all band structure calculations, the standard k-point path of $\Gamma$–$M$–$K$–$\Gamma$ for 2D hexagonal systems was used. $Mn_2CO_2$ supercells and their phonon dispersion spectra were generated using the Phonopy code.[39] The Hessian matrix for phonon calculation was obtained using density functional perturbation theory (DFPT). *Ab initio*

molecular dynamics was performed on $6 \times 6 \times 1$ supercells at 400 K, using the Andersen thermostat and time steps of 2 fs.

The quasi-particle energies $\varepsilon_{n\mathbf{k}}^{\mathrm{GW}}$ were calculated as first-order corrections to the Kohn–Sham energies $\varepsilon_{n\mathbf{k}}$ (*i.e.*, using the so-called single-shot $G_0W_0$ variant).[40] The quasiparticle gap was computed as $\Delta^{\mathrm{GW}} = \varepsilon_{\mathrm{CBM}}^{\mathrm{GW}} - \varepsilon_{\mathrm{VBM}}^{\mathrm{GW}}$, where CBM stands for the conduction band minimum, and VBM denotes the valence band maximum. We note that $G_0W_0$ fundamental gaps obtained on top of GGA PBE densities ($G_0W_0$@PBE) are very accurate (when perfectly converged) for 2D materials composed of sp elements, as we proved recently by comparison with experiment[41,42] or by direct comparison with the independent stochastic many-body fixed-node diffusion Monte Carlo (FNDMC) method.[43] Recently, the $G_0W_0$@PBE gap was in agreement with FNDMC also in the case of nonmagnetic direct semiconducting scandium-based carbide (MXene).[44] Here, we are treating a complicated 3d-metal-element-containing antiferromagnetic/ferromagnetic system, so the GGA PBE density for input wavefunction is not the best solution. To account for the energy of localized 3d orbitals of transition metal (TM) atoms properly, the Hubbard "$U$" correction is typically employed, and it is recommended for $Mn_2CO_2$ too.[45] To avoid the empirical choice of $U$ value, we selected a more general *meta*-GGA SCAN functional, as both SCAN and PBE+$U$ provide similar magnetic moments and bandgaps for 3d-metal ferroelectrics and multiferroics[46] (see also section 3.2). On the other hand, we did not build $G_0W_0$ on top of hybrid functionals as HSE06, mixing some fraction of exact Hartree–Fock exchange, because HSE06 overestimates $Mn_2CO_2$ magnetic moments[5] and can fail because of a multireference system[47] or due to tradeoffs between over-delocalization and under-binding.[48] In addition, subsequent $G_0W_0$@HSE06 gaps often overestimate in experiment, *e.g.*, for antiferromagnetic hematite $\alpha$-$Fe_2O_3$.[49] The $G_0W_0$@HSE06 approach is typically used just in the case of small-gap semiconductors, where PBE provides an artificially negative gap preventing subsequent use of perturbative $G_0W_0$@PBE.[50,51]

The BSE was used in eigenvalue problem form[52] for insulating materials with occupied valence bands ($v$ index), and completely unoccupied conduction bands ($c$),

$$
(\varepsilon_{c\mathbf{k}}^{GW} - \varepsilon_{v\mathbf{k}}^{GW})A_{cv\mathbf{k}}^{\lambda} + \sum_{c'v'\mathbf{k}'}[2\langle\phi_{c\mathbf{k}}\phi_{v\mathbf{k}}|\nu|\phi_{c'\mathbf{k}'}\phi_{v'\mathbf{k}'}\rangle
$$
$$
- \langle\phi_{c\mathbf{k}}\phi_{c'\mathbf{k}'}|W|\phi_{v\mathbf{k}}\phi_{v'\mathbf{k}'}\rangle]A_{c'v'\mathbf{k}'}^{\lambda} = E_{\mathrm{exc}}^{\lambda}A_{cv\mathbf{k}}^{\lambda},
$$

$$(1)$$

where $\nu$ is the Coulomb kernel, $1/|r - r'|$, the eigenvectors $A_{cv\mathbf{k}}^{\lambda}$ correspond to the amplitudes of free electron–hole pair configurations composed of electron states $|\phi_{c\mathbf{k}}\rangle$ and hole states $|\phi_{v\mathbf{k}}\rangle$. *I.e.*, the excitonic wave function stands as

$$
\sum_{cv\mathbf{k}} A_{cv\mathbf{k}}^{\lambda}\phi_{c\mathbf{k}}\phi_{v\mathbf{k}}. \tag{2}
$$

The eigenenergies $E_{\mathrm{exc}}^{\lambda}$ correspond to the excitation energies (with optical gap $\Delta_{\mathrm{opt}}^{\mathrm{BSE}} \equiv E_{\mathrm{exc}}^{\lambda}$, for $\lambda$ from first nonzero transition, *i.e.*, first bright exciton). The difference $E_{\mathrm{b}} = \Delta^{\mathrm{GW,dir}} - \Delta_{\mathrm{opt}}^{\mathrm{BSE}}$ is called the exciton binding energy, where the "dir" index denotes a direct quasiparticle gap.

**19734** | *Phys. Chem. Chem. Phys.*, 2024, **26**, 19733–19741

This journal is © the Owner Societies 2024

# 3 Results and discussion

## 3.1 Geometrical structures and magnetic solutions

The already prepared precursor MAX phase $Mn_2GaC$ was measured to embody AFM behavior up to 507 K (Néel temperature),[20] local magnetic moments of $\sim 1.7\mu_B$ per Mn atom,[19] and have a lattice constant $a = 2.90$ Å both at 150 K[19] and room temperature.[18] During the etching processes, functional groups (–O, –F, –OH,) cover both sides of the clean MXene layers (realistically with some percentage of vacancies). It can be expected that the adsorption of termination groups can slightly alter the lattice constant of the parent MAX phase. It is then possible to obtain MXene sheets with depleted surface terminations. Recently, Persson et al.[53] have subjected the $Ti_3C_2T_x$ MXene to vacuum thermal treatment with subsequent exposure to $H_2$ gas and managed almost completely to deplete the surface of F-terminations. Oxygen terminations were removed only partly with the Ti : O ratio being 3 : 0.6 (i.e., 30% surface coverage). Further depletion of terminations may be possible at higher $H_2$ pressures than those accessible in the environmental transmission electron microscope (ETEM) used. All three mentioned stages of preparation can be seen in Fig. 1 (experimental lattice constant compared to our calculated ones for oxygen-terminated and clean MXene). For reasons stated above, every conformation or spin solution of $Mn_2CO_2$ discussed further has a fixed lattice constant, which belongs to the ground-state $Mn_2CO_2$ MXene.

In our investigation, we have created 6 different geometric conformers of $Mn_2CO_2$ MXene (Fig. 2). These conformers correspond to the T (trigonal) and H (hexagonal) structures of transition metal dichalcogenides and the numbers denote the positions of functional groups (oxygen in our case): hollow site (1), metal site (2), and carbon site (3). After conducting PBE relaxation on those conformers, we have found that the H1 one in its AFM state is energetically the most stable. T2, T3, H2, and H3 conformers were all significantly higher in energy, but the energy difference between T1-AFM and H1-AFM conformers was only 0.06 eV. We have therefore concluded that a closer look at those geometries and possible magnetic states is needed.

To learn more about magnetism in the $Mn_2CO_2$ system, we have created new spin solutions in $2 \times 2$ supercells ($Mn_8C_4O_8$) corresponding to both T1 and H1 structures, namely seven additional antiferromagnetic (AFM) and eight additional ferrimagnetic (FiM) conformers per geometry. The visualizations and labels (combining geometry from Fig. 2 and particular magnetic states, e.g., T1-AFM1) of all such spin conformers can be seen in the ESI† (Fig. S1–S4). With the inclusion of standard unit cells (simple $1 \times 1$ magnetic motifs, denoted as T1/H1-AFM0 and T1/H1-FM0), we obtained 34 structures in total, reducing finally to 28, because some spin states were identical to others due to symmetry. The first approach was to investigate the spin solutions with the GGA PBE density functional (ESI,† Table S1, the PBE ground-state was H1-AFM6 solution). However, the metallic nature of some spin states and the behavior of their band structures was finally classified as an artifact of GGA
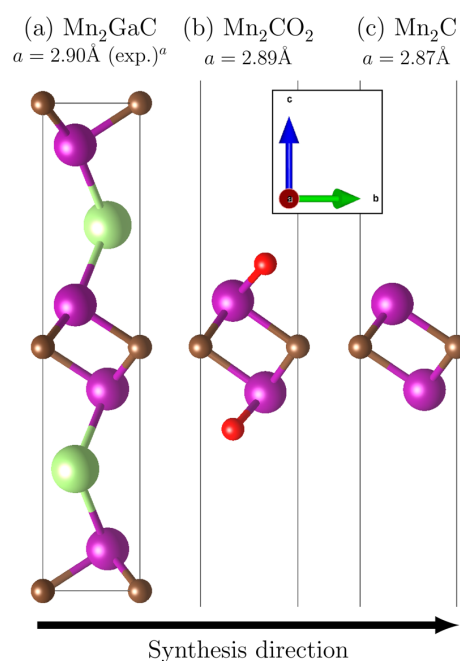


**Fig. 1** (a) $Mn_2GaC$ precursor MAX phase, (b) functionalized $Mn_2CO_2$ MXene, and (c) a clean $Mn_2C$ sheet, all with highlighted unit cell boundaries. Purple atoms = Mn, brown = C, red = O, and light green = Ga. The black arrow signifies the typical progression of MXene's preparation stages. $^a$Experimental results measured at room temperature and at 150 K.[18,19]
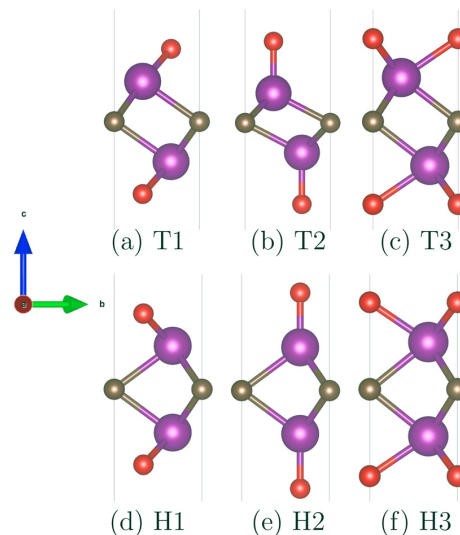


**Fig. 2** Trigonal (T) and hexagonal (H) geometric conformations of $Mn_2CO_2$ with varying positions (1–3) of oxygen atoms. Purple atoms = Mn, brown = C, and red = O.

PBE band underestimation (see more details in the ESI†), and a more reasonable meta-GGA SCAN density functional was used. The use of a meta-GGA functional for $2 \times 2$ supercells with

This journal is © the Owner Societies 2024

Phys. Chem. Chem. Phys., 2024, **26**, 19733–19741 | **19735**

**Table 1** Relative energies (R.E.) per unit ($1 \times 1$) cell at the level of *meta*-GGA SCAN density functional and hybrid functional HSE06 for T1 and H1 $Mn_2CO_2$ conformers and all 28 calculated spin solutions. Each column of relative energies is followed by an indirect ($E_g^{indir}$) and direct ($E_g^{dir}$) electronic band gap at the corresponding level of theory. The lattice constant is fixed at $a = 2.89$ Å for all solutions. For spin-polarized FM and FiM solutions, the lower value of the band gap is reported. All energies are presented in eV

| Phase | SCAN | | HSE06 | |
|---|---|---|---|---|
| | R.E. | $E_g^{indir}$ ($E_g^{dir}$) | R.E. | $E_g^{indir}$ ($E_g^{dir}$) |
| T1-AFM1 | 0.000 | 0.73 (0.92) | 0.000 | 1.53 (1.61) |
| T1-FiM6 | 0.017 | 0.73 (0.87) | 0.051 | 0.86 (1.40) |
| H1-AFM1 | 0.018 | 0.26 (0.41) | 0.072 | 0.68 (1.03) |
| T1-AFM2 | 0.023 | 0.86 (1.13) | 0.043 | 1.48 (1.95) |
| T1-AFM3 | 0.024 | 0.64 (1.03) | 0.096 | 0.76 (1.45) |
| T1-FiM3 | 0.031 | 0.66 (0.66) | 0.078 | 0.80 (1.21) |
| T1-AFM4 | 0.037 | 0.58 (0.73) | 0.182 | 0.49 (1.12) |
| T1-FiM4 | 0.037 | 0.53 (0.70) | 0.140 | 0.63 (1.22) |
| T1-AFM5 | 0.041 | 0.74 (0.92) | 0.123 | 0.81 (1.46) |
| H1-FiM4 | 0.042 | 0.28 (0.48) | 0.109 | 0.51 (0.99) |
| H1-FiM3 | 0.043 | 0.28 (0.51) | 0.103 | 0.33 (0.76) |
| T1-FiM5 | 0.046 | 0.64 (0.76) | 0.104 | 0.87 (1.31) |
| H1-AFM3 | 0.047 | 0.40 (0.79) | 0.124 | 0.77 (1.37) |
| H1-AFM2 | 0.049 | 0.38 (0.78) | 0.131 | 0.51 (0.89) |
| T1-FiM1 | 0.049 | 0.37 (0.52) | 0.168 | 0.50 (1.08) |
| H1-FiM1 | 0.053 | 0.37 (0.65) | 0.130 | 0.66 (0.96) |
| H1-FiM5 | 0.056 | 0.52 (0.75) | 0.144 | 0.47 (0.96) |
| T1-FiM2 | 0.056 | 0.54 (0.54) | 0.110 | 0.91 (1.17) |
| H1-AFM6 | 0.057 | 0.58 (1.03) | 0.172 | 0.88 (1.60) |
| H1-FiM8 | 0.057 | 0.41 (0.88) | 0.153 | 0.74 (1.30) |
| T1-FiM7 | 0.057 | 0.83 (0.95) | 0.115 | 0.98 (1.52) |
| H1-FiM2 | 0.060 | 0.48 (0.55) | 0.131 | 0.51 (0.89) |
| H1-FiM7 | 0.067 | 0.50 (0.90) | 0.173 | 0.74 (1.22) |
| H1-FM0 | 0.069 | 0.45 (0.45) | 0.126 | 0.41 (0.85) |
| H1-AFM7 | 0.069 | 0.67 (1.07) | 0.187 | 1.05 (1.60) |
| T1-FM0 | 0.079 | 0.47 (0.47) | 0.125 | 0.98 (1.11) |
| H1-AFM0 | 0.082 | 0.70 (1.06) | 0.203 | 0.98 (1.62) |
| T1-AFM0 | 0.085 | 1.25 (1.11) | 0.139 | 1.57 (2.13) |

20 atoms in the computational cell was a reasonable choice because *meta*-GGA SCAN functionals often provide band gaps that are in good agreement with DFT+$U$ or hybrid functionals with only a marginal increase in computational time compared to GGA density functionals (see also the discussion below). The final energetics and band gaps provided by the SCAN density functional are collected in Table 1, and the top six conformers are visualized in Fig. 3. Note that the lattice constant of all spin solutions corresponds to the ground state. Table 1 also includes results based on additional hybrid density functional HSE06 calculations.

The ground state corresponds to the T1-AFM1 conformer (Table 1; in contrast to the PBE results of Table S1, ESI†): trigonal geometrical structure with terminal oxygen atoms in hollow sites and spins localized on Mn atoms in spin-up/spin-down zigzag lines. The T1-AFM1 solution is the ground state at both SCAN and HSE06 levels of theory. The order of other spin states is slightly altered, but the top six spin solutions remain on top, and the energy differences between individual solutions increased significantly when the HSE06 density functional was used. Speculatively, a higher, more correlated level of theory could make T1-AFM1 an even more pronounced ground state. These results agree well with recent theoretical studies showing ground-state spin configuration equivalent to our T1-AFM1.[25,45]
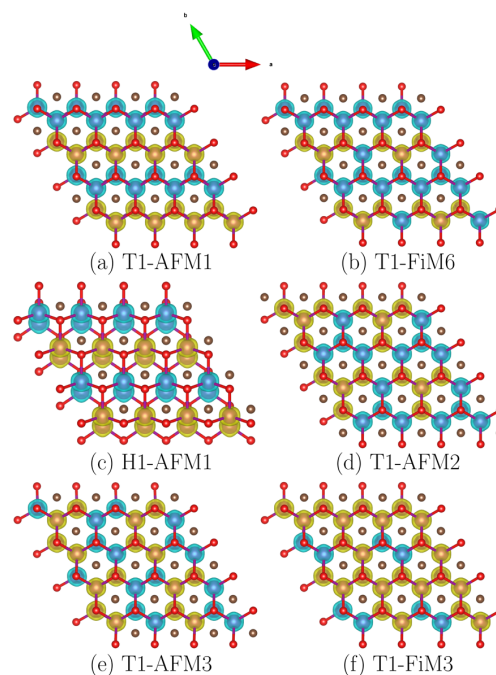


**Fig. 3** Top six most energetically favorable spin solutions for the $Mn_2CO_2$ MXene. Different colors correspond to spin density – the residual spin-up (yellow) or spin-down (blue) on each transition metal. The color code for individual atoms is identical to Fig. 2.

On the other hand, predicted ferromagnetic ground-state and conducting antiferromagnetic states in other studies[24] can be the result of a limited search at the PBE level with different geometries. Interestingly, our original $1 \times 1$ unit cell conformers (T1-FM0, T1-AFM0, and H1-AFM0) are the lowest ones in Table 1, implying that the investigation of only the unit cell of $Mn_2CO_2$ is leading to biased knowledge: ferromagnetic solution (H1-FM0) would be the false ground state with a much smaller band gap than T1-AFM1. Allowing energy-lowering using the right spin ordering (supercell motifs) is crucial for studying the $Mn_2CO_2$ system, similarly to, *e.g.*, antiferromagnetic mackinawite FeS.[28] Such a trend of the antiferromagnetic state overtaking the ferromagnetic phase does not apply only to the oxygen-terminated MXene. As has been recently shown in multiple studies, even the precursor MAX phase $Mn_2GaC$ has an AFM ground-state when more complex spin motifs are taken into account.[18–20,54] The same result holds even for the clean $Mn_2C$ sheet, although both the MAX phase and $Mn_2C$ are conductors.[27,55,56] The semiconducting behavior is therefore only achieved by oxygen termination. The antiferromagnetic ground state can be then also seen in other non-terminated MXenes, such as two-, three-, or four-layer $Ti_nC_{n-1}$ sheets.[9–12]

As can be seen from Table 1, all $Mn_2CO_2$ conformers are semiconducting. We have also used the total energies to estimate the probabilities of $Mn_2CO_2$ in a given state, which were evaluated for different temperatures and can be seen in the last three columns of Table S2 in the ESI†: the simple

**19736** | *Phys. Chem. Chem. Phys.*, 2024, **26**, 19733–19741

This journal is © the Owner Societies 2024

Boltzmann factor prefers only the first conformer to appear at room temperature.

To confirm the stability of the conformers, more realistic energy differences, and their energy ordering, we have investigated the top five conformers (T1-AFM1, T1-FiM6, H1-AFM1, T1-AFM2, and T1-AFM3) using *ab initio* molecular dynamics simulations at 400 K. Results showing the mean energies with the highlighted standard deviation can be seen in the ESI.† From these results, we can conclude that the molecular dynamics simulations indicate no phase change under 400 K. *I.e.*, the T1-AFM1 is confirmed as the ground-state conformer. This is in line with the experimentally prepared parent $Mn_2GaC$ MAX phase holding AFM ordering at higher temperatures with a Néel temperature of 507 K.[20] We have also calculated the phonon dispersion spectra for some of these conformers to further confirm their stability (see the ESI† for no negative frequencies appearance). Due to small total energy differences (*ca.* 0.017 eV), $Mn_2CO_2$ MXene is, therefore, a promising material with its potential AFM-FiM switching properties: the energetically lowest stable antiferromagnetic conformer is the T1-AFM1 conformer (the electronic ground state), and the lowest stable ferrimagnetic conformer is the T1-FiM6 conformer (the electronic first excited state), both with the same geometry (T1) differing just in the magnetic motif (*cf.* Fig. 3).

Furthermore, the biaxial strain on the five energetically most favorable configurations was simulated to see how the indirect and direct electronic band gap changes. The results of these strain calculations can be seen in the ESI,† Fig. S10 – we have also marked the $\Gamma$-point gap to see where the direct electronic band gap moves to a different point in *k*-space. From the results, we can see that the T1-AFM2 configuration should undergo a transition to direct material under −4% compressive strain. Interesting is the result for the configuration H1-AFM1 which exhibits conducting behavior under strain as the indirect gap vanishes. This behavior is similar to the $Ti_2CO_2$ MXene, for which the direct band gap also decreases to zero under compressive −4% biaxial strain.[57,58]

### 3.2 Density functional theory analysis of the ground state configuration

For a further in-depth study of $Mn_2CO_2$, we have decided only to focus on the ground-state configuration T1-AFM1. We have made this decision because the energy difference between the top two configurations (0.017 eV) is the largest of all tested configurations, with the rest being mostly in the range of 3–8 meV and the smallest being only 0.1 meV. This decision is further confirmed by our molecular dynamics results discussed above. Also, Table 1 shows that the individual energy levels are spaced further apart when a hybrid HSE06 density functional is used. The energy difference between the ground state and the second spin solution is then increased more than two-fold. Lastly, the reason for focusing only on the ground state was that the following GW + BSE calculations are highly computationally demanding.

We present the SCAN and additional HSE06 band structures and phonon dispersion spectra of the ground-state conformer

T1-AFM1 of $Mn_2CO_2$ in Fig. 4. The bands corresponding to a different spin are not distinguishable in the spin-polarized band structure near the Fermi level due to the antiferromagnetic nature of the material. We can observe quite flat bands around the Fermi level and an indirect band gap with the smallest energy transition being from the $\Gamma$ point to near the $K$ point. Based on the recommended values of the Hubbard correction $U$ for the Mn-based MXenes from previous studies,[45,54,56] we conclude from band structures (Fig. S11, ESI†) and band gaps (Table S3, ESI†) that PBE+$U$ ($U$ = 3 eV) corresponds well with a non-empiric SCAN approach without any $U$ correction. This agreement can be further seen in the partial density of states (PDOS; Fig. S12, ESI†) where the oxygen contribution to the valence states using the SCAN functional corresponds well with the PBE+$U$ (3 eV), and treatment of 3d orbitals from SCAN seems consistent with PBE+$U$ (3 eV), while over-performed by PBE and underestimated by HSE06. Moreover, the magnetic moments provided by SCAN density functional ($\sim 2.7\mu_B$ per Mn atom; Table S3, ESI†) are smaller than the ones from PBE+$U$ (3 eV) or HSE06 functionals ($\sim 3\mu_B$), which is the right trend compared to experimental measurements on the $Mn_2GaC$ MAX precursor. SCAN density functional, therefore, seems suitable for the DFT description of the Mn-based MXenes. Based on the Bader charge analysis we can conclude that the manganese atoms lose approximately 1.7$e$ (charge of an electron) by bonding to the $Mn_2CO_2$. On the
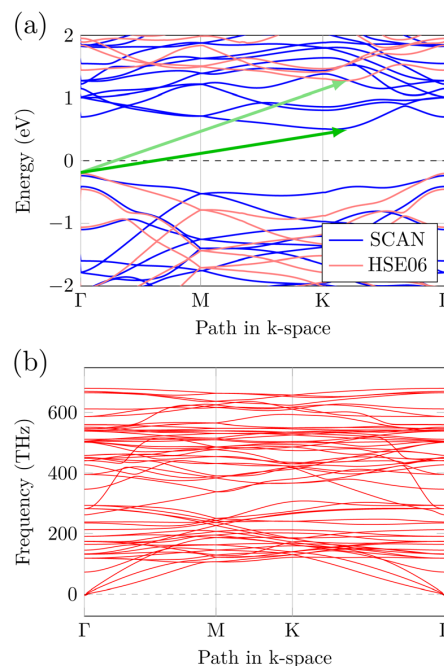


Fig. 4 (a) T1-AFM1 band structure at the *meta*-GGA SCAN density functional and hybrid HSE06 levels. The Fermi energy is set to zero. The green arrows in the band structures signify the HSE06 and SCAN indirect electronic band gap. (b) Phonon dispersion spectra of T1-AFM1 show no signs of instability.

This journal is © the Owner Societies 2024

*Phys. Chem. Chem. Phys.*, 2024, **26**, 19733–19741 | **19737**

other hand, each terminal oxygen has acquired a charge of $1e$ and a similar situation is for carbon atoms which gained approximately $1.4e$ of charge.

Because magnetism is the dominant feature of the $Mn_2CO_2$ material, we have investigated the magnetic anisotropy energy (MAE) for the T1-AFM1 conformation, which determines the orientation of the magnetization at low temperatures. We performed non-collinear total energy calculations with the inclusion of the spin–orbit coupling for a path between two spin orientations, $\theta = 90°$ and $\theta = 0°$, where the angles denote the magnetization in-plane and perpendicular to the monolayer MXene, respectively. The MAE is then calculated by

$$\text{MAE} = E(\theta = 90°) - E(\theta = 0°). \qquad (3)$$

Having the easy axis set to the $z$-direction ($\theta = 0°$), we have calculated the MAE of the $Mn_2CO_2$ MXene to be 0.25 meV per unit cell. The full dependence of the total energy on the angle $\theta$ is shown in Fig. 5. Therefore, the preferred direction of magnetization is along the easy axis. Interestingly, it has been shown that the pure monolayer $Mn_2C$ without terminations prefers the in-plane magnetization (with the MAE of $-0.09$ meV per unit cell),[56] similarly as the precursor MAX phase $Mn_2GaC$.[54] Our result corresponds quite well with a previous study where the MAE for $Mn_2CO_2$ has been calculated to be 0.18 meV per unit cell.[45] The MAE of 2D $Mn_2CO_2$ is larger than that of pure metals, such as Fe and Ni, as for them the reported values of MAE per unit cell are 1.4 μeV and 2.7 μeV, respectively.[59] These advantages render the MXene sheet a very promising candidate for AFM spintronic nanodevices.[45,56] It is obvious that the lowered dimensionality of 2D materials leads to an increase in MAE as a similar effect can be observed in various families of 2D materials.[60]

### 3.3 Many-body calculations

The acquisition of credible GW, and consequently BSE results is highly dependent on the appropriate convergence of the simulation parameters.[42–44] These parameters include the energy cutoff for the response function used in the GW calculation, $E_{cut}^{GW}$, the number of bands, $N_B$, the number of frequency grid points, $N_\omega$, the size of the $k$-point grid in the $xy$-direction or the inter-sheet distance in the $z$-direction. It has been recently
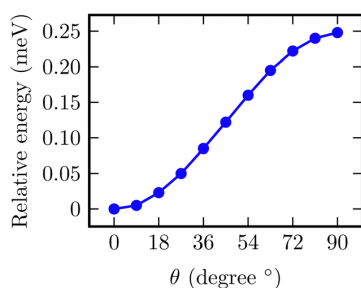
**Fig. 5** The angular dependence of the unit cell total energy for the T1-AFM1 conformation of the $Mn_2CO_2$ MXene. The $\theta$ is the angle between the magnetic moment and the normal to the monolayer plane.
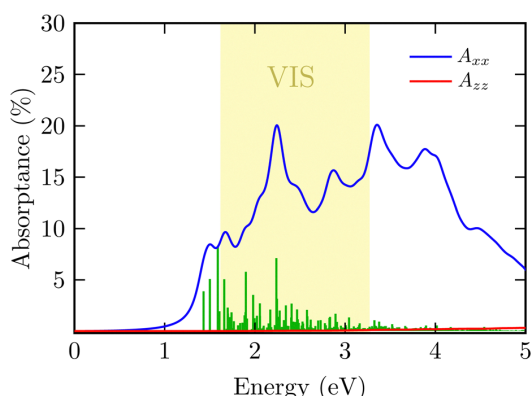
shown[44,61] how the inter-sheet distance can deform the lowest unoccupied orbitals and therefore give untrustworthy many-body results. We have therefore made a partial decomposition of bands to see how prominent the orbitals were in the $z$-direction. As it turned out, orbitals in our system were mostly localized on transition metals (see the ESI,† Fig. S13). During our convergence calculations, we observed that $Mn_2CO_2$ was highly sensitive to computational parameters used in the GW step. Quasiparticle (QP) band gap, and consequently optical gap, could vary significantly (in orders of electronvolts) if less strict parameters were used. Therefore, a careful approach to settings was essential.

The convergence of optical absorption spectra and optical gap $\Delta_{opt}^{BSE}$ with respect to the number of considered GW bands that are used in the solution of the BSE is reported in the ESI,† Fig. S14. As can be seen, 16 occupied and 20 virtual bands used in the BSE step were sufficient for reliable absorption spectra for photon energies up to 5 eV. Therefore, for all subsequent computations, these bands were used. In the ESI,† Fig. S15 are convergences of optical absorption spectra (for $A_{xx} = A_{yy}$) with respect to several computational parameters and the convergence characteristics of the QP band gap ($\Delta_f^{GW}$) and optical gap ($\Delta_{opt}^{BSE}$) on those same parameters. The benchmarking approach for $Mn_2CO_2$ was to use the number of bands $N_B = 3024$, GW energy cutoff $E_{cut}^{GW} = 200$ eV, $6 \times 6 \times 1$ $k$-point grid, the height of the computational cell of $L_z = 20$ Å and the number of frequency-dependent grid points $N_\omega = 128$, where the respective parameter was gradually changed in each convergence study. These parameters were used to avoid extremely demanding GW calculations. The obtained spectra show that in almost all calculations we could observe an emergence of a new peak accompanied by a shift of $\Delta_{opt}^{BSE}$. The only exception was the convergence concerning the $k$-point grid, where we did not observe any significant changes in both $\Delta_f^{GW}$ and $\Delta_{opt}^{BSE}$. Usually $\Delta_f^{GW}$ is quite sensitive to change in the $k$-point grid.[43,44,62]

Both $\Delta_f^{GW}$ and $\Delta_{opt}^{BSE}$ converged sufficiently in most cases with the direct fundamental gap $\Delta_f^{GW}$ changing in the range of $\Delta_f^{GW} = 1.92$–$2.20$ eV and optical gap in the range $\Delta_{opt}^{BSE} = 1.44$–$1.65$ eV. The most problematic computational parameter for the estimation of $\Delta_f^{GW}$ was the height of the computational cell $L_z$, where the change in the gap across calculations was 0.21 eV. As the fundamental gap $\Delta_f^{GW}$ was not fully converged, we fitted the values with the linear fit[44,63–65]

$$\Delta_f^{GW}\left(\frac{1}{L_z}\right) = C\frac{1}{L_z} + \Delta_f^{GW}(0), \qquad (4)$$

where $C$ and $\Delta_f^{GW}(0)$ are fitting parameters. The extrapolation to the zero $1/L_z$ limit yielded the direct gap $\Delta_f^{GW}$ of 2.52 eV, therefore for the subsequent final estimation of the fundamental band gap a corresponding *a posteriori* rigid correction was used, by taking $\Delta_f^{GW}(0) - \Delta_f^{GW}(1/L_z) = 0.40$ eV, where $1/L_z = 0.04$ Å$^{-1}$ was used. Similarly we fitted the values of the optical gap $\Delta_{opt}^{BSE}$ with the linear fit and the extrapolation to the zero $1/L_z$ limit yielded $\Delta_{opt}^{BSE} = 1.43$ eV and therefore *a posteriori* rigid correction of $\Delta_{opt}^{BSE}(0) - \Delta_{opt}^{BSE}(1/L_z) = -0.11$ eV was used in the final estimation of the optical gap.

**19738** | *Phys. Chem. Chem. Phys.*, 2024, **26**, 19733–19741

This journal is © the Owner Societies 2024

**Fig. 6** Optical absorption spectrum ($A_{xx} = A_{yy}$) for monolayer T1-AFM1 at the level of $G_0W_0@SCAN+BSE$ and corresponding oscillator strengths. The yellow region signifies the visible electromagnetic spectrum. The results were obtained with a $6 \times 6 \times 1$ $k$-point grid, $E_{cut}^{GW} = 250$ eV, $L_z = 25$ Å, $N_B = 5904$, $N_\omega = 216$ and 16 occupied and 20 unoccupied bands used in the final BSE step.

Following from the presented convergence results we can see that for the final production estimate the settings of $N_B = 5904$, $E_{cut}^{GW} = 250$ eV, $6 \times 6 \times 1$ $k$-point grid, $L_z = 25$ Å and $N_\omega = 216$ are sufficient for precise results. With this calculation, we can arrive at the final production estimate (with the correction to $L_z$) of the direct (d) and indirect (i) GW quasiparticle band gap for a monolayer $Mn_2CO_2$ MXene of

$$\Delta_f^{GW,d} = 2.39 \text{ eV}$$

$$\Delta_f^{GW,i} = 2.05 \text{ eV}, \quad (5)$$

and the estimate of the BSE optical gap (again with the corresponding correction to $L_z$)

$$\Delta_{opt}^{BSE} = 1.32 \text{ eV}. \quad (6)$$

From the direct QP gap and optical gap the first exciton binding energy consequently amounts to $E_b^{BSE} = 1.07$ eV which is an unusually large amount as many 2D semiconductors show linear scaling between the $\Delta_f$ and $E_b$, $E_b \approx \Delta_f/4$, which is independent on the lattice configuration, bonding characteristics or topological properties.[66]

The final optical absorption spectrum in planes parallel and perpendicular to the MXene sheet is reported in Fig. 6. The visualized quantity is the absorptance $A(E) = 1 - \exp[-\varepsilon_2 E L_z/\hbar c]$,[67] where $E$ is the energy of an incoming photon, $\varepsilon_2$ is the imaginary part of the dielectric function, $\hbar$ is reduced Planck's constant, and $c$ is the speed of light. Absorptance in the visible spectrum of photon energy (1.63–3.26 eV) is from Fig. 6 estimated to amount to $A \approx 10$–20% which shows that $Mn_2CO_2$ could be a very good solar light absorber. Similar efficiency is observed for the absorptance of near UV radiation (up to 4.13 eV). Moreover, the visible radiation absorption fully covers the whole range which is a significant improvement over different MXenes (namely, Cr- or Sc-based) for which only a small region of the visible spectrum is absorbed and which
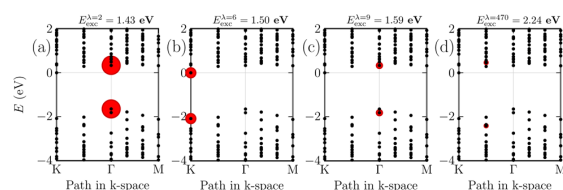


**Fig. 7** Quasi-particle (GW) band structure of T1-AFM1 $Mn_2CO_2$ MXene and all $|A_{cvk}^\lambda|$ coefficients for several bright excitons. The radii of colored circles represent coefficients. The Fermi energy is set to zero.

would make the potential photoabsorption devices less effective.[5] $Mn_2CO_2$ MXene is, therefore, a very promising material with its potential AFM-FiM switching properties (due to small total energy differences) and exceptional absorption efficiency.

Finally, we have analyzed (Fig. 7) the excitonic wave functions (eqn (2)) of four bright excitons important in the optical spectra (Fig. 6). The coefficients $|A_{cvk}^\lambda|$ correspond to the contribution of a given electron–hole pair at a certain $k$-point and band to the exciton wave function. Interestingly, for all excitons in Fig. 7 mostly only one electron–hole pair dominates the excitonic state. The first optical transition ($E_{exc}^{\lambda=2}$, as the exciton with the energy $E_{exc}^{\lambda=1}$ is dark) is dominated by the electron–hole pair in the highest occupied band and the lowest unoccupied band in the $\Gamma$ point while the second transition ($E_{exc}^{\lambda=6}$) is dominated by the pair in the $K$ point. This corresponds with the indirect character of $Mn_2CO_2$ and flat bands around the Fermi level.

# 4 Conclusions

We have systematically investigated geometrical and spin conformations of oxygen-terminated $Mn_2C$ MXene and performed subsequent many-body calculations to obtain reliable electronic and optical properties. The Mn-based MXenes show potential because of the broad palette of their magnetic phases, and the parent MAX phase was already prepared ($Mn_2GaC$).[18,20,21] Typical calculations from basic (GGA) density functional theory (DFT) indicated the conducting behavior of $Mn_2CO_2$,[14,24] while recent studies predicted it was also semiconducting.[5,25–27,45] To reconcile such uncertainties, we systematically generated a large set of $Mn_2CO_2$ magnetic solutions using *meta*-GGA density functional SCAN and hybrid density functional HSE06, proving that all conformers embody the semiconducting behavior (while the band gap varied). Different magnetic states and geometrical conformations were energetically very close, but molecular dynamics simulations have shown us that even at room temperature there should be no spontaneous phase switching. The ground-state $Mn_2CO_2$ conformation is trigonal geometry with terminal oxygen atoms in hollow sites and antiferromagnetic (AFM) spin alignment of Mn atoms in spin-up/spin-down zigzag lines. The AFM ground state is, therefore, consistent with the experimentally prepared parent MAX phase $Mn_2GaC$ (AFM ordering up to a Néel

temperature of 507 K)[20] and even with the clean non-terminated MXene sheet $Mn_2C$. Moreover, this configuration exhibits a strong preference for the magnetization direction along the $z$-axis with magnetic anisotropy energy (MAE) 0.25 meV. Ignoring local magnetic motifs (unit cell use) led to the wrong ferromagnetic ground state with different electronic properties and allowing the energy lowering by supercell motifs was fundamental for the $Mn_2CO_2$ material.

For the ground state, we performed a series of subsequent many-body GW and Bethe–Salpeter equation (BSE) calculations. We showed the $Mn_2CO_2$ was an indirect semiconductor with a fundamental gap of 2.1 eV (and a direct gap of 2.4 eV) and the first bright optical transition at 1.3 eV. The binding energy of the first exciton (1.1 eV) is very high and is almost half of the direct gap. Unlike other MXenes, $Mn_2CO_2$ absorbs the whole visible light range and near UV range efficiently (between 10–20%). We can therefore classify the $Mn_2CO_2$ MXene as a semiconducting antiferromagnet and efficient visible light absorber.

## Data availability

The data supporting this article have been included as part of the ESI.†

## Conflicts of interest

There are no conflicts to declare.

## Acknowledgements

## Notes and references

1 *2D Metal Carbides and Nitrides (MXenes)*, ed. B. Anasori and Y. Gogotsi, Springer, Switzerland, 2020.

2 K. Hantanasirisakul and Y. Gogotsi, *Adv. Mater.*, 2018, **30**, 1804779.

3 B. Anasori and Y. Gogotsi, *Graphene 2D Mater.*, 2022, **7**, 75–79.

4 K. R. G. Lim, M. Shekhirev, B. C. Wyatt, B. Anasori, Y. Gogotsi and Z. W. Seh, *Nat. Synth.*, 2022, **1**, 601–614.

5 T. Ketolainen and F. Karlický, *J. Mater. Chem. C*, 2022, **10**, 3919–3928.

6 C. Si, J. Zhou and Z. Sun, *ACS Appl. Mater. Interfaces*, 2015, **7**, 17510–17515.

7 Y. Zhang and F. Li, *J. Magn. Magn. Mater.*, 2017, **433**, 222–226.

8 H. Tan, C. Wang, H. Duan, J. Tian, Q. Ji, Y. Lu, F. Hu, W. Hu, G. Li, N. Li, Y. Wang, W. Chu, Z. Sun and W. Yan, *ACS Appl. Mater. Interfaces*, 2021, **13**, 33363–33370.

9 B. Vénosová and F. Karlický, *Phys. Chem. Chem. Phys.*, 2024, **26**, 18500–18509.

10 P. Lv, Y.-L. Li and J.-F. Wang, *Phys. Chem. Chem. Phys.*, 2020, **22**, 11266–11272.

11 T. Gorkan, H. Arkin and E. Aktürk, *Phys. Chem. Chem. Phys.*, 2022, **24**, 2465–2475.

12 N. Garcia-Romeral, A. Morales-Garcia, F. Viñes, I. D. P. R. Moreira and F. Illas, *Phys. Chem. Chem. Phys.*, 2023, **25**, 17116–17127.

13 T. Sakhraoui and F. Karlický, *ACS Omega*, 2022, **7**, 42221–42232.

14 A. Champagne and J.-C. Charlier, *J. Phys.: Mater.*, 2020, **3**, 032006.

15 N. Kumar and F. Karlický, *Appl. Phys. Lett.*, 2023, **122**, 183102.

16 C. Xin, Z. Fan, Z. Sun, H. Li, G. Jin, F. Pan and Y. Sui, *Phys. Chem. Chem. Phys.*, 2023, **25**, 8676–8683.

17 C. Xin, B. Song, Y. Yin, A. Wang, Z. Sun, G. Jin, Y. Song and F. Pan, *Nanoscale*, 2023, **15**, 14923–14930.

18 A. Ingason, A. Petruhins, M. Dahlqvist, F. Magnus, A. Mockute, B. Alling, L. Hultman, I. Abrikosov, P. Persson and J. Rosen, *Mater. Res. Lett.*, 2014, **2**, 89–93.

19 M. Dahlqvist, A. S. Ingason, B. Alling, F. Magnus, A. Thore, A. Petruhins, A. Mockute, U. B. Arnalds, M. Sahlberg, B. Hjörvarsson, I. A. Abrikosov and J. Rosen, *Phys. Rev. B*, 2016, **93**, 014410.

20 I. P. Novoselova, A. Petruhins, U. Wiedwald, Á. S. Ingason, T. Hase, F. Magnus, V. Kapaklis, J. Palisaitis, M. Spasova, M. Farle, J. Rosen and R. Salikhov, *Sci. Rep.*, 2018, **8**, 2637.

21 E. B. Thorsteinsson, A. S. Ingason and F. Magnus, *Phys. Rev. Mater.*, 2023, **7**, 034409.

22 A. Mockute, P. O. Å. Persson, F. Magnus, A. S. Ingason, S. Olafsson, L. Hultman and J. Rosen, *Phys. Status Solidi RRL*, 2014, **8**, 420–423.

23 R. Salikhov, R. Meshkian, D. Weller, B. Zingsem, D. Spoddig, J. Lu, A. S. Ingason, H. Zhang, J. Rosen, U. Wiedwald and M. Farle, *J. Appl. Phys.*, 2017, **121**, 163904.

24 V. V. Kozak, N. A. Fedorova, J. S. Olshevskaya, A. V. Kovaleva, A. A. Shubin, A. S. Tarasov, S. N. Varnakov, S. G. Ovchinnikov, F. N. Tomilin and P. V. Avramov, *Comput. Condens. Matter*, 2023, **35**, e00806.

25 P. Gao, M. Song, X. Wang, Q. Liu, S. He, Y. Su and P. Qian, *Nanomaterials*, 2022, **12**, 556.

26 Z. Chen, S. Huang, X. Yuan, X. Gan and N. Zhou, *Appl. Surf. Sci.*, 2021, **544**, 148861.

27 Y. Zhou and X. Zu, *Electrochim. Acta*, 2017, **235**, 167–174.

28 M. Kolos, D. Tunega and F. Karlický, *Phys. Chem. Chem. Phys.*, 2020, **22**, 23258–23267.

29 L. Hedin, *Phys. Rev.*, 1965, **139**, A796–A823.

30 H. Bethe and E. Salpeter, *Phys. Rev.*, 1951, **82**, 309–310.

31 G. Kresse and J. Hafner, *Phys. Rev. B: Condens. Matter Mater. Phys.*, 1993, **48**, 13115–13118.

32 G. Kresse and J. Furthmüller, *Comput. Mater. Sci.*, 1996, **6**, 15–50.

33 G. Kresse and J. Furthmüller, *Phys. Rev. B: Condens. Matter Mater. Phys.*, 1996, **54**, 11169–11186.

19740 | *Phys. Chem. Chem. Phys.*, 2024, **26**, 19733–19741

This journal is © the Owner Societies 2024

34 G. Kresse and J. Hafner, *J. Phys.: Condens. Matter*, 1994, **6**, 8245–8257.

35 P. E. Blöchl, *Phys. Rev. B: Condens. Matter Mater. Phys.*, 1994, **50**, 17953–17979.

36 J. P. Perdew, K. Burke and M. Ernzerhof, *Phys. Rev. Lett.*, 1996, **77**, 3865–3868.

37 J. Sun, A. Ruzsinszky and J. P. Perdew, *Phys. Rev. Lett.*, 2015, **115**, 036402.

38 See VASP manual at **https://www.vasp.at** for definitions and versions of PAWs in VASP.

39 A. Togo and I. Tanaka, *Scr. Mater.*, 2015, **108**, 1–5.

40 M. Shishkin and G. Kresse, *Phys. Rev. B: Condens. Matter Mater. Phys.*, 2006, **74**, 035101.

41 M. Kolos and F. Karlický, *Phys. Chem. Chem. Phys.*, 2019, **21**, 3999–4005.

42 M. Kolos and F. Karlický, *Phys. Chem. Chem. Phys.*, 2022, **24**, 27459–27466.

43 M. Dubecký, F. Karlický, S. Minárik and L. Mitas, *J. Chem. Phys.*, 2020, **153**, 184706.

44 M. Dubecký, S. Minárik and F. Karlický, *J. Chem. Phys.*, 2023, **158**, 054703.

45 J. He, P. Lyu and P. Nachtigall, *J. Mater. Chem. C*, 2016, **4**, 11143–11149.

46 J. Sun, R. C. Remsing, Y. Zhang, Z. Sun, A. Ruzsinszky, H. Peng, Z. Yang, A. Paul, U. Waghmare, X. Wu, M. L. Klein and J. P. Perdew, *Nat. Chem.*, 2016, **8**, 831–836.

47 Y. Cho, A. Nandy, C. Duan and H. J. Kulik, *J. Chem. Theory Comput.*, 2023, **19**, 190–197.

48 B. G. Janesko, *Chem. Soc. Rev.*, 2021, **50**, 8470–8495.

49 P. Liao and E. A. Carter, *Phys. Chem. Chem. Phys.*, 2011, **13**, 15189–15199.

50 M. Grumet, P. Liu, M. Kaltak, J. Klimeš and G. Kresse, *Phys. Rev. B*, 2018, **98**, 155143.

51 J. Kalmár and F. Karlický, *J. Appl. Phys.*, 2024, **135**, 244302.

52 S. Albrecht, L. Reining, R. Del Sole and G. Onida, *Phys. Rev. Lett.*, 1998, **80**, 4510–4513.

53 I. Persson, J. Halim, H. Lind, T. W. Hansen, J. B. Wagner, L.-Å. Näslund, V. Darakchieva, J. Palisaitis, J. Rosen and P. O. Å. Persson, *Adv. Mater.*, 2019, **31**, 1805472.

54 M. Dahlqvist and J. Rosen, *Sci. Rep.*, 2020, **10**, 11384.

55 X. Zhang, W. Meng, T. He, L. Jin, X. Dai and G. Liu, *Appl. Surf. Sci.*, 2020, **503**, 144091.

56 L. Hu, X. Wu and J. Yang, *Nanoscale*, 2016, **8**, 12939–12945.

57 Y. Min Ding, X. Nie, H. Dong, N. Rujisamphan and Y. Li, *Nanoscale Adv.*, 2020, **2**, 2471–2477.

58 X.-H. Li, R.-Z. Zhang and H.-L. Cui, *ACS Omega*, 2020, **5**, 18403–18410.

59 G. H. O. Daalderop, P. J. Kelly and M. F. H. Schuurmans, *Phys. Rev. B: Condens. Matter Mater. Phys.*, 1990, **41**, 11919–11937.

60 X. Jiang, Q. Liu, J. Xing, N. Liu, Y. Guo, Z. Liu and J. Zhao, *Appl. Phys. Rev.*, 2021, **8**, 031305.

61 R. Fanta and M. Dubecký, *J. Phys.: Mater.*, 2023, **6**, 045004.

62 D. Y. Qiu, F. H. da Jornada and S. G. Louie, *Phys. Rev. Lett.*, 2013, **111**, 216805.

63 N. Berseneva, A. Gulans, A. V. Krasheninnikov and R. M. Nieminen, *Phys. Rev. B: Condens. Matter Mater. Phys.*, 2013, **87**, 035404.

64 J.-H. Choi, P. Cui, H. Lan and Z. Zhang, *Phys. Rev. Lett.*, 2015, **115**, 066403.

65 F. Karlický and J. Turoň, *Carbon*, 2018, **135**, 134–144.

66 Z. Jiang, Z. Liu, Y. Li and W. Duan, *Phys. Rev. Lett.*, 2017, **118**, 266401.

67 T. Ketolainen, N. Macháčová and F. Karlický, *J. Chem. Theory Comput.*, 2020, **16**, 5876–5883.

This journal is © the Owner Societies 2024

*Phys. Chem. Chem. Phys.*, 2024, **26**, 19733–19741 | 19741